MECHANICAL AND BIOLOGICAL BEHAVIORS OF TITANIA AND TANTALA NANOTUBULAR ARRAYS DECORATED WITH SILVER OXIDE ON Ti-6Al-4V ALLOY

MASOUD SARRAF

FACULTY OF ENGINEERING
UNIVERSITY OF MALAYA
KUALA LUMPUR

2017

MECHANICAL AND BIOLOGICAL BEHAVIORS OF TITANIA AND TANTALA NANOTUBULAR ARRAYS DECORATED WITH SILVER OXIDE ON Ti-6Al-4V ALLOY

MASOUD SARRAF

THESIS SUBMITTED IN FULFILMENTOF THE REQUIREMENTS FOR THE DEGREE OF DOCTOR OF PHILOSOPHY IN MECHANICAL ENGINEERING

FACULTY OF ENGINEERING
UNIVERSITY OF MALAYA
KUALA LUMPUR

2017

UNIVERSITY OF MALAYA

ORIGINAL LITERARY WORK DECLARATION

Name of Candidate: Masoud Sarraf

Matric No: KHA130095

Name of Degree: PhD of Engineering

Title of Project Paper/Research Report/Dissertation/Thesis ("this Work"):

"Mechanical and Biological Behaviors of Titania and Tantala Nanotubular Arrays decorated with Silver Oxide on Ti-6Al-4V Alloy"

Field of Study: Advance materials/Nanomaterials

I do solemnly and sincerely declare that:

(1) I am the sole author/writer of this Work;
(2) This Work is original;
(3) Any use of any work in which copyright exists was done by way of fair dealing and for permitted purposes and any excerpt or extract from, or reference to or reproduction of any copyright work has been disclosed expressly and sufficiently and the title of the Work and its authorship have been acknowledged in this Work;
(4) I do not have any actual knowledge nor do I ought reasonably to know that the making of this work constitutes an infringement of any copyright work;
(5) I hereby assign all and every rights in the copyright to this Work to the University of Malaya ("UM"), who henceforth shall be owner of the copyright in this Work and that any reproduction or use in any form or by any means whatsoever is prohibited without the written consent of UM having been first had and obtained;
(6) I am fully aware that if in the course of making this Work I have infringed any copyright whether intentionally or otherwise, I may be subject to legal action or any other action as may be determined by UM.

Candidate's Signature Date:

Subscribed and solemnly declared before,

Witness's Signature Date:

Name:

Designation:

ABSTRACT

Ti-6Al-4V alloy is among the most widely-used metallic materials for orthopedic and dental application due to its desirable features such as high strength and low density. However, Ti-6Al-4V cannot meet all of the clinical necessities owing to the lack of osseointegration required for implant longevity. The current research aimed to employ a novel surface modification for development of two different metallic oxides, including TiO_2 and Ta_2O_5 nanotubes on biomedical-graded Ti-6Al-4V plates to improve the mechanical properties, tribological, corrosion behavior, osseointegration, and biocompatibility. The optimized self-organized TiO_2 nanotubular arrays were fabricated by electrochemical anodization, followed by heat treatment at 500°C for 1.5 h to improve the adhesion strength of nanotubular arrays. On the other hand, for development of well-adherent Ta_2O_5 nanotubular coatings, an optimized PVD approach to deposit the thin films tantalum followed by a two-step anodization were performed. To improve the adhesion of nanotubular arrays, heat treatment was carried out at 450°C for 1 hour. Moreover, for improving the antibacterial properties of these two coatings, the Ag_2O nanoparticles were decorated on the nanotube edges via PVD magnetron sputtering approach. The adhesion strengths between the coatings and substrates were evaluated using a microscratch tester under different conditions. The surface topography of the nanostructured coatings was examined by atomic force microscopy (AFM) and field emission scanning electron microscopy (FESEM). The X-ray diffractometry (XRD), energy dispersive X-ray spectroscopy (EDS) and X-ray electron spectroscopy (XPS) were also utilized to investigate the chemical composition of the developed thin films. The corrosion behavior, wear resistance, hardness, surface wettability, in-vitro bioactivity in simulated body fluids (SBF), antibacterial characteristics and biocompatibility of the products were also investigated in order to provide a better understanding of the specimen function in physiological conditions. The effective sputter yield of tantalum during the

magnetron sputtering process was achieved with a DC power of 350W, temperature of 250°C and a deposition time of 6h. The anodization results showed that the time and electrolyte played a key role in the growth of TiO_2 and Ta_2O_5 NTs as well as their microstructural evolution. The optimum pore sizes of TiO_2 and Ta_2O_5 nanotubes were around 72nm and 40nm, while their lengths were identical (1µm). The scratch length, failure point, and adhesion strength of the annealed samples were 1000µm, 557.89µm, and 1814.28mN for TiO_2 NTs as well as 1024µm, 863µm, and 2301mN for Ta_2O_5 NTs respectively. The annealed coating showed the highest wettability (lowest contact angle value), tribology (lowest coefficient of friction), corrosion resistance (highest percentage of protection efficiency) and highest hardness value among the specimens. In-vitro bioactivity tests before and after deposition of Ag_2O NPs showed that the bone-like apatite layer was formed on nanotubular array coating as early as 1 day immersion in SBF, indicating the importance of nanotubular configuration of the in-vitro bioactivity. Finally, cell culture and antibacterial properties also showed promising results after decoration of Ag_2O NPs. This multi-step approach could be considered for the design of various nanostructured titanium implant surfaces.

ABSTRAK

Ti-6Al-4V adalah antara bahan logam yang sering digunakan dalam aplikasi Ortopedik dan pergigian. Hal ini demikian kerana, bahan logam ini mempunyai ciri-ciri yang dikehendaki seperti kekuatan tinggi dan kepadatan yang rendah. Walaubagaimanapun, logam Ti-6Al-4V tidak dapat memenuhi keperluan klinikal kerana kekurangan osseointegrasi yang diperlukan untuk jangka hayat implan. Oleh itu, penyelidikan terkini mensasarkan pengubahsuaian pada permukaan logam Ti-6Al-4V dengan menggunakan dua oksida logam yang berlainan iaitu TiO_2 dan Ti_2O_5 nanotiub. Tujuan pengubahsuaian ini adalah bagi memperbaiki sifat mekanikal bahan, tribologi, kakisan, osseointegrasi dan biokompatibilitas. Susunan nanotubular TiO_2 dihasilkan melalui teknik anodizing elektrokimia dan diikuti dengan rawatan haba pada suhu 500 °C selama 1.5 jam bagi meningkatkan tahap lekatan susunan nanotubular tersebut. Manakala, bagi menghasilkan lapisan Ta_2O_5 yang mempunyai tahap kelekatan yang tinggi, teknik PVD digunakan untuk mendeposit satu lapisan tantalum dan diikuti dengan dua langkah anodizing. Rawatan haba selama 1 jam pada suhu 450°C pula dilakukan pada nanotiub Ta_2O_5 bagi meningkatkan kekuatan lapisan nanotubular. Selain itu, sifat antibakteria pada kedua-dua salutan diperoleh dengan cara mendeposit Ag_2O nanopartikel pada bahagian tepi nanotiub dengan menggunakan kaedah PVD. Tahap kekuatan lekatam antara lapisan salutan dengan substrat dinilai dengan menggunakan alat mikro-calar. Permukaan topografi salutan pula diperiksa dengan menggunakan mikroskopi daya atom (AFM) dan pengimbasan elektron Mikroskop (FESEM). Tambahan pula, sinar-X difraktometer (XRD), sinar-X dispersif (EDS) dan sinar-X electron spektroskopi (XPS) digunakan bagi menyiasat komposisi kimia salutan tersebut. Tindak balas kakisan, rintangan haus, kekerasan, kelembapan permukaan, bioaktif dalam in vitro dalam cecair badan simulasi (SBF), ciri-ciri antibakteria dan biokompatibiliti produk juga disiasat untuk memberikan pemahaman yang lebih baik mengenai fungsi

spesimen dalam keadaan fisiologi. Selepas ujikaji, kami mendapati lapisan salutan tantalum yang paling berkesan diperoleh dalam keadaan proses kuasa DC 320 W, suhu 250 °C dalam masa 6 jam proses pendepositan. Hasil anodisasi menunjukkan bahawa masa dan elektrolit memainkan peranan utama dalam pertumbuhan dan evolusi mikrostruktural TiO_2 dan Ta_2O_5. Saiz lubang optimum bagi TiO_2 dan Ta_2O_5 nanotiub adalah sekitar 72nm dan 40nm dengan ukuran sama panjang iaitu 1µm. Panjang goresan, titik kegagalan lapisam dan kekuatan lekatan sampel yang dikenakan haba adalah 1000 µm, 557.89 µm dan 1814.28 mN untuk TiO_2 manakala 1024 µm, 863 µm dan 2301 mN untuk Ta_2O_5. Salutan yang telah dikenakan haba menunjukkan keboledapatan paling tinggi (nilao sudut sentuhan rendah), tribologi (pekali geseran terndah), rintangan kakisan (peratusan kecekapan perlindungan tertinggi) dan nilao kekerasan tertinggi berbanding dengan sampel-sampel yang lain. Ujian bioaktiviti in-vitro sebelum dan selepas deposit Ag_2O menunjukkan bahawa lapisan apatit terhasil di atas nanotubular seawall 1 hari di dalam rendama SBF. Hal ini membutikan bahawa pentingnya konfigurasi nanotubular dalam sel dan sifar-sifat antibakteria juga menunjukkan hasil yang menjanjikan selepas salutan ditambah dengan Ag_2O nanopartikel. Dengan hasil kajian yang telah ditunjukkan bahawa pendekatan pelbagai langkah ini boleh dipertimbangkan dalam mereka bentuk pelbagai struktur nano atas permukaan implan logam titanium.

ACKNOWLEDGEMENTS

I would like to acknowledge Associate Prof. Dr. Bushroa Binti Abdul Razak and Prof. Dr. Noor Hayaty Binti Abu Kasim for their invaluable guidance and support throughout my graduate study. I would like to thank Prof. Dr. Masjuki Bin Haji Hassan, Prof. Dr. Wan Jefrey Basirun and Prof. Dr. Shamala Devi A/P K.C Sekaran for allowing me to use their lab facilities. I also deeply appreciate Mr. Bahman Nasiri Tabrizi, Dr. Ali Dabbagh and Dr. Saeid Baradaran for their valuable help on my thesis. I would also like to thank all of my lab mates in my group. Without their suggestion and assistance during my graduate study period, I will not be able to finish my PhD degree. Finally, I would like to thank my family for their unending support and encouragement throughout my career. I would like to thank University of Malaya for the financial support offered by IPPP and HIR grant.

TABLE OF CONTENTS

LIST OF FIGURES

LIST OF TABLES

List of Symbols and Abbreviations

AFM	:	Atomic force microscopy
Ag	:	Silver
Ag_2O NPs	:	Silver oxide nanoparticles
ALP	:	Alkaline phosphatase
ANOVA	:	Analysis of variance
ARM	:	acoustic reflection mode
ARRM	:	Analysis, tridimensional force recording, acoustic reflection mode scanning microscope
BIC	:	Bone-implant contact
CAMHB	:	Cation-adjusted Mueller-Hinton broth
CFU	:	Colony-forming units
CLSM	:	Confocal laser scanning microscopy
COF	:	Coefficient of friction
CR	:	Corrosion rate
DMSO	:	Dimethyl sulfoxide
EC	:	Endothelial cells
ECM	:	Extracellular matrix
EDS	:	Energy dispersive X-ray spectroscopy
EG	:	Ethylene glycol
ELISA	:	Enzyme-linked immunosorbant assay
FBS	:	Fetal bovine serum
FESEM	:	Field emission scanning electron microscopy
FRA	:	Frequency response analyzer
HA	:	Hydroxyapatite
HOb	:	Human osteoblast
HF	:	Hydrofluoric acid
H&E	:	Hematoxylin and eoxin
IHC	:	Immunohistochemical
JCPDS	:	Joint Committee on Powder Diffraction and Standards
LbL	:	Layer-by-layer
MSC	:	Mesenchymal stem cells
NaOH	:	Sodium hydroxide
NT	:	Nanotube
NTAs	:	Nanotubular arrays
NAC		N-acetyl cysteine
NPs	:	Nanoparticles
OA	:	Orthogonal array
OCN	:	Osteocalcin
PBS	:	Phosphate buffer solution
PEG	:	Polyethylene glycol
PCR	:	Polymerase chain reaction
PIII	:	Plasma immersion ion implantation
PS	:	Penicillin-streptomycin
PSS	:	Polysodium styrenesulfonate
PVD	:	Physical vapor deposition
RF	:	Radio frequency
ROS	:	Reactive oxygen species
SBF	:	Simulated body fluid
SCE	:	Saturated calomel electrode

SD	:	Standard deviation
SEM	:	Standard error of mean
SPSS	:	Statistical Package for the Social Sciences
Ta	:	Tantalum
TEM	:	transmission electron microscopy
TNF	:	Tumor necrosis factor
Ta_2O_5 NTs	:	Tantalum pentoxide nanotubes
TiO_2 NTs	:	Titanium oxide nanotubes
TRAIL	:	TNF-related apoptosis-inducing ligand
TRAP	:	Tartrate-resistant acid phosphatase
UV	:	Ultraviolet visible
VSMC	:	Vascular smooth muscle cell
XPS	:	X-ray photoelectron spectroscopy
XRD	:	X-ray diffractometry

CHAPTER 1: INTRODUCTION

1.1 Background of Study

In recent years, the number of people demanding replacement of the missed or damaged tissue such as hip joints and teeth with artificial implants has significantly increased as a result of growing elderly population. Therefore over the past few decades, numerous attempts have been made to identify suitable biomaterials for fabrication of long lasting orthopedic implants.

Among various types of biomaterials, metals and their alloys are so far the most widely employed compounds employed for replacement of damaged hard tissues. In particular, pure titanium (Ti) and its biomedical-graded alloy with aluminum and vanadium (Ti-6Al-4V) have been widely utilized as load-bearing implants (Hsieh et al., 2002; Kawagoe et al., 2000; Nunamaker, 1985) due to their relatively higher biocompatibility, fatigue strength, corrosion resistance, formability, and lower modulus of elasticity. In contrast to those of conventional metallic implants such as stainless steel and cobalt-based alloys (Liu et al., 2004).

In spite of the intrinsic advantages of Ti-based compounds, further research is required to obtain higher clinical success rates when these materials are used in fabrication of load-bearing implants. When these materials are utilized for fabrication of orthopedic and dental implant, their low wear resistance, shear strength, and bonding strength to the hard tissue, as well as the lack of osseointegration may result in increased risk of implant loosening and thus hamper the restoration longevity (Kurella et al., 2006; Narayanan et al., 2007; Rack et al., 2006). This feature also leads to detrimental accumulation of wear debris and eventual ion, which are released into bio-systems

(Guleryuz et al., 2005). The release of aluminum and vanadium ions from the Ti-6Al-4V alloys may cause systemic or localized toxic effects in human body.

In order to overcome the chemical, mechanical, and biological limitations of Ti-based implants and improve their clinical longevity, various surface modifications are suggested. In particular, application of surface coatings has been shown as an effective approach to improve the implant functionality without a major alteration of the constituting material. The coating layer generally acts as a protective shield to minimize the tribo-corrosion and thus reduce the risks of implant loosening, local inflammation by the wear products, and toxicological effects of the released ions (Clem et al., 2008; Fauchais et al., 2012). The coating process must provide a homogeneous layer with excellent adhesion to the substrate. This is generally achieved by identification of the critical coating parameters and their optimization according to the desired coating characteristics.

The nanotubular coating structures produced by anodization have recently received increasing interest for fabrication of orthopedic and dental implants. A number of studies have indicated the significant influence of coating structure on the biocompatibility of metallic implants (Mour et al., 2010). In particular the nanotubular structure has been shown to enhance physical interlocked of the osteoblast cells on the implant surface. Moreover, the nanotubes could improve osseointegration via promoting formation and adhesion of a bone-like apatite layer (Brammer et al., 2008; Lamolle et al., 2009). Oh et al. (2006) reported a 400% increase of cell adhesion on the titanium oxide nanotubes (TiO_2 NTs) probably because of an increased mechanical interlocking of the cortical HA layer with the nanotubular structure (Oh et al., 2006).

Therefore, it is envisioned that application of both PVD and anodization as complementary approaches could aid in development of well-adherent coating layers

which exhibit high mechanical strength and corrosion resistance, while simultaneously present sufficient porosity to enhance the implant biocompatibility and bioactivity through promotion of hydroxyapatite (HA) formation and cell adhesion.

As mentioned, one of the possible solutions to improve the bone-implant contact and the healing process is the use of surface modification by bioceramic coatings on metal implants (Bobyn et al., 1980; Liu et al., 2010; Rack et al., 2006; Wu et al., 2015). However, low fracture toughness, delamination and cracking of the conventional ceramic coatings are great obstacles for their clinical application. Moreover, their low capability to tolerate the cyclic loading conditions applied during actual performance in human body remains challenging.

Recently, a novel approach for formation of a bioceramic coating on the metallic Ti-6Al-4V surfaces has been introduced which may overcome the limitations of the conventional ceramic coatings. In this technology, the bioceramic layer is created via oxidation of the own substrate material using anodization, and growing its thickness under controlled experimental conditions. The growth of TiO_2 thin film from the substrate surface could potentially result in higher adhesion strength compared to secondary coating materials and thus increase lifetime of the implant alloys. Moreover, the spontaneous creation of a passive TiO_2 layer could provide relatively higher inertness and biocompatibility (Raphel et al., 2016; Tang et al., 2016). This oxide layer could further be produced in nanotubular structure by incorporation of appropriate ions (e.g. F^-) into the electrolyte solution.

A number of studies have also suggested to coat other metallic oxides with relatively higher corrosion and wear resistances, mechanical strength, and bioactivities on the Ti-6Al-4V instead of TiO_2. Among all these bioactive metals with self-passivation capability, tantalum (Ta) and its oxides have gathered attention for bone repair application

in orthopedic, craniofacial, and dentistry literature over the past few years, due to their high hardness, fracture toughness, wear and corrosion resistance, bending strength, and low cost (e.g. compared to niobium which is also bioactive), (Balla et al., 2010a; Kato et al., 2000), which facilitate biological bonding to the natural hard tissue via the formation of a bone-like apatite layer (Balagna et al., 2012; Frandsen et al., 2014; Rahmati et al., 2016).

Self-passivation of Ta surface through formation of a stable oxide layer results in an excellent corrosion-erosion resistance in biological environment without significant weight or roughness change, compared to the conventional metallic implants (Allam et al., 2008; Balagna et al., 2012; Ruckh et al., 2008). Recent studies have shown that Ta based coatings exhibit relatively high corrosion resistance and wettability, low ion release and toxicity, (Sun et al., 2013), as well as high biocompatibility and excellent cellular adhesion (Balla et al., 2010b).

A dense non-porous tantalum pentoxide (Ta_2O_5) layer could directly be deposited on the substrates through PVD method in presence of oxygen. However, relatively high modulus of elasticity and bulk density of Ta-based biomaterials may intensify bone desorption and implant loosening, leading to increased risk of clinical failure (Balla et al., 2010a; Frandsen et al., 2014). Therefore, these materials are mostly applied as porous structures such as nanotubes (Ta_2O_5 NTs) (Balagna et al., 2012; Frandsen et al., 2014; Rahmati et al., 2016). For this aim, a pure metallic Ta layer is initially deposited on the substrate and subsequently, Ta_2O_5 NTs are produced via anodization, where their physical and mechanical features are controlled by adjustment of the anodization and subsequent annealing conditions. In contrast to dense Ta_2O_5 coatings, Ta_2O_5 NTs have shown higher osseointegration ability, resulting in enhanced fixation ratios (Balla et al., 2010a; Jafari et al., 2010; Sagomonyants et al., 2011).

1.2 Problem Statement

In spite of the intrinsic advantages of Ta_2O_5 NTs and their potential to enhance the chemo-mechanical and biological performance of Ti-6Al-4V substrates, little attention has been paid to fabrication of these nanotubular arrays on the surfaces of biomedical-graded titanium alloys via anodization of an as-deposited Ta coating. Moreover to the best of our knowledge, there are also no reports on the effect of subsequent annealing on the microstructural characteristics of Ta_2O_5 NT arrays.

Bacterial colonization is another challenging postoperative complication which may cause severe local pains and even fatalities (Gao et al., 2014). The implants are thus required to exhibit sufficient antibacterial characteristics in order to prevent formation of bacterial aggregations (Zhao et al., 2009). Ta_2O_5 NTs show insufficient antibacterial capability and little efforts have been made to enhance this characteristic. One particular approach for improvement of the antibacterial properties of these biomaterials is incorporation of antimicrobial agents such as inorganic silver (Ag) (Mei et al., 2014). However, the release rate of ions from Ag is generally fast, resulting in short-term antibacterial activity and increased cytotoxicity. This limitation thus necessitates an antibacterial compound with higher cytocompatibility and controlled ion release.

It is also important to note that although a large part of interest has been previously dedicated for self-assembling of different NT arrays (especially TiO_2 NTs) on the Ti-6Al-4V substrates, their relatively low adhesion to the substrates make them inapplicable in biomedical field. Therefore in order to reduce the risk of coating delamination, the critical anodization parameters need to be determined and optimized according to the desired coating characteristics.

1.3 Aim and Objectives

This study aims to develop thin films of well-adherent Ta_2O_5 NT arrays with decorated silver oxide nanoparticles (Ag_2O NPs) onto Ti-6Al-4V substrate in order to improve their biocompatibility, chemical stability, wettability, mechanical properties, wear and corrosion resistance. Various characteristics of the developed thin film of Ta_2O_5 NTs are further compared with a control group consist of TiO_2 NTs developed on similar substrates via an optimized anodization protocol. The objectives of this study are the followings:

1. To optimize the anodization and heat treatment procedures in order to obtain highly ordered, well-adherent TiO_2 NT arrays on the Ti-6Al-4V substrates with enhanced mechanical, tribological, and corrosion behaviors.
2. To fabricate Ta_2O_5 NT arrays onto Ti-6Al-4V surface with subsequent PVD, anodization, and heat treatment procedures as well as to optimize the fabrication parameters for improving their mechanical, tribological, and corrosion characteristics.
3. To decorate Ag_2O NPs on the edges of TiO_2 NTs and Ta_2O_5 NTs using PVD method.
4. To investigate the antibacterial, osseointegration, and biocompatibility of the nanotubular arrays with Ag_2O NPs decorated on their edges.

1.4 Research Contribution

The first phase of the present work dealt with fabrication of TiO_2 and Ta_2O_5 NT coatings with high adhesion to the Ti-6Al-4V substrate via optimization of both PVD and anodization protocols. The immediate outcome and contribution of this research to the world of knowledge comprises two research articles published in scientific journals.

The second phase of the project concentrated on endowing sufficient antibacterial properties to the nanotubular structures. However, instead of loading pure Ag nanoparticles as antibacterial agents and embedding those within the nanotube (NT) structure, silver oxide nanoparticles (Ag_2O NPs) were decorated on the NT edges using PVD magnetron sputtering to obtain sufficient antibacterial effect with reduced release rate of Ag+ ions and lower concentrations of the antibacterial compound. The microstructural, antibacterial, and in-vitro bioactivity of the fabricated thin film, as well as the viability and proliferation of human osteoblast cells on its surface were evaluated to provide a more detailed understanding on the bio-characteristics of the fabricated thin film on the Ti-6Al-4V surface. The outcome of this part of research has also been published in two research publications.

1.5 Research Scope

The present research aims to integrate the materials science and biomedical engineering to develop implants with desirable mechanical performance, low corrosion rate, and high antibacterial characteristics, while allowing osseointegration and formation of bone-like apatite layer. Development of such biomaterials requires optimization of the various experimental procedures such as PVD magnetron sputtering, anodization and annealing. The fabricated thin films needed to also be characterized in terms of morphological, chemical, mechanical, tribological, and biological behaviours. The morphological properties of the developed thin films were investigated using field emission scanning electron microscopy (FESEM). The X-ray diffractometry (XRD), energy dispersive spectroscopy (EDS), X-ray photoelectron spectroscopy (XPS) were employed for chemical analyses. The chemo-mechanical performance of the thin film was also evaluated by adhesion, wear, corrosion, and microhardnesss tests. E.coli and

human osteoblast (HOb) cells were cultured to respectively investigate the antibacterial capability and biocompatibility of the developed coatings. The possibility of formation of a bone-like apatite layer on the surfaces was also investigated in simulated body fluid (SBF). However, the in-vivo studies fall beyond the scope of this project and may be performed in further research.

1.6 Thesis Outline

In the current chapter, a brief introduction of the project concept was presented and the current challenges addressed in this research were explicated. Based on the existing limitations, the research objectives were clarified and the scope of this study was outlined. In chapter 2, a comprehensive background into the biomechanical performance of TiO_2 and Ta_2O_5 thin films on the Ti-6Al-4V substrates is presented. This chapter also covers a detailed review of various fabrication approaches for development of nanotubular structures on the Ti-6Al-4V substrates as well as the critical parameters which need to be controlled in order to achieve the desired morphological, mechanical, and biological properties. Chapter 3 presents the methodology used for preparation of TiO_2 NTs and Ta_2O_5 NTs on Ti-6Al-4V substrates, decoration of silver oxide nanoparticles on the nanotubular edges, as well as the characterization approaches employed for investigation of the chemical, morphological, tribological, mechanical, and biological properties of the developed coatings. Chapter 4 primary concerns analysis of various characteristics of the developed thin films and chapter 5 finally concludes the obtained results and provides recommendations for potential areas of research in further studies. The flow of the various project activities is summarized in Figure 1.1.

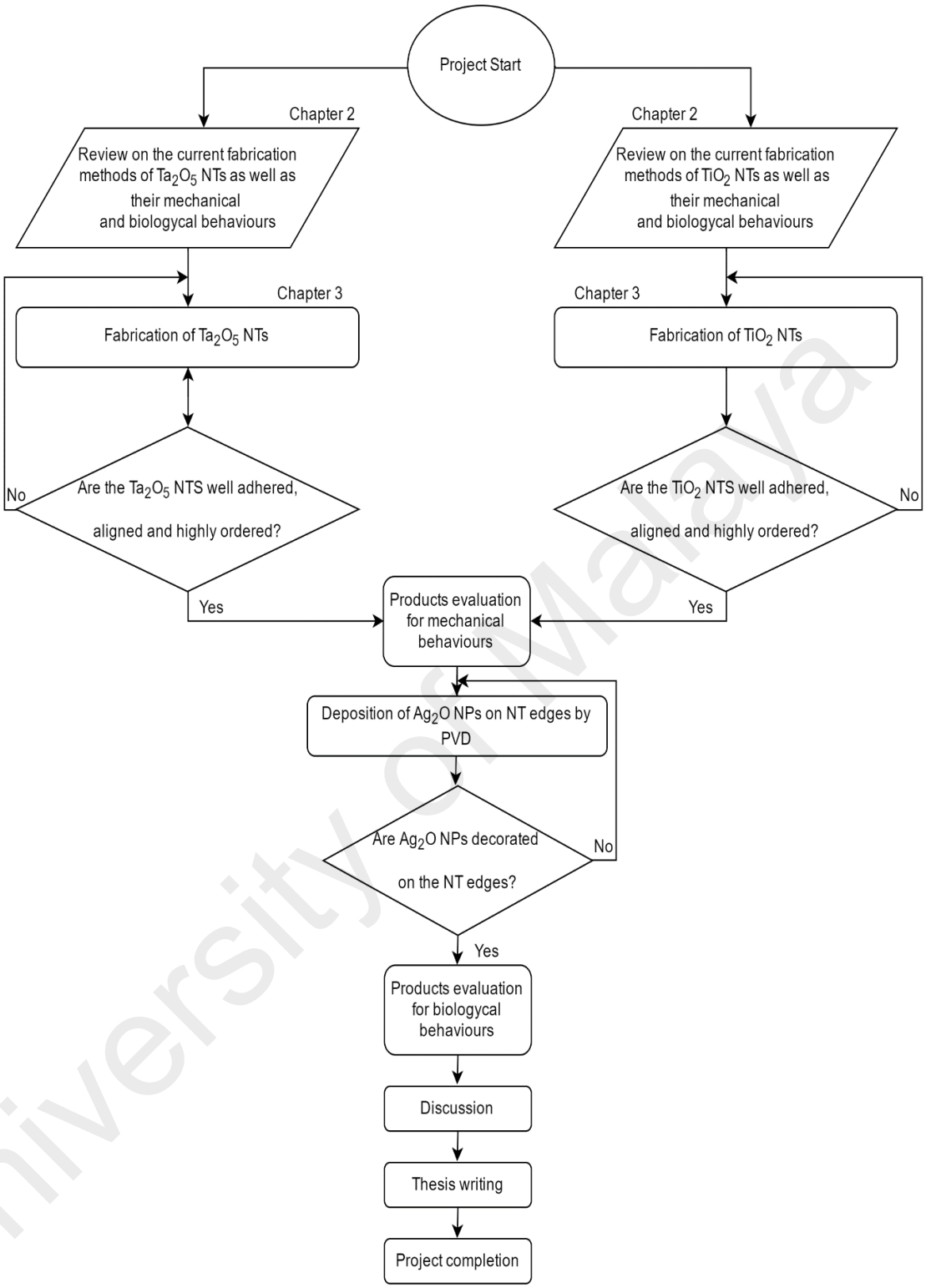

Figure. 1.1: The flow of the various project activities

CHAPTER 2: LITERATURE REVIEW

2.1 Introduction

Selection, development, or customization of appropriate materials according to each clinical case is one of the most challenging tasks in the biomaterials field. Titanium (Ti) and its alloys are among the most popular metallic compounds for fabrication of load bearing implants in dental and orthopedic applications due to their high biocompatibility, corrosion resistance, and mechanical strength. However, lack of a strong bonding between titanium and bone tissue and long-term degradation in physiological condition remain as crucial challenges which may possibly lead to implant loosening and thus increased risk of clinical failure. This matter is more critical when these metallic implants are used in joining points (Baradaran et al., 2014).

Bone comprises of around 70 wt. % carbonated apatite, wherein the inorganic mineral phase of bone (with approximately 20 to 40 nm length) is patterned uniquely inside the collagen network. Therefore, it is believed that an appropriate surface modification of the metallic implants for making their chemical and physical characteristics close to those of collagen and carbonated apatite, could aid in achievement of enhanced and faster bonding of these implants to the bone (Ambard et al., 2006; Legeros, 1988; Narayan, 2010; Wang et al., 2014). Surface modification is known as an effective approach to overcome the implant degradation and improve its bonding with the surrounding hard tissue. Various metallic, ceramic, polymer, and organic coatings have been investigated so far to improve the surface characteristics of Ti-based implants and obtain reduced ion release, improved in-vivo and in-vitro biocompatibility, enhanced mechanical properties, as well as increased wear and corrosion resistance (Prodana et al., 2015; Safonov et al., 2014; Vallet-Regí et al., 2008).

2.2 Titanium Oxide Nanotubes

One particular approach to reduce vulnerability to degradation in body fluids and enhance the wear and corrosion resistance is to produce a uniform titanium oxide (TiO_2) layer on surface of the Ti-based implants. In particular, TiO_2 coatings with self-ordered nanotubular structures (TiO_2 NTs) fabricated by electrochemical anodization technique have recently attracted much attention for fabrication of implants due to their excellent biocompatibility and resistance to bio-corrosion. Such TiO_2 NT arrays and associated nanostructures are reported to significantly improve the functions of various cell lines such as osteoblasts. Therefore, these structures could be used as a well-adhered bioactive surface layer on Ti implant metals for orthopedic and dental implants. These nanostructures have also shown potential in development of novel artificial organs, drug delivery systems, tissue engineering scaffolds, as well as photocatalysts and other biosensor applications (Vasilev et al., 2010).

2.2.1 Synthesis of Titanium Oxide Nanotubes

Fabrication of TiO_2 NTs is classified into two indirect and direct techniques. The indirect methods include hydrothermal, sol-gel, or precipitation processes using various organic, inorganic, and metallic nanorods or nanotubular arrays which act as templates and will be removed after formation of TiO_2 NTs (Wang et al., 2009). On the other hand, the direct techniques such as microwave synthesis (Wu et al., 2005) , low temperature solution chemical method (Sekino, 2010), and anodization involve formation of nanotubes directly from the pre-formed TiO_2 surface without utilization of any template.

Among all the fabrication methods used for fabrication of TiO_2 NTs, anodization is so far the only approach for fabrication of nanotubular structures as thin film coatings

on the metallic surfaces. This technique utilizes the self-passivation behavior of some specific metals such as titanium to produce a protective oxide film with high corrosion resistance on their surface. The term "anodization" thus refers to the substrate which acts as the anode electrode of an electrical circuit. This method generally employs the oxidation-reduction reactions, which respectively occur in the anode and cathode immersed in a particular electrolyte such as sulfuric acid. By continuation of the anodization process, the oxide layer is gradually thickened, forming a non-conductive barrier against the flow of ions. This in turn leads to a decreased oxidation rate over anodization time and ceasing of the process when the oxide thickness reaches to few hundred nanometers (Minagar et al., 2012).

One particular approach in anodization technique to increase the oxide thickness is to create a porous oxide structure in order to provide passages for facilitated penetration of the electrolyte within the oxide layer. This is generally achieved by incorporation of certain ions such as fluoride (F^-), chloride (Cl^-), bromide (Br^-), or perchlorate (ClO^-_4) (Hahn et al., 2007; Likodimos et al., 2008; Raja et al., 2005; Tsuchiya et al., 2005a) into the electrolyte composition which promote dissolution of the metallic oxide in the electrolyte. Consequently, the competition between oxidation of the metallic substrate and dissolution of the oxide layer endows a nano-porous tubular structure which could be self-organized perpendicular to the substrate surface under a controlled anodization condition (Minagar et al., 2012). This technique was initially employed for fabrication of porous/tubular oxide coatings on aluminum substrates (Lee et al., 2014; Li et al., 1998; Schwirn et al., 2008).It was further utilized for fabrication of similar oxide structures on the surfaces of other metals with self-passivation capability such as titanium (Gong et al., 2001; Macak et al., 2005), tantalum (Allam et al., 2008), niobium (Karlinsey, 2005), zirconium (Lee et al., 2005), tungsten (De Tacconi et al., 2006), hafnium (Tsuchiya et al., 2005b) and their alloys (Xie et al., 2011).

The Geometry of TiO_2 NT arrays could be enhanced up to 1 mm (Paulose et al., 2007) in length (growth rate ~ 15 µm h^{-1}), 5 nm (Shankar et al., 2007b) to 35 nm (Varghese et al., 2005) in wall thickness, and 10 nm (Shankar et al., 2007b) to 350 nm (Yoriya et al., 2009) in pore size. The growth of TiO_2 NTs from the substrate surface could potentially result in higher adhesion strength compared to secondary coating materials and thus increase lifetime of the implant alloys. Moreover, the spontaneous creation of a passive TiO_2 NT layer could provide relatively higher inertness and biocompatibility (Raphel et al., 2016; Tang et al., 2016). The history of using anodization for fabrication of TiO_2 nanotubes could be categorized into four generations, detailed in the following. Table 2.1 summarizes different protocols used for synthesis of TiO_2NTs via anodization technique including electrolyte, voltage, time and length.

Table 2.1: Different protocols for synthesis of TiO_2NTs via anodization technique.

Electrolyte	Voltage(V)	Time (s)	length (µm)	Ref.
0.5–3.5 wt.% HF in H_2O	40	1200	0.25	(Gong et al., 2001)
1 wt.% HF in H_2O	20	2700	1	(Şennik et al., 2010)
3 wt.% NH_4F in 1 M Na_2SO_4	20	1800-10800	0.7-2.5	(Sreekantan et al., 2009)
0.5 wt.% NaF in 1 M Na_2SO_4	20	7200	-	(Baram et al., 2010)
0.55 wt.% NH_4F, 1 wt.% H_2O in $C_2H_6O_2$ or 0.7 wt.% NH_4F, 9.3 wt.% H_2O in $C_3H_8O_3$	5-40	900-18000	1-3	(Roman et al., 2014)
0.09 M NH_4F and 2% (v/v) H_2O in $C_2H_6O_2$ or 0.27 M NH_4F and 45% (v/v) H_2O in $C_2H_6O_2$	10-40	3600	0.5-5.9	(Nischk et al., 2014)
0.1 M $HClO_4$	10	-	25	(Antony et al., 2012)
0.05 M $NaClO_4$ and 0.05 M NaCl in H_2O– C_2H_6O	40	1800	220	(Jha et al., 2011)
0.5 wt. % HF in H_2O	20	1200	0.25	(Oh et al., 2005)
2 wt. % HF in C_2H_6OS	30	28800	10	(Roy et al., 2007)

Table 2.1 continued: Different protocols for synthesis of TiO_2NTs via anodization technique.

2 wt. % HF in C_2H_6OS	40	86400	12	(Xiao et al., 2008)
0.2 M sodium citrate tribasic, 1 M $NaHSO_4$, and 0.1 M KF.	10	61200	1	(Peng et al., 2009a)
0.5 wt. % HF in H_2O	5-20	1800	-	(Zhao et al., 2010)
2 wt.% H_2O and 0.3 wt.% NH_4F in $C_2H_6O_2$	100	7200	-	(Vasilev et al., 2010)
0.3 wt.% NH_4HF_2 in $C_3H_8O_3$	10,20,30	7200	-	(Wang et al., 2011).
1 M Na_2SO_4 with 0.5 wt. % NaF	20	1800-16200	-	(Balakrishnan et al., 2013)
0.5 wt. % HF in H_2O	5	1800	-	(Kummer et al., 2013)
1 wt. % NH_4F,20 wt. % H_2O, and 79 wt. % $C_3H_8O_3$	20	3600	1.26	(Lee et al., 2013)
5 %(v/v) H_2O, 5%(v/v) CH_3OH, and 0.5 wt.% NH_4F in $C_2H_6O_2$	10	3600	-	(Huo et al., 2013)
5 vol.% H_2O, 5 vol.% CH_3OH, and 0.5 wt.% NH_4F in $C_2H_6O_2$	40	2400	-	(Huo et al., 2013)

2.2.1.1 The First Generation: Aqueous Electrolyte Containing Hydrofluoric Acid

In 1999, Zwilling et al. employed the anodization approach for formation of TiO_2 NTs on the metallic Ti-6Al-4V surfaces to overcome the limitations of the conventional ceramic coatings. In this work, the nanotubular layer was created via anodic oxidation of the own substrate material using an aqueous solution containing hydrofluoric acid (HF), and growing its thickness under controlled experimental conditions (Zwilling et al., 1999).

Gong et al. (2001) fabricated TiO_2 NTs as thin film coatings in an aqueous electrolyte containing 0.5-3.5 wt. % HF with various voltages ranging from 3 to 20 V (Gong et al., 2001). In 0.5 wt. % HF aqueous electrolyte, the longer anodization times up to 20 minutes led to the increased pore size of the self-organized well aligned nanotube arrays (Figure 2.1). At low voltages (3 V), the porous film with pore sizes of about 15 nm

to 30 nm was obtained. At voltages higher than 10 V, the discrete tube-like structure appeared with larger pore size and longer tube length. At 23 V, the nanotube structure was destroyed and only the sponge-like nanoporous structure was obtained.

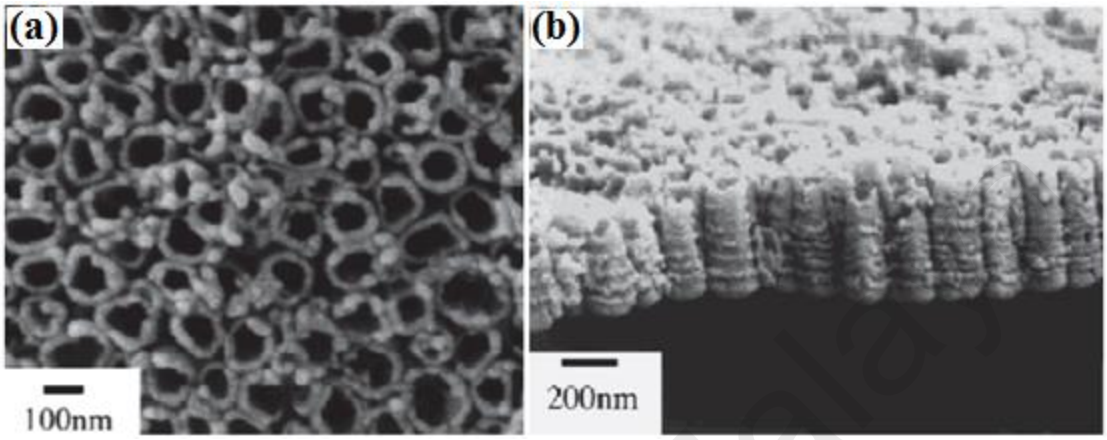

Figure 2.1: FESEM images showing a top view (a) and a cross section (b) of TiO_2 nanotube arrays fabricated in 0.5 wt. % HF aqueous electrolyte at 20 V for 20 min (Gong et al., 2001) .

The pore size of TiO_2 NTs could be improved by using acetic acid (CH_3COOH), boric acid (H_3BO_3) or nitric acid (HNO_3). Using a 2.5% HNO_3/1.0% HF aqueous electrolyte (20 V, 4 h), a large pore size of approximately 100 nm was obtained (Ruan et al., 2006). Replacing HNO_3 with milder acid (0.5 M H_3BO_3), could result in further increase of the nanotube length to 560-nm thick. Furthermore, the tube length could be improved by controlling the synthesis temperature. When the anodization was performed in the low-temperature bath, the length and the wall thickness of nanotubes tended to increase due to the reduced oxide dissolution rate (Mor et al., 2005) . For example, in an aqueous electrolyte containing 0.5% HF and acetic acid in ratio of 7:1 (10 V), anodization at 5 ºC yielded the nanotube arrays with 34 nm wall thickness and 224 nm tube length, compared to 9 nm wall thickness and 120 nm tube length obtained from the 50 ºC condition.

Anodization in 0.5% HF aqueous electrolyte using a potential sweep technique was found to produce tapered, conical-shaped NTs. The voltage was linearly increased from 10 V to 23 V, at the rates from 0.43 to 2.6 $V.min^{-1}$ in order to obtain NTs with conical shape where the pore size at the bottom was larger than that at the top (see Figure 2.2). Pore size at the bottom was strongly affected by the continuously increased voltage that caused the pore widening and pore deepening at the bottom; i.e. the larger pore with a scallop shape was obtained (Mor et al., 2003). Since the field-assisted oxidation/dissolution dominates the process particularly at the bottom, pore size at the top is hence relatively narrower. However, sweeping voltage from high to low, i.e. from 23 V to 10 V, did not result in the conical shape. When the oxide film is thicker, the reduced voltage is not sufficient to induce the oxide dissolution at the bottom pore.

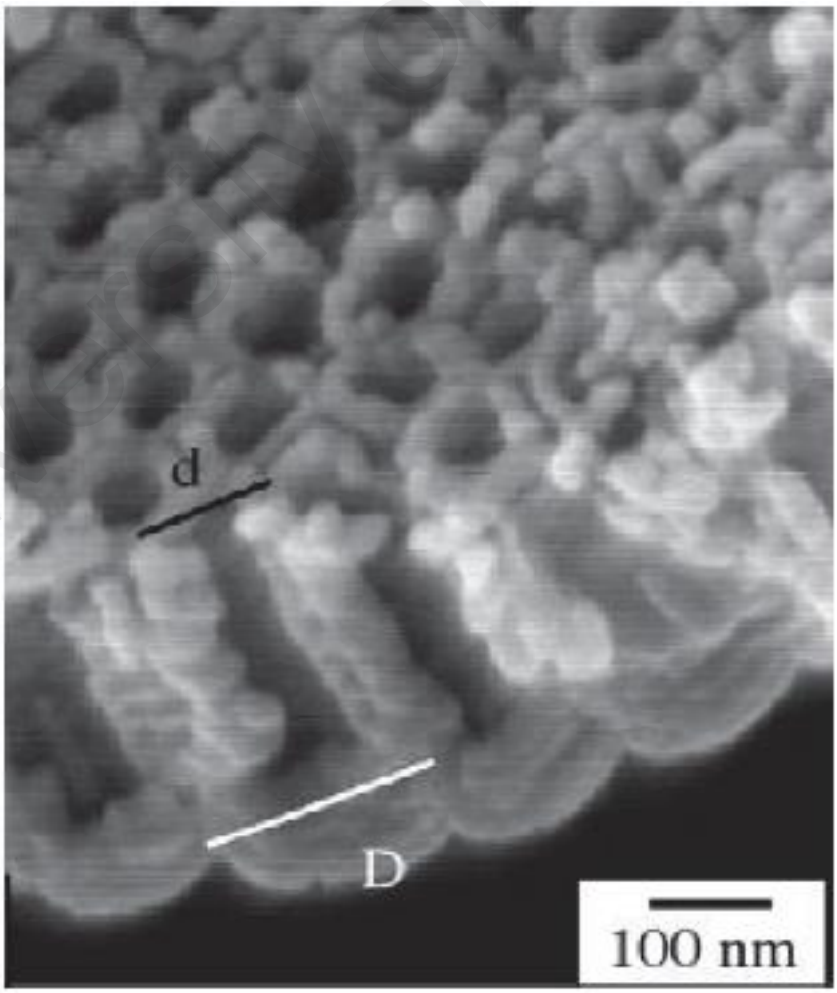

Figure 2.2: FESEM images showing cross-sectional views of TiO_2 nanotube arrays obtained by ramping voltage during anodization. The tapered nanotubes obtained by (i) initially anodizing at 10 V for 20 min (ii) voltage to 23 V with a rate of 1.0 V min-1 within 35 min, and (iii) dwelling at voltage of 23 V for 2 min (Mor et al., 2003).

2.2.1.2 The Second Generation: Buffered Electrolytes

A rapid rate of oxide dissolution was the major limitation of the first synthesis generation, resulting in nanotubes with less than 1 μm length. The properties of electrolyte such as pH, acidity, and conductivity play important roles in affecting the oxide growth process and thus controlling the nanotube morphology. Since HF acid has a dissociation constant (Ka) of 3.5×10^{-4} [pKa = −logKa = 3.45], at pH < 3.45 a large amount of F^- ions will exist in HF, increasing the acidity of electrolyte. Therefore in the second synthesis generation of TiO_2 NTs, HF was replaced with KF or NaF to obtain higher pH values and improve the nanotube length up to ~5 μm. Nanotubes with length of 6 μm could even be achieved in a 0.1 M KF−1.0 M H_2SO_4 0.2 M citric acid aqueous electrolyte (25V and 20 h) when pH was adjusted to 5 (Cai et al., 2005).

2.2.1.3 The Third Generation: Non-Aqueous Electrolytes

The third synthesis generation involved further improvements in the NTs length via utilization of non-aqueous electrolytes or organic polar solvents such as ethylene glycol (EG), formamide (FA), dimethyl sulfoxide (DMSO), dimethyl formamide (DMF), and N-methylformamide (NMF) mixed with fluoride species such as HF, NH_4F, or KF (Paulose et al., 2006; Prakasam et al., 2007; Shankar et al., 2007a; Shankar et al., 2007b; Yoriya et al., 2007). The organic electrolytes are often mixed with water for desirable electrolyte properties. However, influence of the water content in the organic-based electrolytes is substantial to determine the NT length. In order to obtain very long

nanotube arrays, the water content in the anodization bath must be reduced to less than 5% (Paulose et al., 2006) to decreases the oxide dissolution in the electrolyte containing F^- ions. The electrolyte medium and its composition have a strong influence on the NT morphology.

Ruan et al. (2005) anodized titanium in a polar organic solvent containing DMSO with 4.0% HF (20 V, 70 h, at room temperature) (Ruan et al., 2005) to fabricate highly-ordered TiO_2 NTs with 2.3 μm length. The resistivity of film grown in this condition was 14×10^3 Ω/cm (Astrova et al., 2004). Yoriya et al. (2007) further increased the nanotube length to 101 μm through systematic optimization of the anodizing conditions. The nanotubes were obtained by anodizing the pre-anodized Ti in DMSO−2.0% HF at 60 V for 70 h. Without pre-anodization, the 93 μm length was obtained (Figure 2.3). The average pore size and wall thickness were respectively around 150 nm and 15 nm with a calculated surface area per geometric area (geometric roughness factor) of approximately 3475 (Yoriya et al., 2007).

For amide electrolyte group such as FA, DMF, NMF, usually the highly polar electrolytes were mixed with NH_4F. The mixture of FA and NMF (volume ratio of 8:5) and 0.5 wt. % NH_4F resulted in a dramatically increased nanotube length due to an accelerated growth rate (Shankar et al., 2007b). For a given voltage, it was believed that the high dielectric constant of FA ($\varepsilon = 111$) and NMF ($\varepsilon = 182$) could lead to increased electrolyte potential inducing higher charges at the oxide layer, thus elevating the extraction of Ti^{4+} ions (Shankar et al., 2007b). In other words, the high polarity of the organic electrolyte improve dissolution of F^- to be more available at the oxide/metal interface, enhancing ejection of titanium ion from the metal substrate (Paulose et al., 2006). The longest length achieved to date in the formamide based electrolyte is nearly 93 μm, obtained from FA−0.5 wt. % NH_4F−5.0% H_2O (35 V, 48 h), see Figure 2.3. The average outer diameter and wall thickness were 180 nm and 24 nm, respectively, with an

aspect ratio of near 520. Lower anodization voltages resulted in the shorter tube length and thinner tubes. The cation choice was found to be a key factor influencing the tube growth rate and the tube length (Shankar et al., 2007a).

With increasing the cation size, the tube length and aspect ratio were increased. Anodization using electrolytes in the glycol family such as EG and diethylene glycol (DEG) provided TiO_2 NTs with remarkably unique morphological features (Prakasam et al., 2007; Yoriya et al., 2009; Yoriya et al., 2008). First reported by Grimes's group, the TiO_2 NTs prepared in an EG−NH_4F electrolyte yielded the hexagonal close-packed arrays of 223 μm length, with 160 nm outer diameter and 25 nm wall thickness (Shankar et al., 2007b). When Ti foil was completely consumed, the self-standing around 360 μm thick TiO_2 nanotubular membrane were obtained using EG−0.3 wt.% NH_4F−2.0% H_2O v/v (60 V, 96 h), see Figure 2.3 (Prakasam et al., 2007). The outer diameter was 165 nm having an aspect ratio of 2200. In this case, the mass transport effect was more likely to occur, while the potential dependence process dominated earlier in the anodization process.

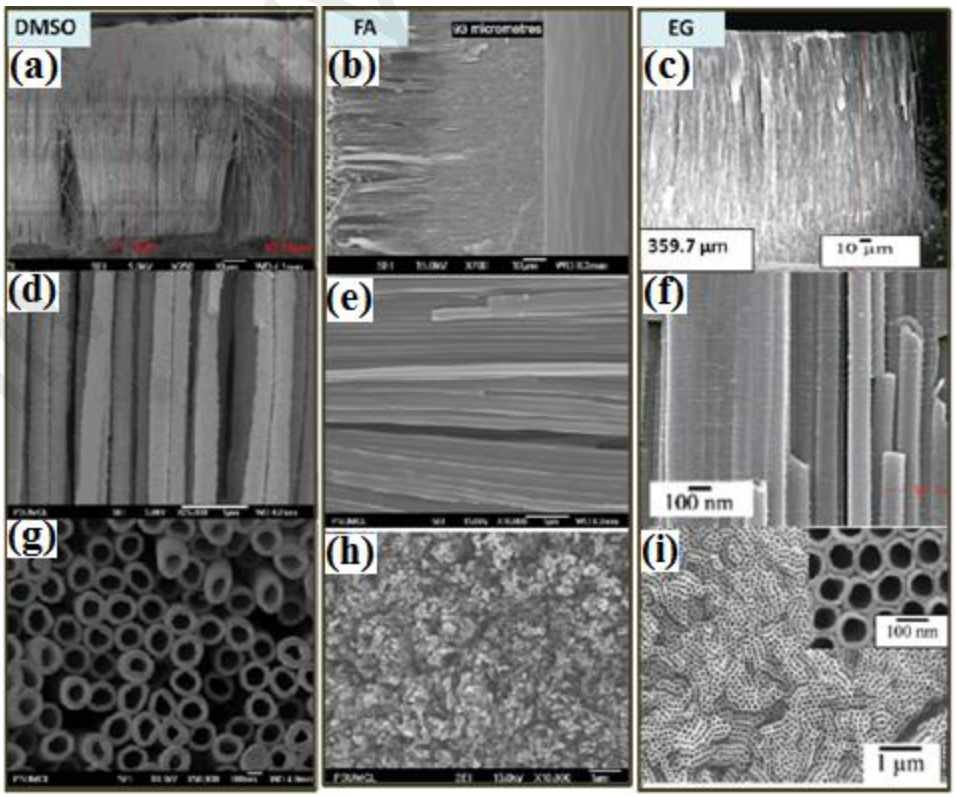

Figure 2.3: FESEM images of TiO_2 nanotube arrays grown in DMSO, FA, and EG based electrolytes showing (a-c) top cross sectional view, (d-f) side view of nanotube wall, and (g-i) top view of nanotube arrays film (Prakasam et al., 2007; Shankar et al., 2007b).

Zhao et al. (2013) also fabricated Strontium (Sr) loaded TiO_2 NTs (NT-Sr) with various NT diameters via hydrothermal treatment of TiO_2 NTs. The NT structures were prepared in EG electrolyte with 5 vol. % water, 5 vol. % methanol, and 0.5 wt. % NH_4F at 10 V for 1 h or 40 V for 40 min. The specimens were afterward immersed in a 0.02 M $Sr(OH)_2$ solution and heated at 200 °C for 1 h or 3 h to incorporate Sr into the NT structure. When the NT were formed at 10 V, multiple nanocues were observed, comprising NTs with diameters of around 30 nm in several bundles of 100 to 400 nm size, which were separated by approximately 80 nm (Zhao et al., 2013).

Ratnawati et al. (2015) employed a sonication-aided anodization technique for producing TiO_2 NTs and investigated their potential in generation of photocatalytic hydrogen from glycerol-water solutions. The NT arrays were grown on the Ti foils by anodization at 30 V in an electrolyte comprising glycerol and water with a temperature of 50 °C. The obtained amorphous NTs were crystallized to anatase by annealing at 500 °C for 3 h in Argon atmosphere. The mean inner diameter and length of the obtained NTs were respectively ranging from 70-84 nm and 0.5-1.5 µm, which both were positively related to the anodization time. The photocatalytic hydrogen generation was also dependent to the NT dimensions. The produced NTs could positively response to the 83% of visible light in hydrogen generation, indicating their reduced band gap energy. Among various NT structures produced in this study, the NTs with 1.46 µm length provided the maximum hydrogen production efficacy (47.22 mmol/m^2 photocatalyst) (Ratnawati, 2015).

More recently, Balasundaram et al. (2016) investigated TiO_2 NT arrays using a low cost electrochemical anodizing method of a Ti thin film foil. The vertically-tailored NT arrays were obtained in an electrolyte solution of 0.44 wt. % NH_4F salt, 4 vol. % water and EG. The samples were finally annealed at 470 °C for 1 h for transition of the amorphous NTs into anatase phase. When a constant DC voltage of 60 V was applied for 1 h, NT structures with 4.177 µm length and 108.35 µm diameter were obtained, while applying the voltage of 75 V for 45 min resulted in NT length and diameter of 17.02 µm and 157.50 µm, respectively. The samples prepared at voltages of 60 V and 75 V respectively showed maximum absorbance ability at wavelengths about 572 nm and 545 nm during ultraviolet visible (UV-Vis) spectroscopy analysis. Due to their higher surface area and well-adjusted NT arrays, the NT arrays produced at DC voltage of 75 V were suggested as the optimal structure for application in dye sensitized solar cells (Balasundaram et al., 2016).

Kaur et al. (2016) fabricated Ti wire-based implants with TiO_2 NT arrays as drug delivery system for localized therapy of breast cancer using pre-clinical cancer models. The tumor necrosis factor (TNF) related apoptosis-inducing ligand (TRAIL) was selected as the model anti-cancer drug for loading on the NT structure. The Ti wires were firstly annealed at 500 °C for 2 h in air, followed by anodization at 75 V for 20 min in an EG electrolyte with 0.3 wt.% NH_4F and 1 vol.% water. The in-vitro investigation of the tumor burden at different time intervals demonstrated that the viability of breast cancer cells was significantly decreased in three days after insertion of the TRAIL-loaded TiO_2 NT implants into the tumor site (Kaur et al., 2016).

2.2.1.4 The Fourth Generation: Using Non-Fluoride Based Electrolytes

Anodization of Ti in the alternative safer chlorine-based electrolyte is a promising choice to successfully produce the TiO_2 NTs similar to those obtained from the fluorine-based electrolytes. Richter et al. (2007) reported the use of 0.4 M NH_4Cl in combination with oxalic, formic, or sulfuric acid for fabrication of non-discrete TiO_2 NTs with thin wall of 4 nm, pore size of 20 nm, and tube length of 60 μm (Richter et al., 2007). However, the as-anodized films appeared to contain carbon element up to 20% when using organic acids as electrolytes, while the films were amorphous similar to those obtained from the fluorine-based electrolytes.

2.2.2 Formation and Growth Mechanism of Titanium Oxide Nanotubes

Generally, the formation sequence of TiO_2 NTs during anodization of Ti-6Al-4V could be described as a chemical dissolution directly followed by electrochemical oxidation. The total structure and geometric parameters of NTs are determined in these steps and controlled by a number of parameters such as acid concentration, anodization voltage, and time. The development of the nanotubular arrays in aqueous based-solutions occur by two common reactions: (i) hydrolysis of pure titanium, and (ii) chemical dissolution of oxide layer at the oxide/electrolyte interface. Once starting the procedure, an oxide film is generated initially due to the interaction of the cationic Ti ions with anionic oxygen in the solution, followed by spreading homogeneously across the metal surface. At the anode, Ti^{4+} ions liberate due to the oxidation of the metal, while the dominant reaction at cathode is hydrogen creation (Grimes et al., 2009).

$$Ti + 2H_2O \rightleftharpoons TiO_2 + 4H^+ + 4e^- \quad (2.1)$$

$$4H^+ + 4e^- \rightarrow 2H_2 \quad (2.2)$$

Therefore, the general reaction can be introduced by eq. (2.3).

$$Ti + 2H_2O \rightleftharpoons TiO_2 + 2H_2 \quad (2.3)$$

More than anodic oxidation of Ti for preparation of TiO_2 which described above, the development of the nanotubular arrays in NH_4F (F^-- containing electrolyte) needs the chemical dissolution of TiO_2 at the oxide/electrolyte interface. Accordingly, the oxide layer partially or thoroughly dissolves in the presence of F^-. The chemical dissolution of resultant TiO_2 happens at the oxide/electrolyte interface and forms $[TiF_6]^{2-}$. The main reaction is:

$$TiO_2 + 4H^+ + 6F^- \rightleftharpoons [TiF_6]^{2-} + 2H_2O \quad (2.4)$$

In fact, the Ti^{4+} ions diffuse through the oxide layer under the electric field and accumulate at the nanopores openings. On the other hand, F^-, O^{2-} and OH^- ions diffuse into the oxide layer and migrate to the Ti/oxide interface in order to react with Ti. Consequently, the migrated F^- ions result in pitting corrosion and thus initiation of pore formation on the substrate surface. Simultaneously, the Ti^{4+} ions transfer into the solution, resulting in precipitation of $Ti(OH)_4$ formed through instantaneous hydrolysis at the pore entrances.

2.2.3 Tribological Properties of Titanium Oxide Nanotubes

The deformation of TiO_2 NTs under compressive loads takes place in two stages including the tubes densification and abrasion of their interfaces. The TiO_2 NTs with diameters ranging from 55–110 nm present compressive strengths near 3 GPa, while those

with 30 nm diameter provide a compressive strength of approximately 5 GPa. The fracture of TiO_2 NTs under the compressive loads is probably due to micro-crazing and buckling of the tube/tube interfaces (Li et al., 2015). However, when the TiO_2 NTs are used as thin films on other materials, not only their fracture strength, but also their adhesion strength to the substrate material plays an important role in the mechanical performance of multilayer system.

A number of studies have investigated the adhesion strength of the TiO_2 NTs on different substrates. It is believed that the adhesion strength is significantly relied on the crystallization phase of the fabricated TiO_2 NTs. In general, TiO_2 NTs with anatase phase provide the highest adhesion to the substrate, followed by rutile and amorphous phase. Therefore with progress of crystallization and phase transformation during heat treatment, the force required for delamination of the coating layer is increased (Li et al., 2015). Zalnezhad et al. (2015) illustrated that the Young's modulus and surface hardness of TiO_2 NT films on the 304 stainless steel enhanced with increase of the annealing temperatures from 280 °C to 620 °C. Heat treatments at 430 °C and 620 °C also improved the adhesion strength respectively to 2860 and 3140 mN (Zalnezhad et al., 2015). Li et al. (2015) also reported that increase of the annealing temperature from 200 ◦C to 800 ◦C could result in enhanced interfacial fusion between the TiO_2 NT coating and the Ti substrate, where the force needed for breaking the coating layer was increased from 1.75 N in unannealed specimens to more than 10 N in those annealed at 800°C (Li et al., 2015).

The wear resistance is another significant tribological parameter which needs to be investigated to determine the reliability of biomaterials in the medical implant applications. The, microscopic wear products accumulated at the implant/tissue interface may increase vulnerability to inflammation, osteolysis, infection, and loosening (Minagar et al., 2012). The implants must also present a sufficient fretting fatigue strength to tolerate not only the static stresses, but also the cyclic loads which are applied for several

million times during their lifetime (Boehlert et al., 2008). Furthermore, it is important to determine the dynamic friction resistance for understanding the micro motion performance of the implant and its failure mechanism.

Ti-6Al-4V shows a poor wear resistance due to its relatively low plastic shear resistance and insufficient protection by the surface oxides (Budinski, 1991). Although formation of a wear-resistant oxide coating such as TiO_2 NT on the Ti-6Al-4V surface could potentially increase its wear resistance, however to best of our knowledge, the performance of TiO_2 NT coated Ti-6Al-4V alloys has not been sufficiently investigated in terms of wear, friction, and fatigue resistance. Therefore, further studies are required to provide better understanding of the effect of TiO_2 NT coating on the mechanical and tribological properties of Ti-6Al-4V substrates.

2.2.4 Corrosion Resistance of Titanium Oxide Nanotubes

When the metallic implants are corroded in-vivo, the ions release into the body fluids and their interaction with various biomolecules may result in severe allergy and cytotoxicity (Liu et al., 2004). Thus improving the corrosion behavior of the metallic implants by various surface treatments is challenging in order to expand their use in the biomedical applications (Liu et al., 2004).

According to literature (Tang et al., 2009; Zalnezhad et al., 2015), fabrication of self-organized TiO_2 NT layers is a suitable surface treatment for improving the corrosion behavior of the Ti-based alloys. It has been shown that the TiO_2 NT layers on Ti-6Al-4V substrates show a better corrosion resistance in the simulated body fluid (SBF) than that of uncoated substrate (Yu et al., 2009). In particular, the crystalline alloys could provide higher corrosion resistance compared to amorphous phase**.** Mazare et al reported the TiO_2 NTs annealed at 750°C has lower corrosion current density (j_{corr}) compared to the as-

formed amorphous NTs or those annealed at lower temperatures. In other words, it was concluded that the rutile phase could provide higher corrosion resistance compared to the amorphous TiO_2 phase (Mazare et al., 2016).

The fabrication protocol has also been shown to affect the corrosion behavior of the obtained NTs. For instance, Balakrishnan & Narayanan (2013) investigated the corrosion behavior of non-oxidized Ti as well as the surfaces oxidized at different anodization intervals via employing the open circuit potential, polarization, and electrochemical impedance measurements. The results showed that the surfaces anodized for 4.5 h possessed superior corrosion resistance in contrast to the other investigated groups (Balakrishnan et al., 2013).

2.2.5 Biological Behavior of Titanium Oxide Nanotubes

TiO_2 NTs have exhibited a promising potential for various biological applications, due to their low immunogenicity, ability to control the fate of stem cells, as well as pro-healing characteristics in the osteoblasts and endothelial cells. It has been shown that TiO_2 NTs could result in increased clot formation in shorter time compared to those of TiO_2 nanoparticles, making them promising candidates to act as scaffolds for facilitating fibrin formation (Roy et al., 2007). Moreover, due to a high encapsulation capability of TiO_2 NTs, this nanotubular structure could be used in sustained release of various proteins or antibiotics on the order of hours (Peng et al., 2009b).

2.2.5.1 Wettability of Titanium Oxide Nanotubes

The degree of hydrophobic and hydration forces in biological systems could strongly influence the protein adsorption as well as the cell adhesion and proliferation.

Therefore, the wetting behavior and surface topography of biomaterials play significant roles in their biomedical application (Wei et al., 2009).

It has been shown that the TiO_2 NTs present a controllable wetting behavior from super-hydrophilic in their unmodified form to super-hydrophobic when modified with some organic molecules such as octadecyl silane or octadecyl phosphonic acid (Balaur et al., 2005). The wetting characteristics of the TiO_2 NT surface could also be adjusted by alteration of the nanoscale geometry rather than the surface chemistry. For instance, the TiO_2 NT layers coated by octadecyl phosphonic acid exhibited a diameter-dependent contact angle from 108 ± 2° (hydrophobic) to 167 ± 2° (super-hydrophobic). This dependence of surface hydrophobicity on the NT diameter could significantly contribute to an effective design of customized implant materials and tissue engineering scaffolds for each specific application (Bauer et al., 2008).

2.2.5.2 Biocompatibility of Titanium Oxide Nanotubes

The cell-implant interaction is important for successful clinical implantation and the surface modification at a nanoscale or a microscale can significantly alter the cellular response (Capellato et al., 2013; Habibovic et al., 2006; Wang et al., 2008b). The influence of TiO_2 NTs on cellular response has been investigated using a number of cell types including human osteoblasts (HObs), fibroblasts, chondrocytes, endothelial cells (ECs), vascular smooth muscle cells (VSMCs), epidermal keratinocytes, and mesenchymal stem cell (MSCs) (Tan et al., 2012).

Assessment of the responses of ECs and VSMCs to the TiO_2 NTs also indicated that the NT surface could significantly enhance EC proliferation, while decreasing the VSMC proliferation. The altered behavior of both EC and VSMC in the presence of NT

arrays could potentially be useful for stent and other vascular applications (Peng et al., 2009a).

Park et al. (2009) studied the influence of highly-defined spacing variation between the vertically-aligned TiO_2 NTs with six different diameters ranging from 15 and 100 nm on the MSCs response and their differentiation to bone-forming cells. The results indicated that beside the surface chemistry, the nanoscale geometry also affects the cell response to the biomimetic surfaces. The adhesion, proliferation, migration, and differentiation of MSCs were maximized on the NTs with 15 nm diameter, while the higher NT diameters resulted in decreased cell differentiation and the NTs with 100 nm diameter induced cell death (Park et al., 2009).

The influence of different NT diameters (30 nm, 70 nm and 100 nm) was also studied in-vivo on the biological mechanism of bone attachment to the implant surface, 1 to 5 weeks after implantation. The results indicated that TiO_2 NTs could govern the bone generation at the bone-implant interface in order to achieve a desirable osseointegration. In addition, dynamic bone deposition was also observed in the sequential fluorescent labeling images. In contrast to the conventional Ti implants, the bone-implant contact and gene expression levels were significantly increased in implants with NT coatings (In particular for NTs with 70 nm diameter) (Wang et al., 2011).

Das et al. studied the effect of anodized TiO_2 NTs on HObs using an osteo-precursor cell line (OPC1) that was established from human foetal bone tissue. The TiO_2 NTs were grown by anodization at 20 V for duration of 2 and 4 h. The produced NTs had the inner diameter of 51–54 nm, a length of 288–600 nm and a wall thickness of 39–51 nm. For the evaluation of bone cell-material interaction, the NTs grown in 4 h were utilized due to their uniform nanoporous structure and better surface properties. The NTs were then crystallized into rutile phase at 580 °C. The NTs showed better cell spreading

and adhesion by forming filamentous network structures that acted as excellent anchorage sites for the filopodia extension. The nanoscale morphology also exhibited early differentiation by showing increased alkaline phosphatase (ALP) activity and statistically significant bone cell proliferation as indicated by MTT assay compared to a polished Ti control surface (Das et al., 2009). All these results indicated a higher osteoconductivity of TiO_2 NTs compared to conventional polished Ti surface.

A sustained and controllable release of Sr ions was reported from the NT structure without a noticeable cytotoxicity. The incorporated Sr ions could significantly enhance proliferation of rat MSCs. In particular, the NT structures produced at 40 V could promote spread of the cells into a polygonal osteoblastic morphology. According to the gene expression data, osteogenesis was promoted in both the NT and NT-Sr structures compared to the conventional Ti surface. In particular, expressions of the osteogenesis-related genes (including the runt-related transcription factor 2 (RUNX2), ALP, osteocalcin (OCN), Col-1, and bone morphogenic protein 2 (BMP-2)) in NT-Sr structures fabricated at voltage of 40 V and heat treated for 1h (NT40-Sr), as well as the specimens fabricated at 10 V and heat treated for 3 h (NT10-Sr3) was significantly up-regulated in absence of extra osteogenic agents, demosnstrating their excellent osteogenic behavior. However unexpectedly, the amount of nodular ALP products as well as the ECM mineralization were significantly higher in NT10-Sr3 compared to the NT40-Sr specimens, which was not in accordance with the results of gene expression analysis. This could due to of the multiple scaled nanostructure and more proper Sr amount in NT10-Sr3, and impairment of the cell function by the uneven distribution of proteins in NT40-Sr. Therefore, NT10-Sr3 was suggested as the optimal surface for clinical application due to its favorable osteogenic activity (Zhao et al., 2013).

Lv et al (2015 also demonstrated the significant impact of nanotopography on differentiation of the human adipose-derived stem cells (hASCs) in both in-vitro and in-vivo studies and indicated that the NT diameter of 70 nm obtained at voltage of 20 V could provide the optimal condition for promoting the osteogenic differentiation of hASCs (Lv et al., 2015).

2.2.5.3 Bioactivity of Titanium Oxide Nanotubes

In the implant studies, the bioactivity term often refers to formation of cortical bone-like hydroxyapatite (HA) on the implant surface when immersed in SBF. Recent studies have shown that the kinetics of HA formation and growth in SBF could be enhanced in presence of nanotubular structure (Gong et al., 2001; Goudarzi et al., 2014; Lee et al., 2013; Oh et al., 2005), probably due to their high specific surface area (Xiao et al., 2008). When the NTs were formed on the Ti surface, almost all the osteoblast functions were maintained or improved, which could potentially endow faster bone formation around the implants without compromising its density (Zhao et al., 2010). Moreover, the hierarchical micro/nanostructure of the implant surface improves its osseointegration ability though mechanical interlocking with bone in-vivo (Zhao et al., 2010).

In general, HA formation on the TiO_2 NTs with anatase phase is higher than that of other phases i.e. amorphous or rutile (Xiao et al., 2008), probably due to a higher lattice match with HA phase (Wang et al., 2011). The anatase phase exhibited a high apatite forming capability and generated a dense and uniform apatite film on the surface upon immersion in SBF for 30 h (Balakrishnan et al., 2013). Immersion of the crystallized NTs in SBF for 14 days resulted in formation of a thick (~13 μm) apatite layer on the NT

surfaces, confirming their high bioactivity mainly due to the presence of anatase phase (Xiao et al., 2008).

The NTs could also be treated by sodium hydroxide (NaOH) to improve their bioactivity and stimulate HA formation. The obtained TiO_2 NTs induce growing of bioactive sodium titanate with extremely fine nanofibers structure on the NT edges. When subsequently immersed in SBF, the sodium titanate nanofibers could in turn induce nucleation and growth of HA phase with nano-sized particles on the implant surface (Gong et al., 2001; Oh et al., 2005).

2.2.5.4 Antibacterial Effect of Titanium Oxide Nanotubes

The implant infections caused by adhering the antibiotic resistant strains of bacteria on their surfaces may not be treated by the common antibiotics and often lead to implant removal to eradicate the infection. Therefore, there has been a growing interest to find alternative approaches for treatment of orthopedic device-related infections without utilization of antibiotics. Modification of the surface chemistry and crystalline structure is a particular technique to minimize the initial bacterial attachment to the implant surface (Kummer et al., 2013). In particular, TiO_2 NTs present distinct advantages over other Ti-6Al-4V coatings in bacterial inactivation (Hayden et al., 2010).

Kummer et al. (2013) investigated the bacterial responses to Ti-6Al-4V alloys with different surface characteristics and showed a significant decrease in growth of *Staphylococcus aureus* (*S. aureus*) and *Staphylococcus epidermidis* (*S. epidermidis*) on the TiO_2 NTs compared to the conventional Ti surface. It was also found that the degree of bacterial growth on the TiO_2 NTs strongly depends on their diameter where the NTs with 20 nm diameter exhibited better antibacterial characteristics than that of 80 nm NTs.

Furthermore, it was concluded that the rutile phase could provide improved antibacterial performance compared to anatase (Kummer et al., 2013).

The nanotubular structures could also be employed for encapsulation and localized delivery of antibacterial drugs. Popat et al. (2007) used TiO_2 NTs for localized delivery of gentamicin off-implant at the implantation site. The release kinetics of gentamicin from the TiO_2 NTs and its influence on adhesion of *S. epidermidis* were also studied. The obtained results confirmed a high capability of TiO_2 NTs for encapsulation of the selected antibiotic drug. As a result, the bacterial adhesion on the surface was reduced significantly (Popat et al., 2007).

The antibacterial activity of the alloys coated by TiO_2 NTs could further be enhanced by incorporation of other antibacterial agents such as silver nanoparticles (Ag NPs) into the coating composition. In a proof-of-concept study, Lai et al. (2013) deposited Ag nanoparticles onto the TiO_2 NT arrays to improve the implant resistance against *Escherichia coli* (*E coli*) as a model for Gram-negative bacteria (Lai et al., 2013). Mei et al. (2014) also fabricated TiO_2 NTs incorporating Ag NPs to improve the antibacterial performance of dental implants against post-surgical bacterial infections. The Ag concentrations that were capable to retain the nanotubular morphology, were shown to effectively sterilize oral pathogens. The characterization tests also revealed that utilization of lower plasma voltages (i.e. 0.5 kV) could result in accumulation of a large Ag amounts on the surface, which significantly compromised their in-vitro and in-vivo biocompatibility. In contrast, when high plasma voltages (1.0 kV) were applied, smaller amounts of Ag NPs were deposited on the surface with unimpaired effects. The samples fabricated at plasma voltage of 1.0 kV were further reported to exhibit sustained antibacterial activity due to the sufficient Ag concentrations embedded in proper NT depths (Mei et al., 2014).

Gao et al. (2014) embedded silver oxide (Ag_2O) NPs in the NT walls instead of Ag NPs in order to provide a long lasting antibacterial ability against the biomaterial-related infections without compromising the implant biocompatibility. The TiO_2 NT-Ag_2O NP arrays were produced on a pure Ti surface via magnetron sputtering using a TiAg target, followed by anodization at 30V for 4h in an electrolyte solution. Embedding of Ag_2O NPs showed negligible influence on the NT diameter, while significantly decreasing their length. The high flexibility of this approach allowed formation of well-defined TiO_2 NT-Ag_2O NP arrays with a wide range of crystallized Ag_2O concentration from 0 to 15 wt.% and particle sizes from 5 nm to 20 nm, which could provide adequate rate of Ag^+ release without an appreciable cytotoxicity (Gao et al., 2014). Even after 28 days, the TiO_2 NT-Ag_2O NP arrays could effectively kill *Escherichia coli* (*E. coli*) and *S. aureus*, showing their long-term antibacterial activity. The negative effect of TiO_2 NT-Ag_2O NP arrays on the viability, proliferation, and differentiation of osteoblast cells was reported negligible and even some favorable effects on promoting the spread of osteoblasts were observed (Gao et al., 2014).

2.3 Tantalum Oxide Nanotubes

During the past few years, tantalum (Ta) and its pentoxide (Ta_2O_5) are gathering increasing attention in bone repair application, owing to their high biocompatibility and bioactivity, which facilitate biological bonding to the natural hard tissue through stimulating formation of bone-like apatite layers (Anselme, 2000; Frandsen et al., 2014; Roy et al., 2010; Wang et al., 2012a). Self-passivation of the Ta surface via formation of a stable oxide layer gives rise to a superb corrosion-erosion resistance in biological media without any significant weight or roughness alterations, compared to the conventional metallic implants (Allam et al., 2008; Ruckh et al., 2008). Though, regardless of the

inherent characteristics of Ta-based biomaterials, their relatively high modulus of elasticity and bulk density are obstacles for their application in manufacturing of load-bearing implants (Balla et al., 2010a; Frandsen et al., 2014). Moreover, the mechanical mismatch between the Ta-based implants and bone tissue causes bone desorption and implant loosening, which raises the clinical failure risk. Hence, Ta and its oxides are typically employed as thin porous coatings on the metallic implants (Yang et al., 2007).

2.3.1 Synthesis Techniques of Tantalum Oxide Nanotubes

The Ta_2O_5 NT coatings are mostly fabricated by anodization of a thin Ta layer, which has been deposited by physical vapor deposition (PVD) on the substrate. The physical and mechanical features of the Ta_2O_5 NT coatings are controlled by various governing parameters of PVD, anodization and subsequent annealing processes (Horwood et al., 2014; Singh et al., 2007; Su et al., 2015; Zhang et al., 2015b).

2.3.1.1 Physical Vapor Deposition (PVD)

Among various techniques which have been developed for deposition of different coating layers on the biomaterials surfaces, PVD is known as an effective method for produce highly-adherent thin films of pure metals or alloys. In this technique, the coating component is first vaporized to generate a plasma of metallic ions. The highly-charged ions are then accelerated by an electric field and deposited on a substrate with sufficient electrical conductivity. The procedure is generally conducted using a cathodic arc source operating in a vacuum chamber with approximate pressure range of 6-10 torr. The

metallic vapor may also be accompanied with different gases to produce coatings in oxide, nitride, or carbide phases (Mattox et al., 2010).

The high flexibility of PVD and controllability over the deposition parameters could provide numerous advantages including desirable coating homogeneity, adhesion, density, and purity. This technology could be employed for various applications from decorative to super-conducting high temperature coatings and production of coating thicknesses ranging from angstroms to millimeters with high deposition rates (25 µm/sec) (Ding et al., 1999; Kelly et al., 2000; Nelea et al., 2003; Shi et al., 2008; Swann, 1988; Toque et al., 2010). A wide variety of metallic and ceramic compounds as well as a number of organic materials could be coated via PVD technique (Mubarak et al., 2005). Moreover, the coating layer could be produced in both single and multi-layer structures in one process cycle. However, evidence shows that the multi-layer coatings could provide enhanced fracture strength, hardness, and corrosion resistance in contrast to single-layer coatings (Aouadi et al., 2001) .

2.3.1.2 Anodization

Ta_2O_5 NTs can be fabricated by different techniques such as Sol-gel (Zhang et al., 2013) , template and Ta filament (Hulteen et al., 1997), and anodization which is the most common method (Allam et al., 2008; Horwood et al., 2014; Su et al., 2015; Zhang et al., 2015b). Table 2.2 summarizes the anodization conditions which have been previously utilized in the synthesis of Ta_2O_5 NTs. However, the NTs developed so far are relatively long, which increases the delamination tendency of the coating layer.

Table 2.2: Different protocols used for synthesis of Ta_2O_5 NTs via anodization.

Electrolyte	Voltage (V)	Time (s)	Length (μm)	Ref.
H_2SO_4 + 1.7%(v/v) HF (room temperature (one-step))	15	600	5	(Zhang et al., 2015a)
H_2SO_4 + 1%(v/v) HF (0° C (two-step))	15	600	2	(Zhang et al., 2015a)
H_2SO_4 + 1%(v/v) HF (0° C (optimized two-step))	25	300	270.3	(Zhang et al., 2015a)
1M H_2SO_4 + 2%wt HF (room temperature)	20	60	0.035	(Singh et al., 2007)
16 M H_2SO_4 + 0.2-0.9M HF (room temperature)	15	300	1.2	(Horwood et al., 2014)
H_2SO_4 +10% (v/v) HF+ 0.1M H_3PO_4 (room temperature)	15	600	1.3	(Allam et al., 2008)
H_2SO_4 +10% (v/v) HF+ 5%(v/v) $C_2H_6O_2$ (room temperature))	10-15	1200	5.1	(Allam et al., 2008)
H_2SO_4 +10% (v/v) HF+ 5%wt C_2H_6OS (room temperature)	10-15	1200	2.3-11.1	(Allam et al., 2008)
H_2SO_4 + 1% (v/v) HF + 4%(v/v) H_2O (0-50 °C)	50	1200	2.5	(Gonçalves et al., 2012)
5.5ml HF + 223ml H_2SO_4 + 21.5ml H_2O (room temperature)	15	90	0.02-0.92	(Wang et al., 2012b)
H_2SO_4 + 13.6%wt H_2O + 0.8%wt NH_4F (room temperature)	1.2*	2	7.7	(Su et al., 2015)
$C_2H_6O_2$ + 3%wt H_2O + 0.5%wt NH_4F (room temperature)	100	120	0.525	(Banerjee et al., 2009)
H_2SO_4 + 0.28%(v/v) HF + 4.29%(v/v) H_2O (room temperature)	30	300	1.8	(Barton et al., 2009)
H_2SO_4 + 1.13%(v/v) HF + 5.17%(v/v) H_2O (room temperature)	30	300	4.8	(Barton et al., 2009)
H_2SO_4+ 0.2%(v/v) HF + 12%(v/v) H_2O (room temperature)	30	1200	35	(Barton et al., 2009)
2.9M HF + 16.4MH_2SO_4 (room temperature)	15	5-120	0.25-2.5	(El-Sayed et al., 2009; Horwood et al., 2011)
H_2SO_4 +10% (v/v) HF (room temperature)	10-40	600-1200	-	(El-Sayed et al., 2007)
1M H_2SO_4 + 2%wt HF (room temperature)	20	14400	0.35-0.4	(Sieber et al., 2005)

* Value is in terms of A cm^{-2}.

2.3.2 Growth Mechanism and Formation of Tantalum Oxide Nanotubes

During anodization of the as-deposited Ta, an initial barrier layer is firstly generated, resulting in an exponential decrease in the anodic current density until it reaches a steady-state. A decrease in the current is caused by formation of a compact oxide film that increase the resistance. After development of the initial oxide layer, the O_2 or H_2O ions transfer through the oxide layer towards the metal/oxide interface where they react with the Ta metal. By continuation of the anodization process, uniformly-distributed pores are generated due to dissolution of Ta_2O_5, leading to a slight increase in the current with time. In this stage, nanopores are generated as a result of random local dissolution of the Ta_2O_5 surface. Fluoride ions are known to chemically attack the Ta_2O_5 during the anodization and provide the required dissolution rate of the oxide layer at certain sites, thus creating a porous oxide film. The applied electrical field ensures that a compact oxide film incessantly restructures at the base of the pores (El-Sayed et al., 2010).

The third stage involves division of the interconnected pores into nanotubes, followed by stabilization of the current density. With an adequate applied voltage, the electric field becomes strong enough for the migration of the tantalum ions, leaving behind voids in the inter-pore areas, which in turn will divide one pore from one another, leading to development of separate tubes oriented vertically to the substrate (Rahmati et al., 2016). During this stage, NTs will form as a result of the simultaneous growth of voids (regions between pores that are susceptible to field assisted oxidation/dissolution) and pores. It has also been reported that separation of pores into individual NTs may be a consequence of the repulsive forces between the cation vacancies (Crawford et al., 2007; El-Sayed et al., 2010).

From a chemical aspect, formation process of Ta_2O_5 NTs can be also divided into three steps: (i) migration of Ta^{5+} ions from Ta, (ii) formation of $Ta_2(OH)_{10}$ and Ta_2O_5

layers on the metal surface; and (iii) chemical dissolution of Ta_2O_5 to form Ta_2O_5 NTs . However, Ta_2O_5 is soluble in HF, which may result in the etching of the interface between the Ta_2O_5 NTs material and the substrate in the third step (El-Sayed et al., 2010). The etching process leads to deterioration of the adhesion of Ta_2O_5 NTs, which explains why lower amounts of HF could enhance the connection. The exact reactions are represented in equations 2.5 to 2.14. Besides this, the lower temperature and fast ejection of heat during the anodization could decrease the rate of oxidation reaction, which decelerates the volume expansion during the formation of Ta_2O_5 for the sufficient release of the deformational stress. Accordingly, tightly-adhered nanotubular arrays could be generated by decreasing the anodization temperature at a reasonable rate to reach a balance between the volume expansion and relieve of the deformational stress (Zhang et al., 2015b). The chemical reactions governing these processes are as follows:

$$10H^+ + 10e^- \rightarrow 5H_2\,(g) \tag{2.5}$$

$$2Ta \rightarrow 2Ta^{5+} + 10e^- \tag{2.6}$$

$$2Ta^{5+} + 10H_2O \rightarrow Ta_2(OH)_{10} + 10H^+ \tag{2.7}$$

$$Ta_2(OH)_{10} \rightarrow Ta_2O_5 + 5H_2O \tag{2.8}$$

The overall reaction can be written as follows:

$$2Ta + 5H_2O \rightarrow Ta_2O_5 + 5H_2\,(g) \tag{2.9}$$

In acidic solutions the tantalum oxide-fluoride anions with Ta–O–Ta bridging bonds are formed after the initial formation of $[TaOF_5]^{2-}$. The $[TaF_6]^-$ anions are formed in the $[F^-]$ solution, the $[TaF_7]^{2-}$ is the dominant species. The tantalum fluoride species $[TaF_6]^-$ and $[TaF_7]^{2-}$ are successively formed as the result of this mechanism. Throughout these reactions, it should be noted that the successive formation of the tantalum oxide-

fluoride/fluoride anions $[TaOF_5]^{2-}$, $[TaF_6]^{-}$ and $[TaF_7]^{2-}$ occur in higher concentration of HF.

$$HF \leftrightarrow H^+ + F^- \quad (2.10)$$

$$Ta_2O_5 + 6H^+ + 8F^- \leftrightarrow 2(TaOF_4.H_2O)^- + H_2O \quad (2.11)$$

$$(TaOF_4.H_2O)^- \leftrightarrow (TaOF_4)^- + H_2O \quad (2.12)$$

$$(TaOF_4)^- + F^- \leftrightarrow (TaOF_5)^{2-} \quad (2.13)$$

$$(TaOF_5)^{2-} + H^+ + F^- \leftrightarrow (TaF_6)^- + OH^- \quad (2.14)$$

$$(TaF_6)^- + F^- \leftrightarrow (TaF_7)^{2-} \quad (2.15)$$

2.3.3 Tribological Properties of Tantalum Oxide Nanotubes

In spite of a high potential of the vertically-oriented Ta_2O_5 NT architecture in different applications such as orthopedic and dental implants, drug delivery systems, photoelectrochemical hydrogen generation from water, optics, sensors, heterojunction solar cells, very little attention has been devoted to its tribological characteristics. Recently, Khalid (2016) investigated the effect of surface roughness induced by anodization at three different potentials including 15, 25 and 50 V on the tribological properties. It was found that the Ta surface anodized at 15 V after mechanical polishing had a lower dynamic friction coefficient than the surface anodized at the same potential after etch treatment. This could be related to the quality of oxide film that formed on both surfaces. The anodized Ta surface may have worn off more easily due to the poor adherence of the oxide film to the metal surface. However, this argument makes sense as the wear track of this sample showed a shinier surface than the etched sample, hence a higher degree of wear. The samples anodized at higher potentials had lower dynamic friction coefficients compared to the samples anodized at 15 V. These thicker oxide layers may have been more easily worn away. The surface shear strength may have changed as

surface texturing occurred at higher potential. A greater intensity of electrochemical attack on the surface at higher potentials may reduce the surface strength. This would cause surface wear to occur at lower dynamic friction forces. The anodized Ta surfaces had nano textured amorphous oxide layer and showed a higher degree of wear than the un-anodized Ta surfaces (Khalid, 2016).

2.3.4 Corrosion Resistance of Tantalum Oxide Nanotubes

To the best of our knowledge, there is no coherent interpretation on the role of anodization and subsequent annealing on the corrosion behavior and mechanical characteristics of Ta_2O_5 NTs coating on the biomedical grade Ti-6Al-4V substrates. Therefore, a systematic investigation is required to gain more insight into the effect of various fabrication parameters on the corrosion behavior of the obtained Ta_2O_5 NT structures.

2.3.5 Delamination, cracking and detachments of Tantalum Oxide Nanotubes

One of the most common disadvantages of Ta_2O_5 NTs are related to cracking, delamination and detachments of NTs. El-Sayed (2009) showed that the detachment of Ta_2O_5 NTs from the substrate was intensified by increase of the anodization time. Increase of the anodization times resulted in altered surface topographies including rough surfaced dimples (Figure 2.4 a), short NTs of around 250 nm in length arranged in smaller patches (Figure 2.4 b), vertically-aligned NTs with around 20–25 nm pore diameters (Figure 2.4 c), longer nanotubes arranged in smaller patches than observed at 20 s (Figure 2.4 d), respectively (El-Sayed et al., 2009). However, the cracked NTs were observed in all the surfaces anodized at different times.

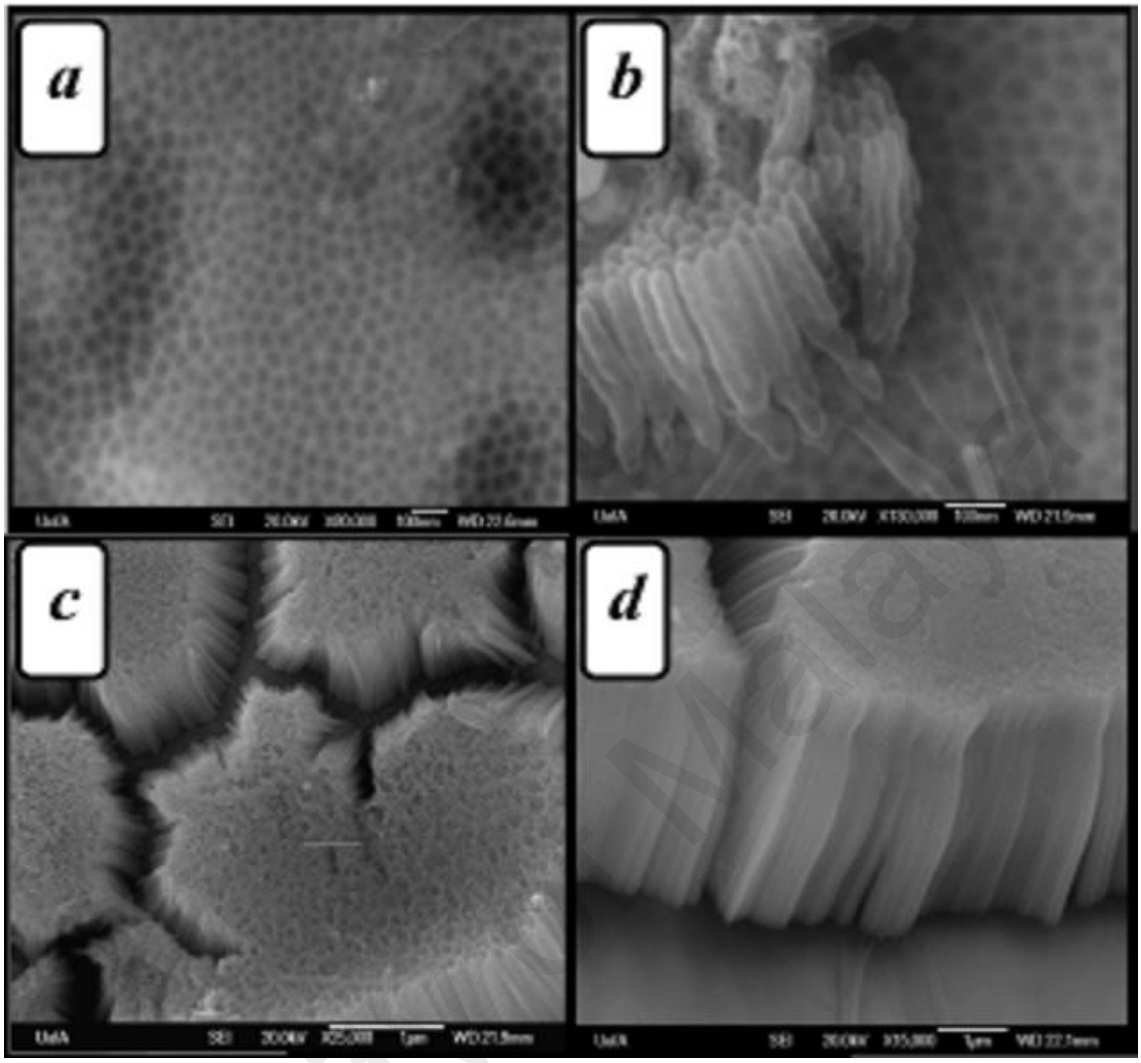

Figure 2.4: FESEM images of the Ta surfaces anodized in 16.4 M H_2SO_4 + 2.9 M HF at 15 V for (a) 5, (b) 10, (c) 20 and (d) 60 (El-Sayed et al., 2009).

Figure 2.5 presents a field emission scanning electron microscopy (FESEM) image of fractured Ta_2O_5 NTs fabricated in an aqueous electrolyte containing HF and H_2SO_4 (1:9) with 5% dimethyl sulfoxide at 15 V.

It is believed that the NTs detachment from the substrate is due to incorporation of F^- ions into the anodic layer. The inward mobility of F^- ions is approximately 100% higher than that of O^{2-} ions, resulting in generation of a thin TaF5 layer which separates the growing anodic oxide film from the tantalum. Formation of this thin layer has been shown to reduce adherence of the anodic film to the substrate (Allam et al., 2008).

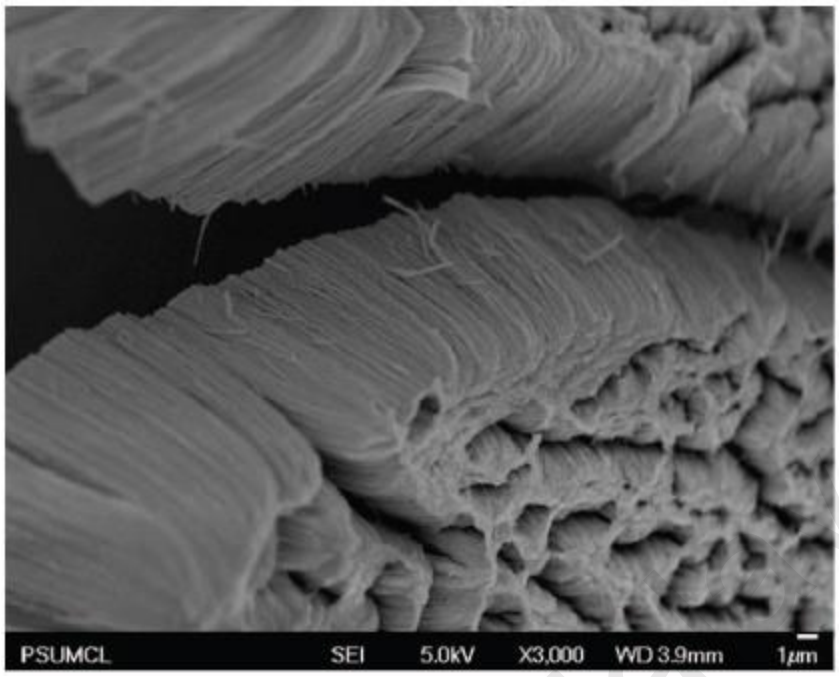

Figure 2.5: A typical FESEM image of the anodized Ta surfaces in aqueous electrolytes with HF + H_2SO_4 (1:9) + 5% dimethyl sulfoxide at 15V (Allam et al., 2008).

Figure 2.6a shows an example of a cross-sectional crack in the porous Ta_2O_5 layers formed in 1 M H_2SO_4 + 2 wt % HF at 20 V after 4 h. The open pores on top of the layer are also evident in Figure 2.6 b. The transient of the potentiostatic current density reflects the process of delamination of porous Ta_2O_5 layers. The current transient exhibits some current peaks corresponding to the film cracking time (delamination events) (Sieber et al., 2005). Several parameters such as vigorous gas evolution, acidification inside of the pore during the oxide layer growth, or stress effects due to the mismatch of oxide and substrate are considered responsible for cracking of the metal/ film interface. However, it is not clear which factor is the most dominant in the process of porous oxide growth and its cracking (Schmuki, 2001).

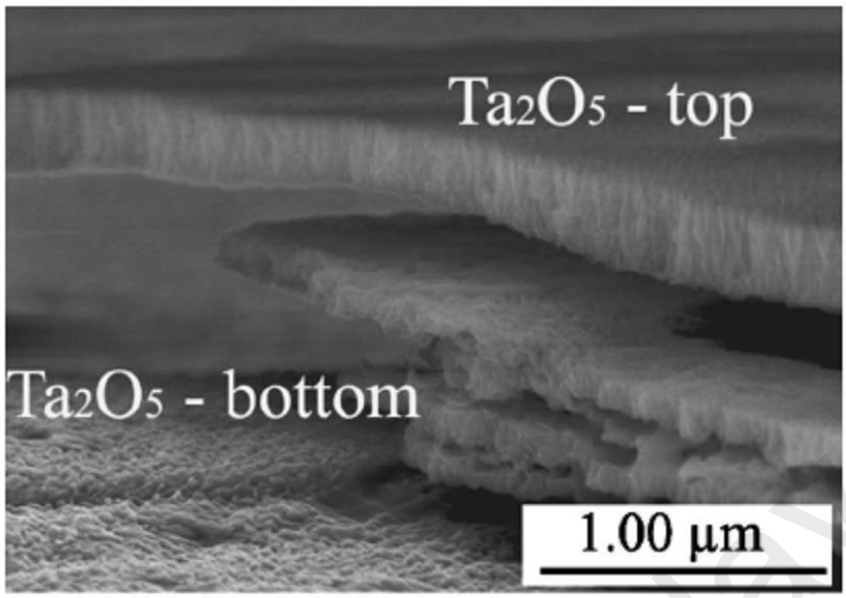

(a)

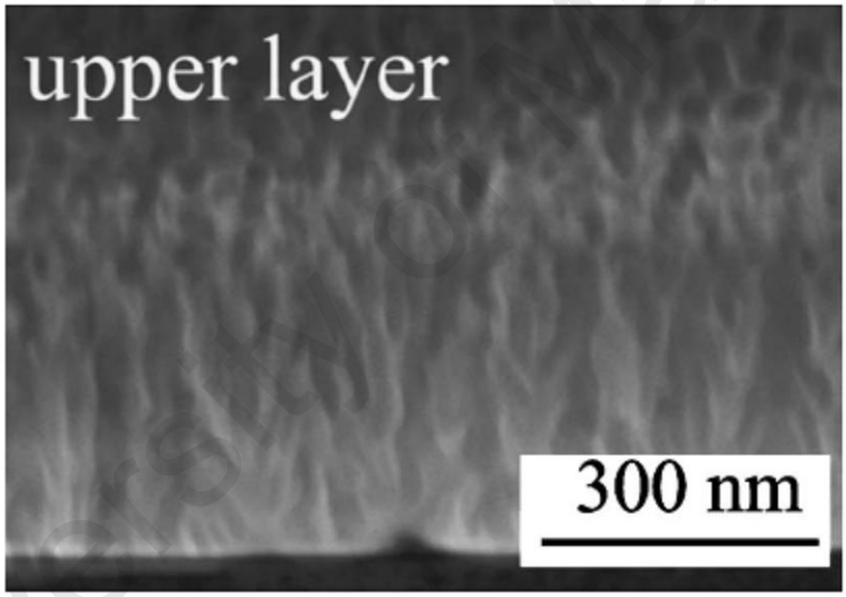

(b)

Figure 2.6: SEM cross section of the porous Ta_2O_5 prepared by anodic oxidationin 1 M H_2SO_4 + 2 wt % HF for 4 h: the cracked porous Ta_2O_5 layer (a), the upper layer (b) (Sieber et al., 2005).

Figure 2.7a illustrates the presence of cracks with high tendency to peel off in a Ta_2O_5 NTs coating fabricated via anodization of a Ta foil in an aqueous solution containing H_2SO_4 and HF at 15 V for 10 min. The NT openings were also bundled together, resulting in decreased area of the inner surface (Figure 2.7b, c).

A number of strategies were employed to optimize the anodization condition and overcome the delamination problem. For instance, the HF concentration was reduced to decelerate the anodization reaction rate and thus enhance the NTs adhesion to the substrate surface. By reducing the HF concentration to 1.0% (v/v), the NT layer became more continuous, while a number of relatively large cracks were still present (Figure 2.7d). The coating surface was also rough containing blocked NT openings (Figure 2.7e, f). Therefore, a multi-step anodization was carried out to enhance the uniformity and quality of the fabricated NTs. In this approach, anodization was firstly carried out using a high bias (30 V) for 15 min. The obtained NTs were then removed from the Ta substrate via ultrasonication, followed by performing the second anodization to fabricate well-defined and ordered Ta_2O_5 NTs (Figure 2.7h, i). However, several small cracks were still observed in the coating layer (Figure 2.7g).

The anodization temperature was also shown to strongly affect the adhesion strength of Ta_2O_5 NTs. Therefore, the generated heat during anodization was removed in an ice-water bath to moderate the chemical reactions. As a result of using a two-step anodization approach at decreased reaction temperatures in electrolytes with low HF concentrations, well-defined and ordered Ta_2O_5 NTs with desirable surface topography and high adhesion strength to the substrate were fabricated (Figure 2.7j-l). (Zhang et al., 2015a).

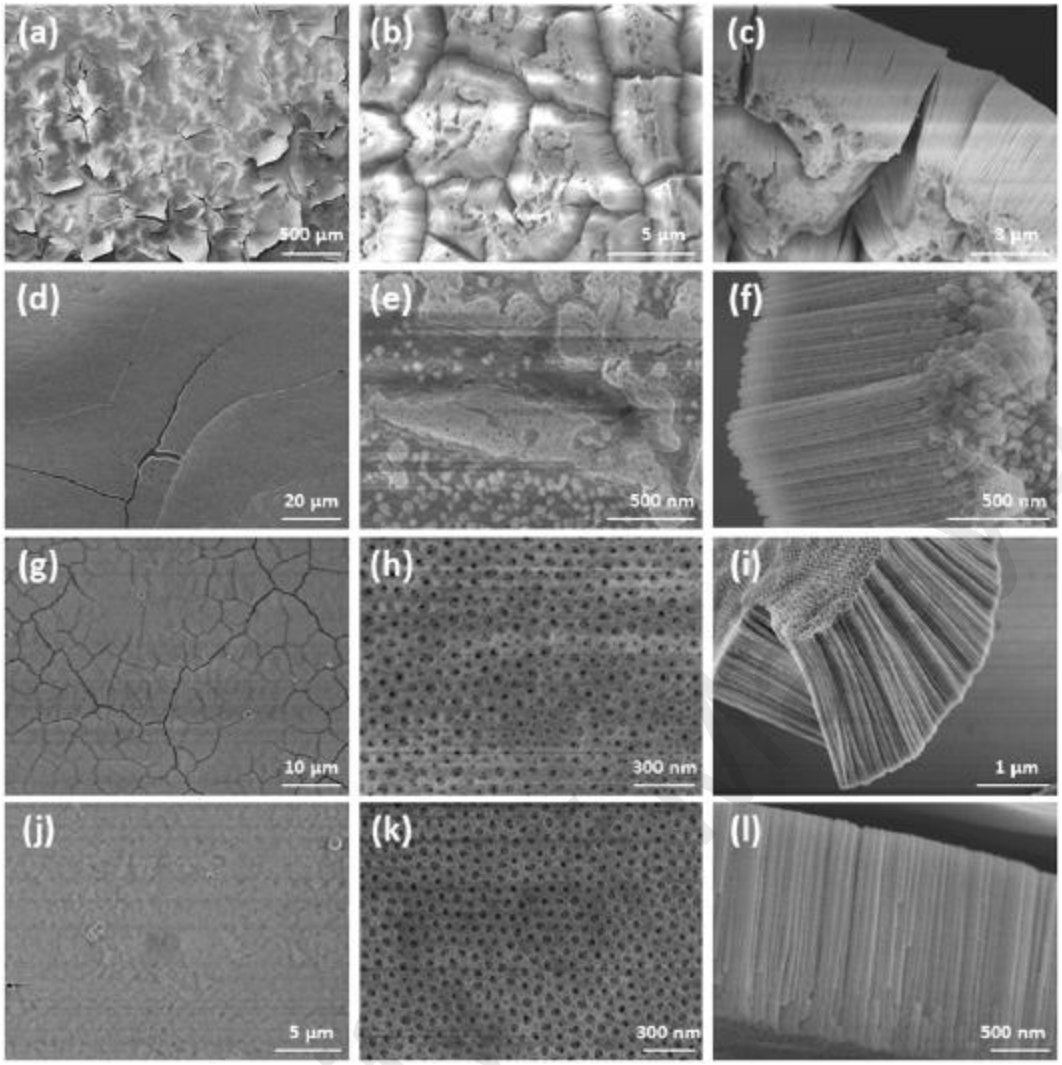

Figure 2.7: (a, b and c) One-step anodization in a H_2SO_4 solution consisted of 1.7% (v/v) HF at room temperature. (d, e and f) one-step anodization in a H_2SO_4 solution consisted of 1.0% (v/v) HF at room temperature; (g, h and i) two-step anodization in a H_2SO_4 solution consisted of 1.0% (v/v) HF at room temperature; (j, k and l) two-step anodization in a H_2SO_4 solution consisted of 1.0% (v/v) HF at 0 °C. The anodization reactions were conducted with a bias of 15 V for 10 min (Zhang et al., 2015a).

2.3.6 Biological Properties of Tantalum Oxide Nanotubes

2.3.6.1 Wettability of Tantalum Oxide Nanotubes

In general, the Ta_2O_5 NTs exhibit superior surface energy and wettability compared to TiO_2 NTs, potentially resulting in improved bioactivity and enhanced cell attachment and proliferation when used as orthopedic or dental implant material (Khalid, 2016). Similar to the TiO_2 NTs, the surface morphology and roughness of Ta_2O_5 NT coatings could significantly affect their wettability. Furthermore, illumination of the Ta_2O_5 NT films by ultra violet lights with higher energies than the band gap energy of Ta_2O_5 (4.2 eV), could result in their transformation into super-hydrophilic state (contact angle < 10°). This transformation is generally faster in the crystalline phases than that of amorphous phase, indicating that the size of crystal domains at the NT surface could significantly affect the transition kinetics (Rico et al., 2009).

2.3.6.2 Biocompatibility of Tantalum Oxide Nanotubes

The cytotoxicity and biocompatibility of Ta_2O_5 NTs have been investigated in a number of in vitro studies (Donkov et al., 2009). In particular, it was shown that the viability and growth of osteoblasts and MSCs were increased on Ta_2O_5 NTs in contrast to the flat Ta surfaces (Wang et al., 2012a). The osteoinductive study by Wang et al. (2012) also showed that the Ta_2O_5 NTs could activate the osteogenesis response via inducing differentiation of the rabbit bone MSCs into osteoblasts (Wang et al., 2012b). These results suggest that Ta_2O_5 NTs could promote the osteointegration process by presenting desirable interface for cell adhesion, proliferation, differentiation, and matrix production which subsequently result in better implant stabilization (Ruckh et al., 2008).

2.3.6.3 Antibacterial Effect of Tantalum Oxide Nanotubes

Similar to TiO_2 NTs, different antibacterial agents could be incorporated into the Ta_2O_5 NT arrays in order to minimize bacterial infection. However to best of our knowledge, no study has been carried out to investigate the antibacterial performance of these nanotubular structure or improve their antibacterial resistance via incorporation of antibacterial agents.

2.4 Summary of Literature Review

One of the potential approaches to enhance the bone-implant contact and thus the healing process is anodization of the metallic implants (Bobyn et al., 1980; Liu et al., 2010; Rack et al., 2006; Wu et al., 2015). However, low fracture toughness, fracture of the nanotubular structures, and their low adhesion on the substrates are great obstacles for their clinical application. Moreover, their low capability to tolerate the cyclic loading conditions applied during actual performance in human body remains challenging.

CHAPTER 3: MATERIALS, METHODS AND PROCEDURES

This chapter provides a detailed account of the fabrication methods of thin film of TiO_2 and Ta_2O_5 nanotubular arrays with decorated Ag_2O nanoparticles on Ti–6AL–4V Alloy as well as its characterization for mechanical and biological properties. Figure 3.1 shows the flowchart of methodology.

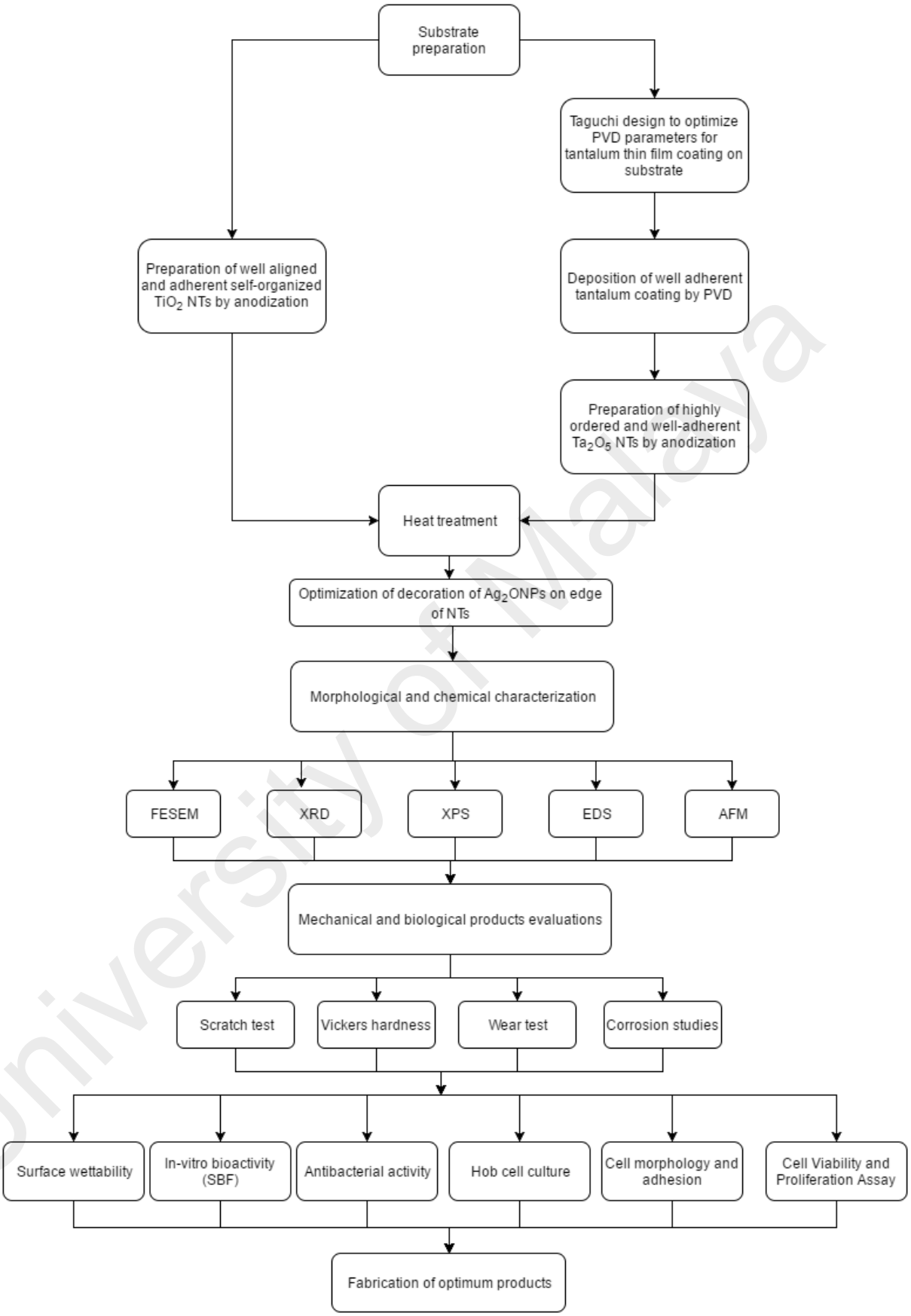

Figure 3.1: Flowchart of methodology.

3.1 Substrate preparation

The substrates were fabricated from titanium alloy Grade 5 (Ti– 6Al–4V, E Steel Sdn. Bhd, Klang, Malaysia) plates with dimensions of 15 mm × 15 mm × 2 mm. The specimens were prepared by polishing with 800–2400 grit silicon-carbide emery papers, followed by wet-polishing using a diamond slurry and sonication in acetone for 10 minutes at 40 °C. The substrates were then washed three times with distilled water, followed by drying at 100 °C for an hour for each experiment to fabricate thin film of TiO_2 and Ta_2O_5 nanotubular arrays with decorated Ag_2O nanoparticles.

3.2 Preparation of TiO_2 Nanotubular arrays with Decorated Ag_2O Nanoparticles on Ti–6AL–4V Alloy

3.2.1 Preparation of Self-organized TiO_2 Nanotubular arrays

Electrochemical anodization was conducted in a two-electrode electrochemical cell in which a graphite rod (D = 7 mm) was joined to the cathode and the sample was fastened to the anode (Figure 3.2). The distance between the electrodes was fixed at 20 mm in all experiments. Anodizing was carried out using a direct current (DC) power source (Model E3641A, Agilent Technologies, Palo Alto, USA) at various potentials for 4 h with a magnetic stirring speed of 150 rpm. The anodization electrolyte was a mixture of 0.2 M H_3PO_4 and different concentrations of NH_4F (0.3-0.5 M). Details regarding the anodization and annealing conditions are summarized in Table 3.1. After anodization, samples were washed with de-ionized water to move residual materials from their surface. Finally, to form the crystalline phases, the anodized specimens were annealed at 500, 600 or 700 °C for 1.5 h under a normal atmosphere at a heating and cooling rate of 10 °C/min.

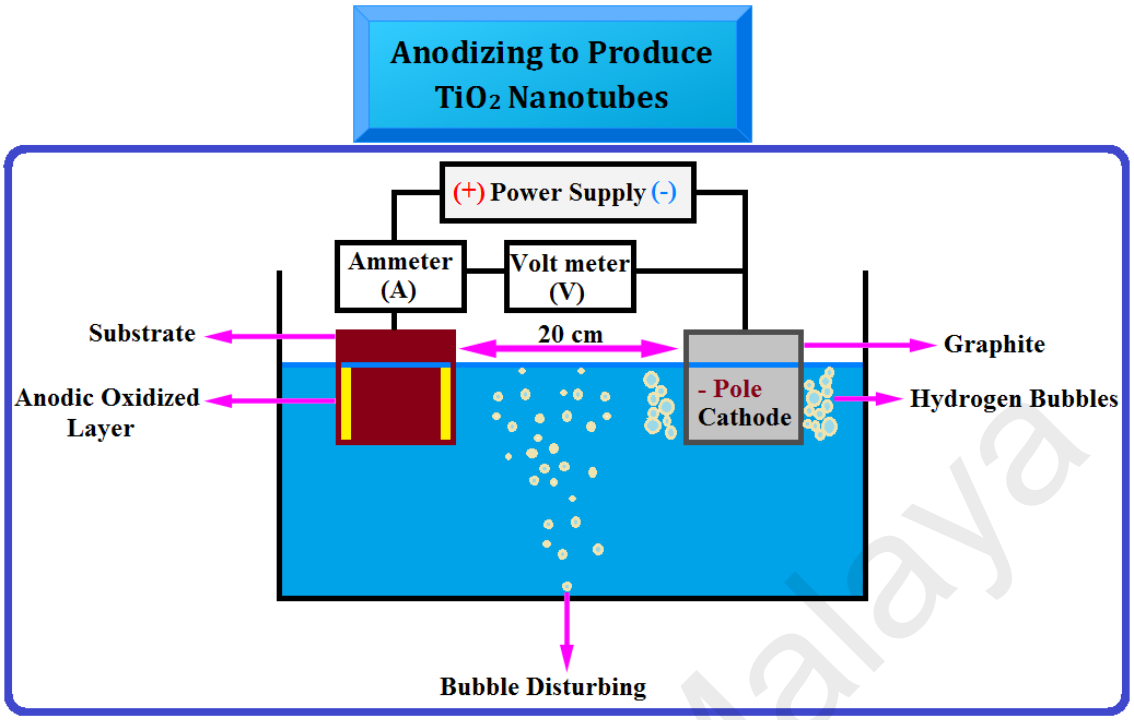

Figure 3.2: Schematic view of the anodization process to produce TiO_2 nanotubes.

Table 3.1: Details of anodization and annealing conditions.

*Sample	Anodization potential (V)	Electrolyte composition		Thermal treatment (°C)
		H_3PO_4 (M)	NH_4F (M)	
S1	10	0.2	0.3	500, 600, 700
S2	10	0.2	0.4	500, 600, 700
S3	10	0.2	0.5	500, 600, 700
S4	20	0.2	0.3	500, 600, 700
S5	20	0.2	0.4	500, 600, 700
S6	20	0.2	0.5	500, 600, 700

*Anodization time (4 h) and stirring speed (150 rpm) were identical in all experiments.

3.2.2 Decoration of Ag_2O NPs on the TiO_2 NTs

The PVD magnetron sputtering was finally applied for 10 s, 30 s, 45 s and 60 s to deposit Ag_2O NPs on the NT edges. A 150 mm distance between the specimens and the target, chamber evacuation below 5.2×10^{-5} Torr, base pressure of 1.92×10^{-5}, radio frequency (RF) power of 200 W, argon and oxygen flow rates of 25 and 3.75 sccm,

substrate temperature of 200°C, and DC bias of 75 V were the experimental conditions applied in these PVD coating experiments.

3.3 Preparation of Ta_2O_5 Nanotubular arrays with Decorated Ag_2O nanoparticles on Ti–6AL–4V Alloy

3.3.1 Taguchi Design of Experiments

Selection of the processing parameters and identification of the orthogonal array (OA) are considered the most crucial step in the experimental design of the Taguchi approach (Ghani et al., 2004). In this study, three influential parameters which are the DC power, temperature and time, each comprised of three different levels were examined. Hence, a standard L_9 (3^3) orthogonal array was developed in order to allow the verification of the interactions between the various parameters. The control parameters and their corresponding levels selected in the experimental design of the Taguchi approach are given in Table 3.2.

Table 3.2: Factors and levels used in the experiment.

experiment	DC power (W)	Temperature (°C)	Time (h)
1	250	200	2
2	250	250	4
3	250	300	6
4	300	200	4
5	300	250	6
6	300	300	2
7	350	200	6
8	350	250	2
9	350	300	4

3.3.2 Deposition of Ta Coating

The Ta thin film was deposited on Ti-6Al-4V substrates using PVD magnetron sputtering technique (SG control engineering Pte Ltd series, Singapore) equipped by a pure Ta target (99.995%) with 150 mm distance from the substrate. The Ti-6Al-4V

substrates were ultrasonically washed sequentially in acetone and ethanol, prior to the deposition of the Ta layer. It should be noted that the oxide layer on the target was removed by pre-sputtering in an argon atmosphere. The chamber was then vacuumed to less than 2×10^{-5} Torr, prior to the argon gas flow, to initiate the sputtering. The applied pressure, the argon gas flow rate and the direct current (DC) bias were fixed at 5×10^{-3} Torr, 35 sccm, and 75 V, respectively.

3.3.3 Fabrication of Ta_2O_5 NTs by Anodization

In the present study, to reduce the rate of the anodization reaction and to strengthen the adhesion of the Ta_2O_5 NTs, the HF concentration was kept constant (1% (v/v)). On the other hand, to form a continuous coating and to prevent severe cracking, a two-step anodization technique was conducted using a DC power source (E3641A, Agilent Technologies, Palo Alto, CA). The as-deposited Ta films were firstly ultrasonicated sequentially in acetone and ethanol for 30 min. The specimens were then connected to the positive terminal (anode) while a platinum foil (15 mm×15 mm) was used as the negative terminal (cathode) 10 mm away from the anode. The Ta-coated specimens were immersed in an electrolyte of 5% ethylene glycol (EG) dissolved in a 99: 1 sulfuric acid (H_2SO_4 98%, Ajax chemicals, Sydney, Australia) and hydrofluoric acid (HF 40%, Ajax chemicals, Sydney, Australia). The anodization experiments were performed at 0°C at a constant potential of 15 V with different anodization time intervals (0.5, 1, 3, 5, 10, and 20 min). After the anodization, Ta_2O_5 NTs were rinsed with deionized water to remove the excess H_2SO_4 and HF. The Ta_2O_5 NTs were then removed by sonication in deionized water and dehydrated in flowing nitrogen. In order to re-grow the Ta_2O_5 NTs, the anodization procedure was repeated with the same experimental conditions. The anodized specimens were then ultrasonicated in ethanol for 15 min and dried at 100 °C to clean the surface which resulted in a color change from light gray to white. To improve the

adhesion of coating, heat treatment was carried out at 450, 500, 550, 750 and 1000 °C for 1 h under atmospheric pressure with a heating/cooling rate of 1°C min^{-1}. The growth of highly oriented arrays of Ta_2O_5 NTs on Ti-6Al-4V via the PVD magnetron sputtering, electrochemical anodization and subsequent annealing processes are shown in Figure 3.3.

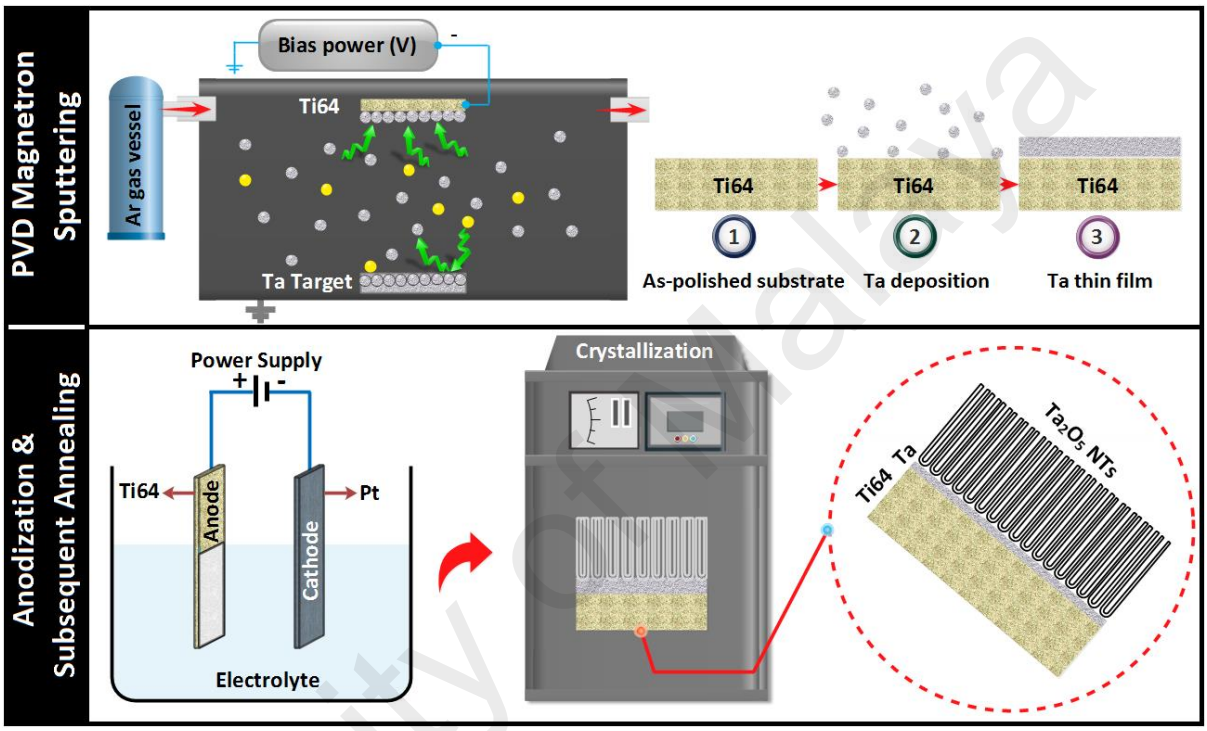

Figure 3.3: Schematic view of the growth of the highly oriented arrays of Ta_2O_5 NTs on Ti-6Al-4V derived by PVD magnetron sputtering, electrochemical anodization and subsequent annealing.

3.3.4 Decoration of Ag_2O NPs on the Ta_2O_5 NTs

The PVD magnetron sputtering was again applied for 10, 30, and 60 seconds to deposit Ag_2O NPs on the NT edges. A 150 mm distance between the specimens and the target, chamber evacuation below 5.2×10^{-5} Torr, base pressure of 1.92×10^{-5} Torr, radio frequency power of 200 W, argon and oxygen flow rates of 25 and 3.75 sccm, substrate temperature of 200°C, and DC bias of 75 V were the experimental conditions applied in this PVD coating experiment.

3.4 Physical, Mechanical and Biological Characterization

3.4.1 Phase Analysis and Microstructural Characterization

The morphology of coatings was investigated using a field emission scanning electron microscope (FESEM, SU8000, Hitachi, Japan) with an acceleration voltage of 1 to 2 kV. The cross-sections of the specimens were prepared with a destructive technique using a high-precision cutter equipped with a diamond blade. The phase composition and purity of the substrates, TiO_2 NTs, annealed TiO_2, Ag_2O-decorated on TiO_2 NTs, Ta-coated, Ta_2O_5 NTs, annealed Ta_2O_5 NTs, and Ta_2O_5 NTs-Ag_2O NPs specimens were analyzed by X-ray diffractometry (XRD; Philips PW1840, the Netherlands) with Cu Kα radiation (λ=1.54178 $\overset{o}{A}$) functioning at 45 kV and 30 mA, 2 theta range of 30°-80°, scan rate of 0.1°.s^{-1}, and step size of 0.026°. The "*PANalytical X'Pert HighScore*" software was also employed to check the XRD patterns, wherein all the reflections were equated with the standards gathered by the Joint Committee on Powder Diffraction and Standards (JCPDS, card #005-0682 for Ti, JCPDS#01-071-1167 for TiO_2 (Anatase),JCPDS#01-072-1148 for TiO_2 (Rutile), #001-1182 for Ta, #008- 0255 for Ta_2O_5 and #42-0874 for Ag_2O).The atomic concentration as well as the two-dimensional distribution of the constitutive elements were respectively determined using energy dispersive X-ray spectrometry (EDS) and elemental mapping approaches equipped in the FESEM. The X-ray photoelectron spectroscopy (XPS; ULVAC-PHI Quantera II, Physical Electronics GmbH, Ismaning, Germany) with Al K_a radiation was also employed to quantify the elemental composition and confirm formation of the metallic oxides.

3.4.2 Adhesion Strength

The adhesion strength of the coatings was measured quantitatively using a Micro Materials Nano Test (Wrexham U.K) equipped with a diamond indenter with radius and angle of 25.0 ± 2.0 μm and 90.0 ± 5.0°, respectively. The experiments were performed

with a velocity of 5 mm s^{-1} and the loading rate gradually increased to 9.2 mN s^{-1}. The scratch tests were repeatedly performed on each sample and the damage profile was investigated under a light optical microscope (Olympus BX61, Tokyo, Japan). Here, the adhesion strength is defined as total coating failure. The sample was moved perpendicular to the scratch probe whilst the contact was either held constant or ramped at a user-defined rate. Throughout the test the probe penetration depth and frictional load were continuously monitored. A pre-scratch scan was accomplished using an ultra-low contact force in order to assess baseline sample topography. After that, the scratch test was repeated three times within the specified load range using a diamond indenter.

Following the adhesion tests, the obtained data were analyzed by a signal-to-noise (S / N) response method in order to determine the influential process parameters and to optimize the deposition characteristics. The S / N ratios were calculated using three methods based on the required values (small, large or nominal) to obtain the optimal results. Here, the following equation was used to calculate the S/N ratio (in dB):

$$S/N = -10\log\left(\frac{1}{n}\sum_{i=1}^{n}\frac{1}{Y_i^2}\right) \qquad \text{Eq. (3.1)}$$

Where the term Y is the obtained results and n represents the number of observations.

For further investigation, the scratch hardness test was performed on the TiO_2 NTs, annealed TiO_2 NTs thin films at 500°C for 1.5 h, as-deposited Ta coating and the 5 min anodized Ta_2O_5 NTs, after annealing at 450 °C for 1 h. This test was executed to measure the resistance of the thin films to permanent deformation under the action of a single point (stylus tip) and involves a different combination of properties of the surface because the indenter, in this case, a diamond stylus, moved tangentially along the surface. The scratch hardness test, is more appropriate technique to measure the damage resistance of a material, like the two-body abrasion. This technique is applicable to a wide range of materials including metals, alloys and some polymers. This test is based on the

measurement of the residual scratch width, after the stylus is removed to compute the scratch hardness number. Therefore, it reflects the permanent deformation resulting from the scratch and not the instantaneous state of combined elastic and plastic deformation of the surface. Since the state of stress at the stylus tip is a function of contact geometry and applied force, the magnitude of the scratch hardness number is dependent upon both the stylus tip radius and the normal load. The scratch hardness number is calculated by dividing the applied normal force on the stylus by the projected area of the scratch contact, assuming that the hemispherically-tipped stylus produces a groove whose leading surface has a radius of curvature *r*, the tip radius of the stylus. The projected area of the contact surface is therefore a semi-circle, whose diameter is the final scratch width. The critical load is defined at the onset of the coating loss, which is associated with the appearance of the metallic substrate inside the scratch channel. This measurement was accomplished with the help of an optical microscope. The tester was also enabled to obtain the frictional coefficient at the critical load (Astm, 2003; Jaworski et al., 2008; Ruckh et al., 2008). The scratch hardness HS_p was estimated following the specification of ASTM G171-03 norm:

$$HS_P = \frac{8P}{\pi w^2} \qquad \text{Eq. (3.2)}$$

Where HS_p, P and w are the scratch hardness number, normal force and the scratch width, respectively.

3.4.3 Microhardness

The microhardness of the samples were quantified using a Vickers microhardness testing machine (Mitutoyo-AVK C200-Akashi Corporation, Kanagawa, Japan) by the indentation-strength method at room temperature using an applied load of 98.07 mN and a dwell time of 15 s. Five indentations per sample were done to determine the average value of the mechanical properties.

3.4.4 Tribological studies

The wear tests were carried out under dry sliding condition using a pin-on-disc configuration (Ducom Reciprocating Friction Monitor – TR 282 Series). This machine is designed to assess the friction and wear characteristics of the samples, under reciprocating sliding motion. A reciprocating engine is used to create a bi-directional sliding motion between the samples while a loading mechanism applies the desired load upon the test samples. In addition, a friction measurement system allows for the instantaneous friction force to be measured. Coefficient of friction (COF) and a variety of optional facilities are also calculated and demonstrated on the "*WinDucom*" software. The dry-sliding test starts as the pin glides against a stationary counterpart plate. In all cases, cylindrical Ti-6Al-4V pins with a length of 8 mm and diameter of 6 mm were utilized. Prior to the wear testing process, both specimens and pins were cleaned thoroughly with distilled water and degreased with acetone. Three normal loads (15, 20, and 25 N) with a reciprocating frequency of 10 Hz and amplitude stroke of 1 ± 0.02 mm were then applied to the disc, where the tangential frictional force was incessantly calculated using a load cell sensor attached to the pin-holder arm and reported as a root mean square value. As mentioned above, the kinetic COF (μ_k) was displayed in the instrumentation output which was determined by dividing the recorded frictional force by the normal load. Moreover, an atomic force microscope (AFM, Ambios Technology) was utilized to assess the topographical texture of the surfaces and wear scars using a Nanoscope IIIA scanning probe in tapping mode. Here, the roughness average (R_a; the arithmetic average of absolute values) is used:

$$R_a = \frac{1}{n}\sum_{i=1}^{n}|y_i| \qquad \text{Eq. (3.3)}$$

Where y_i and n are a vertical distance from the centerline and the total number of vertical measurements taken within a specified cutoff distance, respectively.

3.4.5. Corrosion Studies

Corrosion testing of the samples was performed using a potentiostat/galvanostat AutoLab PGSTAT30 from Ecochemie (Netherlands) equipped with frequency response analyzer (FRA). The polarization experiments were executed using a three-electrode set-up. The substrate, TiO_2 NTs, as-deposited Ta coating, as-anodized Ta_2O_5 NTs and the annealed samples were the working electrodes, with a surface of 0.5 cm × 0.5 cm exposed into the phosphate buffer solution (PBS, pH 7.2). Platinum wire and saturated calomel electrode (SCE) were the counter electrodes and reference, respectively. The corrosion current (I_{corr} / μA cm^{-2}), corrosion potentials (E_{corr} / V_{SCE}) and polarization resistance (R_p / Ω cm^{-2}) were achieved from the Tafel plots. The corrosion protection efficiency (*P.E.*) was also estimated using the following equation (Yu et al., 2014):

$$P.E.(\%) = \frac{I_{corr}^{0} - I_{corr}^{c}}{I_{corr}^{0}} \times 100 \qquad \text{Eq. (3.4)}$$

Where I_{Corr}^{0} is the corrosion current of the bare Ti-6Al-4V and I_{Corr}^{c} is the corrosion current of the coated sample.

3.4.6. Surface Wettability

The surface wettability (hydrophilicity) of the specimens was examined by measuring the contact angles of sessile drops of deionized water deposited on each specimen surface. A video-based optical contact angle measuring system (OCA 15EC, Data Physics Instruments GmbH, Germany) was utilized to inspect the optical wettability. A constant liquid volume of 10 μl was used for the contact angle evaluations of all the specimens using a drop velocity of 2 μl s^{-1} at a temperature of 26±1 °C. The droplet height "*h*" and width "*d*" were measured to calculate the contact angle "*θ*" as follows (Elias et al., 2008):

$$\theta(^\circ) = 2\tan^{-1}\left(\frac{2h}{d}\right) \qquad \text{Eq. (3.5)}$$

3.4.7 In-vitro Bioactivity

Simulated body fluid (SBF) is a metastable buffer solution, wherein even a small, unwanted discrepancy in the preparation step and the storage temperature, may severely affect the phase purity and high temperature stability of the formed hydroxyapatite powders, as well as the kinetics of the precipitation processes (Ohtsuki et al., 1992). Here, to characterize the bone-like apatite layer, two preparation methods of SBF solution were applied. In the first approach (Kokubo method (Kokubo et al., 2006; Ohtsuki et al., 1992)), the required precursors were dissolved in DH_2O and the pH settled to 7.3. After that, the samples were immersed in 10 ml SBF solution and held for 1 to 14 days at a constant temperature and pH of 37 °C and 7.3, respectively. In the second approach, reagent-grade NaCl, $NaHCO_3$, KCl, $Na_2HPO_4{\cdot}2H_2O$, $MgCl_2{\cdot}6H_2O$, Na_2SO_4, $(CH_2OH)_3CNH_2$, $CaCl_2.2H_2O$ and HCl were utilized in the preparation of SBF according to the method described by Tas (Bayraktar et al., 1999). For this purpose, SBF solution was prepared by dissolving proper amounts of the above chemicals in deionized water. Reagents were added, one by one, after each one was fully dissolved in 700 ml of water. For pH adjustments during the preparation of SBF solution, a total of 40 ml of 1 M HCl solution was consumed. A 15 ml aliquot of this amount was added just before the addition of $CaCl_2.2H_2O$ and the second portion of the HCl solution was utilized in the remainder of the titration process. Following the addition of the $(CH_2OH)_3CNH_2$, the temperature of the solution was increased from ambient to 37 °C. This solution was then titrated with 1 M HCl to the pH of 7.4, at 37 °C. Besides, the solution was diluted steadily with successive additions of deionized water during the titration process to reach a final volume of 1 liter. Finally, similar to the previous method, the specimens were incubated

in SBF solution for 14 days. The soaked specimens were then removed and rinsed in ethanol and were analyzed by FESEM/EDS to examine the apatite formation on the surface. However, the main differences between these two methods in terms of the SBF concentrations can be summarized as below (Bayraktar et al., 1999):

(i) The nominal, initial HCO_3^- ion concentration of Kokubo-SBF increased from 4.2 to 27.0 mM, which is the same concentration of human plasma,

(ii) The concentration of Cl^- ion decreased from 147.8 mM to 125 mM, whereas the Cl^- ion concentration in human plasma is 103 mM.

3.4.8 Antibacterial Activity

The in-vitro antibacterial activity of the substrate, TiO_2 NTs, TiO_2 NTs-Ag_2O NPs, as well as the specimens coated by Ta, Ta_2O_5 NTs, and Ta_2O_5 NTs-Ag_2O NPs was evaluated against *Escherichia coli* (*E.coli*, ATCC®25922™), using an Ti-6Al-4V specimen as control. The specimens were firstly sterilized in 70% ethanol, washed twice with sterile deionized water, and dried under sterile condition. The bacteria environment was prepared by suspending few colonies from 18 to 24 hours-old culture of *E.coli* in 3 ml of cation-adjusted Mueller-Hinton broth (CAMHB; Becton Dickson, Sparks, MD) and adjusting to an optical density (OD_{625}) of 0.8- 0.1, corresponding to 1 to 2 $\times 10^8$ colony-forming units per millilitre ($CFU.ml^{-1}$). The bacteria suspension was then diluted to obtain a starting inoculum of 1×10^6 $CFU.ml^{-1}$. Then, 200 µL of the bacteria suspension was pipetted on each specimen and gently spread evenly across their surfaces, followed by incubation of the specimens at 37°C in a humid atmosphere. At the predetermined time intervals of 0, 2, 4, 6, and 24 hours, 10 µL of the suspension was removed, serially diluted with CAMHB and spread on nutrient agar plates. The nutrient plates containing the bacteria suspension were incubated for 24 hours and the cell viability on each plate was quantified via CFU measurement. The antibacterial experiments were repeated for at least

three times and the obtained data were reported as mean ± standard deviation (SD). The differences in antibacterial properties of the specimens and the control group at respective time points were statistically analysed using the Statistical Package for the Social Sciences (SPSS) software (version 22, SPSS Inc., Chicago, IL) and applying the two way analysis of variance (ANOVA) method followed by Bonferroni post-test ($P < 0.001$).

3.4.9 Human Osteoblast Cell Culture

The cell culture suspension was prepared by mixing 1 ml of the human osteoblast cells (HObs) with 10 ml Dulbecco's Modified Eagle's Medium and Ham's F-12 Nutrient Mixture (DMEM/F12; Gibco-Invitrogen, Thermo Fisher Scientific, Waltham, MA) in presence of 10% fetal bovine serum (FBS; Gibco-Invitrogen, Thermo Fisher Scientific, Waltham, MA) and 1% penicillin-streptomycin (PS), followed by transferring to a cell culture dish and storage at 37°C in normal atmosphere comprising 5% CO_2. When the cell population reached to around 3.0×10^5 cells.ml^{-1}, the cells were seeded on the specimens using 6-well polystyrene plates (around 1.0×10^5 cells/well) and incubated in 5% CO_2 environment for 1, 3, or 7 days to investigate the influence of incubation time on the cell viability and morphology.

3.4.10 Cell Morphology and Adhesion

After each incubation interval, the specimens were rinsed with distilled water and 0.1M PBS, followed by fixation with glutaraldehyde (2.5% in 0.1 M PBS; Sigma-Aldrich, St. Louis, MO) for 1 hour and washing three times with 0.1 M PBS for 10 minutes. The specimens were then dehydrated by subsequent ethanol treatments using a graded sequence of ethanol with concentrations of 50, 70, 90, and 100% each for 10 minutes, desiccated by supercritical-point CO_2, and sputter coated with a gold film. The morphological properties of the adhered cells were investigated by FESEM (FEI Quanta 200, Philips, Netherlands).

Confocal laser scanning microscopy (CLSM) was also used to observe the cell proliferation on the tested specimens. For this aim, the cells were fixed using 4% paraformaldehyde (Sigma-Aldrich, St. Louis, MO) at 25°C for 15 minutes and then supplied with blocking buffer (0.03% Triton X-100/PBS and normal serum) for 1 hour, followed by treatment with 4′,6-diamidino-2-phenylindole (DAPI; Sigma-Aldrich, St. Louis, MO) to stain the cells nuclei, and examination under the confocal microscope (Leica TCS-SP5 II, Leica Microsystem, Mannheim, Germany).

3.4.11 Cell Viability and Proliferation Assay

The viability and proliferation of HOb cells on the specimen surfaces were investigated using alamar blue (Thermofisher Scientific, Waltham, MA) assay with an alamar blue: culture media ratio of 1:10. After each incubation interval, the specimens were rinsed with PBS, followed by transferring to 6-well polystyrene plates and addition of 1 ml of alamar blue reagent to each well. After 3 hours of storage in 5% CO_2 incubator, the optical density changes were evaluated using a multimode microplate reader (Infinite® 200 PRO, Tecan, Männedorf, Switzerland) at wavelength 450 nm with 650 nm as background reference. Cell viability was calculated as reduction in the absorbance recorded compared to reference, representing the percentage of viable cells.

CHAPTER 4: RESULTS AND DISSCUSIONS

4.1 Structural, Mechanical and Biological Behavior of TiO_2 Nanotubular Arrays Thin Films with Decorated Ag_2O Nanoparticles on Ti–6AL–4V Alloy

4.1.1 Formation of TiO_2 Nanotubes with Decoration of Ag_2O NPs on the Ti-6Al-4V

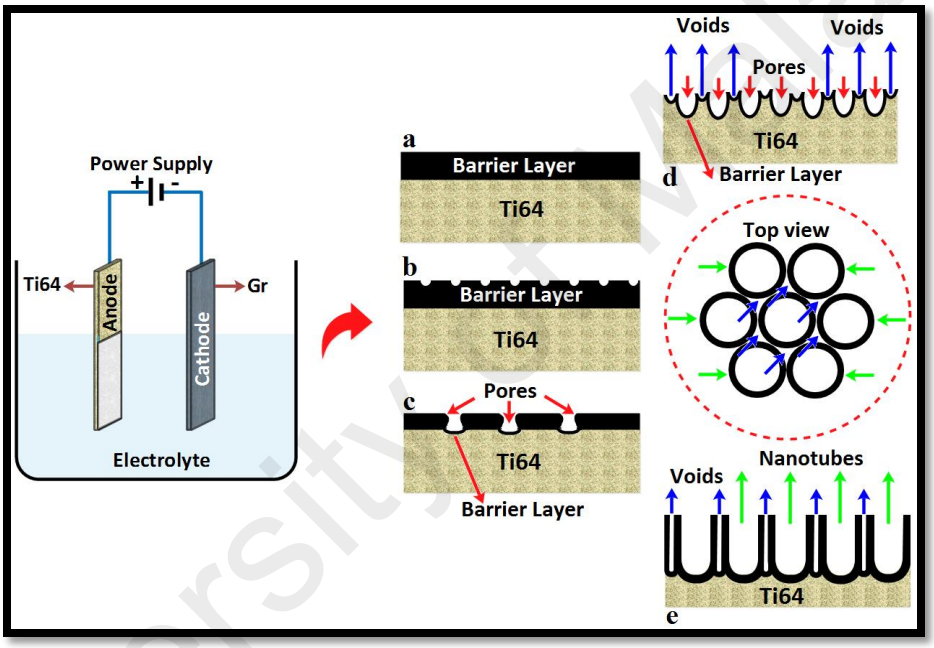

Figure 4.1: Schematic of the anodization process and generation of the nanotubes at constant anodization voltage: (a) oxide layer formation, (b) pit generation, (c) growth of the pit, (d) oxidation and field assisted dissolution of the metallic region between the pores, and (e) fully developed nanotubular arrays with a corresponding top view.

As shown in Figure 4.1a, a thin layer of oxide develops on the Ti-6Al-4V surface with anodization onset. From Figure 4.1b, small pits form in this oxide layer as a result of the localized dissolution of the oxide, making the barrier layer at the bottom of the pits relatively thin. This in turn, raises the intensity of the electric field across the remaining barrier layer resulting in further pore growth as shown in Figure 4.1c. It has been proven

that the pore entrance is not influenced by electric field assisted dissolution. Therefore, the pore entrance remains relatively narrow while the electric field distribution in the curved bottom surface of the pore causes pore widening, as well as deepening of the pore. The result is a pore with a scallop shape (Mor et al., 2006). Since the Ti–O bond energy is high (323 kJ/mol), in the case of TiO_2 it is reasonable to assume that only pores having thin walls can be formed due to the relatively low ion mobility and relatively high chemical solubility of the oxide in the electrolyte. Hence un-anodized metallic portions can initially exist between the pores. As the pores grow deeper the electric field in these protruded metallic regions increases, enhancing field assisted oxide growth and oxide dissolution. These processes all occur simultaneously with the pore's well-defined inter-pore voids formation initiation (Figure 4.1d). Thereafter, both voids and tubes grow in equilibrium. The nanotube length increases until the electrochemical etch rate equals the chemical dissolution rate of the nanotube top surface. Once this point is reached, the nanotube length will be independent of the anodization duration as determined for a given electrolyte concentration and anodization potential. The Ag_2O NPs were finally decorated on the NT edges using PVD magnetron sputtering with controlled parameters. Schematic of the anodization process generation of the TiO_2 nanotubes at constant anodization voltage and decoration of Ag_2O NPs on the TiO_2 NTs in 30 sec are shown in Figure 4.2.

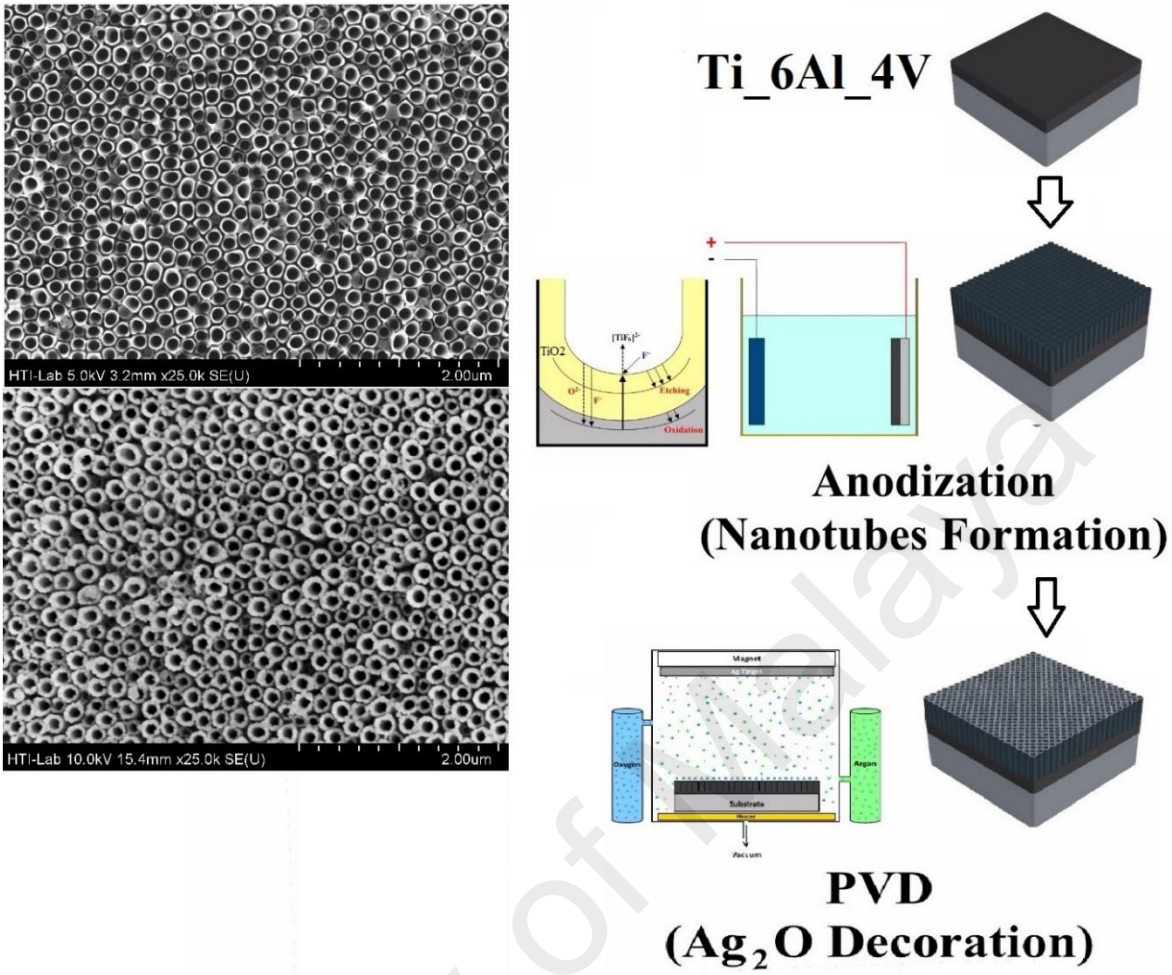

Figure 4.2: Schematic of the anodization process generation of the TiO_2 nanotubes at constant anodization voltage and decoration of Ag_2O NPs on the TiO_2 NTs in 30 sec

4.1.2 XRD Analysis

Figure 4.3 displays the XRD profiles of the substrate (Ti-6Al-4V), the 4 h anodized sample, and the annealed sample at 500 °C for 1.5 h before and after Ag_2O decoration. As can be seen in Figure 4.3a, the XRD reflection of the substrate illustrates only the diffraction peaks of Ti (JCPDS#005-0682) located at 2θ = 35.1°, 38.4°, 40.2°, 53.1°, 63.1°, 70.6° and 76.4°, which are related to the (1 0 0), (0 0 2), (1 0 1), (1 0 2), (1 1 0), (1 1 2) and (2 0 1) planes, respectively. After the 4 h anodization, a coating with an amorphous structure was formed as shown in Figure 4.3b. During annealing at 500 °C (Figure 4.3c), a highly crystalline single anatase phase (JCPDS01-071-1166, crystal

system: tetragonal; space group: *I*41/ *and*; space group number: 141) was formed as a result of thermally induced crystallization. Accordingly, new diffraction peaks ((1 0 1) plane at 2θ = 25.3°, (0 0 4) plane at 2θ = 38.4°, (2 0 0) plane at 2θ = 48.1°, (1 0 5) plane at 2θ = 53.2°, and (2 0 1) plane at 2θ = 55.2°) corresponding to TiO_2 (anatase) became apparent in the XRD profile. The successful decoration of Ag_2O nanoparticles on the edges of TiO_2 nanotubes is also confirmed in Figure 4.3d. As can be seen, two characteristic peaks of Ag_2O including (1 0 1) plane at 2θ = 38.6° and (1 0 2) plane at 2θ = 50.4°) became evident in the XRD profile of the Ag_2O decorated on TiO_2 nanotubes after annealing at 500 °C. Based on the XRD results, the phase composition and preferred crystal orientation may change after subsequent annealing. In addition, the fraction of anatase is likely altered at higher temperatures due to the anatase to rutile phase transition.

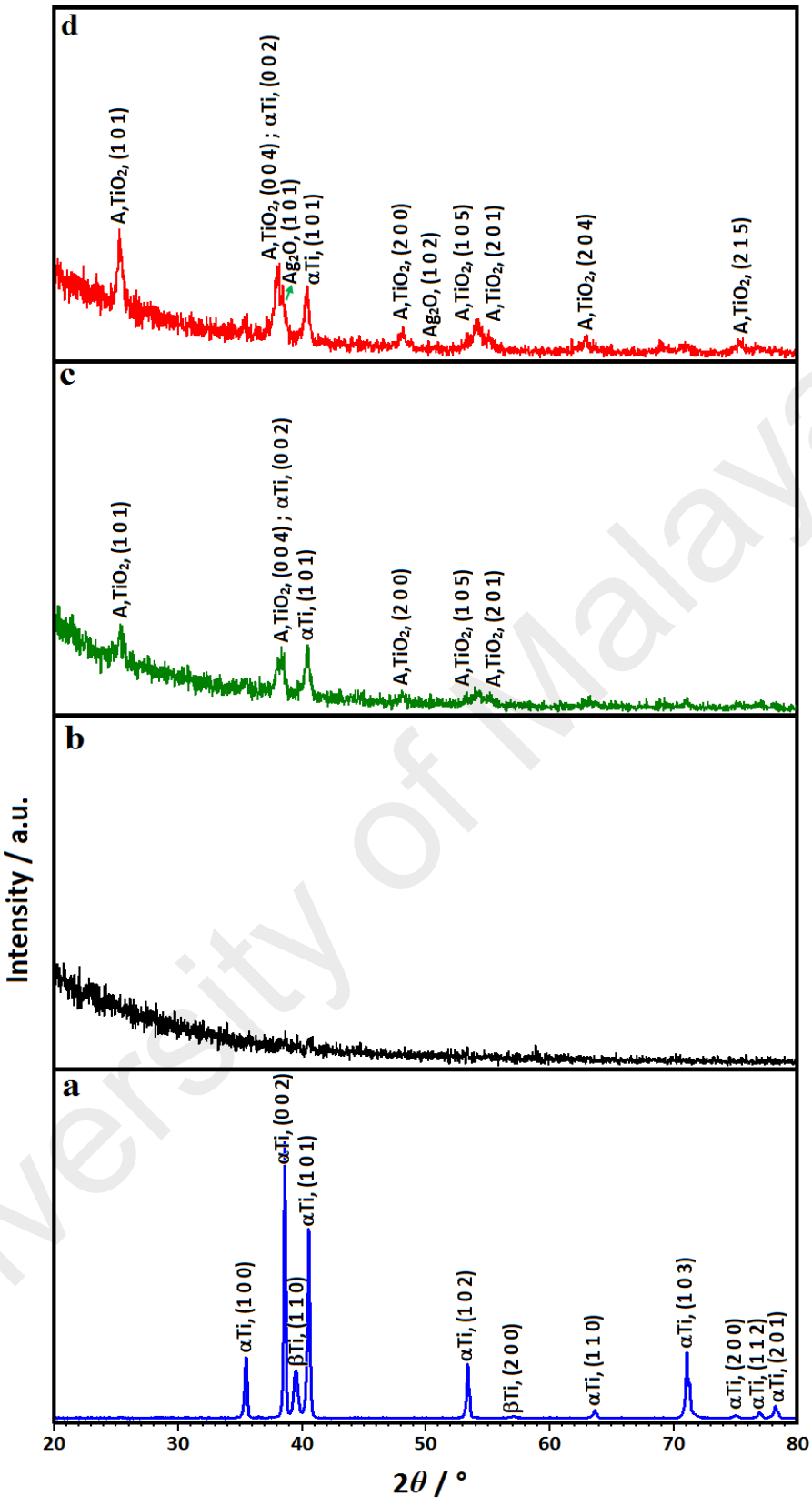

Figure 4.3: XRD profiles of the (a) substrate, (b) the 4 h anodized sample, and the annealed sample at 500 °C for 1.5 h (c) before and (d) after Ag_2O decoration.

4.1.3 XPS Analysis

Figure 4.4 shows the XPS spectra of the annealed sample at 500 °C for 1.5 h after Ag_2O decoration. High-resolution XPS indicated that the nanotubes formed on Ti-6Al-4V alloy are comprised of a mixture of TiO_2 and Ag_2O. An observed intense C1s peak in this spectrum can be related to the elemental carbon at the surface of the nanotubular arrays. In addition, the absence of C1s peak at 282.4 eV confirmed that no replacement of an oxygen atom by a carbon atom occurred in the TiO_2 lattice. A broadening in the core level O 1s peak at 530.2 eV may be linked to physic-adsorbed or trapped water (Figure 4.4a). Figure 4.4b displays the XPS spectrum of Ti2p, where the peaks positioned at 458.9 and 464.4 eV are connected to the spin–orbit splitting of $Ti2p_{3/2}$ and $Ti2p_{1/2}$, respectively, which is in good agreement with those of titanium (IV) dioxide. This shows that Ti in the nanotubular configuration is present in the 4-valent state. Figure 4.4c demonstrates the high-resolution XPS spectra of Ag3d, where two characteristic peaks observed in the Ag3d spectrum at 368.1 eV and 374.1 eV are ascribed to $3d_{5/2}$ and $3d_{3/2}$ orbitals.

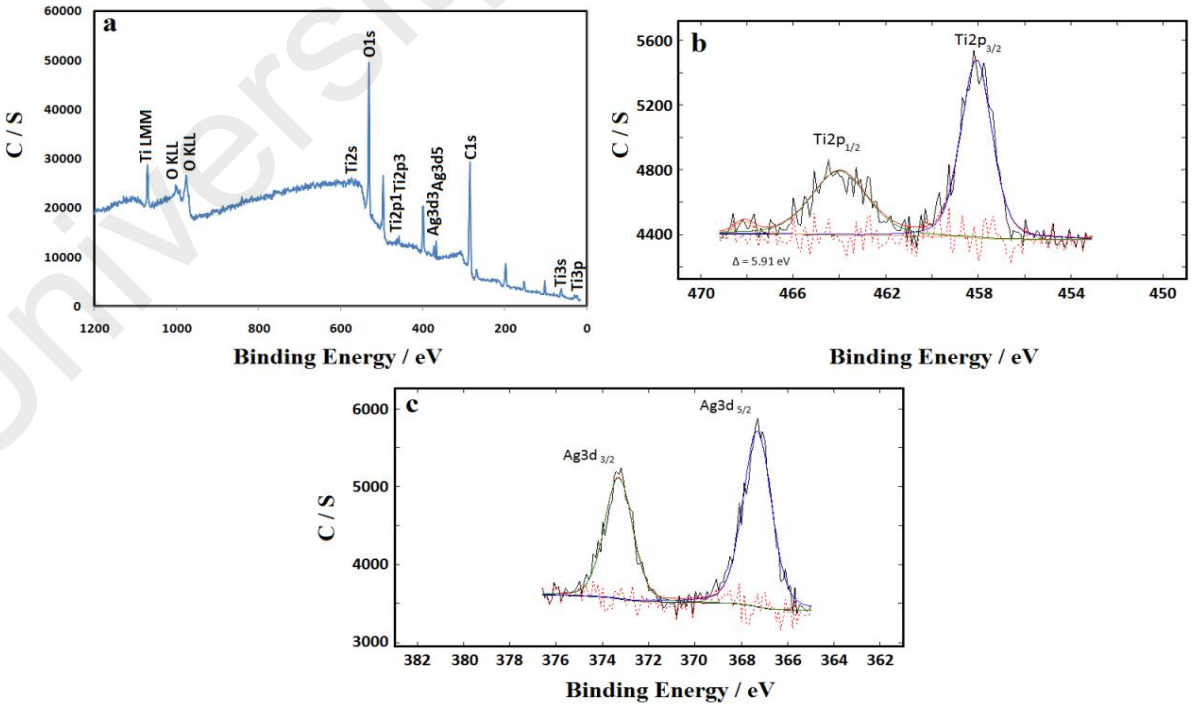

Figure 4.4: (a) XPS spectra and high-resolution of (b) Ti2p and (c) Ag3d regions of the annealed sample at 500 °C for 1.5 h after Ag_2O decoration.

4.1.4 Microstructural Evolution of TiO_2 and Heat Treated TiO_2 NTs

Since the structure and geometric dimensions of the nanotubular arrays play a critical role in the biomedical functionality, the microstructural characterization is a fundamental step in order to understand their behavior. Figure 4.5 shows FESEM images of the sample anodized for 4 h at 20 V in an electrolyte containing 0.2 M H_3PO_4 and 0.4 M NH_4F before thermal treatment. As mentioned earlier, in the initial stages of anodizing, irregular pits were developed due to the localized dissolution of the oxide layer, followed by the pits conversion to larger pores. With a prolonged anodization time, more uniformly distributed pores were formed, where a pore's ordering is a consequence of local surface perturbations (Crawford et al., 2007). When the anodization time is extended to 4 h, significant changes from a non-porous structure to a nanotubular configuration were observed as shown in Figure 4.5a. It is clear that highly oriented TiO_2 nanotubes were formed after 4 h of anodization where the nanotubes are uniformly distributed over the anodized surface. From the higher magnification FESEM image in Figure 4.5b, the average inner diameter is 72 nm. During the early stages of anodization, field assisted dissolution over shadows the chemical dissolution due to the high electric field across the electrode. As anodization continues and the oxide layer thickens, chemical dissolution dominates over field assisted dissolution. This effect increases the size and density of the pores. Following this stage, the growth and propagation of the pores occur by internal motion at the oxide/metal interface, which leads to the formation of hollow cylindrical oxide particles that develop into a nanotubular structure.

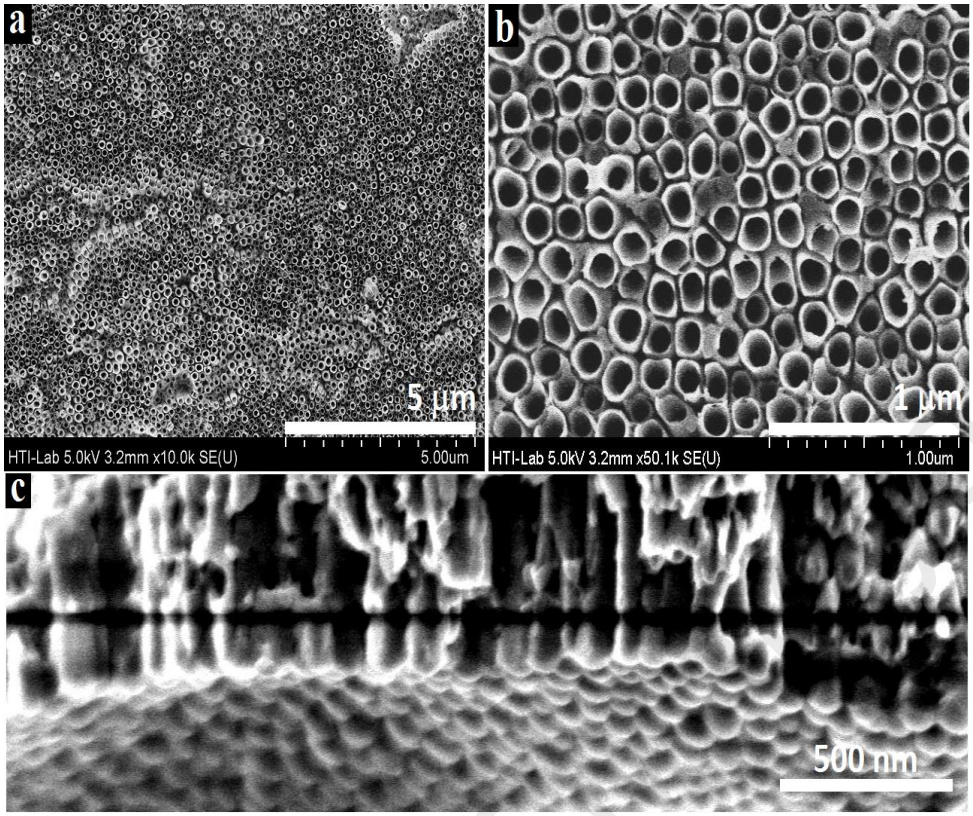

Figure 4.5: FESEM images of a Ti-6Al-4V surface after one pot anodization with exposure time of 4 h at 20 V in an electrolyte containing 0.2 M H_3PO_4 and 0.4 M NH_4F; (a,b) top view and (c) bottom.

As shown in Figure 4.5c, the bottom of the TiO_2 nanotubes demonstrates a series of evenly spaced "bumps" that signify the pore tips of each individual nanotube. Given that a barrier layer at the bottom of nanotubes is scalloped, this layer can be divided into upper and lower parts, which are called the pure barrier layer and interface barrier layer, respectively (Grimes et al., 2009). The pure barrier layer is considered to be pure TiO_2 while the interface barrier layer is considered a mixture of TiO_2 and substrate material (Ti-6Al-4V). As the oxide layer at the bottom of the pore is subjected to chemical dissolution, it becomes thinner with time. As the thickness declines, electric field assisted dissolution occurs again in this region, and consequently, the pores penetrate into the substrate making the nanotubes increasingly longer. As the oxide layer at the bottom of the pore is subjected to chemical dissolution, it becomes thinner with time. If anodization is conducted in fluorine concentrated solution, the rate of attack would be faster thus

thickness reduction would be faster. As the thickness reduces, electric field assisted dissolution will reoccur at this region. By this process, the pores will penetrate inside the Ti and the nanotubes become longer and longer. However, as voltage is continuously applied, anodization would reoccur at the bottom of the pore, forming nanotubes with closed bottom. The growth of the nanotubes is therefore determined by the amount of fluorine in the bath and the degree of electric field dissolution i.e. the voltage applied. When the anodization voltage is very high, the rate of electric field dissolution at the barrier layer inside the nanotubes would be higher hence longer nanotubes would be produced (Lockman et al., 2010).

Figure 4.6 shows typical cross-sectional and bottom view FESEM images of the TiO_2 nanotube arrays anodized for 4 h at 20 V in an electrolyte containing 0.2 M H_3PO_4 and 0.4 M NH_4F. A highly ordered nanotubular structure with an average individual length of 1 μm was formed after the anodization. In addition, this figure shows that the TiO_2 nanotubes possessed a bamboo-shaped structure with good density, which could lead to enhanced chemical activity and stronger interactions. Indeed, this feature is a crucial parameter contributing to good mechanical properties (Baradaran et al., 2013).

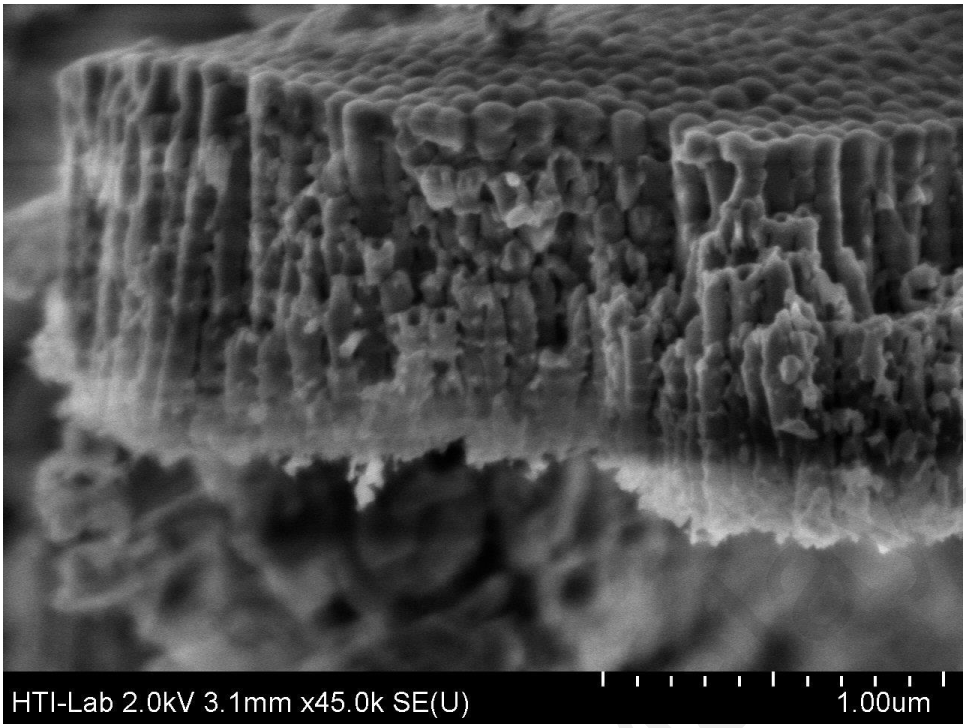

Figure 4.6: FESEM cross-section images of TiO_2 nanotube arrays anodized for 4 h at 20 V in an electrolyte containing 0.2 M H_3PO_4 and 0.4 M NH_4F

To investigate the effect of subsequent heat treatment on the microstructural evolution, annealing was done at a low heating and cooling rate of 5 °C min^{-1} at 500 and 700 °C for 1.5 h in an argon gas furnace. Figure 4.7 shows top view FESEM images of the 4 h anodized sample after annealing at 500 °C at different magnifications.

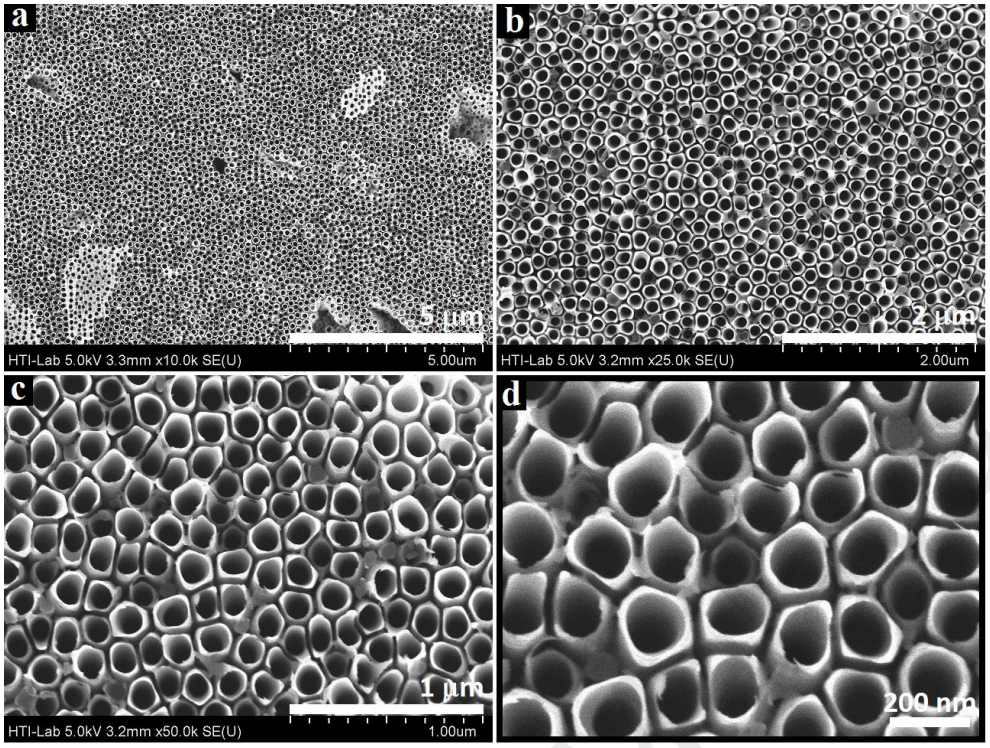

Figure 4.7: Top view FESEM images of the 4 h anodized sample after annealing at 500 °C at different magnifications.

The results for the TiO_2 nanotubes annealed at higher temperature (700 °C) are presented in Figure 4.8. As can be seen in Figure 4.7, a highly ordered TiO_2 nanotube array was constructed during annealing at 500 °C for 1.5 h. It is clear that there were no considerable alterations in the morphological characteristics after annealing at this temperature. Accordingly, the morphology and tube diameter did not change noticeably during annealing at 500 °C. It has been found that the nanotubes may collapse at particular annealing conditions such as high temperature and long annealing duration. Here, the surface morphology of the nanotubular arrays were transformed after annealing at 700 °C for 1.5 h as shown in Figure 4.8. In this particular case, annealing at 700 °C for 1.5 h completely destroyed the nanotubes (Figure 4.8a and b), where the tubular configuration was changed to a coarse particle structure (Figure 4.8c). Similar results of the collapse of the TiO_2 nanotubes under annealing at high temperatures have also been reported (Albu

et al., 2008) This indicates that temperatures exceeding 500 °C cause collapse of the TiO_2 nanotubular array.

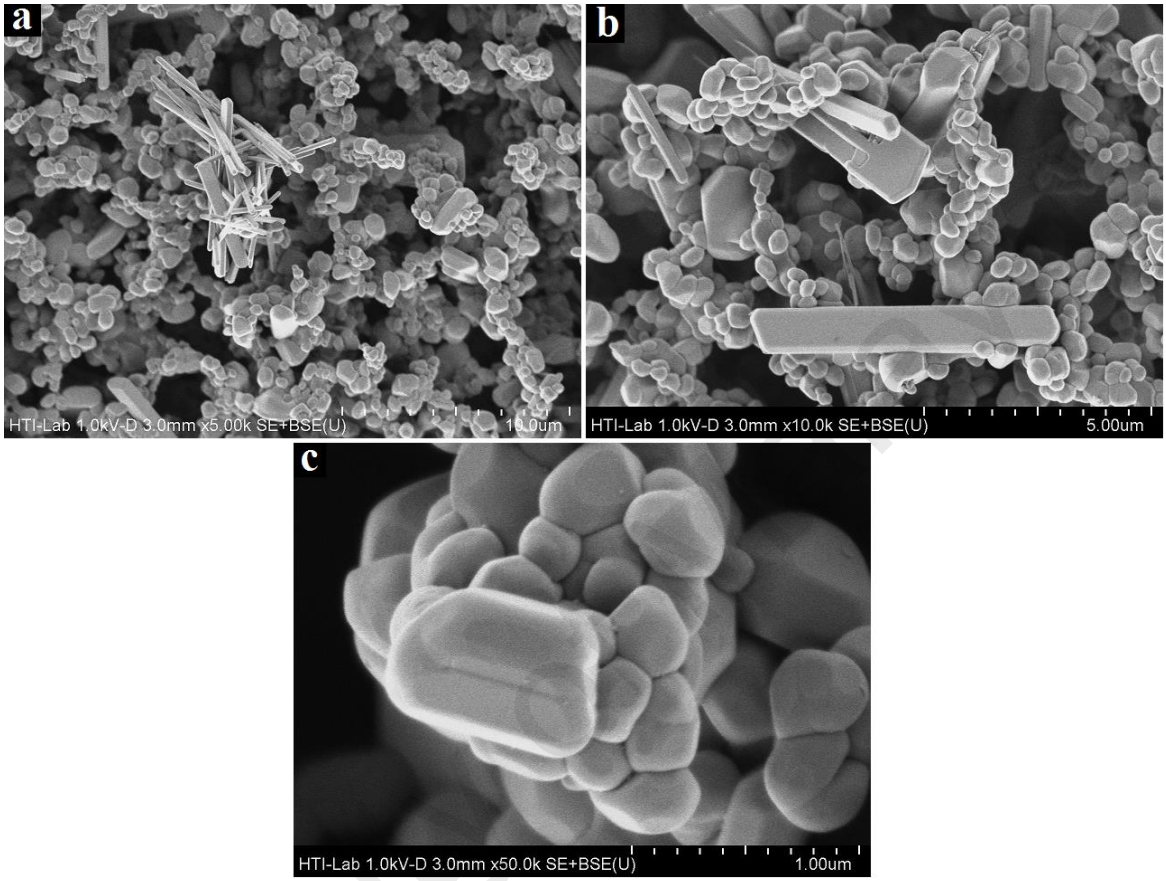

Figure 4.8: FESEM images of the 4 h anodized sample after annealing at 700 °C for 1.5 h at different magnifications; (a, b) detachment of nanotubes and (c) formation of a coarse particle structure.

4.1.5 Adhesion Strength of TiO_2 and Heat Treated TiO_2 NTs

On account of the long periods of presence in the living body, the main features of the implant materials are the stability and durability. Accordingly, improving the adhesion strength between the coating layers and implant is vital (Tomsia et al., 2005). Figure 4.9 shows the optical micrograph of a scratch track and profiles of depth, load, friction, and COF versus distance for the 4 h anodized specimen at a constant potential of

20 V. The variation of scratch length, failure point and adhesion strength of the sample are also provided. Here, the scratch direction was from left to right for all the samples. Concerning the critical load determination, there are different methods such as microscopy observation (optical microscopy, SEM), acoustic emission analysis, tridimensional force recording, acoustic reflection mode scanning microscope (ARM), and measurement of the penetration depth of the scratching point (Sekler et al., 1988). Optical microscopy was used to examine the surface damage caused by the scratch test. The distance between the start (or the end) of the scratch and the damage site can be measured and directly related to the load. In principle, any optical microscope can be used to perform this measurement. If such a microscope is integrated in the instrument, there are obvious advantages as follows: (a) The scratching site can be chosen precisely with respect to the sample geometry, to surface irregularities and to previous scratches; (b) A precise correlation between the sample displacement and the applied load and therefore more reliable critical load data can be obtained; (c) The optical microscope can be equipped with a video system which provides a useful and convenient tool when many samples have to be examined or for instruction and demonstration purposes.

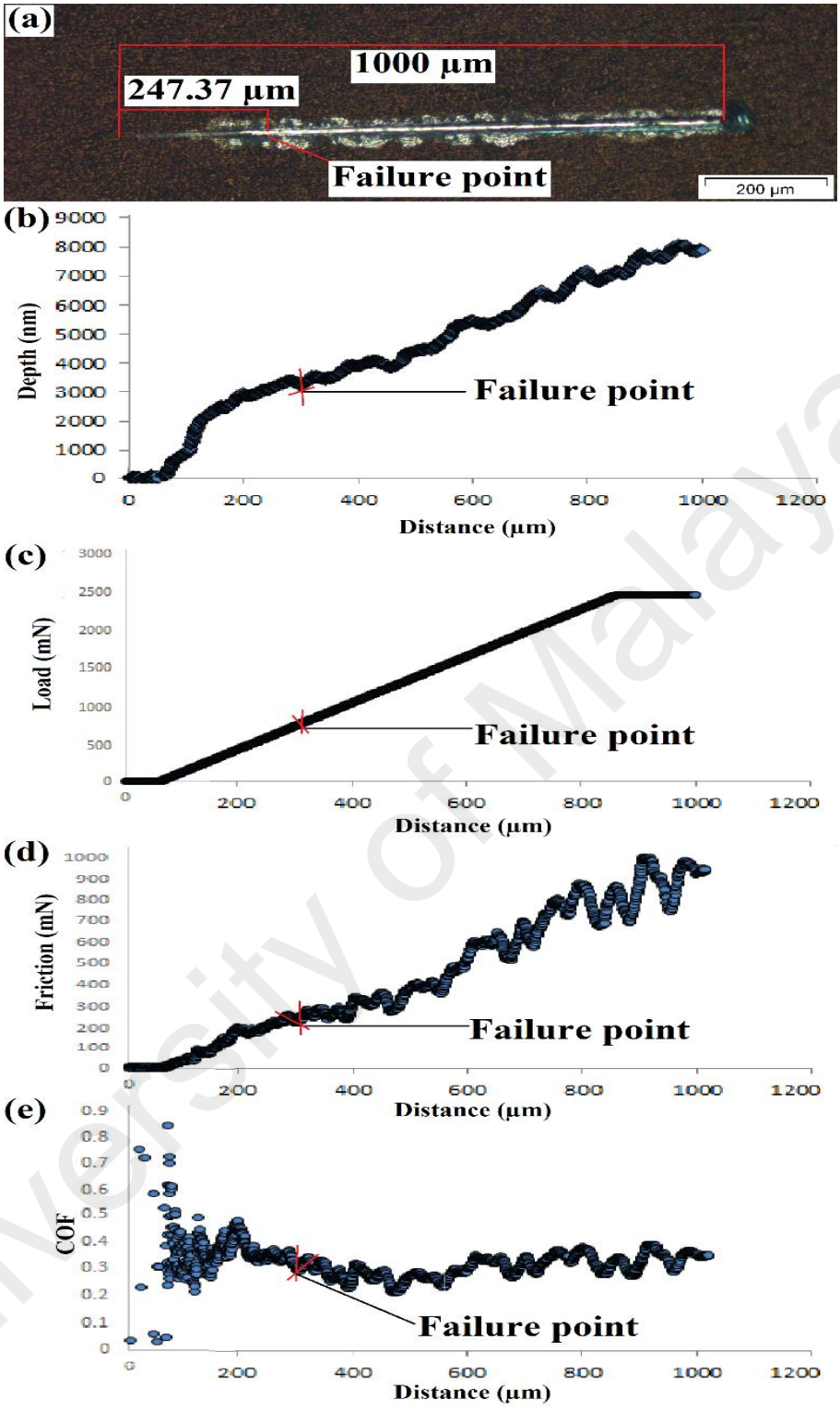

Figure 4.9: (a) The optical micrograph of scratch track and profiles of (b) depth, (c) load, (d) friction and (e) COF against scan distance after anodization.

Generally, the critical loads ($L_{e\text{-}p}$, L_{c1}, L_{c2}, and L_{c3}) are defined by the abrupt changes in depth against distance profile. $L_{e\text{-}p}$ refers to elastic-to-plastic transition and cohesive

failure and L_{c1} denotes to lower critical load and shows the beginning of parallel and edge cracking. Failure or upper critical load L_{c2} is characterized by partial coating delamination along with a subsequent intermittent substrate exposure. Finally, L_{c3} demonstrates a total coating failure by complete exposure of the surface material (Baradaran et al., 2013). In the present case, the respective failure modes were identified to denote the critical loads required to break the bond between the TiO_2 nanotubes and the substrate. It is obvious that the nanotubular configuration was initially in an elastic-to-plastic transition mode. L_{c1}, became visible as cracking on the trackside followed by mild tensile cracking along the scratch tracking. By increasing the scratch load, the delamination trackside gradually became clear which was recorded as L_{c2}. A further increase in the load led to a variety of failures along the scratch path involving trackside cracking, delamination, and chipping L_{c3}. From Figure 4.9a-c, the scratch length and the failure point of the coated sample are 1000 and 247.37 µm, respectively, where the applied load gave an adhesion strength of 862.06 mN. As well, the calculated friction and COF were 250.88 mN and 0.29, respectively (Figure 4.9d and e).

Figure 4.10 shows the optical micrograph of the scratch track and graphs of depth, load, friction, and COF versus distance for the 4 h anodized sample after thermal treatment at 500°C.Over the same scratch length (1000 µm), the failure point shifted to 557.89 µm and the applied load increased to 1814.28 mN after annealing at 500 °C. As well, the calculated friction and COF were 381.89 mN and 0.21, respectively. For further investigation, the scratch hardness test was evaluated to measure the resistance of TiO_2 nanotubular arrays to permanent deformation under the action of a single point (stylus tip). Since the indenter (in this case a diamond stylus) moves tangentially along the surface, the scratch hardness test contains a different combination of surface properties. Based on the obtained data, the scratch hardness of the anodized sample before and after annealing was 0.45 and 5.86 GPa, respectively. These results show that after annealing

the scratch hardness increases by over an order of magnitude compared to the untreated sample.

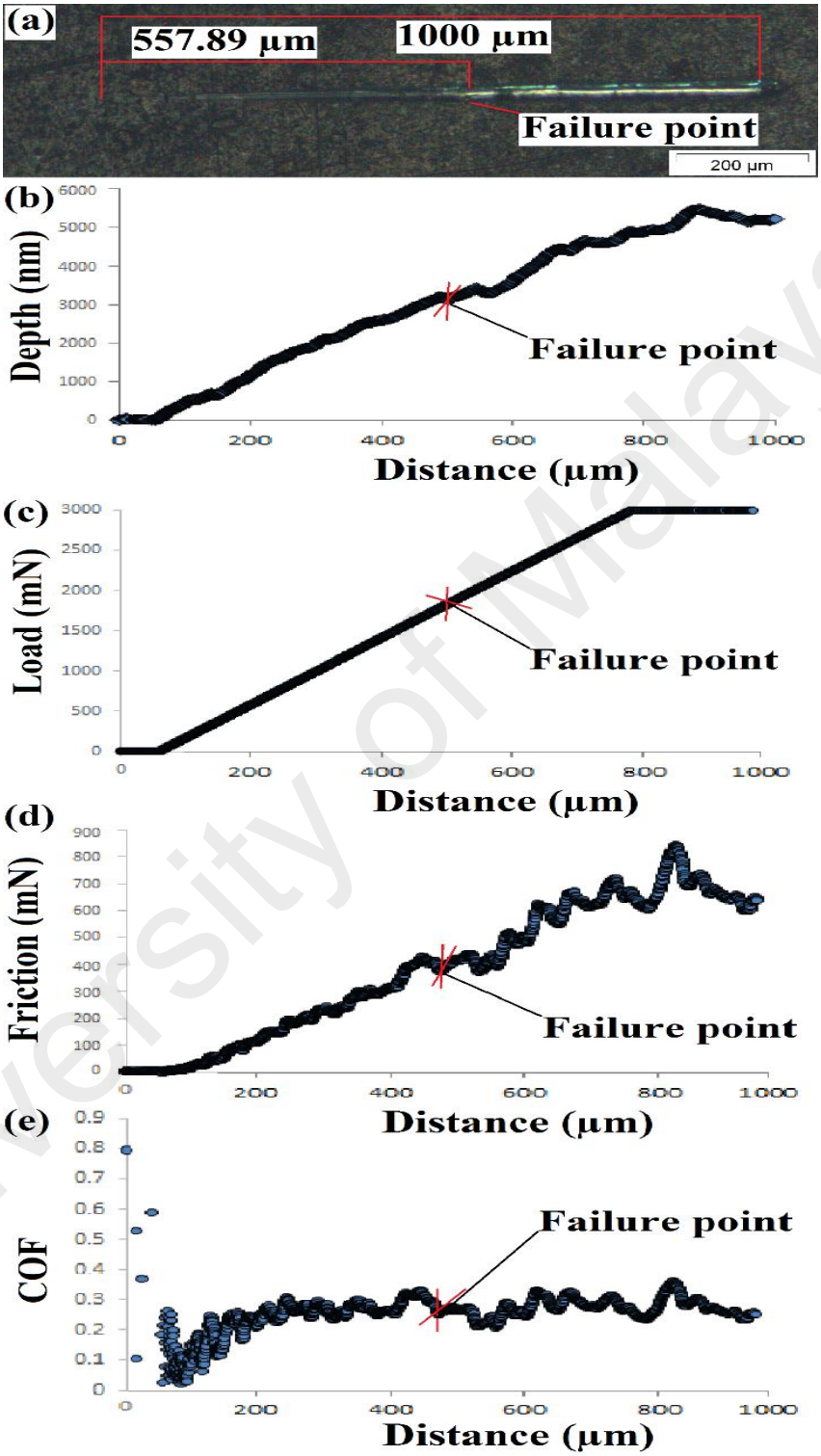

Figure 4 .10:(a) optical micrograph of scratch track and graphs of (b) depth, (c) load, (d) friction, and (e) COF versus distance for the 4 h anodized sample after thermal treatment at 500 °C.

4.1.6 Microstructural Evolution of Ag_2O NPs on the NTs

Figure 4.11(a-h) presents FESEM images of the nanoparticle deposited Ag_2O on nanotubular arrays (NTAs) at 500°C.The Ag_2O coating was performed by PVD magnetron sputtering machine on the edge of nanotubes. To deposit a conformal layer with high control of the Ag_2O thickness, different time deposition values are examined and the optimum time is 30 sec (figure 4.11c, d). Prior study showed this unique structure leads to controlled release of Ag^+ with long-term antibacterial ability without showing cytotoxicity. Ag incorporation even shows some favorable effects on promoting cell spreading (Gao et al., 2014). The EDS spectrum (Figure 4.12) and elemental distribution patterns (Figure 4.13) of the TiO_2 NTs with Ag_2O NPs decorated by PVD sputtering for 30 s (TiO_2 NTs-Ag_2O NPs) also confirm formation of a uniform array of Ag_2O NPs on the NT walls.

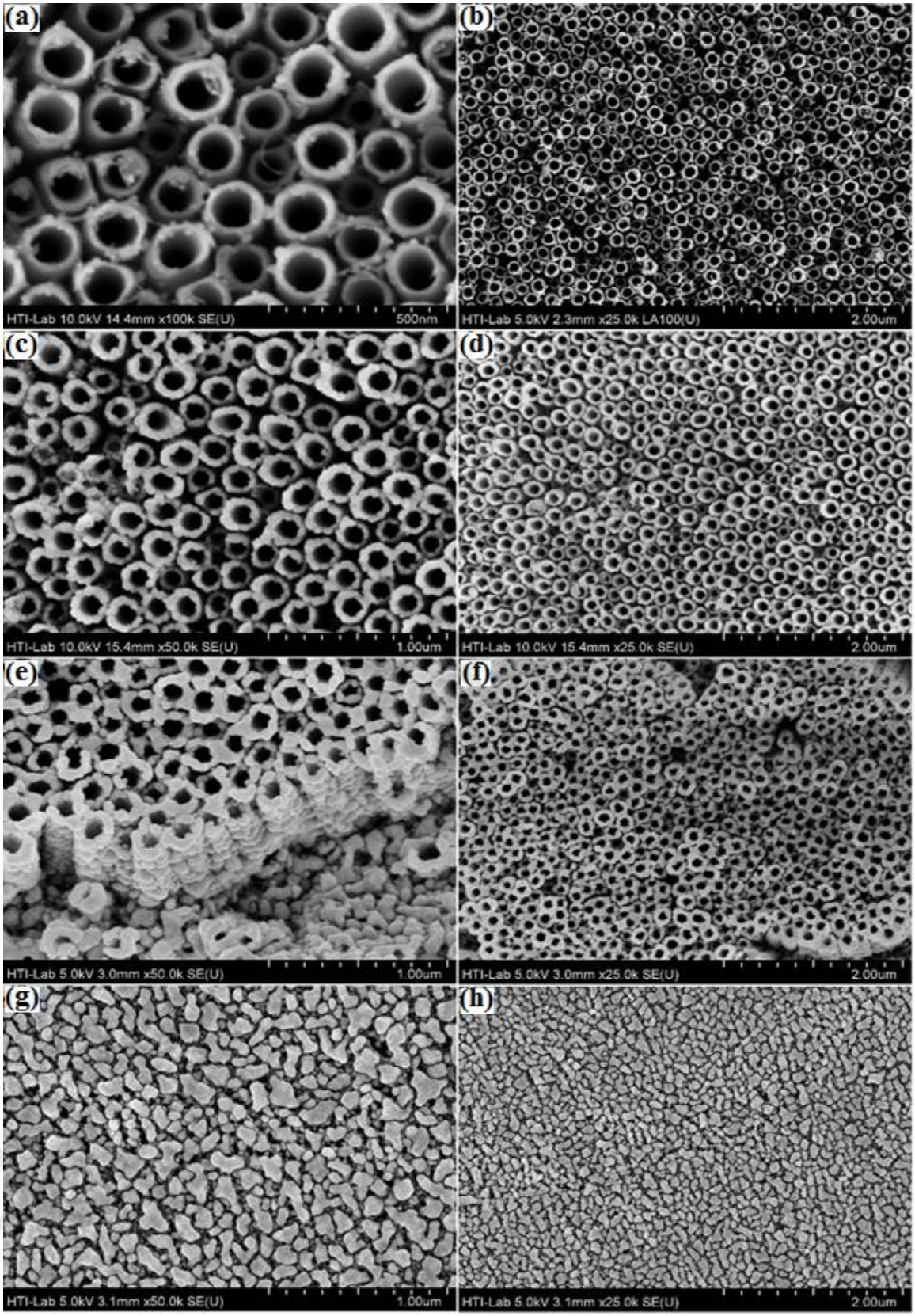

Figure 4.11: Shows the FESEM images of Ag_2O NPs after PVD coating on edges of TiO_2 NTs in (a, b) 10 s, (c, d) 30 s, (e, f) 45 s and (g, h) 60 s.

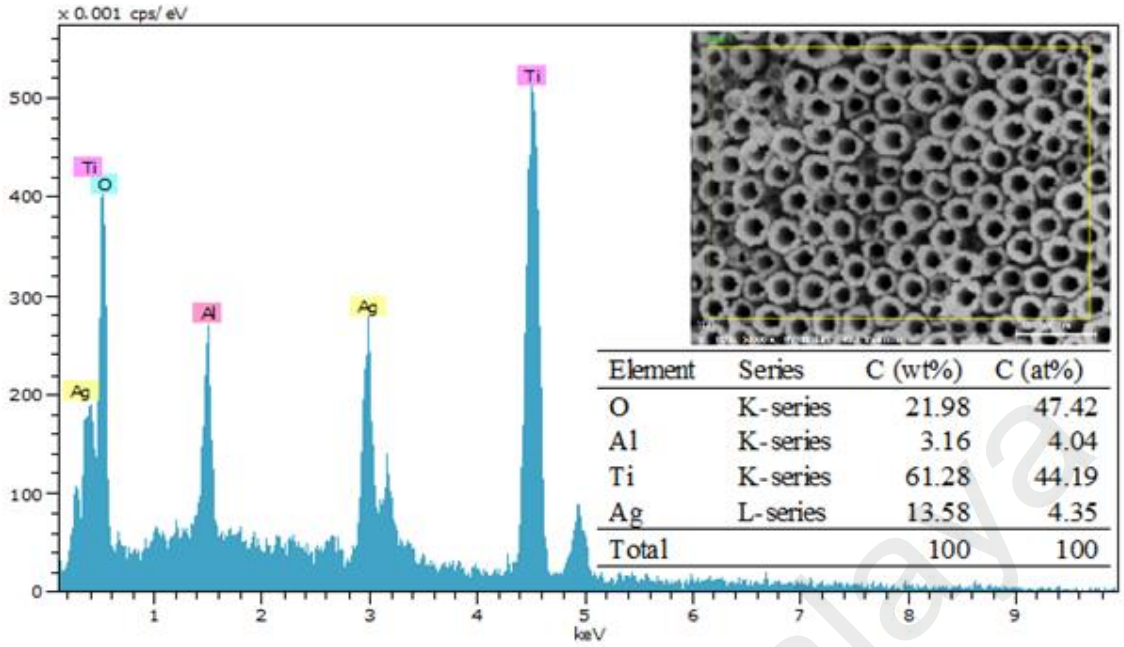

Element	Series	C (wt%)	C (at%)
O	K-series	21.98	47.42
Al	K-series	3.16	4.04
Ti	K-series	61.28	44.19
Ag	L-series	13.58	4.35
Total		100	100

Figure 4.12: EDX analysis of Ag_2O NPs (30 sec) on the TiO_2 NTs

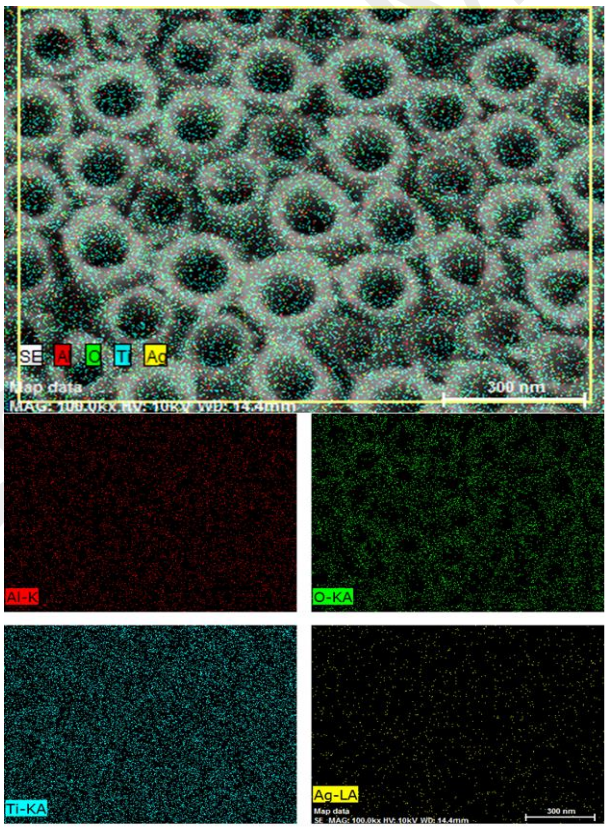

Figure 4.13: The elemental distribution patterns of the constituting elements of the TiO_2 NTs-Ag_2O NPs (30 sec).

4.1.7 Vickers Microhardness

Table 4.1 displays the disparity in the Vickers hardness values of the substrate, the un-annealed TiO_2 nanotubular arrays and the arrays heat treated at 500 and 700 °C. The hardness value of the substrate was 269 HV. During anodization, an amorphous TiO_2 phase was formed, which dominated the hardness of the entire specimen. In this case, the hardness value was 373 HV. After thermal annealing at 500 °C, crystallization of TiO_2 (transition from amorphous to a highly crystalline structure) occurred and as a result the surface hardness was enhanced and reached a value of 435 HV. For the anodized sample crystallized by further annealing at a temperature of up to 700 °C, the fraction of the rutile structure increased notably; this effect increased the surface hardness value to 489 HV because among three types of TiO_2 oxides (rutile, anatase and brookite), the rutile structure exhibits the highest hardness and lowest friction coefficient (Krishna et al., 2005). However, based on microstructural observations (see Fig. 5), the nanotubular arrays collapsed completely after thermal annealing at 700 °C which suggests that annealing at 500 °C in a normal atmosphere is the optimum condition for the thermal treatment of TiO_2 nanotube arrays on Ti-6Al-4V.

Table 4.1: Disparity in Vickers hardness values of substrate, un-annealed TiO_2 nanotubular arrays and arrays heat treated at 500 and 700 °C.

Samples	substrate	TiO_2 NTs after anodization	TiO_2 NTs heat treated at 500°C	TiO_2 NTs heat treated at 700°C
Vickers hardness values (HV)	269	373	435	489

4.1.8 Surface Topography and Tribology

Figure 4.14 shows the friction coefficient (μ_k) as a function of cumulative sliding time under normal loads of 15, 20 and 25 N. It is clear that a feature common to all of the profiles is an increase in the friction coefficient with the normal load (see the tables in Figure 4.14). Moreover, based on the obtained data, the wear loss increased linearly with an increase in the load from 15 to 25 N. According to this figure, the value of μ_k was clearly enhanced at the beginning and reached a steady-state within a short period. This behavior was due to the initial consecutive wear of the surfaces' micro asperities and increased conformity of worn surfaces. Hence, in the early stages, wear damage was caused by brittle micro-fractures within surface grains and by tribochemical reactions (Ezazi et al., 2014). As shown in Figure 4.14, the plotted friction lines of the substrate and anodized sample under a load of 15 N were very similar to each other and reached a steady-state condition within 2 s. Similar trends were also observed under applied loads of 20 and 25 N. These results demonstrate that the substrate and anodized specimen exhibited similar wear behavior over the range of loads examined. In addition, all samples remained stable under a load of 15 N and showed friction coefficient values ranging from 0.093 to 0.280; however, as the normal load was increased to 20 and 25 N, higher coefficients of friction ranging from 0.106 to 0.314 were observed. It should be noted that the sudden increase in the friction coefficient of the anodized sample after annealing at 500 °C indicates that coating failure occurred. On the other hand, it can be observed that the values of the friction coefficient decreased significantly after subsequent annealing. This behavior can be related to the formation and crystallization of TiO_2 as well as the change in phase structure from anatase to rutile. Thus, it can be concluded that the high hardness and low COF of the highly crystalline structure of the TiO_2 nanotubes noticeably improved the wear resistance of Ti–6Al–4V a result that can be considered in practical applications.

In general, the elimination and displacement of material during wear causes changes in surface topography. AFM in contact mode was used to assess the topographical characterization of plain and worn surfaces as shown in Figure 4.16. AFM images were gathered for all samples over an area of 20 µm × 20 µm. All roughness values are reported in terms of R_a, which represents the arithmetic mean of height deviations from the mean profile value (50 scan line). As shown in Figure 4.15a, micro-pores appeared on the surface of the substrate, which could be attributed to the method used to manufacture. As shown, the dominant characteristic of the worn surface was the appearance of coarse ridges and grooves (Figure 4.15b,d,f and h). Ezazi et al.(2014) reported similar behavior (Ezazi et al., 2014). According to the AFM images of the worn surfaces, lateral grooves surrounded by high peaks were formed, representing the formation of microgrooves on the surface of the samples due to the severe plastic deformation of the substrate, a ductile alloy. These results demonstrate that wear occurred by homogeneous deformation in isothermal mode, whereby material was eliminated by the extrusion and lip formation. As indicated in Figure 4.15d, the anodized sample showed a coarser area with protruding hillocks. In the case of the anodized sample annealed at 500 °C (see Figure 4.15e), a highly ordered nanotube structure was achieved which, resulted in the lowest surface roughness among the specimens. In addition, the deep groove configuration was not trivial in the case of the anodized sample annealed at 700 °C, in which the topographical heterogeneity in width and depth were obvious (Figure 4.15h). Table 4.2 shows the average roughness value before and after wear. Based on the obtained data, the average roughness value inside the wear tracks of the annealed sample at 500 °C was 140.4 nm, nearly 2 times less than the value measured for the substrate (300.7 nm). This result confirmed the important role played by the self-organized TiO_2 nanotubular arrays in reducing wear, which is very important in biomedical applications.

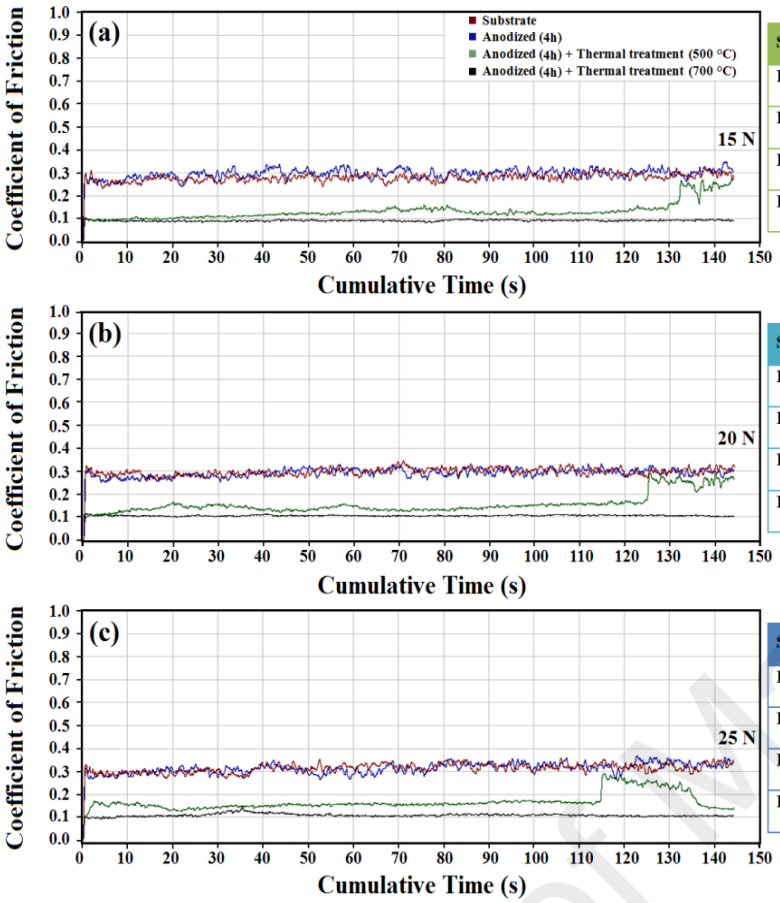

Series	Surface treatment	Load (N)	Friction coefficient (μ_k)
I	Substrate	15	0.280
II	Anodize (4h)	15	0.296
III	Anodize (4h) + 500 °C	15	0.133
IV	Anodize (4h) + 700 °C	15	0.093

Series	Surface treatment	Load (N)	Friction coefficient (μ_k)
I	Substrate	20	0.297
II	Anodize (4h)	20	0.296
III	Anodize (4h) + 500 °C	20	0.156
IV	Anodize (4h) + 700 °C	20	0.106

Series	Surface treatment	Load (N)	Friction coefficient (μ_k)
I	Substrate	25	0.314
II	Anodize (4h)	25	0.313
III	Anodize (4h) + 500 °C	25	0.168
IV	Anodize (4h) + 700 °C	25	0.110

Figure 4.14: Friction coefficient as a function of cumulative sliding time under loads of (a) 15, (b) 20 and (c) 25N.

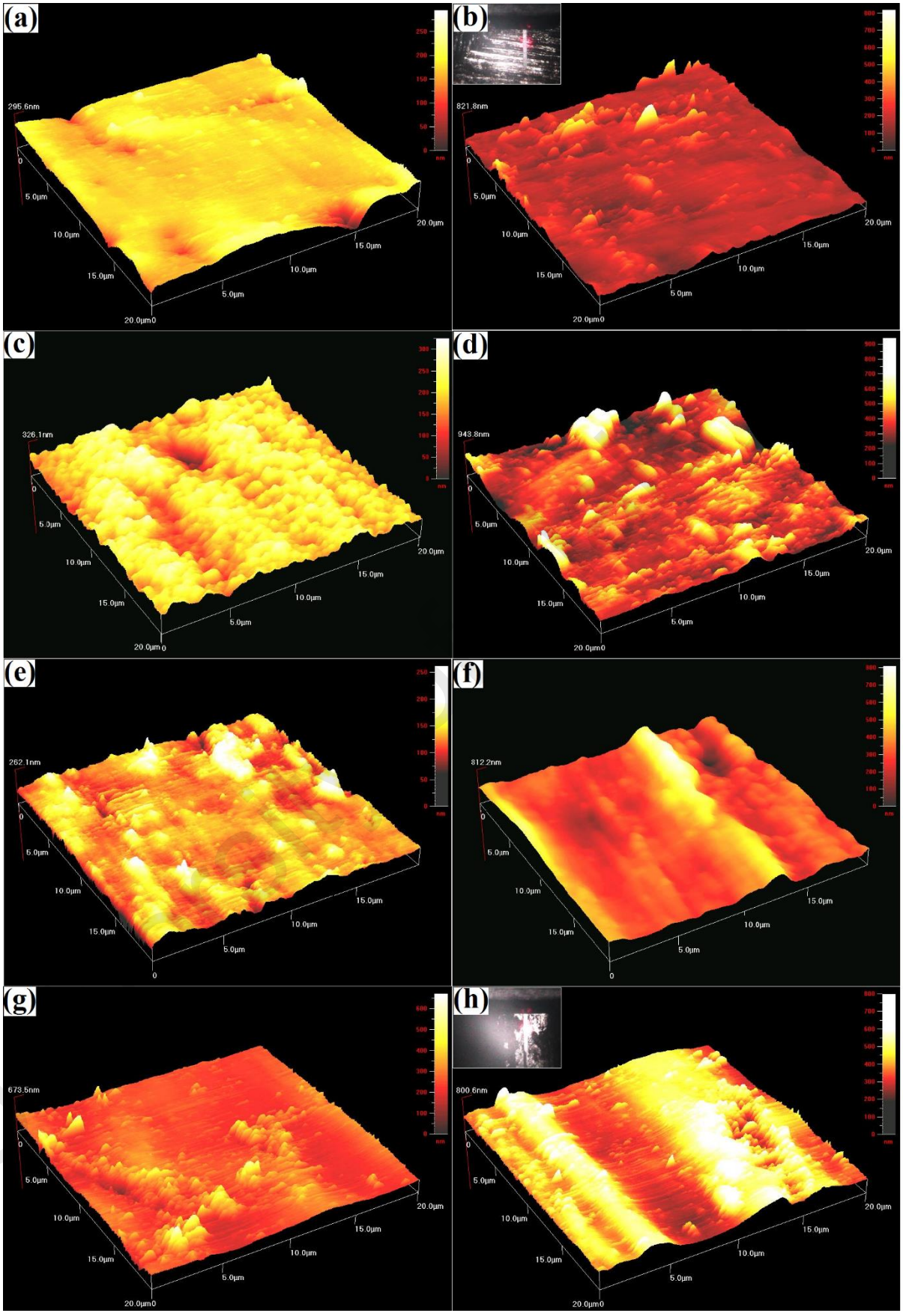

Figure 4.15: AFM images of undamaged and worn surfaces for (a,b) substrate, (c) un-annealed TiO_2 nanotubular arrays and arrays heat treated at (d) 500 and (e,f) 700 °C.

Table 4.2: Average roughness value before and after wear

Sample	Before wear RA(nm)	After wear RA(nm)
Substrate	41.2	300.7
TiO_2 NTs	30.8	222
500°C	25.4	140.4
700°C	24.4	119

4.1.9 Effectiveness of Corrosion Protection

The potentiodynamic polarization studies (as an integral method to characterize the corrosion and passivation kinetics of a substrate) were performed on the substrate (Ti-6Al-4V), anodized and heat treated samples which were immersed in PBS solution as shown in Figure 4.16. The corresponding corrosion potential (Ecorr), corrosion current density (Icorr) and polarization resistance (Rp) are summarized in Table 4.3, where, Ecorr is representative of the substrate's tendency to corrode, while Icorr denotes the effectiveness of corrosion protection (*P.E.*) values. From the presented data, the Ecorr of the samples are -0.143±0.005 V for Ti-6Al-4V, -0.135±0.005 V for TiO_2 nanotubes and -0.089±0.005 V for heat treated sample. In addition, the Icorr of Ti-6Al-4V is 4.334 x 10^{-6}±0.005×10^{-6} A cm^{-2}, and reaches to 5.498 x 10^{-7}± 0.005×10^{-6} A cm^{-2} for the heat treated sample. In accordance with the polarization curves, the anodized alloy exhibited a stable surface film since the specimens were immersed for 30 min had a very low Icorr value. Accordingly, the polarization resistance of the system increased from 7.674 x 10^3 to 1.799 x 10^4 Ohm/cm^2. The lowest Icorr was for TiO_2 nanotubes, followed by heat treated sample at 500 °C. The heat treated TiO_2 nanotubes at 500°C shows the most negative potential for the Ecorr which could be due to the n-type semiconductor of the material.

As compared to the bare substrate, the anodized and heat treated samples showed a 71% and 87% increase in *P.E.*, respectively. It was found that the 500 °C annealed sample had a significant improvement over *P.E.* and exhibited the highest percentage of

protection efficiency. Therefore, it can be concluded that 500 °C annealed sample can improve *in-vitro* corrosion behavior of native Ti-6Al-4V substrate. This behavior can be ascribed to the crystallization of nanotube arrays which resulted in the formation of nanotubular arrays with higher stability (enhanced resistance of the outer nanotube layer) than the amorphous structure. Similar to previous reports, Al-Mobarak et al (2014) reported that the nanotubular Ti shows a slightly higher passivation current than the mechanically polished titanium in Hank's solution, which is attributed to the large surface area created by the nanostructure (Al-Mobarak et al., 2014). Moreover, the electrochemical stability of Ti nanotubes is enhanced, from the more noble open circuit potential values compared to that of Ti. The electrochemical stability of the nanotubular surface depends on the dimensions of the TiO_2 nanotube which is controlled by optimizing the electrolyte composition. Hence, it can be concluded that the corrosion behavior of the self-organized TiO_2 nanotubular arrays is influenced by the type of substrate and electrolyte as well as subsequent thermal treatment (Rafieerad et al., 2015).

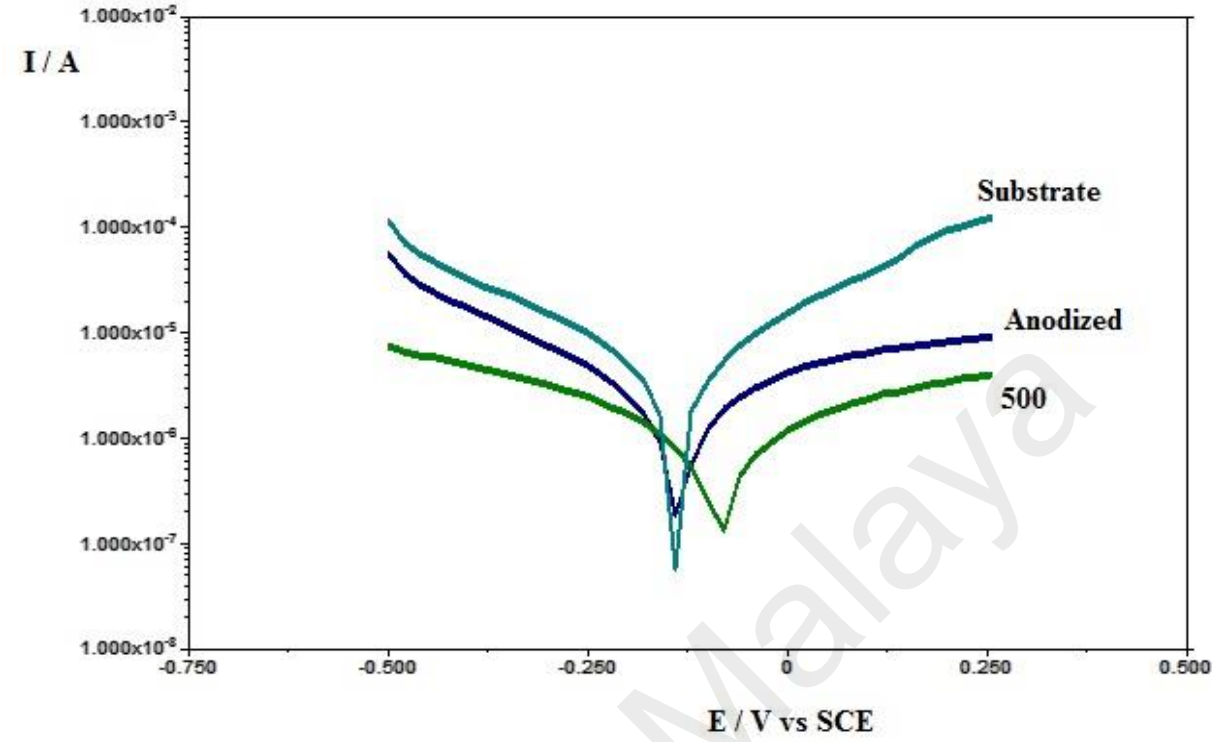

Figure 4.16: Polarization curves of (a) substrate (b) TiO_2 nanotubes and (c) heat treated TiO_2 nanotubes at 500°C.

Table 4.3: Corrosion potential (*E*corr), corrosion current density (*I*corr), polarization resistance (*Rp*) and effectiveness of corrosion protection (*P.E.*) values.

Sample	Ecorr / V	Icorr / A	Rp / Ohm	P.E (%)
Substrate	-0.143±0.005	$4.334 \times 10^{-6} \pm 0.005 \times 10^{-6}$	7.674×10^{3}	-
Anodized	-0. 135±0.005	$1.272 \times 10^{-6} \pm 0.005 \times 10^{-6}$	1.799×10^{4}	71
500 °C	-0.089±0.005	$5.498 \times 10^{-7} \pm 0.005 \times 10^{-6}$	4.978×10^{4}	87

4.1.10 Surface Wettability

Anodization processes form nano-porous films with microscopic coarse structures (Kobayashi et al., 1988; Wang et al., 2008a). These structures have different surface wettabilities (hydrophilicities) depending on the processing parameters applied. In

general, surface wettability is a measure of surface energy and is most commonly quantified by the contact angle θ (Aronov et al., 2007). As shown in the inset of Figure 4.18a, the shape of a drop of water on a material's surface is governed by forces pulling at the contact line of the drop in the plane of the solid, where the solid (S)/liquid (L), liquid (L)/vapor (V) and solid (S)/vapor (V) interfaces meet. In this context, the contact angle is defined by the equilibrium state reached between these forces acting on the contact line, separating the wetted and non-wetted portions of a homogenous smooth solid surface such that each interface is described by a certain free energy per unit area (γ_{SL}, γ_{LV}, and γ_{SV}). Hence, the contact angle on a smooth and flat surface can be expressed using Young's model ($\cos(\theta) = (\gamma_{SV} - \gamma_{SL})/\gamma_{LV}$) (Young, 1805).

It is clear that anodization can play an important role in determining the surface wettability of a material. The contact angle of the substrate was $\theta = 72.8°$ (see Figure 4.17a). After anodization, due to the formation of a porous structure, the hydrophilicity of the surface was improved such that the contact angle decreased to 11.6° (see Figure 4.17b). A highly ordered nanotubular array was formed during annealing at 500 °C due to the transition from an amorphous to a highly crystalline structure, resulting in an improvement in hydrophilicity. Accordingly, the contact angle decreased notably to $\theta = 7.5°$ (see Figure 4.17c). In the case of the decorated Ag_2O NPs on edges of nanotubes, the contact angle increased to $\theta = 17.3°$ (see Figure 4.17d). Based on these observations, it can be concluded that the improved wettability of the anodized specimens was due to the combination of the effects induced by both the surface oxide layer and the increased surface roughness after anodization. It has been reported that the extents of cell attachment, spreading, and cytoskeletal organization are greater on hydrophilic surfaces than on hydrophobic surfaces (Lan et al., 2013).

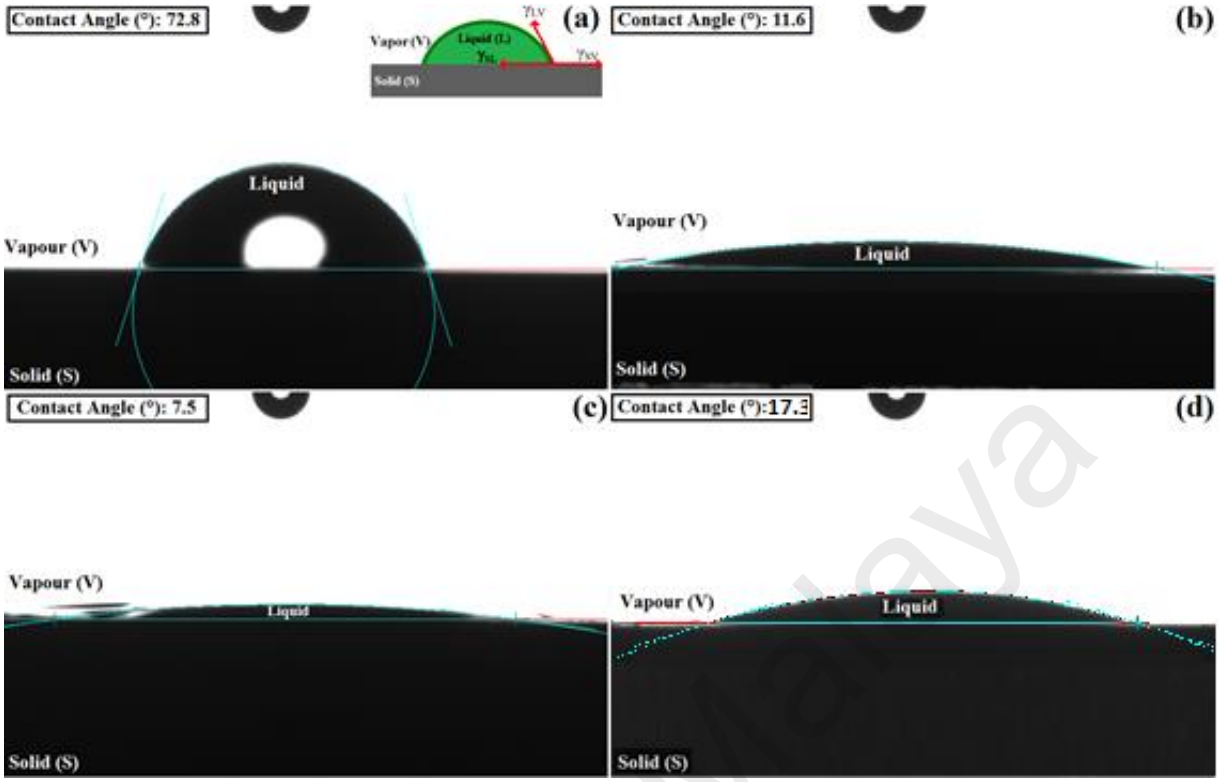

Figure 4.17: Optical images of the contact angles of (a) substrate, (b) un-annealed TiO_2 nanotubular arrays and arrays heat treated at (c) 500 and (d) Ag_2O NPs decorated on NTs.

4.1.11 In-Vitro Apatite Formation

After being implanted into the human body, the implant surface directly contacts and interacts with the tissues and cells. Hence, the *in-vitro* bioactivity should be checked before using metallic implants because this feature plays a vital role in influencing the biological responses (Shirazi et al., 2014). Figure 4.18 shows surface morphologies and EDS results of the 500 °C annealed sample after exposure to SBF for 1 to 14 days. After 1 to 7 days immersion in SBF, a trace of apatite deposition could be observed on TiO_2 NTs, where most of the top ends of the nanotubular arrays are not covered with the bone-like apatite layer (Figure 4.18a to d). As the immersion time increased to 14 days, the amount of apatite deposition soared clearly and thereby a thick layer of apatite with Ca/P ratio of 2.22 was developed on TiO_2 NTs (Figure 4.18e to h). Consistent with previous studies (Huang et al., 2010), the EDS pattern shows that the deposited layer is a type of

carbonated apatite containing calcium, phosphorus, oxygen, and carbon as the main constituents. To validate the *in-vitro* bioactivity, apatite-inducing ability of the annealed sample was also tested by using a different SBF solution for 14 days according to the method described by Tas (Figure 4.18i to l.) (Bayraktar et al., 1999). It was found that very thick apatite deposition (Ca/P ratio of 1.99) composed of large agglomerates with a chemical composition similar to previous sample (Ohtsuki et al., 1992) was formed on TiO_2 NTs. There was no significant difference in the apatite formation on the nanotubular arrays in Tas-SBF solution relative to Kokubo method.

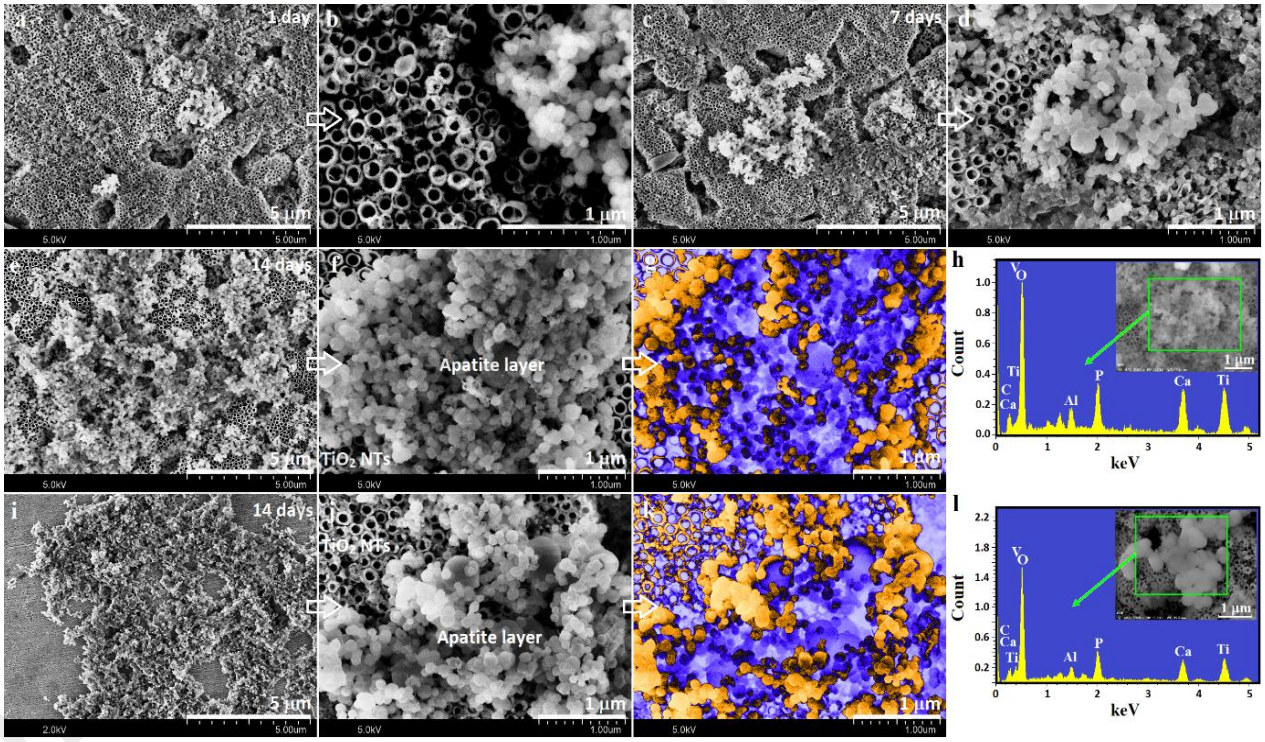

Figure 4.18: Surface morphologies and EDS results of the 500 °C annealed sample after exposure to Kokubo-SBF for (a,b) 1, (c,d) 7, and (e–h) 14 day as well as Tas-SBF(i-l) for 14 day

Moreover, after decorating Ag_2O NPs on the edges of TiO_2 NTs, Figure 4.19 shows surface morphologies and EDS results of the Ag_2O NPs (30 sec) on the TiO_2 NTs sample after exposure to SBF for 1 to 14 days. After 1 to 7 days immersion in SBF, a trace of

apatite deposition could be observed on Ag_2O NPs-TiO_2 NTs, where most of the top ends of the nanotubular arrays are not covered with the bone-like apatite layer (Figure 4.19a to d). As the immersion time increased to 14 days, the amount of apatite deposition soared clearly and thereby a thick layer of apatite with Ca/P ratio of 1.57(by Kokubo method) was developed on Ag_2O NPs-TiO_2 NTs (Figure 4.19e to h)(Ohtsuki et al., 1992). To validate the *in-vitro* bioactivity, apatite-inducing ability of the annealed sample was also tested by using a different SBF solution for 14 days according to the method described by Tas (Figure 4.19i to l.) (Bayraktar et al., 1999). It was found that very thick apatite deposition (Ca/P ratio of 2.31) composed of large agglomerates with a chemical composition similar to previous sample (Ohtsuki et al., 1992) was formed on Ag_2O NPs-TiO_2 NTs. During the early stage of immersion in SBF, the nanotubes surface straightly contacted with the SBF, so wettability can have a major impact on the formation of apatite layer. After that, the surface of nanotubes progressively changed to the as-deposited apatite surface, which is in direct contact with SBF. Consequently, the wettability effects on the development of apatite layer formation is weakened (Huang et al., 2010) . In a nutshell, although it is very important to know whether and how such nanotubular surface modification can improve biofuctionallity of metallic implants in biological systems, it is beyond the scope of the present study as we principally focus here on the fabrication and nanostructural characterization of the modified surfaces. More efforts are being implemented to find out the optimum conditions for bioactivity and biocompatibility.

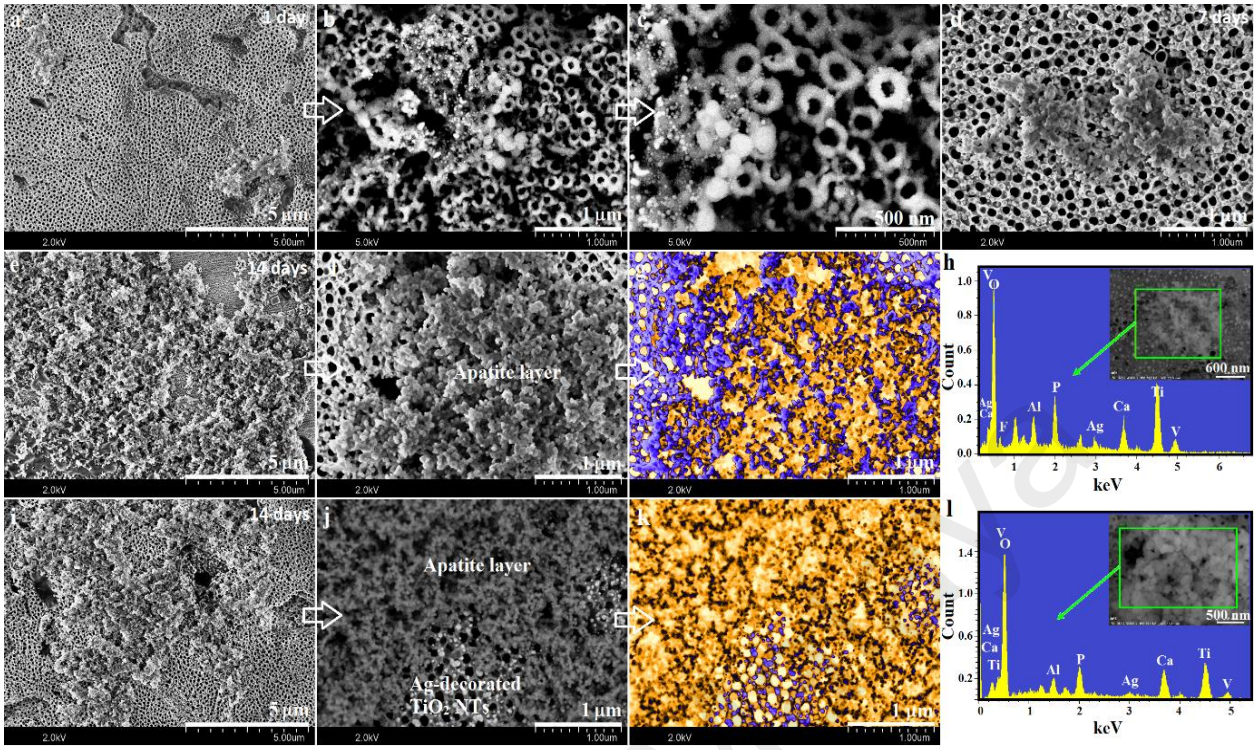

Figure 4.19: Surface morphologies and EDS results of the Ag_2O NPs (30 sec) on the TiO_2 NTs sample after exposure to Kokubo-SBF for (a,b) 1, (c,d) 7, and (e–h) 14 day as well as Tas-SBF(i-l) for 14 day

4.1.12 Antibacterial Activity

The antibacterial activity of the substrate, TiO_2 NTs and TiO_2 NTs-Ag_2O NPs film against *E.coli* was determined as shown in Figure 4.20. Each data point represents mean ± standard error of mean (SEM) of two independent experiments. Statistical significance of coated films versus control at respective time point was analyzed using two-way ANOVA followed by Bonferroni post-test (***$P < 0.001$). *E.coli* is recognized as the common pathogen in biomaterial-associated infections (Danese et al., 2002). As compared to the uncoated titanium film (Ti-6Al-4V), TiO_2 NTs able to reduce and inhibit the growth of *E.coli* cells within 6 hours but it demonstrates bacteriostatic effect as growth of *E.coli* cells observed after 24 hours of incubation. For TiO_2 NTs-Ag_2O NPs, it significantly reduced the number of viable *E.coli* cells ($P < 0.001$) and killed 100% of the

bacteria within 2 hours. It exhibits a bactericidal activity as complete killing was observed after 24 hours of incubation.

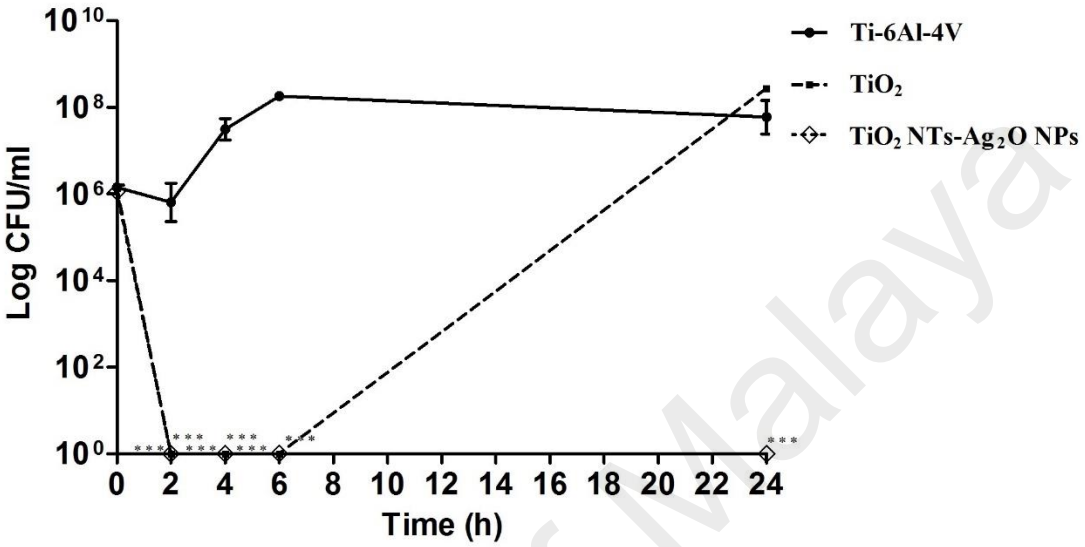

Figure 4.20: The antibacterial activities of Ti-6Al-4V substrate as well as the TiO_2 NTs, and TiO_2 NTs-Ag_2O NPs films against *E.coli* ATCC 25922.

Based on Figure 4.20, TiO_2 NTs-Ag_2O NPs exhibited good bactericidal property and significantly inhibited the growth of *E.coli* within 2 hours. The antibacterial activity of TiO_2 NTs-Ag_2O NPs film could be attributable to the synergism effect of the TiO_2 NTs, the released Ag^+ and direct contact with Ag_2O NPs as reported in other studies (Gao et al., 2014; Juan et al., 2010). It has been proposed that silver nanoparticles (Ag NPs) possess a large total surface to volume ratio which provides an effective contact with microorganisms. The nanoparticles release great amount of Ag^+ and attach to, or penetrate the bacterial cell membrane to induce damage (Morones et al., 2005; Sondi et al., 2004).

4.1.13 HOb Morphology and Adhesion

Figures 4.21 shows the FESEM images of HOb cells cultured on the TiO_2 NTs-Ag_2O NPs after 1, 3, and 7 days of culture. As disclosed in low-magnification images, at day 1

the majority of cells were still spherical without exhibition of cluster formation on the surfaces. In contrast at day 3, the cells showed a spreading morphology with increased cluster formation as well as a typical osteoblastic shape, indicating the positive impact of nanotopography on induction of typical phenotypic behavior for osteoblasts. The high-magnification images illustrate abundant pronounced finger-like protrusions and extensive filopodial activity by HOb cells to interact with the NTs. The finger-like filopodia are a cell-sensing parts which can detect both chemical and nano-topographical cues (Oh et al., 2006). The presence of many filopodia on the NT surfaces indicates that the HOb cells are relatively activated by the NT architecture. Although the cell spreading at day 7 was generally higher than days 1 and 3, no significant difference in cell morphology could be observed at this time interval compared to those observed at day 3. The CLSM results (Figure 4.22) also showed a uniform cell distribution on the NT surfaces with increasing population over the examined interval.

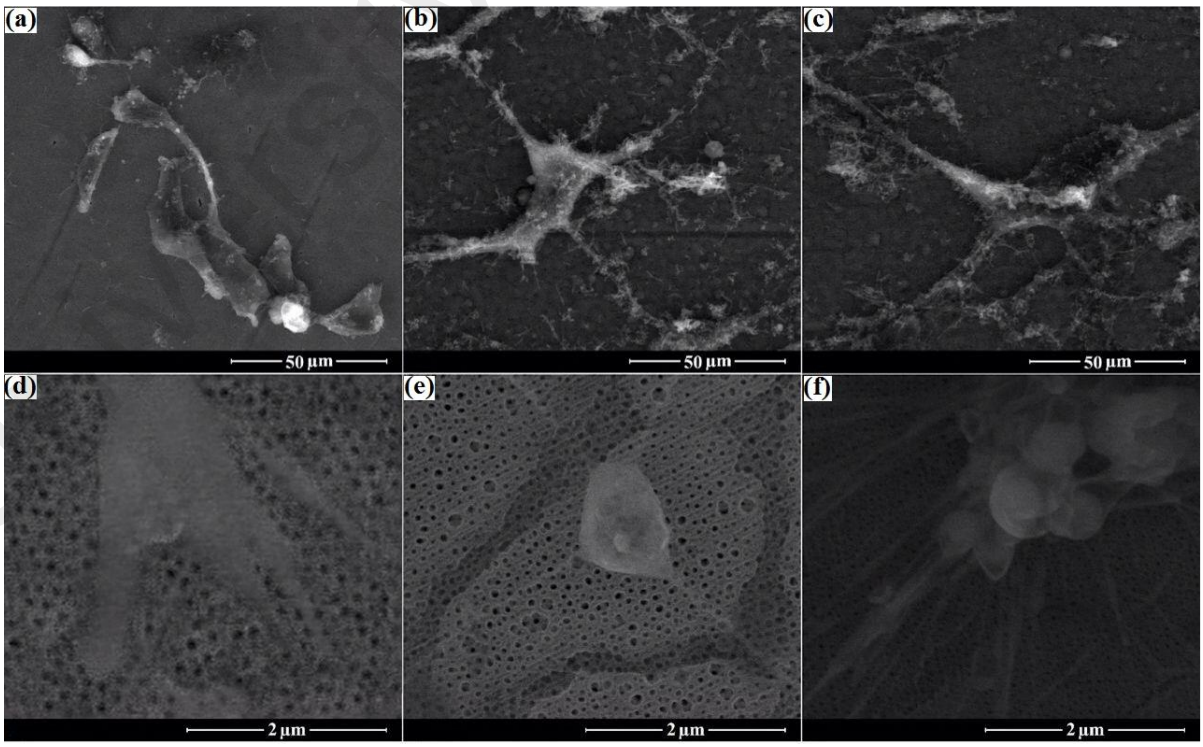

Figure 4.21: The FESEM images of HOb cells after culturing for a,d) 1, b,e) 3, and c,f) 7 days on the TiO_2 NTs-Ag_2O NPs surface

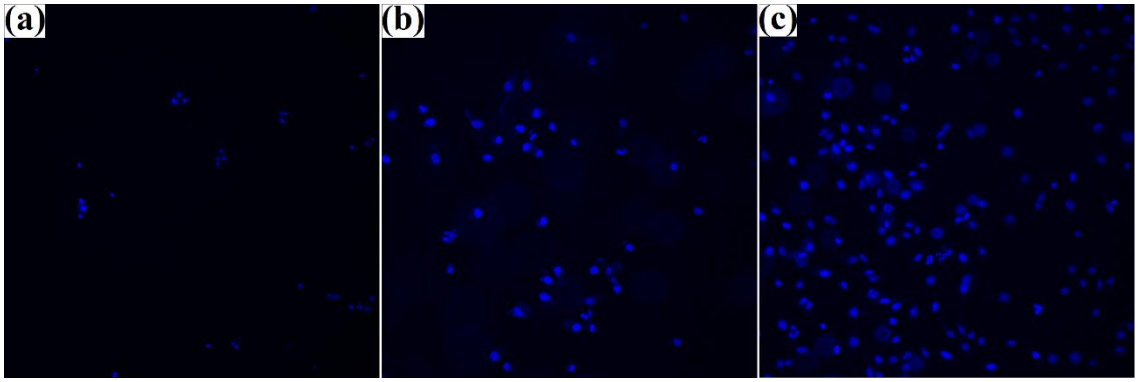

Figure 4.22: The confocal laser scanning images of the stained HOb cells after culturing for a) 1, b) 3, and c) 7 days on the TiO_2 NT-Ag_2O NPs.

4.1.14 Cell Viability and Proliferation

A higher adhesion on the surface does not necessarily indicate the cell viability and functionality. The alamar blue assay is known as an effective indicator of cell metabolism, which allows to quantify the viability of human, animal, plant, bacteria, and fungi cell lines. The alamar blue reagent contains non-toxic, weakly-fluorescent, cell-permeable, and blue-colored resazurin as the active ingredient, which is reduced to highly-fluorescent and red-colored resorufin in the reducing environment of living cells. During exposure to the alamar blue reagent, the viable cells continuously reduce resazurin to resorufin, altering the fluorescence properties and color of the surrounding media (Rampersad et al., 2012).

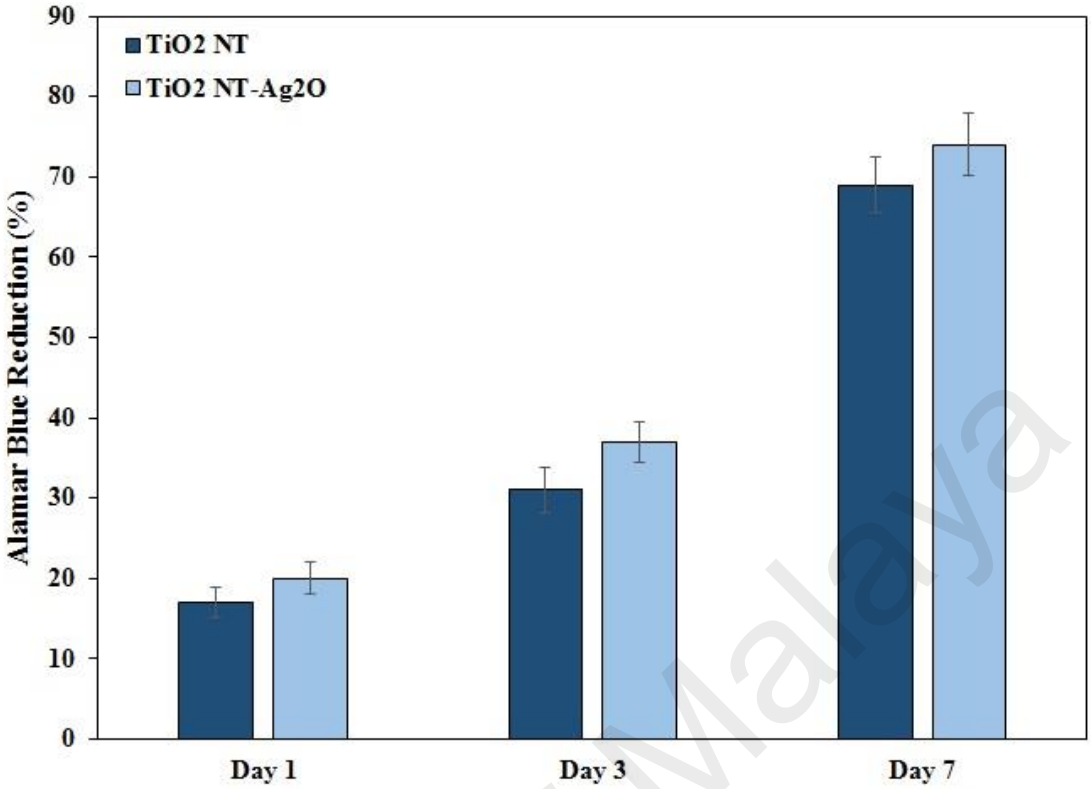

Figure 4.23. The reduced ratio of alamar blue for HOb cells after 1, 3 and 7 days of culturing on the TiO_2 NTs and TiO_2 NTs-Ag_2O NPs.

The obtained alamar blue results of the HOb cells attached on the TiO_2 NTs and TiO_2 NTs- Ag_2O NPs films after 1, 3, and 7 days (Figure 4.23) were consistent with the CLSM images of the stained cells, showing the continuous proliferation of HOb cells throughout the culture time. In addition, the absorbance values of the HOb cells cultured on the TiO_2 NTs and TiO_2 NTs-Ag_2O NPs were not statistically different ($p < 0.05$) at all examined culture periods, confirming the negligible effect of Ag_2O NPs on the cell viability.

4.2 Structural, Mechanical and Biological Behavior of Ta_2O_5 Nanotubular Arrays Thin Films with Decorated Ag_2O Nanoparticles on Ti–6AL–4V Alloy

4.2.1 Data Analysis of the Adhesion Strength Measurements for Tantalum Thin Film

The *S / N* ratio is a measurement to determine the degree of predictable performance of a process and to decrease the process sensitivity to noise factors (Baradaran et al., 2013). The *S / N* ratios calculated for the adhesion strength are presented in Tables 4.4, whereas the corresponding *S / N* values for the coating parameters are provided in Table 4.5 and Figure 4.24. According to ''*the higher the better*'' criteria, the higher *S / N* ratios indicate more desirable responses, resulting in lower negative effects caused by the noise in the machine set-up. Therefore, a DC power of 350 W, temperature of 250 °C and a deposition time of 6 h were considered as the optimal conditions for attaining the highest adhesion strength. In order to validate this finding, a confirmation study was performed with these optimal parameters. The adhesion strength achieved in this experiment was 2154 mN, which indicates a 19.8 % improvement compared to the maximum adhesion strength value achieved from the experimental conditions shown in Table 4.4.

Table 4.4: The measured scratch force and calculated S/N ratio

Experiment No.	Scratch Force (mN)				*S / N* ratio
	1st	2nd	3rd	Mean	
1	812	823	833	823	58.31
2	1535	1479	1441	1485	63.42
3	1643	1702	1732	1692	64.56
4	1650	1632	1699	1660	64.40
5	1695	1714	1766	1725	64.73
6	1122	1236	1002	1120	60.89
7	1790	1821	1782	1798	65.09
8	1342	1450	1501	1431	63.08
9	1644	1656	1776	1692	64.55

Table 4.5: The S/N response values obtained from the adhesion strength

Coating Parameters	*S / N* ratio		
	Level1	Level2	Level3
DC Power (W)	62.10	63.34	64.24
Temperature (°C)	62.26	63.74	63.33
Time (h)	60.76	64.12	64.79

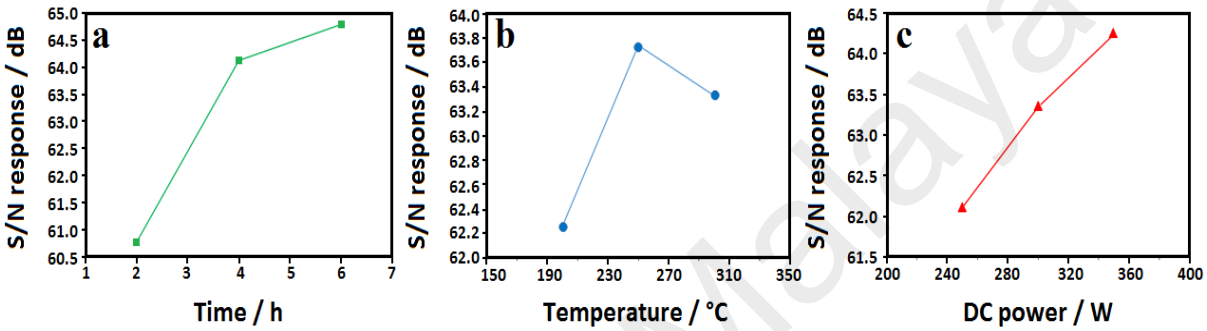

Figure 4.24: The S/N response of (a) time, (b) temperature, and (c) DC power for adhesion strength.

4.2.2 Adhesion Strength of Tantalum Coating

Figure 4.25 illustrates the top view and cross-sectional FESEM images of the Ta thin films under different PVD conditions. The FESEM images indicate a lamellar coating structure which became denser as the DC power increased from 250 to 350 W. Furthermore, the process duration exhibited a positive effect on the coating thickness. Therefore, the increased DC power and process duration resulted in higher a coating compaction and density along with an improved coating adhesion, which subsequently increased the surface adhesion. Such improved adhesion could arise from the higher available energy for the film growth. With increasing the DC power, the ionized particles become more energetic, resulting in a decreased distance between the energized atoms and increased sputtering rate. This shows that the energetic atoms with higher motilities are preferably deposited onto the lower-energy surfaces, causing greater coating density and adhesiveness (Baradaran et al., 2013). Accordingly, the combination of a DC power

of 350 W, temperature of 250 °C and a deposition time of 6 h are the optimal operating conditions for obtaining the highest adhesion strength.

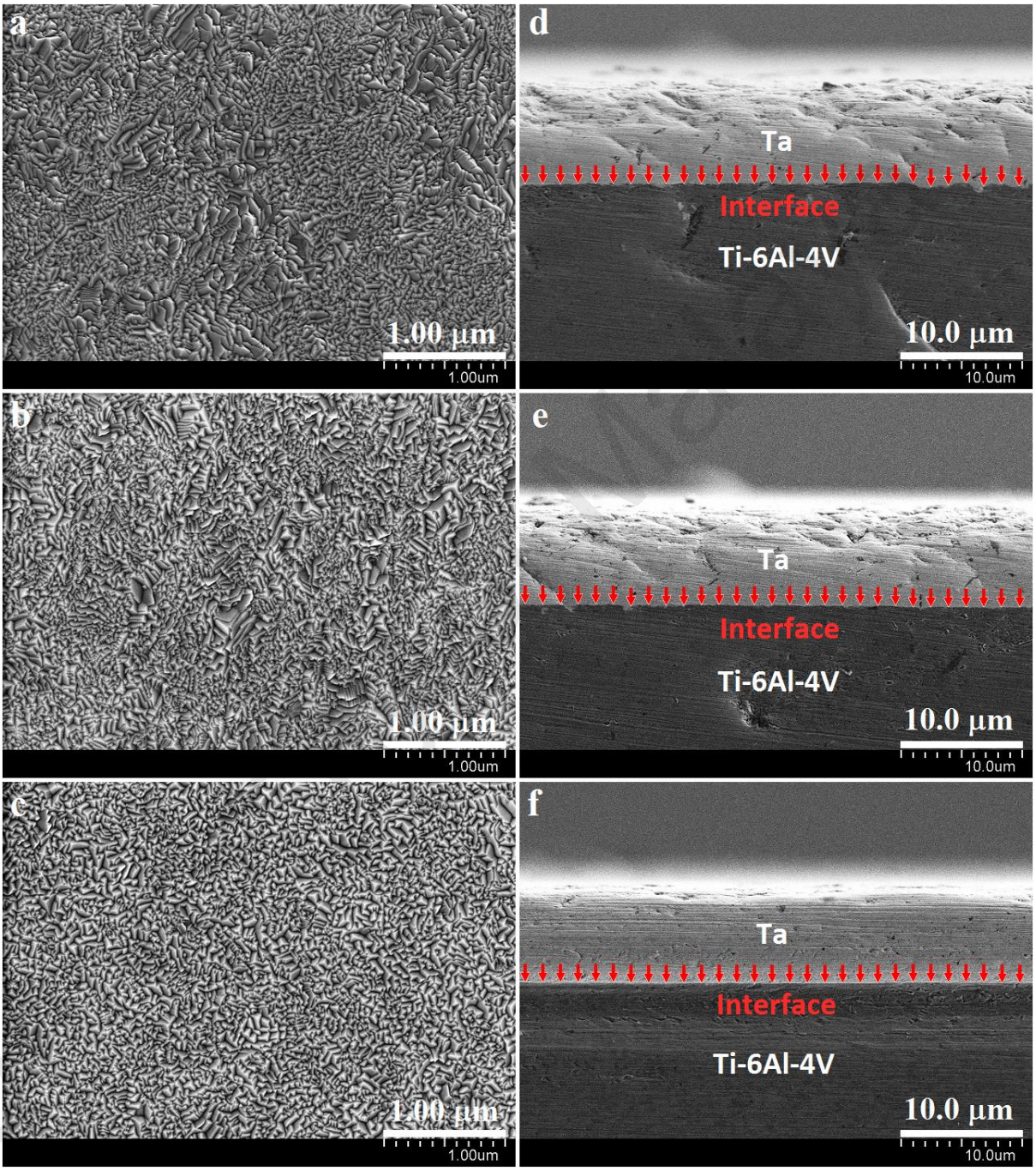

Figure 4.25: Top view and cross-sectional FESEM images of the as-deposited Ta thin films with different operating conditions; (a and d) 250W– 300°C – 6 h, (b and e) 300 W – 250 °C – 6 h and (c and f) 350 W – 250 °C – 6 h.

As already mentioned, the durability and functionality of a thin film depend not only on the hardness and elastic modulus of the film, but also on the adhesion between the film and the substrate that supports the film (Venkataraman et al., 1993). Figure 4.26 illustrates the optical micrograph of the scratch track and profiles of depth, load, friction and COF *vs.* scan distance for the optimized sample. Here, the scratch direction was from left to right. As shown in Figure 4.26a, the scratch length and the failure point of the as-deposited Ta layer were 1127 and 887 µm, respectively. The critical loads (Le-p, Lc_1, Lc_2 and Lc_3) delineated by a drastic alteration of depth vs. distance profile, where Le-p refers to an elastic-to-plastic transition and cohesive failure (Figure 4.26b). Moreover, the L_{c1}, L_{c2}, and L_{c3} refers to a lower critical load, with the initiation of a parallel and edge cracking, failure or upper critical load by partial coating delamination along with a subsequent intermittent substrate exposure, and total coating failure by complete exposure of the surface material, respectively (Tomsia et al., 2005). From Figure 4.26c, the optimized sample under the applied load gave an adhesion strength of 2154 mN. The friction can also be denoted as the resistance tangential force to a relative motion between two surfaces in contact. Hence, during the scratch adhesion test, the friction and COF were calculated and plotted *vs.* the scratch length. According to Figure 4.26d and e, the calculated friction and COF for the optimized sample with the highest adhesion were 1356 mN and 0.59, respectively.

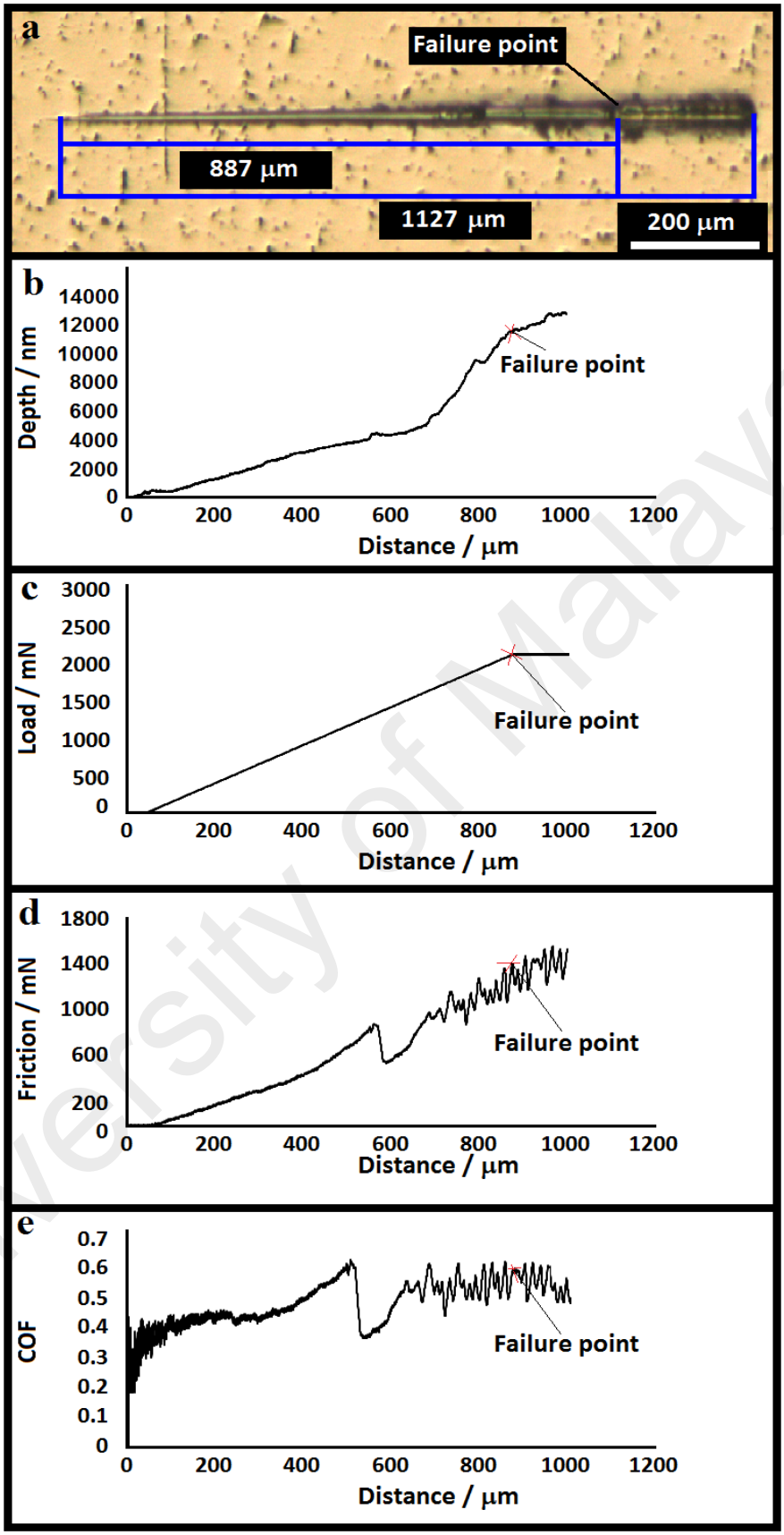

Figure 4.26: (a) The optical micrograph of the scratch track and (b) profiles of depth, (c) load, (d) friction, and (e) COF vs. scan distance for the optimized sample.

Figure 4.27 displays the different types of failure mode during the scratch test of the Ta coating on the substrate. The as-deposited coating process began to fail in the advent of some cracking on the trackside. This critical load was recorded as L_{c1}, which was followed by a mild tensile cracking during the scratch path. By gradually increasing of the load amount, delamination occurred on the trackside, and the load value was recorded as L_{c2}. With further increase in the load rate, the cracking and delamination became dominant and the spacing between the tensile cracks areas became smaller than before, until the coating was delaminated (recorded as L_{c3}). When the load value increased continuously, the spallation around the trackside substituted the trackside delamination and the width of the scratch became constant, as shown in Figure 4.27. A similar trend was observed in previous studies (Bushroa et al., 2011; Singh et al., 2012; Toque et al., 2010).

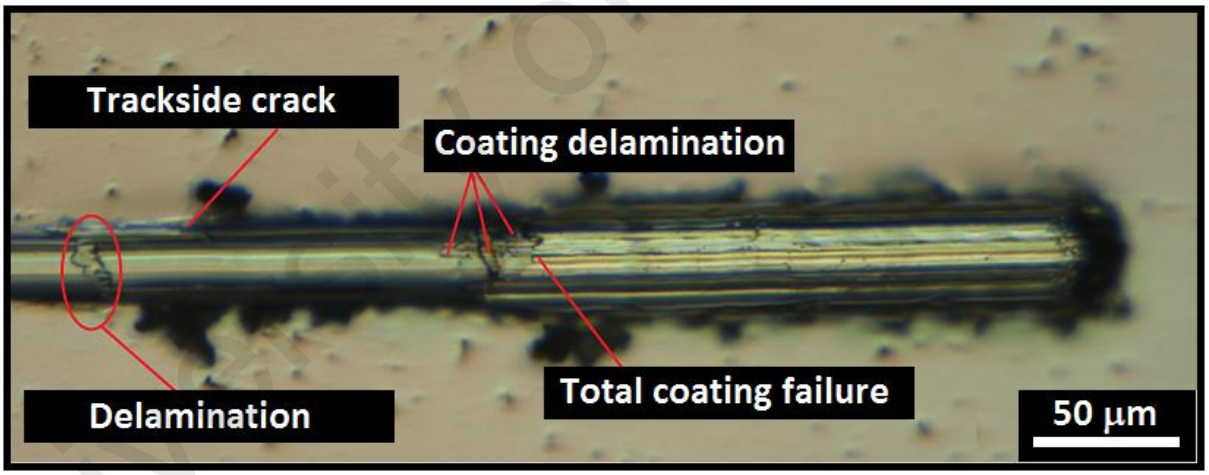

Figure 4.27: Failure mode of the tantalum coating on Ti–6Al–4V during the scratch test.

4.2.3 Formation of Ta_2O_5 Nanotubes with Decoration of Ag_2O NPs on Ti-6Al-4V

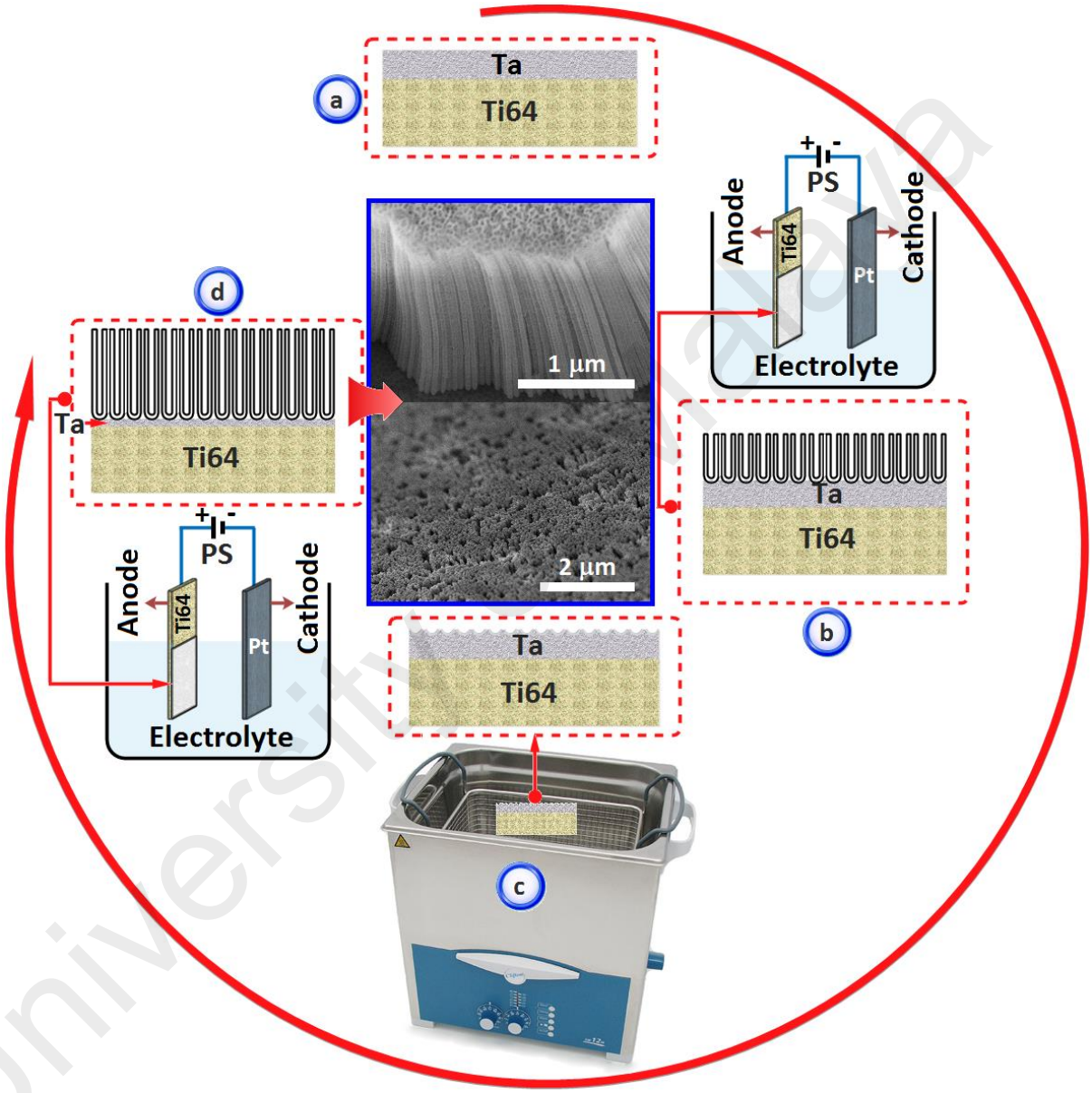

Figure 4.28: A schematic diagram of the anodization process and the different stages of Ta_2O_5 NTs preparation.

A schematic diagram of the anodization process and the different stages of Ta_2O_5 NTs preparation is shown in Figure 4.28. For preparation of Ta_2O_5 NTs on the metallic substrate, a thick layer of pure Ta was firstly coated on the substrate using PVD

magnetron sputtering approach. Then, the anodization method was utilized for formation of a primary layer of Ta_2O_5 NTs. The NTs were then removed by acid etching and again re-grown by a secondary anodization with identical experimental condition to that of the first anodization process. The Ag_2O NPs were finally decorated on the NT edges using PVD magnetron sputtering with controlled parameters (Figure 4.29).

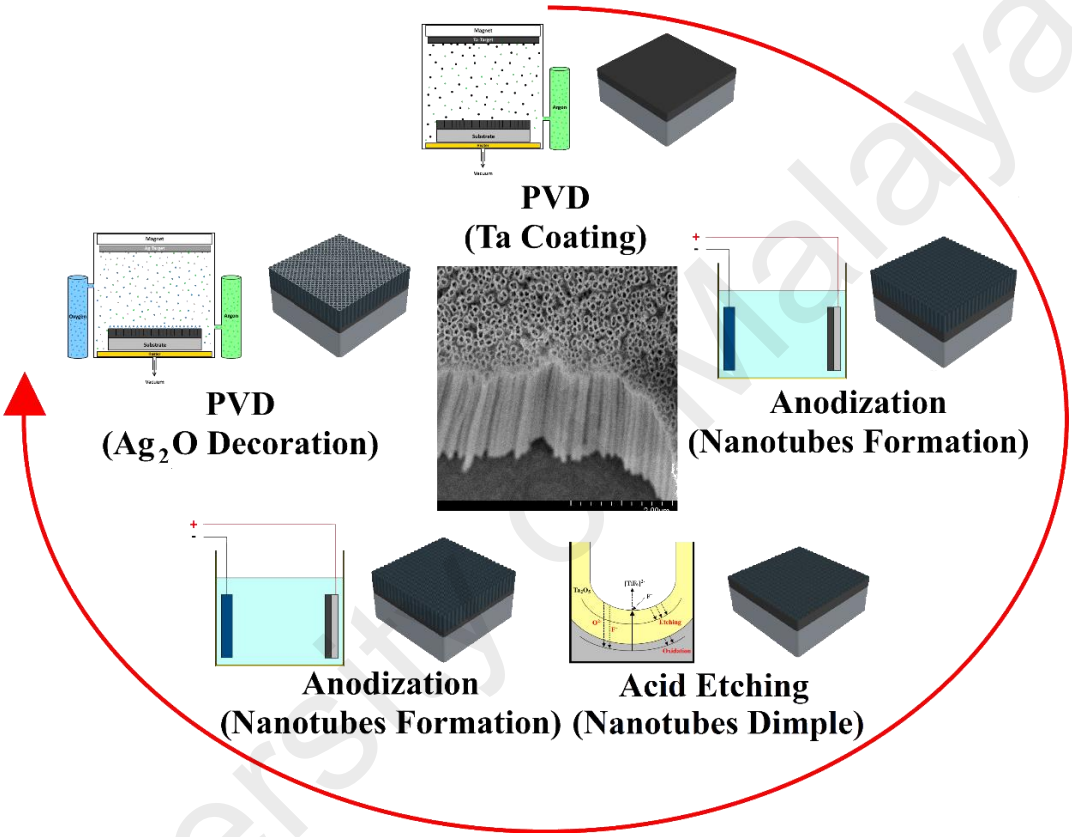

Figure 4.29: Illustration of the synthetic process of Ta coating, Ta_2O_5 NTAs: first anodization step, sonication, the second anodization step and Ag_2O NPs decorated.

4.2.4 XRD Analysis

Figure 4.30 shows the XRD reflections of the substrate as well as the Ta coating, as-anodized Ta_2O_5 NTs, annealed Ta_2O_5 NTs, and Ta_2O_5 NTs-Ag_2O NPs. The XRD pattern of the substrate illustrates the Ti peaks (JCPDS#005-0682) at $2\theta = 35.1°$, 38.4°, 40.2°,

53.1°, 63.1°, 70.6° and 76.4°, which were respectively related to the (1 0 0), (0 0 2), (1 0 1), (1 0 2), (1 1 0), (1 1 2) and (2 0 1) planes. After applying the Ta coating, two diffraction peaks corresponding to the (1 1 0) and (2 1 1) planes of metallic Ta with cubic structure appear at 2θ values of 38.4° and 69.7°, respectively (JCPDS#001-1182). The XRD spectrum of as-anodized specimens also indicated the formation of Ta_2O_5 phase with an orthorhombic structure (JCPDS#008-0255) after 5 minutes of anodization in an electrolyte containing H_2SO_4:HF (99:1) + 5% ethylene glycol with a constant potential of 15 V. Depending on the anodizing conditions a variety of ordered and disordered structures can be formed. Moreover, the fraction of oxide phase and preferred crystal orientation may change by further anodization steps. Heat treatment of the Ta_2O_5 NTs results in decrease of the Ta_2O_5 peaks, indicating their transition from a crystalline to an amorphous phase. The XRD pattern of the Ta_2O_5 NTs-Ag_2O NPs confirm Ag_2O NPs presence on the Ta_2O_5 NT surfaces.

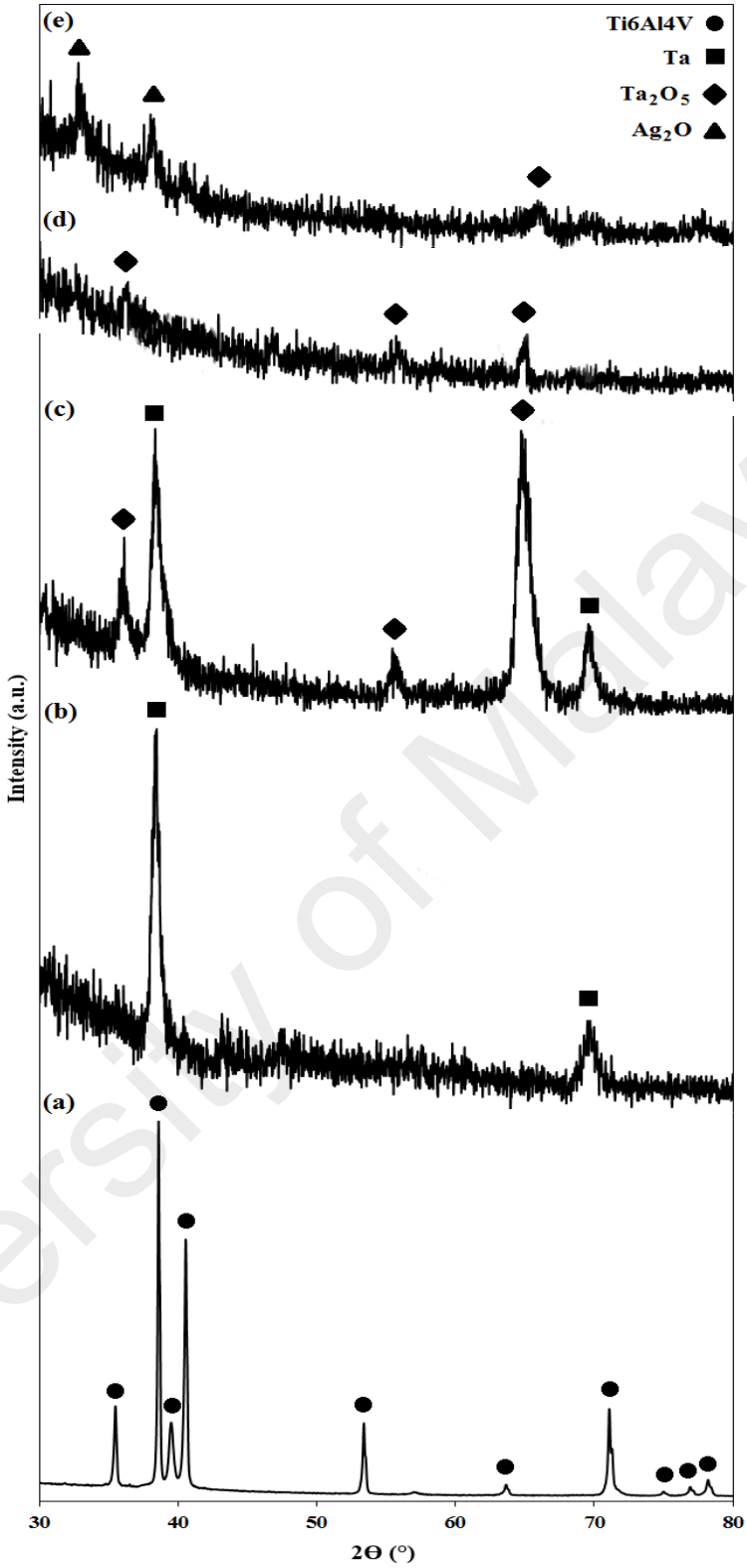

Figure 4.30: The XRD spectra of (a) Ti-6Al-4V, (b) Ta-coated specimens, (c) Ta_2O_5 NTs, (d) Ta_2O_5 NTs annealed at 450°C, and (e) Ta_2O_5 NTs-Ag_2O NPs.

4.2.5 XPS Analysis

The surface chemistry (elemental and chemical bonding state) of the samples was investigated by XPS. Figure 4.31 shows the XPS spectra of the 5 min anodized specimen before and after annealing at 450 °C for 1 h and XPS high-resolution spectra of the Ta4f region. The photoelectron peaks O1s, Ta4p, Ta4d, Ta4f and C1s are exposed in the survey spectra in Figure 4.32, where the binding energies were adjusted at C1s line 284.8eV. An intense C1s peak is visible in these spectra which can be linked to the elemental carbon at the surface of Ta_2O_5 (Guo et al., 2009). Here, the absence of C1s peak at 282.4eV shows that no substitution of an oxygen atom by a carbon atom occurred in the Ta_2O_5 lattice (Zhang et al., 2012). From Figure 4.31a and c, it can be seen that the as-anodized sample before and after annealing at 450 °C for 1 h is comprised of tantalum and oxygen atoms, which suggests that the main composition of the nanostructured coating is tantalum oxide. Further examination was done on the narrow scan spectra of the coating for detailed information about shape and position of peaks as shown in Figure 4.31b and d. It is clear that there is a perfect match between the measured spectrum and peak synthesis for both samples which shows the fitting curves a well reflection of the essence of the coating. Generally, each oxidation state of Ta is shown by a $Ta4f_{7/2}$ and $Ta4f_{5/2}$ doublet. According to the curve fitting, the Ta4f line can be decomposed into several peaks including $Ta4f_{7/2}$ at 27eV and $Ta4f_{5/2}$ at 28.9eV which are the typical Ta chemical bonding states in Ta_2O_5 (Guo et al., 2009). Besides, the manifestation of a Ta4f peak at 21.6eV confirmed the presence of metallic Ta, which agreed well with the XRD results (Kerrec et al., 1998). It should be noted that the loss feature for Ta metal appeared at ~38eV for Ta_2O_5. In addition to the characteristic peaks of Ta_2O_5, a shoulder at low energies ($22 < E_b < 26$eV) was detected, attesting that the as-prepared nanotubes contain small amounts of sub-oxides (Kerrec et al., 1998). This shoulder completely disappeared in the case of the annealed sample. Concerning the O1s peak, the absence of a distinct

chemical shift of the characteristic peak as a function of the oxidation state make it impossible to split the O1s signal into different components corresponding to different Ta oxidation states. The O1s peak at 529.7eV is related to Ta_2O_5, and the extra peak at higher binding energy 532.1eV is attributed to physic-adsorbed or trapped water (Guo et al., 2009).

Moreover, the elemental composition and chemical states of the Ta_2O_5 NTs-Ag_2O NPs arrays investigated by XPS analysis are shown in Figure 4.32. The presence of Ta, O, and Ag elements was again confirmed by the XPS pattern (Figure 4.32a). Moreover, the high-resolution spectra of Ta4f peak in Figure 4.32b indicated the exclusive presence of Ta_2O_5, while the peak at 367.9 eV in Figure 4.32c confirmed the oxidized state of Ag element. The atomic concentrations of O1s, Ta4f, and Ag3d shown in were respectively 94.45, 5.43, and 0.11. The high oxygen content probably originated from to the presence of air in the XPS chamber and around x% of the total oxygen concentration was attributed to the Ta_2O_5 and Ag_2O components. However, by calculation of the oxygen contents of Ta_2O_5 and Ag_2O components according to their stoichiometric values, a molar fraction of 0.8% was obtained for Ag_2O NPs.

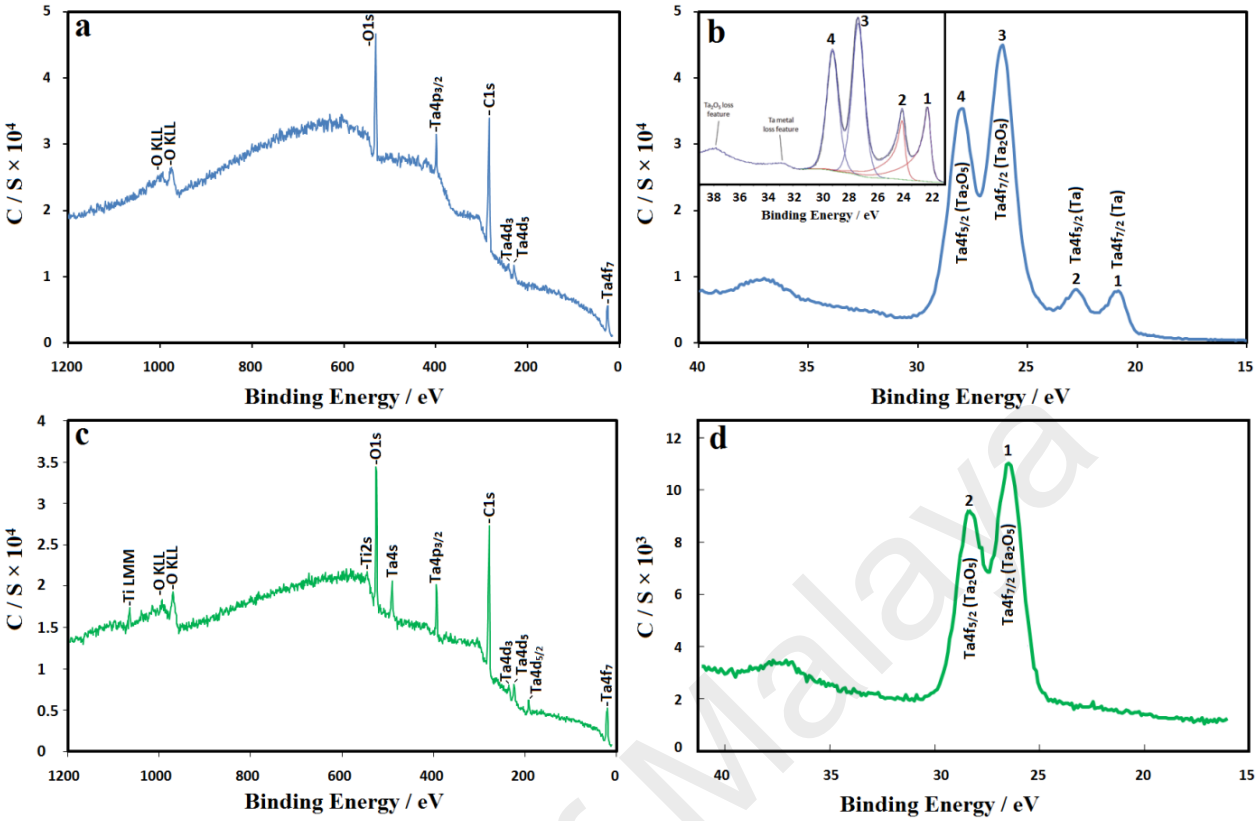

Figure 4.31: XPS spectra and high-resolution of Ta4f region of the 5 min anodized specimen (a,b)before and (c,d) after annealing at 450 °C for 1 h.

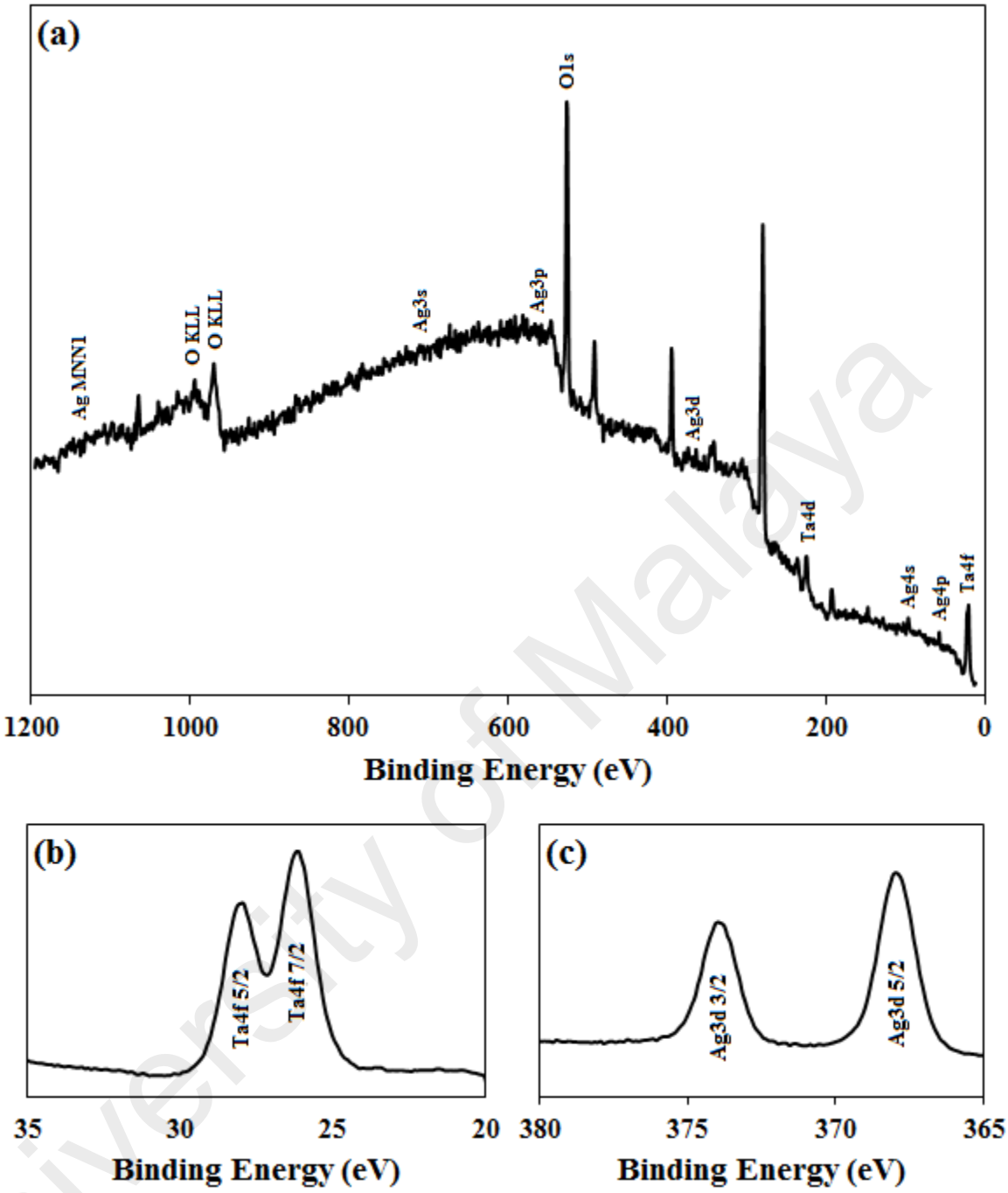

Figure 4.32: The XPS spectra of Ta_2O_5 NTs-Ag_2O NPs (a), as well as the high-resolution scans of Ta4f (b), and Ag3d (c) peaks.

4.2.6 Microstructural Evolution of Ta_2O_5 NTs and Heat Treated Ta_2O_5 NTs

Given that the microstructural properties and chemical composition of the nanostructured coatings have a significant effect on the biomedical functionality, the microstructural evolution and chemical constituents of the anodized specimens were

observed by FESEM and EDS imaging techniques, respectively. As mentioned in the experimental section, the nanostructured coating was firstly synthesized by the anodization of the as-prepared Ta thin film in H_2SO_4:HF (99:1) + 5% EG electrolyte with a constant potential of 15 V. The obtained coating appeared to have several cracks and tended to peel off or delaminate easily as shown in Figure 4.33. The peeling of the oxide film grown under a one-step anodization results in a clean surface of the pure Ta substrate covered with the native oxide (Singh et al., 2007). The underlying Ta surface demonstrates a more shallow dimpled morphology after the peeling of the film, formed after the one-step anodization process (Figure 4.33b). To overcome the existing problem, various strategies were applied to modify the anodization conditions.

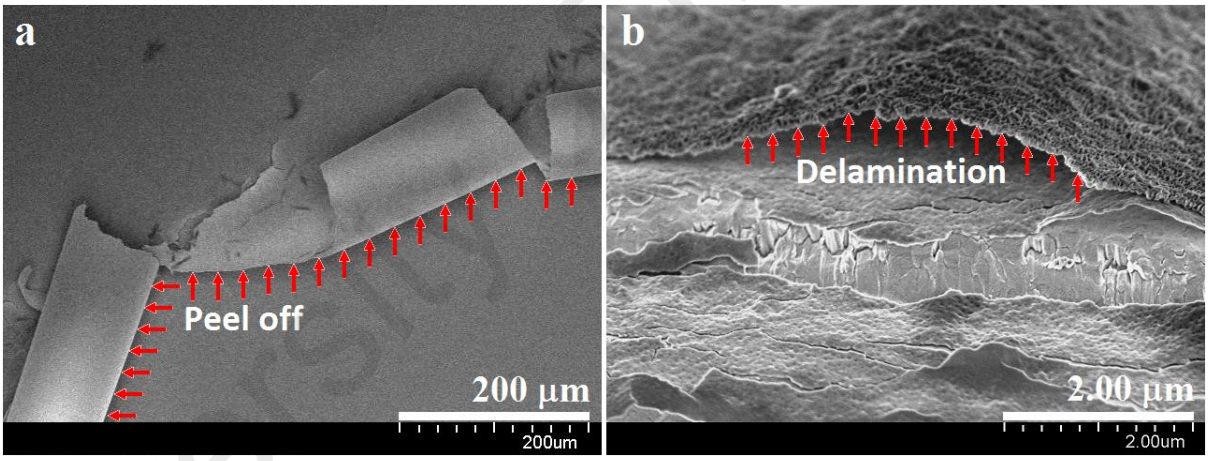

Figure 4.33: Peeling of an oxide film grown with a one-step anodization process.

The concentration of HF was kept constant to control the anodization rate and to strengthen the adhesion of the Ta_2O_5 NTs. In addition, to form a continuous coating and to prevent severe cracking, a two-step anodization approach was conducted at constant potential of 15 V at different anodization times. For this purpose, the as-prepared Ta coating was anodized for 20 min at a constant potential of 15 V in the first step. The resulting film could be easily removed from the as-prepared Ta coating by ultra-sonication, ensuring a clean Ta surface. This was followed by a second anodization step, to develop a well-adherent Ta_2O_5 NTs with a highly ordered surface topography. Figure

4.34 illustrates the FESEM images of a Ta surface after a two-step anodization process, with exposure times ranging from 0.5 to 20 min in H_2SO_4: HF (99:1) + 5% EG electrolyte, at a constant potential of 15 V. At the brink of the anodization (Figure 4.34a to d), some irregular pits were formed due to the localized dissolution of the oxide layer and followed by the pits conversion to larger pores, while most of the areas are still covered with the oxide layer. With extended anodization time to 3 min (Figure 4.34e to f), the compact oxide layer disappeared and more uniformly distributed pores were achieved. It is proposed that the pore's ordering is due to the local surface perturbations, where the strain energy increases causing the migration of F^- ions to regions with higher strain energy and more hydrogen ions, in order to maintain the electrical neutrality, leading to the dissolution of the Ta^{5+} ions (Crawford et al., 2007; Sobieszczyk, 2009). When the anodization time increased to 5-20 min, clear evolution of nano-porous structure could be observed. From Figure 4.34g, well-aligned Ta_2O_5 NTs are formed after 5 min of anodization, where the nanotubes are uniformly distributed over the anodized surface. A higher magnification FESEM image in Figure 4.34h reveals that the average inner diameter and tube length are 40 nm and 1 µm, respectively. After 10 min of anodization (Figure 4.34i), the top opening of nanotubes are bundled together, which decreases the inner surface area of the nanotubes. In this case, the average inner diameter and tube length are 36 nm and 2 µm, respectively (Figure 4.34j). With the increase of the anodization time to 20 min, the tubes are arranged in tight bundles of ~10 µm length as shown in Figure 4.34k and l.

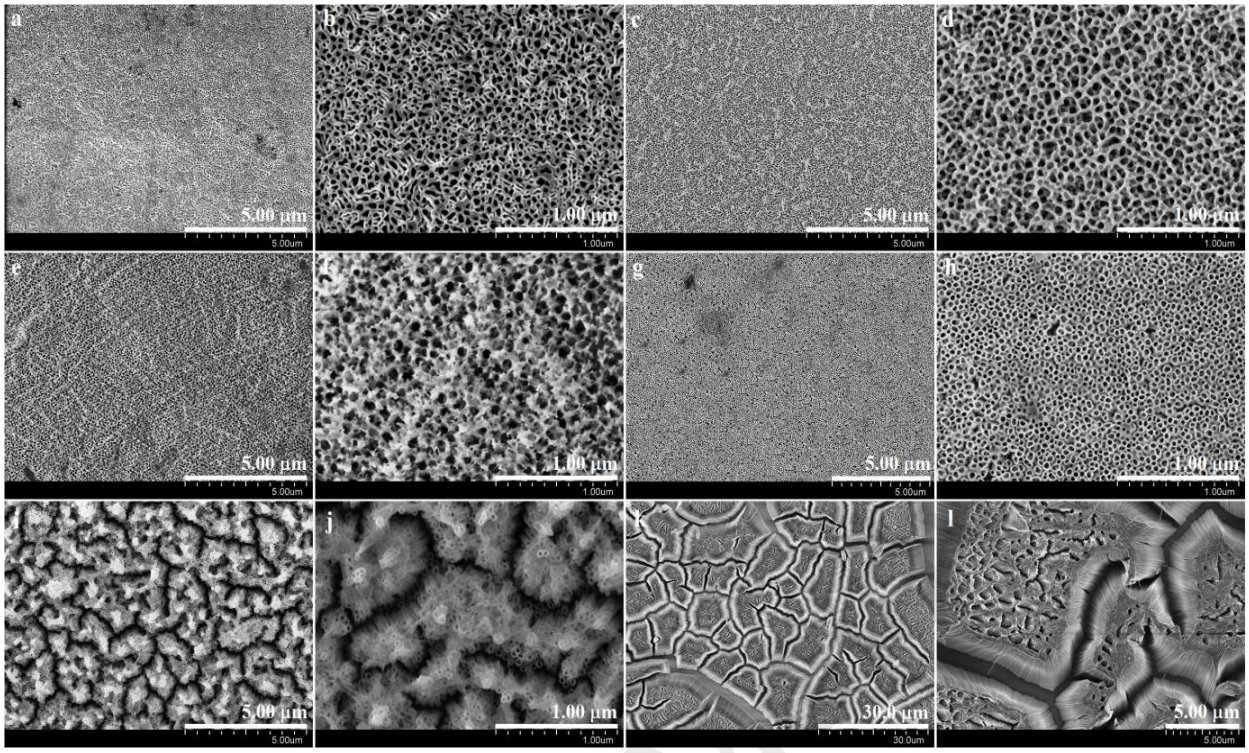

Figure 4.34: FESEM images of a Ta surface after the two-step anodization process with exposure times from 0.5 to 20 min in H_2SO_4: HF (99: 1) + 5% EG electrolyte at a constant potential of 15 V; (a and b) 0.5, (c and d) 1, (e and f) 3, (g and h) 5, (i and j) 10, and (k and l) 20 min.

The effect of the anodization time on the thickness of the nanostructured coatings was determined from a cross-sectional view of the FESEM images. Figure 4.35a–f shows the FESEM cross-sectional views of the Ta surface after a two-step anodization process with different durations, from 0.5 to 3 min in H_2SO_4 : HF (99:1) + 5% EG electrolyte, at a constant potential of 15 V. From these figures, the Ta_2O_5 NTs are not fully formed between 0.5 to 3 min, this may be the reason of the peeling off or delamination of the coatings. In general, the detachment of the films becomes gradually more difficult as the thickness of the oxide layer increases. Here, the most easily detachable coatings are obtained by growing the oxide for no longer than 3 min, at a constant potential of 15 V. A closer view of the cross-sectional images of the 0.5 to 3 min anodized samples shows a heterogeneous structure, where a very porous film rests on a more compact looking

oxide with a narrow stripe at the interface to the substrate that likely plays a role in the detachment (Singh et al., 2007). In contrast, the anodic oxide films grown for 5 min or more are very stable as shown in Figure 4.36. As can be seen, the resulting Ta_2O_5 NTs show a strong adhesion and fully covered the underlying Ta. In a diluted HF solution, the growth rate of nanotubes is significantly lowered, allowing the controlled formation of Ta_2O_5 NTs (~ 1 μm) in a reasonable anodizing time (5 min) as shown in Figure 4.36a. With further increase of the anodization time to 10 and 20 min (Figure 4.36b and c), the average coating thickness increases to ~ 2 and 4 μm, respectively. From Figure 4.36d, the bottom of the oxide nanotubes shows a series of evenly spaced ‘‘bumps” that signify the pore tips of each individual nanotube. Regarding the thinning of the nanotubes with time, Lockman et al. (2010) reported that during the first stage of anodization, the field assisted dissolution dominates the chemical dissolution, as the electric field across the electrode is very high. When the anodization progresses and oxide layer thickens, the chemical dissolution will be dominant over the field assisted dissolution (Lockman et al., 2010). Under such circumstances, chemical dissolution will increase the size and density of the pores. The growth and proliferation of the pores arise by the inward movement at the oxide/metal interface. Accordingly, the discrete hollow-like cylindrical oxide will be formed, which would develop into the nanotubular structure. Given that the oxide layer at the bottom of the pore is exposed to chemical dissolution, it becomes thinner with time. Besides, if the anodization is performed in a concentrated fluoride solution, the dissolution rate would be faster thus the thinning would increase. As the thinning increases, the electric field assisted dissolution will reoccur in this region and thus the pores will penetrate into the sample and the nanotubes grow longer. However, since the voltage is constantly applied, the anodization process would reoccur at the bottom of the pore, developing the nanotubes with a closed bottom.

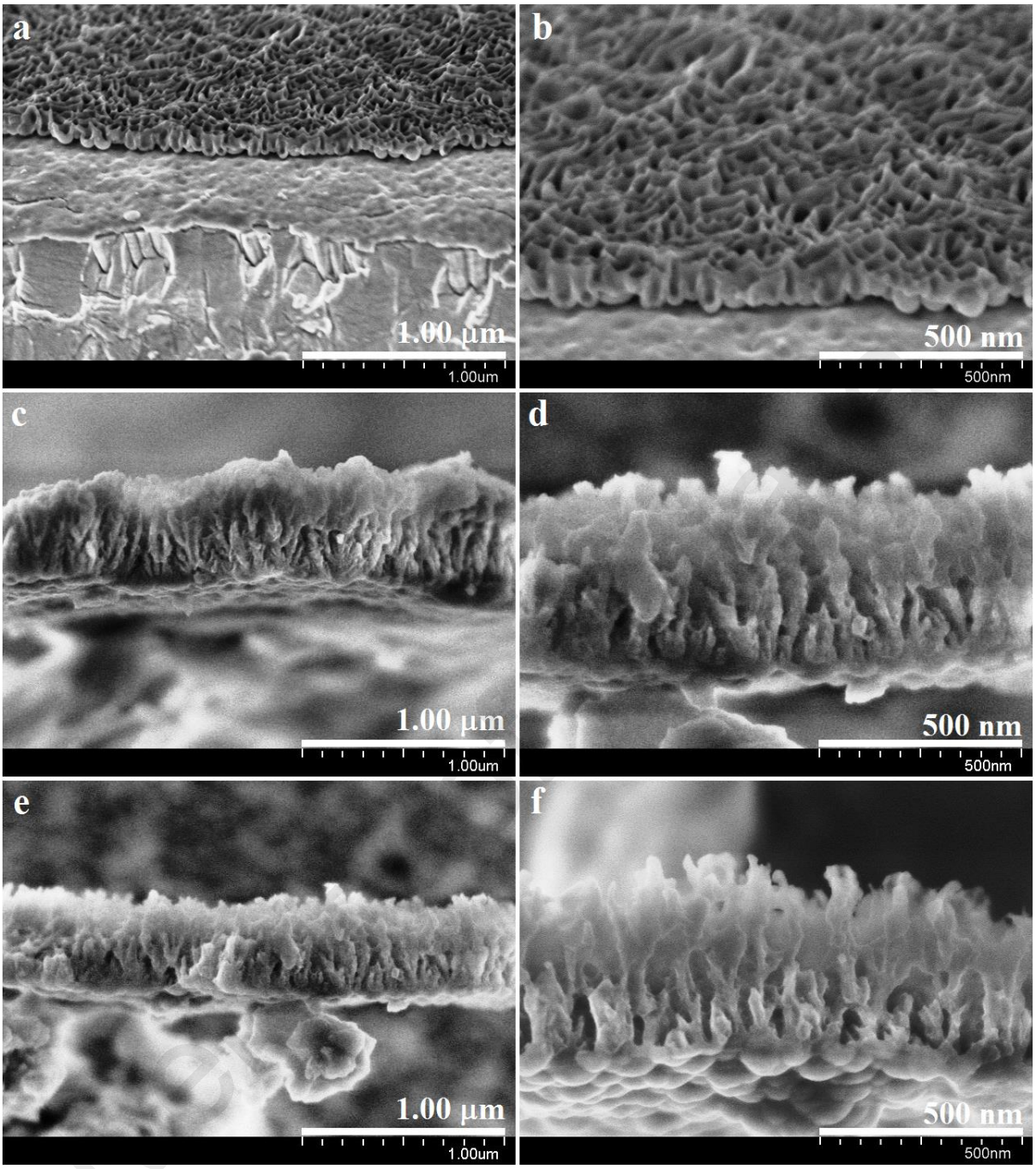

Figure 4.35: FESEM cross-sectional views of the Ta surface after the two-step anodization process with different durations from 0.5 to 3 min in H_2SO_4: HF (99: 1) + 5% EG electrolyte at a constant potential of 15 V; (a and b) 0.5, (c and d) 1, and (e and f) 3 min.

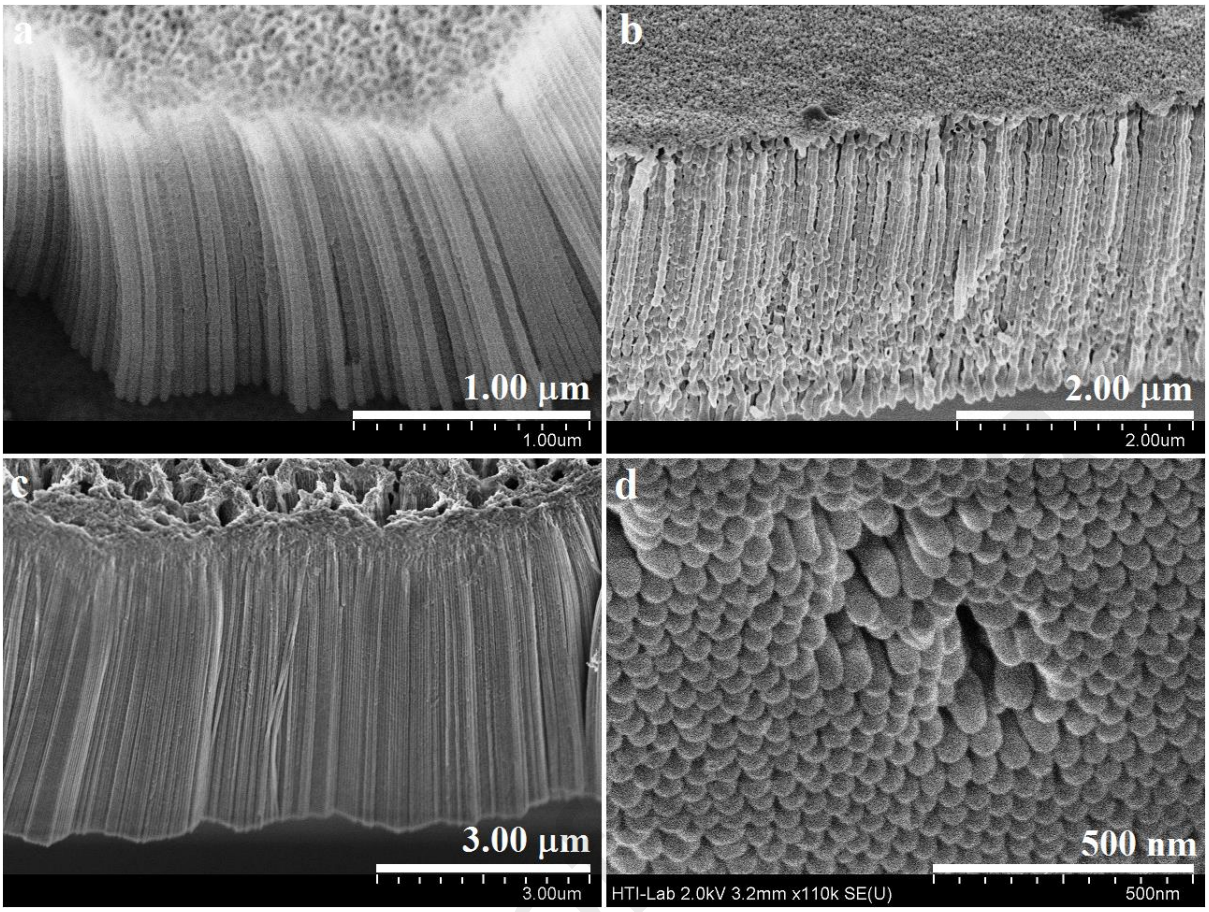

Figure 4.36: FESEM cross-sectional views of the Ta surface after a two-step anodization with different durations ranging from 5 to 20 min in H_2SO_4 : HF (99 : 1) + 5% EG electrolyte with a constant potential of 15 V; (a) 5, (b) 10, and (c) 20 min as well as (d) bottom of the oxide nanotubes.

The relationship between the dimensions of the fabricated Ta_2O_5 NTs and the anodization time, under constant applied anodization voltages is shown in Figure 4.38. From this figure, the average length of the nanotube increases with the increase of anodization time to 20 min, but the average inner diameter of the nanotube showed a different trend. The results are consistent with previous studies (Crawford et al., 2007; Ku et al., 2010). For the experiments conducted at shorter exposure times, the length of the NTs gradually increased from 73 to 487 nm, for the 0.5 and 3 min anodized samples, respectively, and thereafter the nanotube lengths steadily approached stable values. After 5 min of anodization, the nanotube lengths reached ~1 µm, and with further increase in the anodization time to 20 min, this value rapidly increased to ~4 µm (Figure 4.36c). It is

believed that the electrochemical oxidation rate is likely related to the movement of oxygen-containing anionic species such as O^{2-} and OH^- from the bulk electrolyte to the oxide/metal interface (Ku et al., 2010). The mass transport of the oxygen-containing anionic species to the bottom of the nanotube might be hindered with the increase in the nanotube length. When the rates of the electrochemical oxidization of as-prepared Ta coating and the chemical dissolution of Ta_2O_5 NTs reach a dynamic equilibrium, the nanotube lengths approach stable values. From the results of Figure 4.37, a small increase in tube diameter is observed with the increase in the anodization time from 0.5 to 3 min. In return, the length of the Ta_2O_5 NTs is strongly affected by the anodization time.

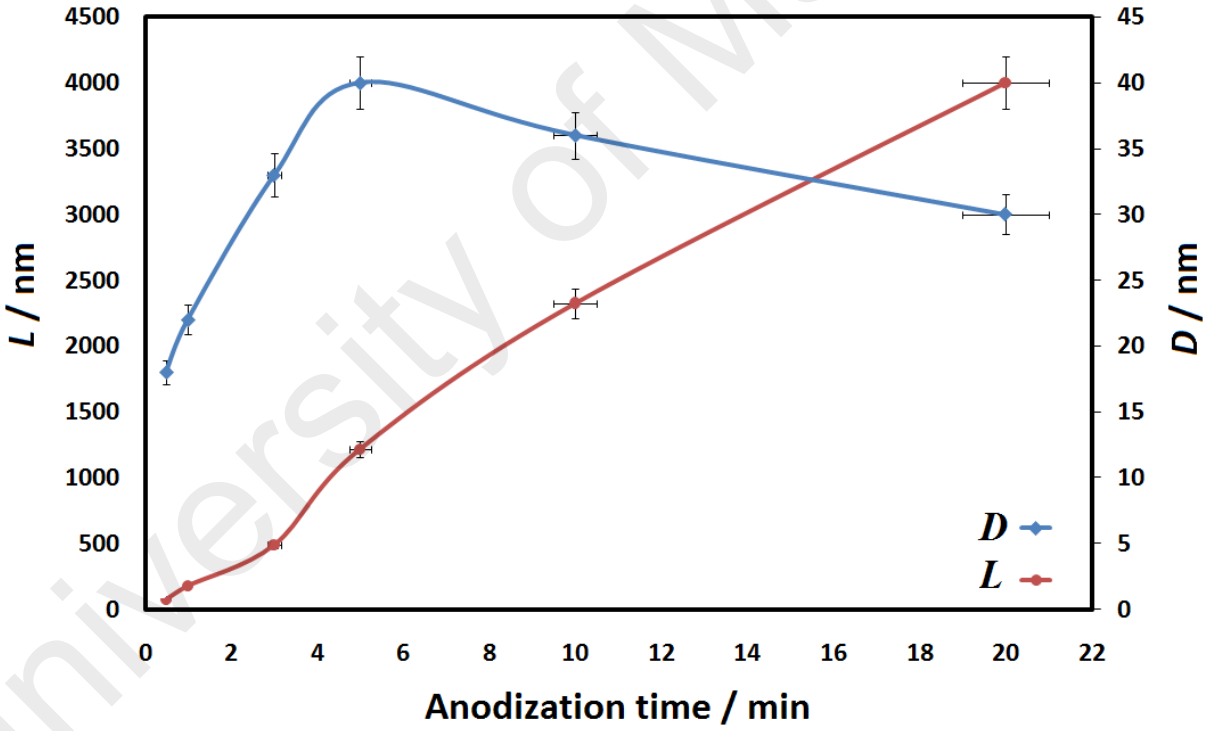

Figure 4.37: The relationship between the dimensions of the fabricated Ta_2O_5 NTs and anodization time at constant anodization voltages.

Figure 4.38 shows the EDS spectra of the coatings on Ti-6Al-4V after the two-step anodization process with different durations in H_2SO_4: HF (99:1) + 5% EG electrolyte, at a constant potential of 15 V. Tantalum and oxygen are the main elements of the coatings from the EDS profiles, which shows the absence of any impurity during the anodization

process, up to 20 min (Figure 4.38a-c). It should be noted that some chemical elements such as hydrogen or other elements in trace quantities are not detected by the EDS analysis. Oxygen composition gradients seem also to appear in some areas of the FESEM images. Thus, to further understand the nature of the NTs, the EDS cross-sectional analysis confirmed that the ionic diffusion and the formation of Ta_2O_5 occur all along the tubular structure and not limited to the surface (Figure 4.38d).

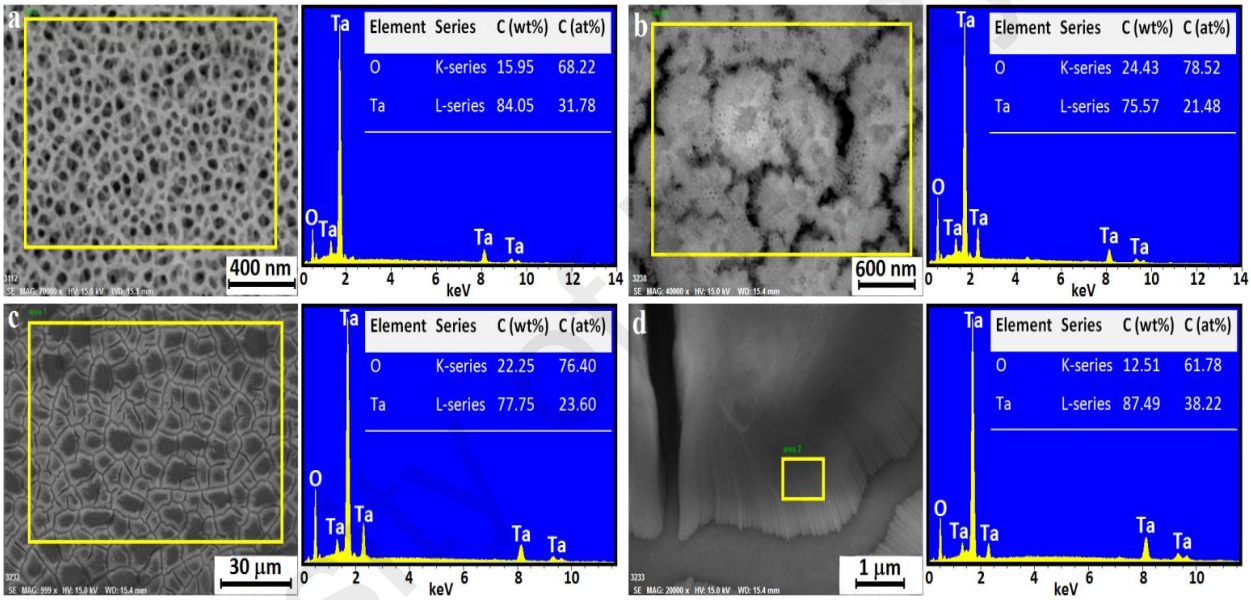

Figure 4.38: EDS spectra of the coatings on Ti-6Al-4V after the two-step anodization process with different durations in H_2SO_4 : HF (99:1) + 5% EG electrolyte at a constant potential of 15 V; (a) 1, (b) 10, (c) 20 min, and (d) EDS cross-sectional analysis.

To improve the adhesion of the Ta_2O_5 NTs, heat treatment was performed at a lower heating and cooling rates of 1 °C min^{-1} at 450, 500, 550, 750 and 1000 °C, for 1 h in an atmospheric furnace. The FESEM analysis of the annealed NTs at 450 °C is shown in Figure 4.39. The results for the Ta_2O_5 NTs annealed at other temperatures ranging from 500 to 1000 °C are also provided in this figure. As can be seen in Figure 4.39a, highly oriented arrays of Ta_2O_5 NTs were formed after the heat treatment at 450 °C for 1 h.

Besides, there are no major changes in the microstructural features after annealing at 450 °C. In this case, the length of the NTs and the average inner diameter are ~ 2 μm and 45 nm, respectively (Figure 4.39b and c). Similar to the as-prepared NTs, the bottom of the 450 °C annealed sample reveals a series of evenly spaced ‘‘bumps’’ (Figure 4.39l). The figure shows that the morphology of the NTs did not collapse and the wall thickness, as well as the tube diameter did not change considerably after the heat treatment. It has been reported that the NTs might collapse with specific heat treatment conditions, such as high temperature and extended annealing time (Ghicov et al., 2006; Mohamed et al., 2011). In the present case, the surface and the cross-sectional morphologies of the NTs changed after the annealing process at 500 and 550 °C for 1 h (Figure 4.39d-i). The FESEM top view images of the annealed samples at these temperatures show distinct patches of Ta_2O_5 NTs, with the underlying dimpled Ta surface uncovered between the oxide film patches. In accordance with the cross-section image in Figure 4.39i, severe oxidation of the barrier layer and minor distortion of the NTs are visible, leading to the shortening of the nanotubes. Any further heat treatment at higher temperatures (typically above 550 °C) will result in the detachment of most of the NTs in an uncontrolled manner as shown in Figure 4.39j and k. As shown in Figure 4.39j, the nanotubular arrays collapsed at 750 °C. Therefore, the nanotubes will be completely destroyed if the annealing temperature exceeds 1000 °C. Consequently, the nanotubular arrays were converted into a coarse particle structure (Figure 4.39k). Gonçalves et al. (2014) previously reported similar observations of the collapse of the Ta_2O_5 NTs under heat treatment (Gonçalves et al., 2014). These findings indicate that temperatures higher than 550 °C are likely to result in structural damage and collapse of the nanotube array structure.

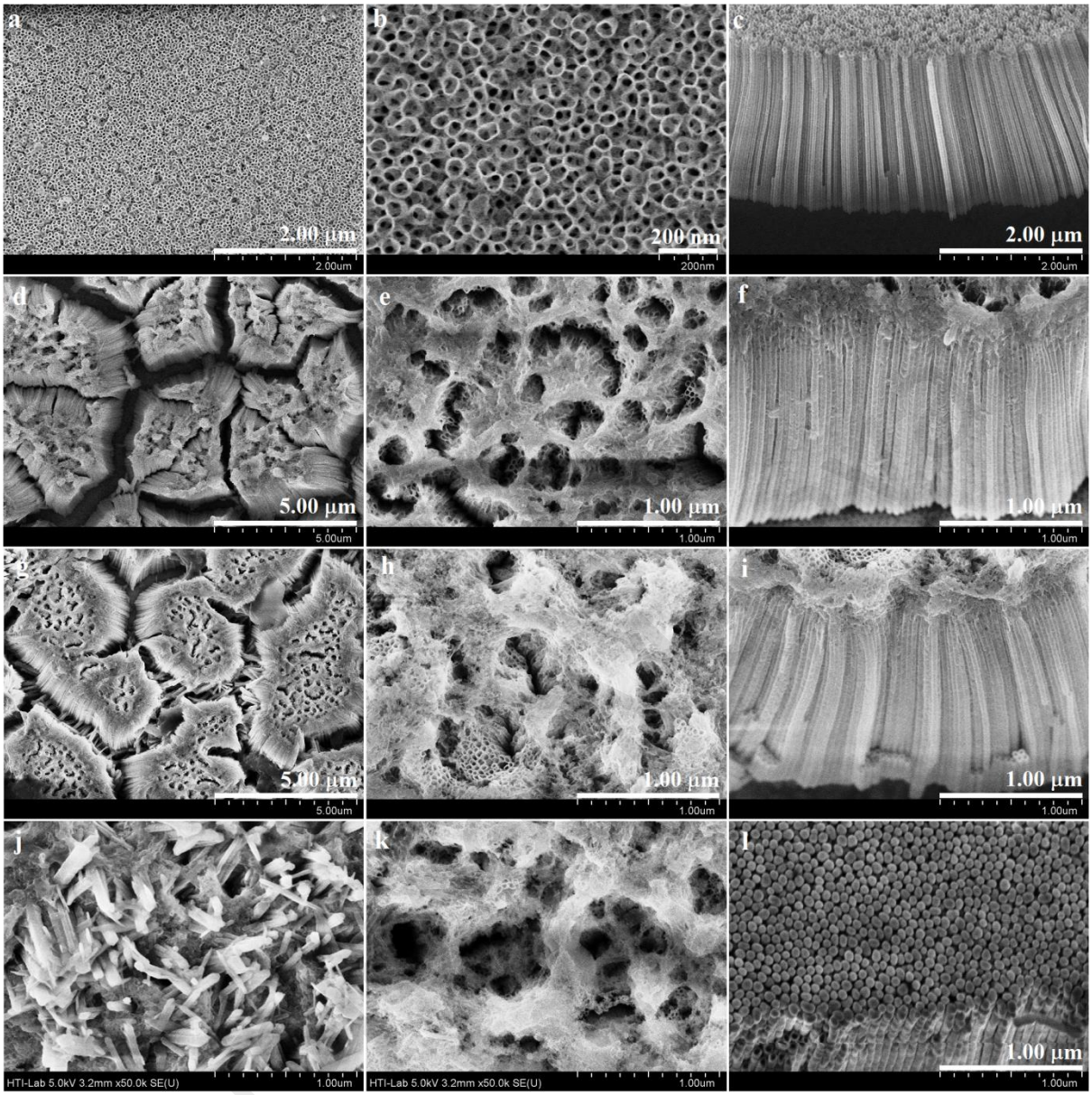

Figure 4.39: FESEM images (top- and cross-sectional views) after annealing at (a–c) 450,(d–f) 500, (g–i) 550, (j) 750, and (k) 1000 °C for 1 h; (l) FESEM image (bottom view) of the Ta_2O_5 NTs annealed at 450 °C for 1 h.

To sum up, Figure 4.40 shows top view and cross-sectional FESEM micrographs as well as EDS spectra of the as-deposited Ta thin film using the optimum factors (350 W–250 °C–6h) befor and after a two-step anodization for 5 min in H_2SO_4: HF (99:1) + 5% EG electrolyte at a constant potential of 15 V and after annealing at 450 °C for 1 h. The FESEM images of the as-deposited Ta layer indicate that the coating is dense with a lamellar structure (Figure 4.40a and b). So the proposed conditions are highly desirable

to increase adhesion of the coating to the substrate. Such an improvement in coating adhesion can be derived from the higher available energy for film growth. With the increase in DC power, the ionized particles become more energetic At the beginning of the anodization, irregular pits were formed due to the localized dissolution of oxide layer and following that the pits conversion to larger pores, whereas most of the areas covered with oxide layer. With further increasing of anodization duration (5 min), the compact oxide layer disappeared completely and a clear evolution of nano-porous structure to nanotubular configuration could be observed (Figure 4.40d and e). As can be seen, well-aligned Ta_2O_5 NTs were formed and uniformly distributed over the anodized surface after 5 min of anodization. In this case, the higher magnification FESEM image shows that the average inner diameter and tube length are 40 nm and ~1 μm, respectively. This shows that by using a low HF concentration, the growth rate of nanotubes sharply reduces, allowing the controlled formation of Ta_2O_5 NTs (~ 1 μm) at a justified time (5 min). Figure 4.40g and h display top view and cross-sectional FESEM images of the 450 °C annealed sample. From these micrographs, highly ordered arrays of Ta_2O_5 NTs was formed after annealing at 450 °C for 1 h. Although there was no significant changes in the microstructural features after annealing at 450 °C, the length of the NTs and the average inner diameter increased to ~ 2 μm and 45 nm, respectively. Figure 4.40f and i shows the EDS spectra of the as-anodized layer befor and after annealing at 450 °C for 1 h. As can be seen, tantalum and oxygen are the main elements of the coatings, which suggests that there is no impurity formed during anodization and subsequent annealing.

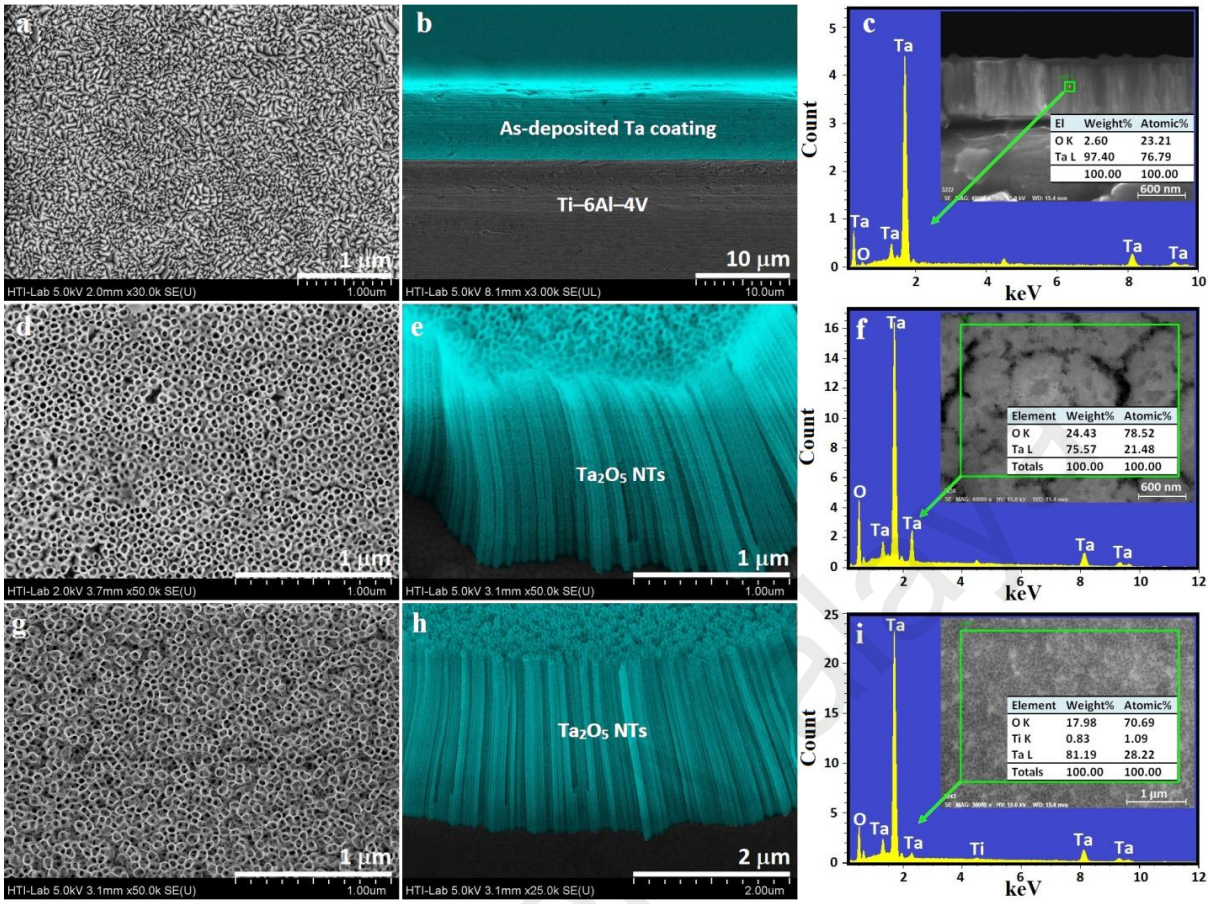

Figure 4.40: Top view and cross-sectional FESEM micrographs as well as EDS spectra of the as-deposited Ta thin film using the optimum factors (a–c) before and (d–f) after a two-step anodization for 5 min in H_2SO_4: HF (99:1) + 5% EG electrolyte at a constant potential of 15 V and (g–i) after annealing at 450 °C for 1 h.

4.2.7 Adhesion Strength of Heat Treated Thin Film

As mentioned earlier, depending on the application, enhancement of the adhesion strength between coating layers and implant materials is very important. In reality, the adhesion of a coating to a substrate and the integrity of the substrate/coating interface are always connected to the performance and reliability of any coated surface (Baradaran et al., 2013) . Figure 4.41 illustrates the graphs of depth, load, friction and COF versus the distance, as well as the failure points of the 5 min anodized specimen after annealing at

450 °C for 1 h during the scratch test. The critical loads were defined on the basis of the load-displacement graph. It should be noted that the scratch direction was from left to right, as shown in Figure 4.41a. As can be seen, the total scratch length of the 450 °C annealed sample is 1024 μm, against which the coating total failure was detected at a distance 863 μm. In addition, the adhesion strength of the coating increased to 2301 mN after the heat treatment. From Figure 4.41d and e, the calculated friction and COF of the annealed coating decreased to 1056 mN and 0.56, respectively. Concerning the scratch depth (~ 6 μm) of the anodized sample after annealing, this behavior could be due to the complementary effect of the Ta coating as an intermediate layer. In fact, the observed value of the penetration depth is related to Ta/Ta_2O_5 NTs layer, where the inter diffusion of Ta between substrate and nanotubular configuration has contributed to strong interlock for higher adhesion strength. According to Figures 4.26 and 4.41, the scratch width of the annealed sample is narrower than the as-deposited Ta coating and consequently the scratch hardness of the annealed coating (2.9 GPa) is higher than that of the as-deposited thin film (1.8 GPa). These findings imply that the subsequent annealing process may have a dramatic impact on the adhesion of the thin films.

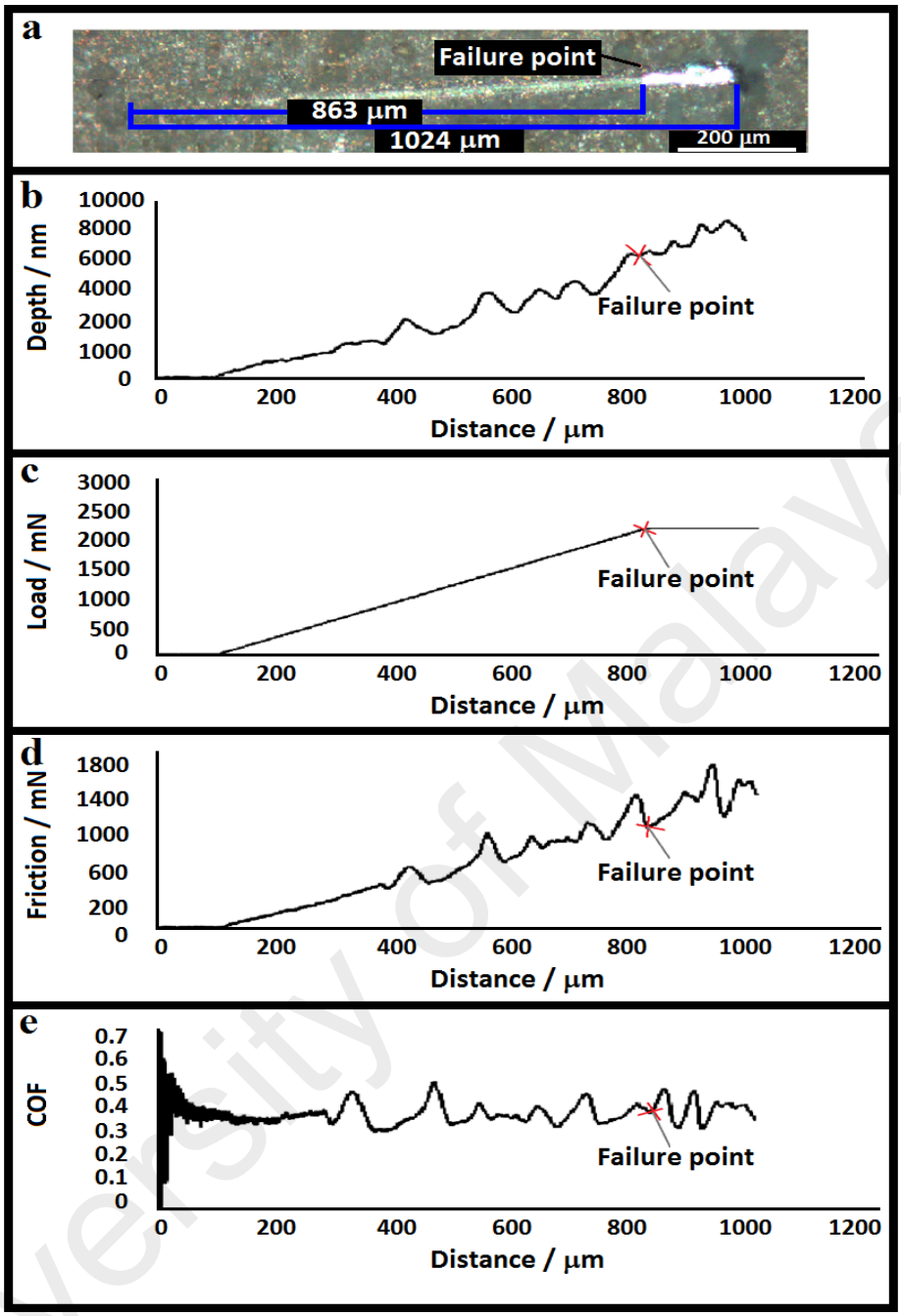

Figure 4.41: (a) The optical micrograph of the scratch track and (b) graphs of depth, (c) load, (d) friction and (e) COF versus distance as well as the failure points of the 5 min anodized specimen after annealing at 450 °C for 1 h.

4.2.8 Microstructural Evolution of Ag_2O NPs on the NTs

The FESEM images in Figure 4.42 present the thickness and morphology of the Ag_2O layer formed on the annealed specimens via PVD magnetron sputtering at different time intervals. In contrast to those of pure Ag NPs, the amounts of Ag^+ release from the Ag_2O NPs is probably lower due to the presence of an oxide barrier, which potentially results in improved cytocompatibility (Gao et al., 2014). Moreover, the Ag concentration deposited on the implant surface needs to be carefully controlled in order to effectively kill bacteria without impairing the human cell functions. This could be generally achieved by optimization of the PVD sputtering time in order to deposit sufficient amounts of Ag_2O NPs, which uniformly cover the NT walls without formation of large aggregates and blocking the NT openings. As shown in Figure 4.42, by reducing the sputtering time, the concentration of Ag_2O NPs on the NTs surfaces as well as the particles aggregation was gradually reduced. At sputtering time of 10 s, a well-decorated uniform layer of Ag_2O NPs was produced on the edges of the NT walls, without clogging the NT openings. Figure 4.43 shows the cross-section FESEM images of Ta_2O_5 NTs-Ag_2O NPs. The EDS spectrum and elemental distribution patterns of the Ta_2O_5 NTs with Ag_2O NPs decorated by PVD sputtering for 10 s (Ta_2O_5 NTs-Ag_2O NPs) also confirm formation of a uniform array of Ag_2O NPs on the NT walls (Figure 4.44). However, further decrease of the sputtering time leads to excessively low concentration of Ag_2O NPs on the NTs surfaces. The results also confirmed the negligible influence of decorated Ag_2O NPs on the morphology of Ta_2O_5 NTs.

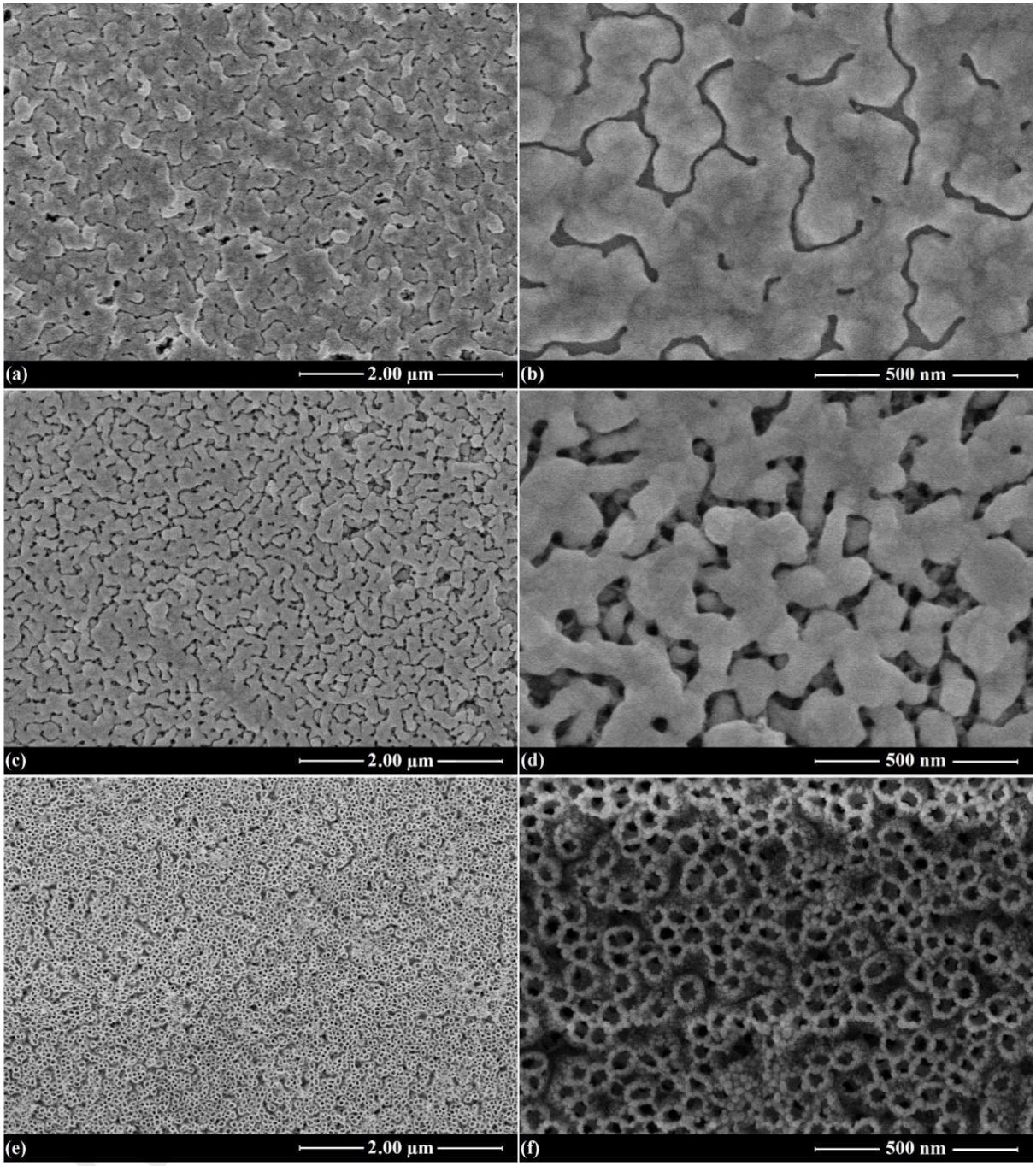

Figure 4.42: The FESEM images of the Ag_2O NPs layer formed via PVD magnetron sputtering on edges of Ta_2O_5 NTs for 60 s (a, b) and 30 s (c, d), and 10 s (e, f).

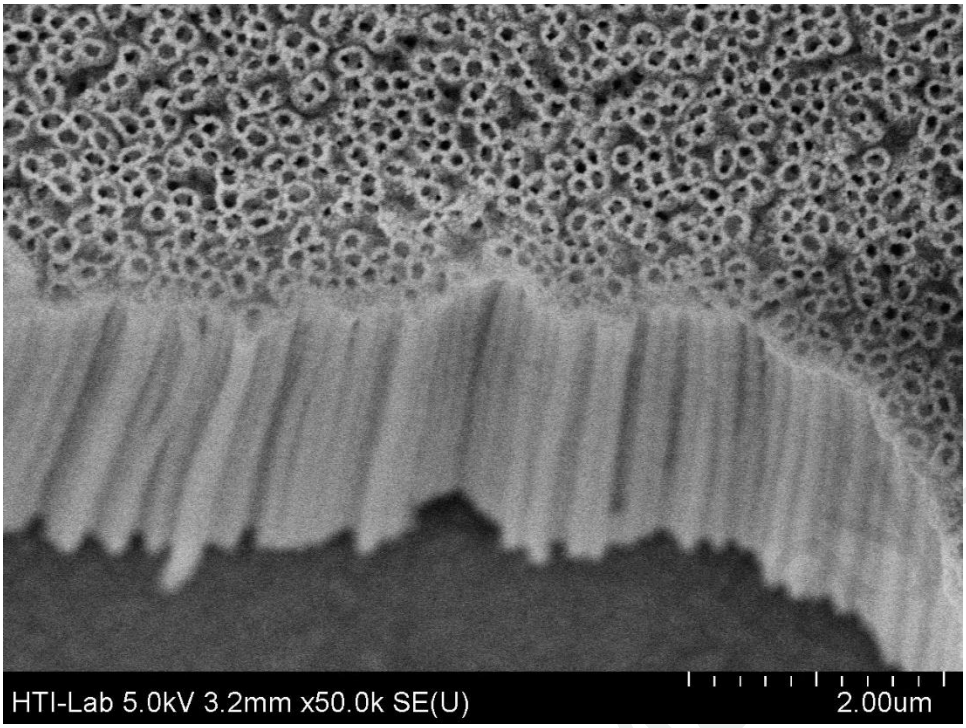

Figure 4.43: Cross-section FESEM images of Ta_2O_5 NTs-Ag_2O NPs after 10 s PVD deposition

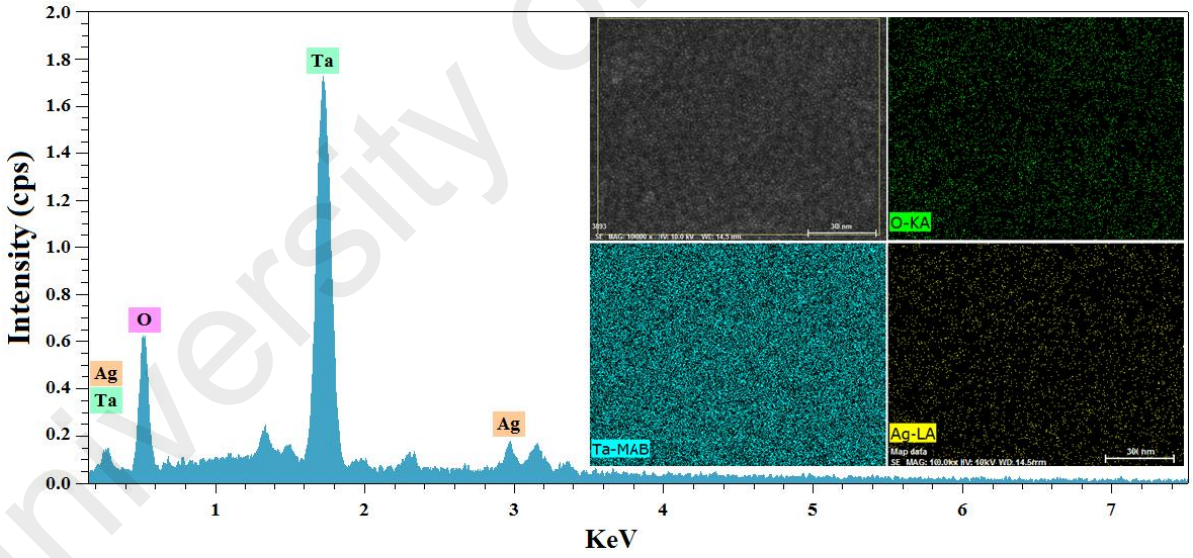

Figure 4.44: The EDS spectrum of the Ta_2O_5 NTs-Ag_2O NPs and the elemental distribution patterns of the constituting elements.

4.2.9 Vickers Microhardness

To control the quality of the coatings, Vickers microhardness test was conducted. Table 4.6 shows the disparity in the Vickers hardness of the substrate, as-deposited Ta

layer and 5 min anodized sample before and after the annealing process at 450 °C for 1 h. The microhardness of the substrate and the as-sputtered Ta layer was 263 and 290 HV, respectively, and rose to 297 HV after 5 min of anodization. This effect can be linked to the presence of the nanotubular arrays which can improve the mechanical properties of the material (Yaghoubi et al., 2010). The annealing process at 450 °C for 1 h resulted in an increase in surface hardness to 356 HV. This result is entirely consistent with the FESEM observations, where a highly oriented array of Ta_2O_5 NTs was detected after annealing at 450 °C for 1 h. Accordingly, the heat treatment at 450 °C at atmospheric pressure is the most favorable condition for the annealing of the Ta_2O_5 NTs.

Table 4.6: The disparity in the Vickers hardness of the substrate, as-deposited Ta layer and 5 min anodized sample before and after the annealing process at 450 °C for 1 h.

samples	substrate	as-deposited Ta layer	5 min anodized sample	Annealed sample at 540°C
Vickers hardness (HV)	263	290	297	356

4.2.10 Surface Topography and Tribology

Generally, the composition and features of the surface and near-surface areas can be changed during wear, where the materials which divides two sliding surfaces can be acted as a separate '*third-body*' with its own evolutionary history and properties. These features will frequently change during the lifetime of the system. Besides, the surface topography

can be altered due to the removal or displacement of material during wear. On the other hand, the recognition and interpretation of the wear mechanisms are often multifaceted because it often involves a combination of chemical and mechanical processes (Stachowiak, 2006). Figure 4.45 displays the COF versus cumulative sliding time for bare substrate, the as-deposited Ta coating, the as-anodized specimen, and the 450 °C annealed sample under normal loads of 15, 20 and 25 N. From this figure, a common feature in all cases is the increase in friction coefficient when the normal load increases. On the brink of testing, the COF rose sharply and reached a steady-state in a short time interval. This effect is caused by the consecutive wear of surface asperities and improved compliance of smooth worn surfaces. Accordingly, wear is due to brittle micro-fractures in the surface grains and tribochemical reaction in the initial and final stage, respectively (Stachowiak, 2006). Furthermore, this primary rapid rise in COF can be attributed to the development of a thin superficial outer layer during PVD. It is clear that the plotted friction lines of 15, 20, and 25 N are very close to each other and have reached steady-state in the first few seconds, signifying that each sample has a similar wear pattern for the applied load range. For all tests, the COF rose progressively as load increased from 15 to 25 N. All specimens stayed stable under a load of 15 N and revealed COF values in the range of 0.106 to 0.279; however, when the normal load intensified to 20 and 25 N, higher COF ranging from 0.107 to 0.297 and from 0.110 to 0.314 was detected, respectively. It should be mentioned that no unexpected increase in COF value of the 450 °C annealed specimen was observed, suggesting that the nanostructured coating is quite stable after annealing process. In addition to this finding, COF values of the annealed specimen declined dramatically in the applied load range compared to other samples, which can be linked to the development of a highly oriented arrays of Ta_2O_5 NTs.

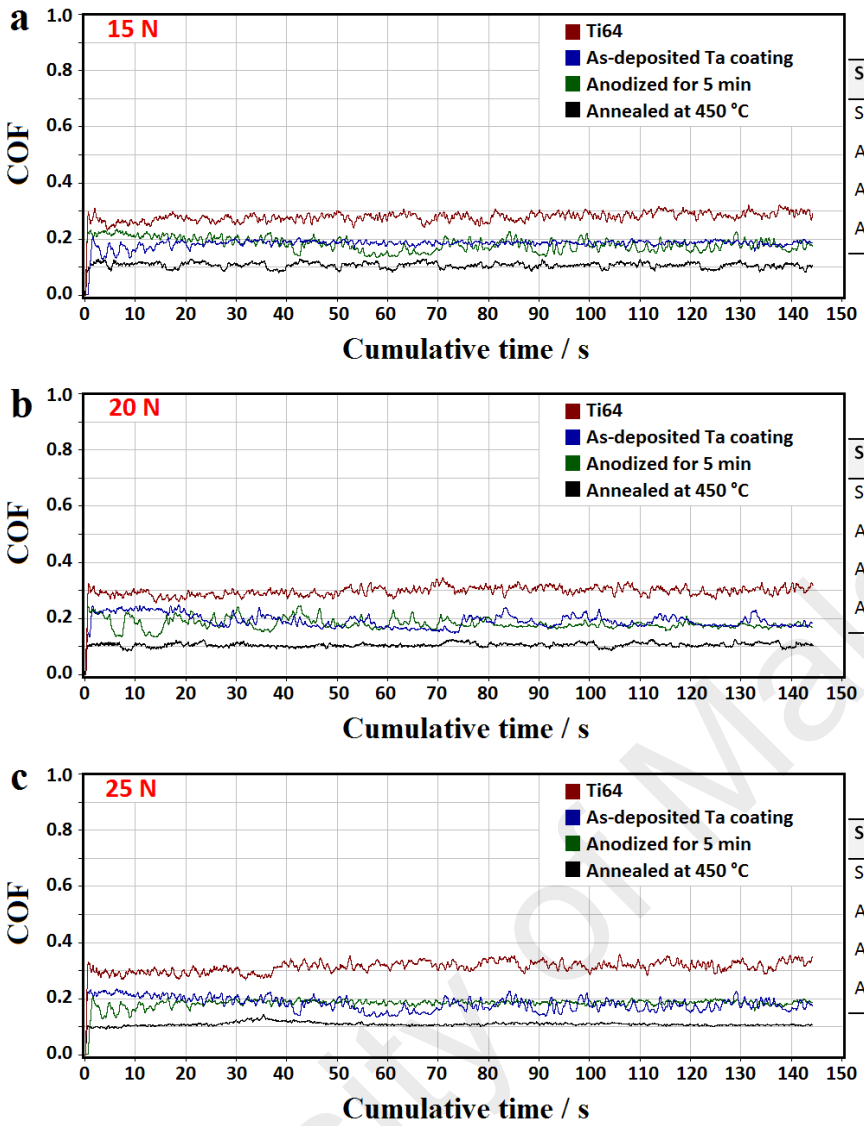

Series	Load (N)	COF
Substrate (S1)	15	0.279
As-deposited Ta coating (S2)	15	0.194
Anodized for 5 min (S3)	15	0.188
Annealed at 450 °C (S4)	15	0.106

Series	Load (N)	COF
Substrate (S1)	20	0.297
As-deposited Ta coating (S2)	20	0.198
Anodized for 5 min (S3)	20	0.194
Annealed at 450 °C (S4)	20	0.107

Series	Load (N)	COF
Substrate (S1)	25	0.314
As-deposited Ta coating (S2)	25	0.218
Anodized for 5 min (S3)	25	0.201
Annealed at 450 °C (S4)	25	0.110

Figure 4.45: COF versus cumulative sliding time for bare substrate, the as-deposited Ta coating, the as-anodized specimen, and the 450 °C annealed sample under normal loads of (a) 15, (b) 20 and (c) 25 N.

AFM imaging was employed to assess the topographical properties of plain and worn surfaces. With the same loads, the wear showed different upshots on the coatings, where different wear modes were observed. By observing the widths and depths of wear grooves, different deductions can be achieved which are presented in detail in this section. Figure 4.46 illustrates the topographic images of undamaged and wear surfaces on bare substrate, the as-deposited Ta coating, the as-anodized sample, and the 450 °C annealed specimen over an area of 20 µm × 20 µm. From Figure 4.46a. as can be seen in Figure

4.46b, the occurrence of coarse ridges and grooves caused by the severe plastic deformation is the main feature of the worn surface. This observation is consistent with the findings of previous studies that demonstrated the wear occurred by homogeneous deformation in isothermal mode and through which the material was detached as a result of the extrusion and lip formation (Ezazi et al., 2014). AFM images were also gathered of a surface covered with Ta layer as well as nanotubular arrays before and after annealing. The as-deposited Ta layer (primary surface) exhibits a dense structure (Figure 4.46c). The presence of tantalum as the main component of coating gives good reason for the less extent of wear as compared to bare substrate (Figure 4.46d). The anodized surface topography was characterized by a homogenous structure consisting of hillocks and dimples, originating from the tubular configuration (Figure 4.46e). A similar observation was made in the case of the 450 °C annealed specimen as shown in Figure 4.46g. As demonstrated in Figure 4.46f, the level of plastic deformation in terms of ploughing and transverse tracks was found to be less than the substrate. For the 450 °C annealed specimen, the fewer deep grooves that are barely visible in Figure 4.46h are due to greater coating thickness of Ta_2O_5 NTs which led to the reduced ductile effect of Ti-6Al-4V substrate and noticeably prevented plastic deformation.

Based on the obtained data, R_a value is approximately 59.2, 66.7, 22.6, and 20.3 nm for bare substrate, as-deposited Ta layer, the anodized sample and the annealed coating, respectively. This suggests that the surfaces of nanotubular arrays are not smooth although the roughness become lower as compare to bare substrate and the as-deposited Ta layer. On the other hand in the case of the worn surfaces, a different behavior is observed. R_a value inside the wear tracks of the anodized and annealed samples is nearly 291 and 186 nm, almost 27 and 53%, respectively, less than the value measured for the substrate (397 nm). This indicates the important role of Ta_2O_5 NTs in diminishing wear, which is very important from the perspective of orthopedic applications.

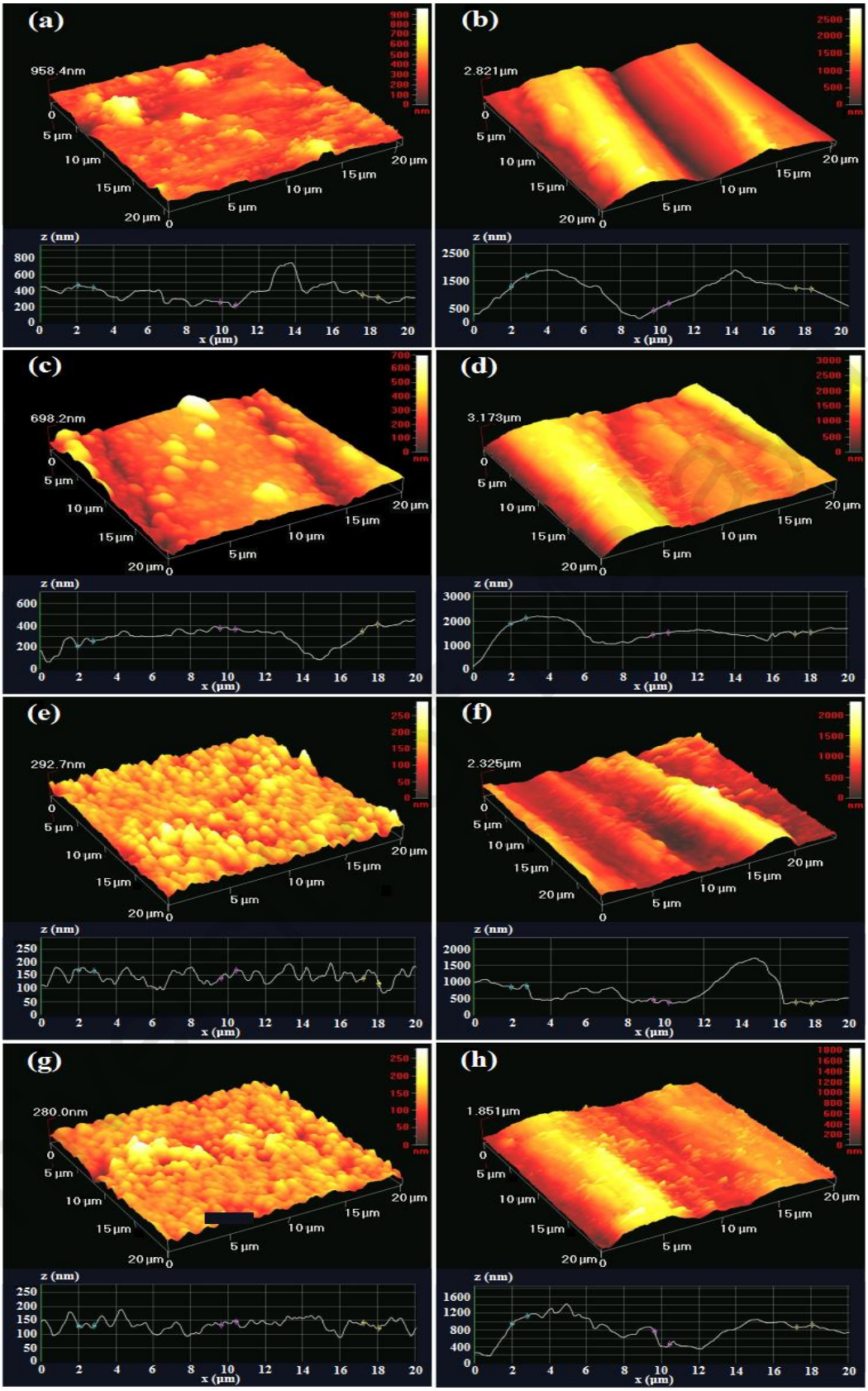

Figure 4.46: Topographic images of undamaged and wear surfaces on (a,b) bare substrate, (c,d) the as-deposited Ta coating, (e,f) the as-anodized sample, and (g,h) the 450 °C annealed specimen over an area of 20 μm × 20 μm.

4.2.11 Effectiveness of Corrosion Protection

In general, the toxicity of metallic implants is controlled not only by their composition and toxicity of the constituent elements but also by their wear and corrosion resistance (Gu et al., 2009). Corrosion of a metallic implants happens as elements in the alloy ionize. Consequently, the elements that are primarily uncharged inside the alloy lose electrons and become positively charged ions when they are liberated into solution (Wataha, 2000). Corrosion generally occurs at a rate determined by an equilibrium between opposing electrochemical reactions as follows: (i) anodic reaction, in which a metal is oxidized, releasing electrons into the metal; (ii) cathodic reaction, in which a solution species is reduced, removing electrons from the metal. When these two reactions are in equilibrium, the flow of electrons from each reaction is balanced, and no net electron flow happens. The necessity of conducting corrosion test as a chemical property is that has important consequences on implant biofunctionality. Corrosion behavior can be measured in different ways such as observing the alloy surface, many forms of electrochemical analysis, and measuring the release of the elements directly by spectroscopic methods. Here, the corrosion behavior of the bare substrate before and after surface modifications was examined in PBS (pH 7.2) using potentiodynamic polarization. The polarization plots of the bare substrate, as-deposited Ta layer, the as-anodized specimen, and the 450 °C annealed sample are shown in Figure 4.47. In addition, E_{corr}, I_{corr}, R_p and *P.E.* values are presented in Table 4.7. The bare substrate exhibits a corrosion potential of -0.143 V_{SCE} and current density of 4.334×10^{-6} μA cm^{-2}. Regarding the anodized sample before and after annealing at 450 °C which is demonstrated in Figure 4.47, E_{corr} became noticeably more negative indicating an increase in the activity of the specimen for corrosion, while I_{corr} decreased considerably (polarization curves moved towards lower current densities) form 4.334×10^{-6} to 5.360×10^{-8} μA cm^{-2}. Meanwhile, the annealed sample demonstrates a higher *Rp* value of 4.864×10^{5} Ω cm^{-2} than those of

7.674×10^{3} Ω cm^{-2} for native Ti-6Al-4V substrate. This suggests that although the corrosion tendency became more feasible after anodization and subsequent annealing on thermodynamic ground but the process became less feasible kinetically in these circumstances. The protection efficiencies were also determined for all cases. As compared to the bare substrate, the as-deposited Ta coating and the 5 min anodized sample showed a 94 and 97% increase in *P.E.*, respectively. It was found that the 450 °C annealed sample had a significant improvement over *P.E.* and exhibited the highest percentage of protection efficiency (99%). Therefore, it can be concluded that Ta oxide coating can improve *in-vitro* corrosion behavior of native Ti-6Al-4V substrate, which is in agreement with previous studies (Xu et al., 2015).

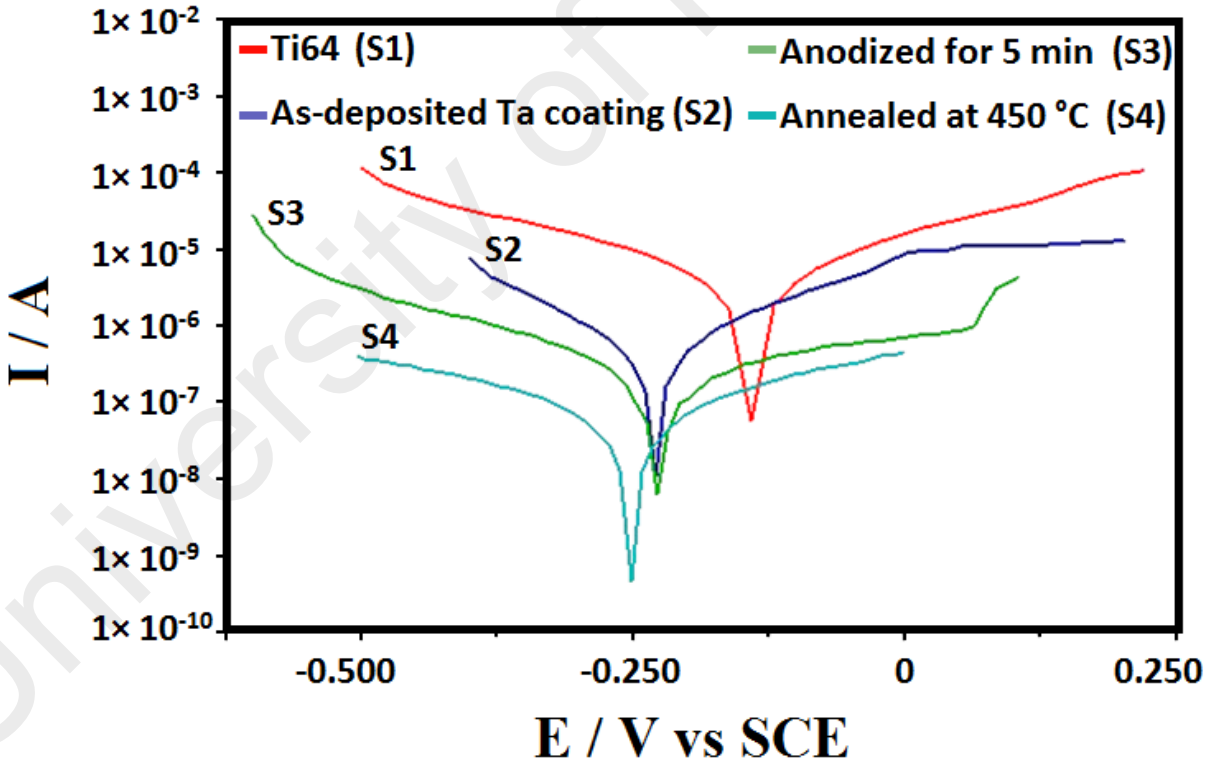

Figure 4.47: Polarization plots of the bare substrate, as-deposited Ta layer, the as-anodized specimen, and the 450 °C annealed sample.

Table 4.7: Corrosion potential (*E*corr), corrosion current density (*I*corr), polarization resistance (*Rp*) and effectiveness of corrosion protection (*P.E.*) values.

Electrode	E_{corr} (V_{SCE})	I_{corr} ($\mu A\ cm^{-2}$)	R_p ($\Omega\ cm^{-2}$)	*P.E.* (%)
Substrate	-0.143	4.334×10^{-6}	7.674×10^{3}	-
Ta PVD	-0.224	2.522×10^{-7}	1.798×10^{4}	94
Anodized for 5 min	-0.227	1.216×10^{-7}	9.352×10^{4}	97
Annealed at 450 °C	-0.251	5.360×10^{-8}	4.864×10^{5}	99

4.2.12 Surface Wettability

In general, wettability is the tendency of a fluid to spread on, or adhere to, a solid surface in the presence of other immiscible fluids. In reality, wettability refers to the interaction between the fluid and solid phases and is defined by the contact angle of the fluid with the solid phase. The degree of wetting (wettability) is determined by a force balance between the adhesive and cohesive forces, where wetting deals with the three states of matter: gas, liquid and solid. Due to the appearance of a wide range of nanomaterials in the recent years, this technique is gaining popularity in nanotechnology and nanoscience investigations (Aronov et al., 2007). The contact angle values indicate whether the surface is hydrophilic or hydrophobic. Figure 4.48 displays the variation of the deionized water contact angle of the substrate, as-deposited Ta layer, 5 min anodized sample, the annealing process at 450 °C for 1 h and Ag_2O nanoparticles decorated on edge of nanotubes. It is clear that the 5 min anodization and subsequent annealing at 450 °C play an important role in determining the surface wettability of the material. According to Figure 4.48a and b, the substrate and the as-sputtered Ta layer show a contact angle value of 72.8° and 54.8°, respectively. After 5 min of anodization, this value decreases to 37.7°, which suggests that the wetting of the surface is very favorable, where the hydrophilic properties of the substrate has improved after 5 min of anodization (Figure 4.48c). So it can be concluded that the nanotubular configuration can increase the

hydrophilicity of the titanium implant surfaces, thereby the cell attachment, extension and spreading, as well as cytoskeletal organization can improve the biomedical functionality (He et al., 2014; Yaghoubi et al., 2010). As shown in Figure 4.48d, an improvement in the surface hydrophilicity (28.1°) was observed after annealing at 450 °C, which can be interpreted by the superficial cleanliness, crystal structure, oxygen vacancy defects and surface morphology (Yang et al., 2014).But the value increased to 38.4° after Ag_2O nanoparticles decorated on edge of nanotubes (Figure 4.48e). It has been reported that the protein activities on the surface of the orthopedic implants is dependent on the surface properties, especially on adsorption and adhesion (Elias et al., 2008). The implant surface wettability also influences the cell behavior in the initial osseointegration process, whereas the osseointegration mechanism begins when the implant is in contact with the blood. Hydrophobic surfaces decreases the cell adsorption and the hydrophilic surfaces increases the cell adsorption (Macak et al., 2007). Therefore, the surface modification by Ta coating and subsequent anodization and annealing can change the composition, topography, roughness and wettability and when in connection with the cell behavior, it can modify in the initial mechanisms of osseointegration.

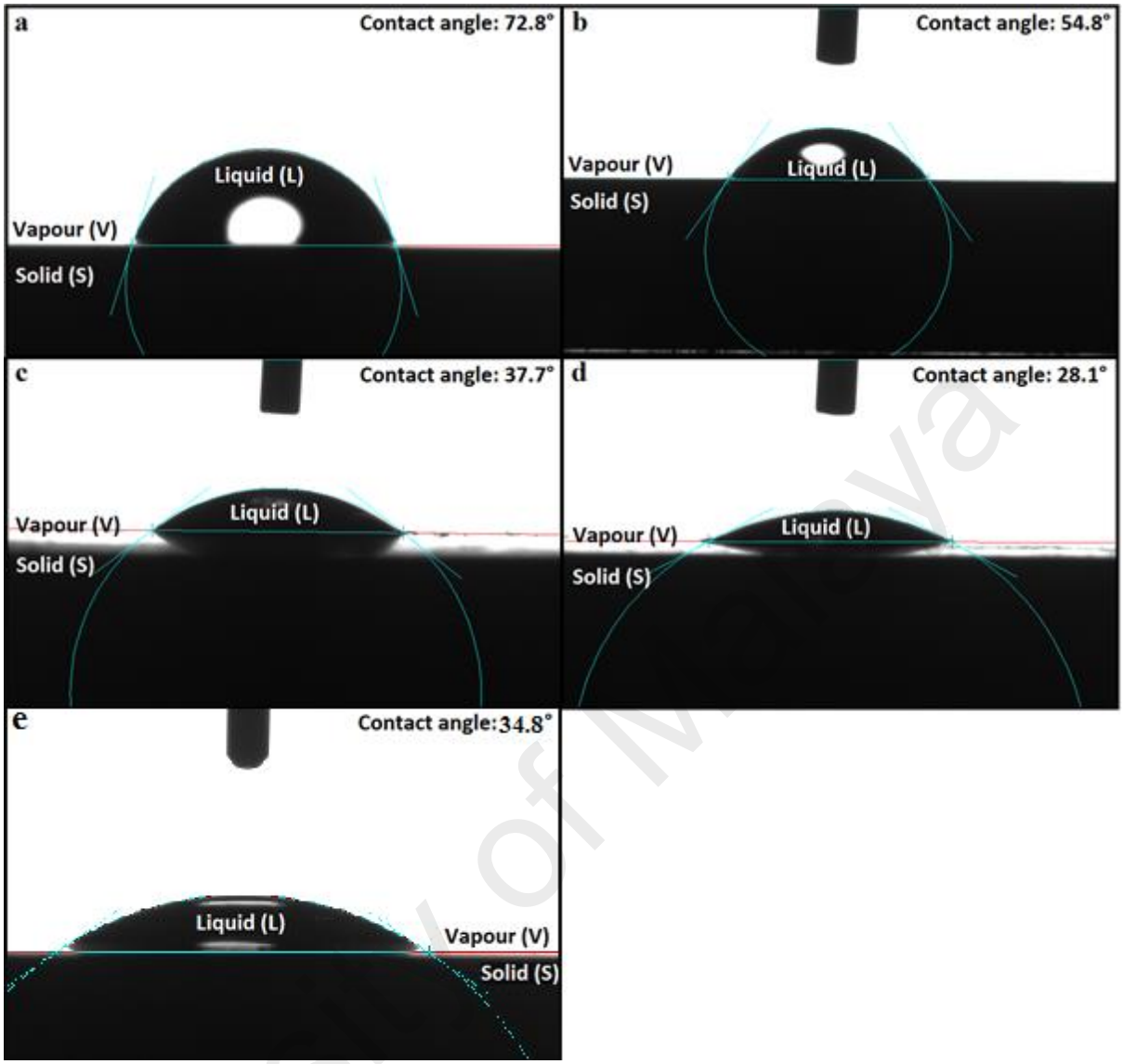

Figure 4.48: The variation of the deionized water contact angle of the (a) substrate, (b) as-deposited Ta layer and 5 min anodized sample (c) before and (d) after annealing at 450 °C for 1 h (e) decorated Ag_2O NPs on NTs

4.2.13 In-vitro Apatite Formation

Figure 4.49 shows surface morphologies and EDS results of the 450 °C annealed sample after exposure to SBF for 1 to 14 days. After 1 to 7 days immersion in SBF, a trace of apatite deposition could be observed on Ta_2O_5 NTs, where most of the top ends of the nanotubular arrays are not covered with the bone-like apatite layer (Figure 4.49a to

d). As the immersion time increased to 14 days, the amount of apatite deposition soared clearly and thereby a thick layer of apatite with Ca/P ratio of 2.4 was developed on Ta_2O_5 NTs (Figure 4.49e to h). Consistent with previous studies (Huang et al., 2010), the EDS pattern shows that the deposited layer is a type of carbonated apatite containing calcium, phosphorus, oxygen, and carbon as the main constituents. To validate the *in-vitro* bioactivity, apatite-inducing ability of the annealed sample was also tested by using a different SBF solution for 14 days according to the method described by Tas (Bayraktar et al., 1999). It was found that very thick apatite deposition composed of large agglomerates with a chemical composition similar to previous sample (Ohtsuki et al., 1992) was formed on Ta_2O_5 NTs (Ca/P ratio of 1.88). There was no significant difference in the apatite formation on the nanotubular arrays in Tas-SBF solution relative to Kokubo method. During the early stage of immersion in SBF, the nanotubes surface straightly contacted with the SBF, so wettability can have a major impact on the formation of apatite layer. After that, the surface of nanotubes progressively changed to the as-deposited apatite surface, which is in direct contact with SBF. Consequently, the wettability effects on the development of apatite layer formation is weakened (Huang et al., 2010).

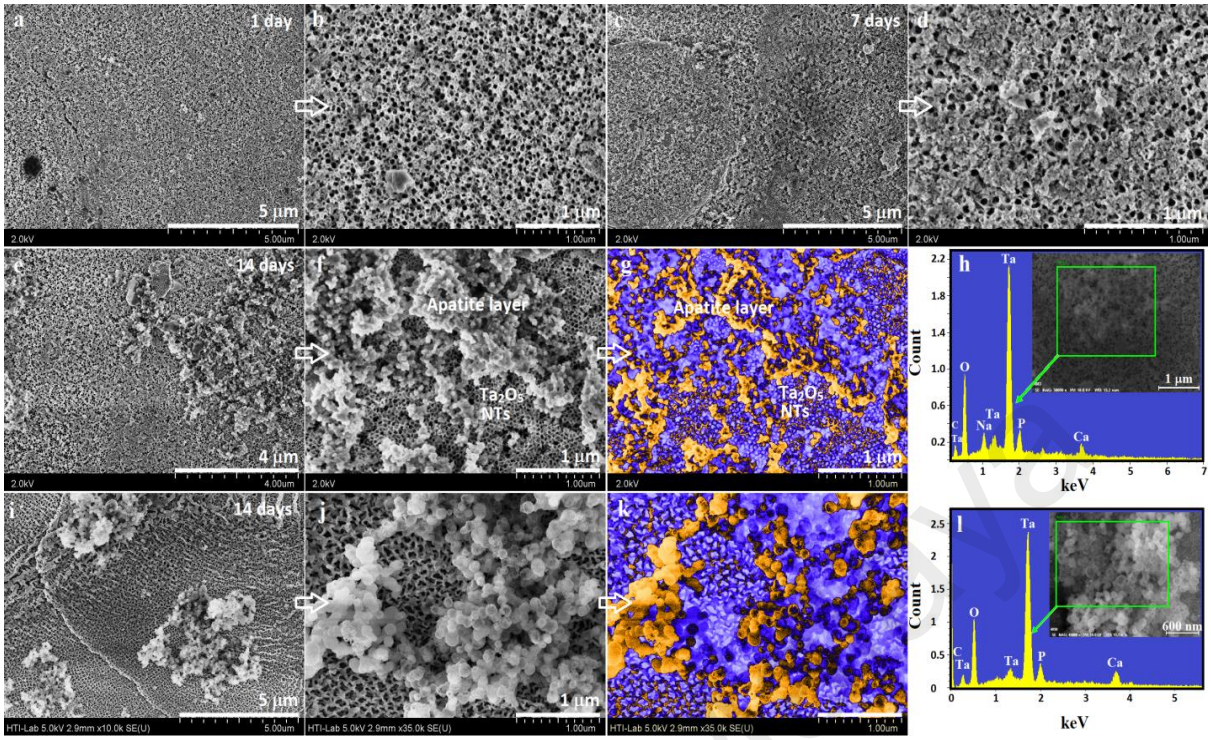

Figure 4.49: Surface morphologies and EDS results of the 450 °C annealed sample after exposure to Kokubo-SBF for (a,b) 1, (c,d) 7, and (e–h) 14 days as well as to (i–l) Tas-SBF for 14 days.

Moreover, the implant ability to stimulate generation of a bone-like apatite layer is considered as a key feature for a rapid bone rehabilitation. The FESEM images of the Ta_2O_5 NTs-Ag_2O NPs soaked in SBF for 1, 7, and 14 days are given in Figure 4.50. A dense precipitate with increasing quantity over the soaking time could be observed on surface of Ta_2O_5 NTs-Ag_2O NPs. The EDS analysis of these precipitates (Figure 4.50h and Table 4.8) indicated a Ca/P atomic ratio of approximately 1.61, which is close to the stoichiometric molar ratio of hydroxyapatite (1.67). It is believed that the long Ta_2O_5 NTs with wide openings could increase the nucleation sites for formation and ingrowth of calcium and phosphorous species, resulting in uniform and thick apatite layers on the implant surface (Siriphannon et al., 2002). Moreover, a relatively high wettability of Ta_2O_5 NTs-Ag_2O NPs in contrast to that of flat substrate may favor the apatite formation. These indicate the capability of Ta_2O_5 NTs-Ag_2O NPs to promote hydroxyapatite

formation and bone growth, thus provide improved implant fixation. In a nutshell, although it is very important to know whether and how such nanotubular surface modification can improve biofuctionallity of metallic implants in biological systems, it is beyond the scope of the present study as we principally focus here on the fabrication and nanostructural characterization of the modified surfaces. More efforts are being implemented to find out the optimum conditions for bioactivity and biocompatibility.

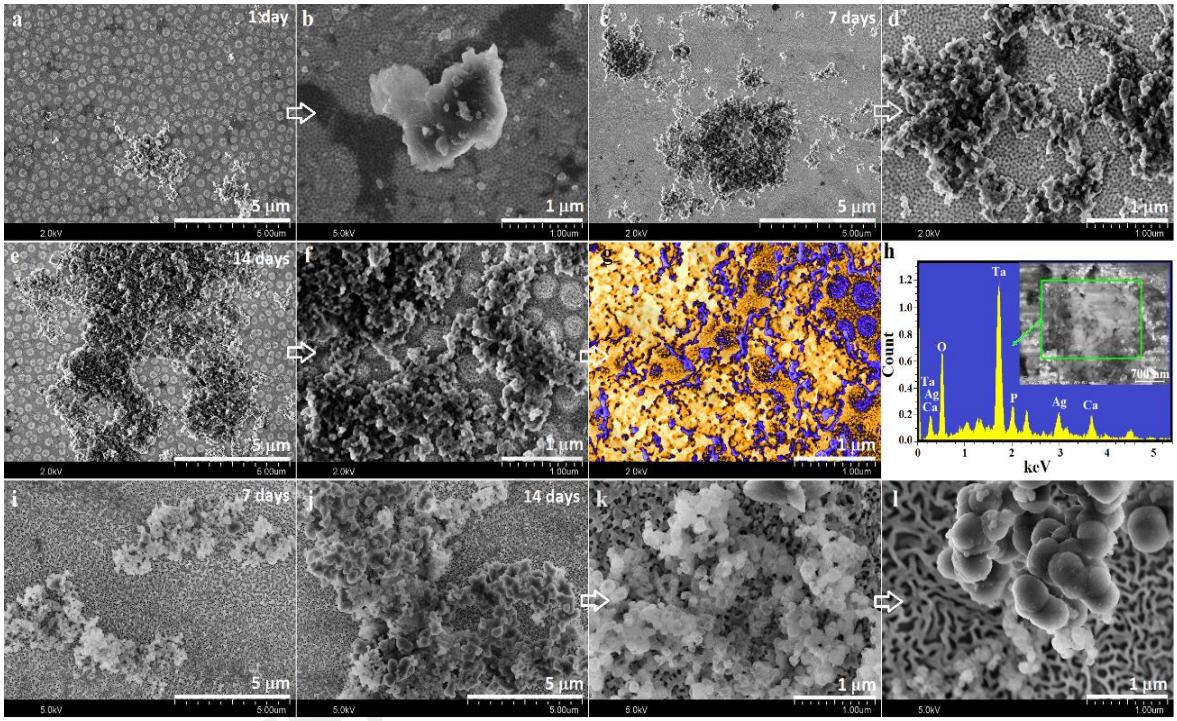

Figure 4.50: FESEM images and EDS analysis of Ta_2O_5 NTs-Ag_2O NPs after exposure to Kokubo-SBF for (a,b) 1days, (c,d) 7days, and (e-h) 14 days soaking in the SBF solution as well as to (i–l) Tas-SBF for 14 days.

Table 4.8: The elemental composition of Ta_2O_5 NTs-Ag_2O NPs coating and the precipitate formed after immersion in SBF for 14 days.

Element	Normalized Weight Ratio (%)	Atomic Ratio (%)
O	28.9	70.07
Ta	52.8	11.28
Ag	1.3	0.50
Ca	11.5	11.20
P	5.5	6.95
Total:	100	100

4.2.14 Antibacterial Activity

The antibacterial activities of pure Ta, annealed Ta_2O_5 NTs, and Ta_2O_5-Ag_2O NPs films against *E.coli* are shown in Figure 4.51. *E.coli* is recognized as the common pathogen in biomaterial-associated infections (Danese et al., 2002). From the results obtained, the control (pure Ti) and pure Ta could not exert antimicrobial activity against *E.coli* within 24 hours. In contrast, the annealed Ta_2O_5 NTs and Ta_2O_5 NTs-Ag_2O NPs significantly reduced the viability of *E.coli* cells within 2 hours ($P < 0.001$) without allowing bacteria re-growth after 24 hours of incubation. In order to compare the antibacterial effectively of Ta_2O_5 NTs and Ta_2O_5 NTs-Ag_2O NPs films, the specimens were sterilized and subjected to secondary antibacterial investigations. In contrast to Ta_2O_5 NTs-Ag_2O NPs, the annealed Ta_2O_5 NTs showed loss of antibacterial activity after sterilization, suggesting the role of Ag_2O NPs in achieving effective and long lasting antibacterial activity (Gao et al., 2014).

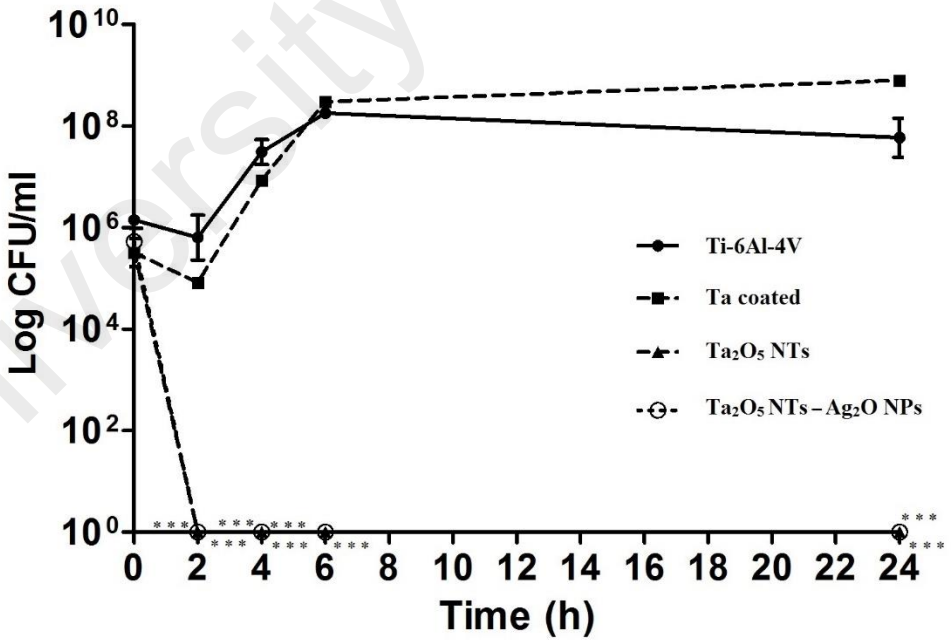

Figure 4.51: The antibacterial activities of Ti-6Al-4V substrate as well as the Ta, Ta_2O_5 NTs, and Ta_2O_5 NTs-Ag_2O NPs films against *E.coli* ATCC 25922.

The enhanced antibacterial activity of Ta_2O_5 NTs-Ag_2O NPs could be attributable to the synergistic effect of Ta_2O_5 NTs, the released Ag^+ ions, and direct contact with Ag_2O NPs (Gao et al., 2014; Juan et al., 2010). It has been reported that Ag_2O NPs possess a large total surface to volume ratio, which provides a relatively high contact area with microorganisms. The Ag_2O NPs could provide sufficient degrees of bacterial cell damage via penetration or attachment of Ag^+ ions to the bacterial cell membranes, while reducing the negative effects on the function of surrounding mammalian cells in contrast to the pure Ag NPs (Morones et al., 2005; Sondi et al., 2004).

4.2.15 HOb Morphology and Adhesion

Figures 4.52 shows the FESEM images of HOb cells cultured on the Ta_2O_5 NTs-Ag_2O NPs after 1, 3, and 7 days of culture. As disclosed in low-magnification images, at day 1 the majority of cells were still spherical without exhibition of cluster formation on the surfaces. In contrast at day 3, the cells showed a spreading morphology with increased cluster formation as well as a typical osteoblastic shape, indicating the positive impact of nanotopography on induction of typical phenotypic behavior for osteoblasts. The high-magnification images illustrate abundant pronounced finger-like protrusions and extensive filopodial activity by HOb cells to interact with the NTs. The finger-like filopodia are a cell-sensing parts which can detect both chemical and nano-topographical cues (Frandsen et al., 2014). The presence of many filopodia on the NT surfaces indicates that the HOb cells are relatively activated by the NT architecture. Although the cell spreading at day 7 was generally higher than days 1 and 3, no significant difference in cell morphology could be observed at this time interval compared to those observed at day 3. The CLSM results (Figure 4.53) also showed a uniform cell distribution on the NT surfaces with increasing population over the examined interval.

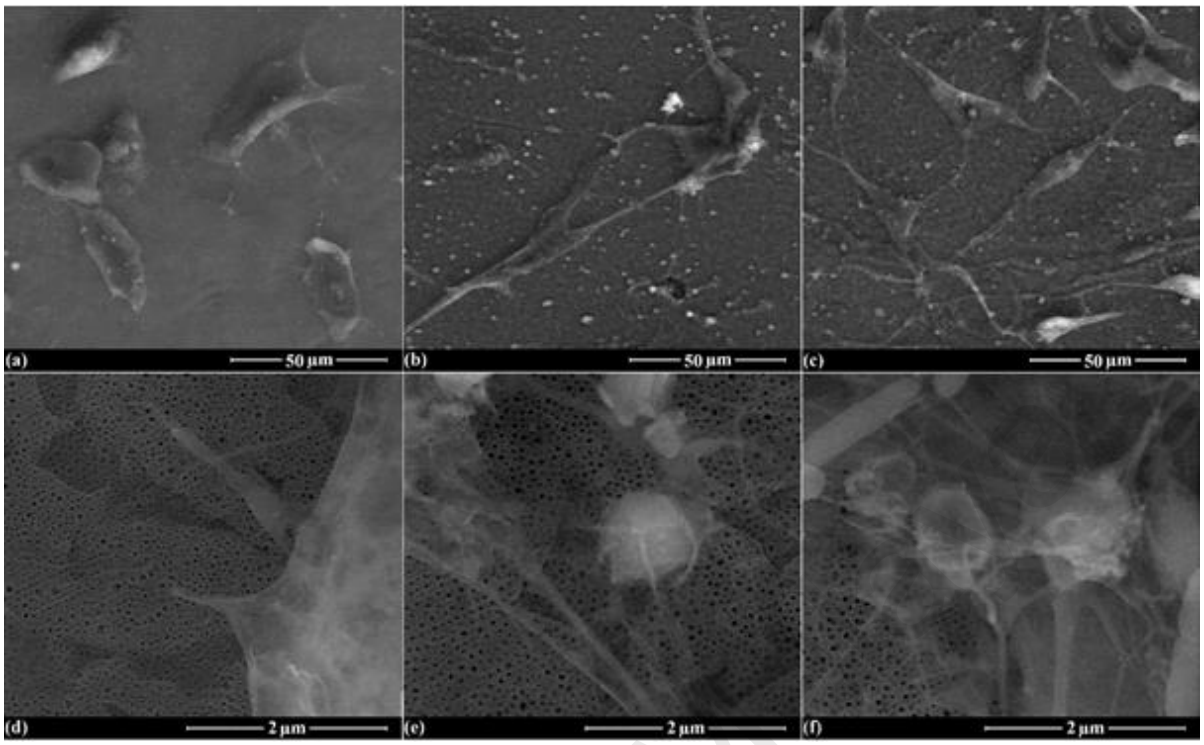

Figure 4.52: The FESEM images of HOb cells after culturing for a,d,) 1, b,e,) 3, and c,f,) 7 days on the Ta_2O_5 NTs-Ag_2O NPs surface

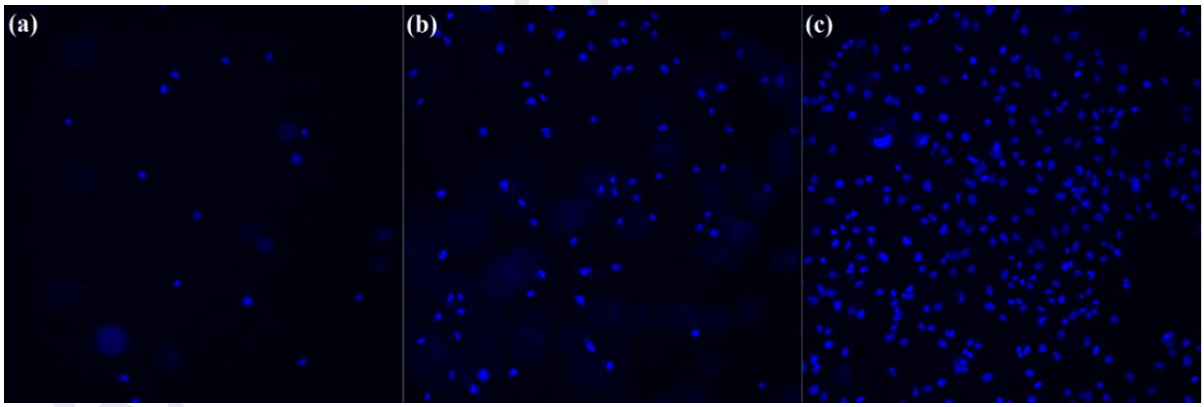

Figure 4.53: The confocal laser scanning images of the stained HOb cells after culturing for a) 1, b) 3, and c) 7 days on the Ta_2O_5 NT-Ag_2O NPs.

4.2.16 Cell Viability and Proliferation

A higher adhesion on the surface does not necessarily indicate the cell viability and functionality. The alamar blue assay is known as an effective indicator of cell metabolism, which allows to quantify the viability of human, animal, plant, bacteria, and fungi cell lines. The alamar blue reagent contains non-toxic, weakly-fluorescent, cell-permeable,

and blue-colored resazurin as the active ingredient, which is reduced to highly-fluorescent and red-colored resorufin in the reducing environment of living cells. During exposure to the alamar blue reagent, the viable cells continuously reduce resazurin to resorufin, altering the fluorescence properties and color of the surrounding media (Rampersad et al., 2012).

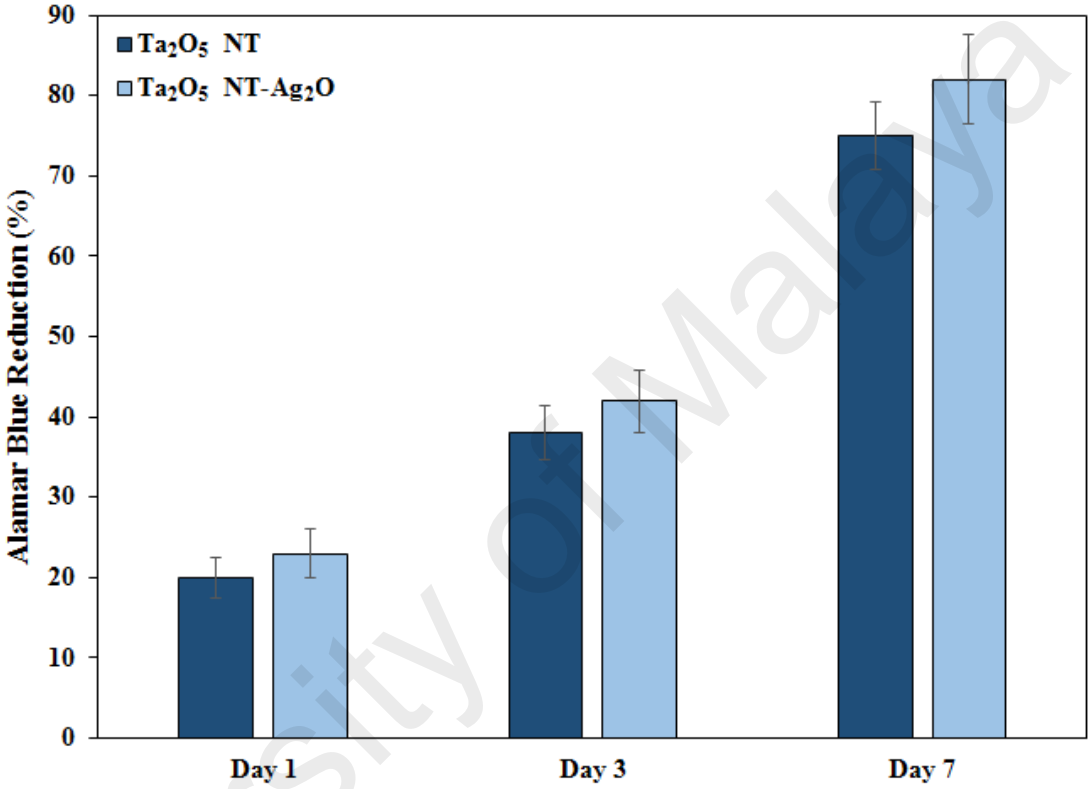

Figure 4.54: The reduced ratio of alamar blue for HOb cells after 1, 3 and 7 days of culturing on the Ta_2O_5 NTs and Ta_2O_5 NTs-Ag_2O NPs.

The obtained alamar blue results of the HOb cells attached on the Ta_2O_5 NTs and Ta_2O_5 NTs- Ag_2O NPs films after 1, 3, and 7 days (Figure 4.54) were consistent with the CLSM images of the stained cells, showing the continuous proliferation of HOb cells throughout the culture time. In addition, the absorbance values of the HOb cells cultured on the Ta_2O_5 NTs and Ta_2O_5 NTs-Ag_2O NPs were not statistically different ($p < 0.05$) at all examined culture periods, confirming the negligible effect of Ag_2O NPs on the cell viability.

CHAPTER 5: CONCLUSIONS AND SUGGESTIONS FOR FUTURE WORK

5.1 Conclusion

In the present work, TiO_2 and Ta_2O_5 NTs with decorated Ag_2O NPs were successfully synthesized on the Ti-6Al-4V alloy, followed by optimization of their mechanical and biological behavior for orthopedic applications. Systematic investigation revealed an improved adhesion between substrate and thin films, scratch hardness, surface hardness, wear, roughness, corrosion resistance, wettability, *in-vitro* bioactivity, antibacterial activity, and biological behavior of the Ti–6Al–4V alloy. The *in-vitro* biocompatibility studies suggest a non-cytotoxic response with a positive influence on cell activity. The specific conclusions on performance of these products have been listed as follows:

5.1.1 Fabrication, Mechanical, Tribological and Corrosion Behaviors of TiO_2 NTs on Ti-6AL-4V

1. Anodization in an electrolyte containing 0.2 M H_3PO_4 and 0.4 M NH_4F with constant potential of 20 V for 4 h was found the optimal condition to fabricate highly ordered and uniform TiO_2 NTs with diameter and length of 72 nm and 1 µm. To investigate the effect of the subsequent heat treatment on the microstructural evolution, annealing was done at 500 and 700 °C for 1.5 h.
2. Collapse and coarsening of the TiO_2 NTs occurred at temperature above 500 °C and increased as the elevated annealing temperature up to 700 °C.
3. The adhesion strength of the anodized sample before and after annealing at 500 °C was 862.06 and 1814.28 mN, respectively. The calculated friction and

COF before annealing were 250.88 mN and 0.29 and after annealing were changed to 381.89 mN and 0.21, respectively.

4. The scratch hardness of the anodized sample before and after annealing was 0.45 and 5.86 GPa, respectively. These results show that after annealing, the scratch hardness increases by over an order of magnitude compared to the untreated sample.

5. During annealing at 500 °C, a transition from an amorphous (anodized sample) to a highly crystalline structure occurred, and consequently, the substrate surface hardness was increased from 269 to 435 HV (62% improvement).

6. The results of tribological evaluation showed that the COF values ranging from 0.133 to 0.280 in normal load of 15 N. However, as the normal load raised to 20 and 25 N, higher COF values ranging from 0.156 to 0.314 were observed. The results showed that the COF significantly decreased after subsequent annealing. According to AFM results, the average roughness value inside the wear tracks of the sample annealed at 500 °C was 140.4 nm, which was nearly two times less than the value measured for the substrate (300.7 nm).

7. The results of *in-vitro* corrosion tests indicated that the samples annealed at 500 °C had a significant improvement over corrosion rate compare to the substrate.

5.1.2 Fabrication, Mechanical, Tribological and Corrosion Behaviors of Ta_2O_5 NTs on Ti-6AL-4V

1. An optimization study on the PVD magnetron sputtering conditions using the Taguchi method suggested a DC power of 350 W, temperature of 250 °C, and a deposition time of 6 h for obtaining the highest adhesion strength.

2. The optimized sample under the applied load gave an adhesion strength of 2154 mN. The friction and COF for the optimized sample with the highest adhesion were 1356 mN and 0.59, respectively.

3. The optimized parameters of the two-step anodization approach applied for growing Ta_2O_5 NTs on the substrate were an H_2SO_4: HF (99:1) + 5% EG electrolyte and a constant potential of 15 V from 30 s to 20 min. The anodic oxide films grown for 5 min, showed strong adhesion and full coverage of the underlying Ta with diameter and length of 40 nm and 1 µm, respectively.

4. To improve the coating adhesion, thermal annealing process was done in the temperature range of 450-1000 °C for 1 h in atmospheric pressure. The results showed that heat treatment at 450 °C was the most favorable regimen, resulting in an adhesion strength, calculated friction and COF of 2301 mN, 1056 mN, and 0.56, respectively.

5. The scratch hardness of the annealed coating (2.9 GPa) was higher than that of the as-deposited thin film (1.8 GPa).

6. The surface hardness of the annealed coating (356 HV) was almost 35% higher than the bare substrate.

7. During the wear tests, all specimens stayed stable under 15 N load and showed COF values in the range of 0.106 to 0.279. However, when the normal load increased to 20 and 25 N, higher COF in the range of 0.107 to 0.297 and 0.110 to 0.314 were perceived, respectively. After AFM assess, R_a values inside the wear tracks of the anodized and annealed samples were nearly 291 and 186 nm, almost 27 and 53% respectively less than the value measured for the substrate (397 nm).

8. The results of corrosion studies demonstrated that annealing at 450 °C led to a significant improvement in *P.E.* (99%).

5.1.3 Decoration of Ag_2O NPs on the TiO_2 NTs and Ta_2O_5 NTs

For improving the antibacterial properties of the coatings, the Ag_2O nanoparticles were decorated on the TiO_2 NTs edges via PVD magnetron sputtering approach with optimum time of 30 sec moreover, the Ag_2O nanoparticles were decorated on the Ta_2O_5 NTs edges via PVD magnetron sputtering approach with optimum time of 10 sec.

5.1.4 Antibacterial, Osseointegration, and Biocompatibility of TiO_2 NTs-Ag_2O NPs and Ta_2O_5 NTs-Ag_2O NPs films

1. The fabricated TiO_2 NTs-Ag_2O NPs and Ta_2O_5 NTs-Ag_2O NPs showed sufficient antibacterial effect against *Escherichia coli* and 100% eradicated the bacterial cells within 2 hours.
2. Due to the formation of a highly ordered TiO_2 NTs- Ag_2O NPs sample, an improvement in hydrophilicity was observed and the contact angle noticeably declined from $\theta = 72.8°$ (the substrate) to $\theta = 17.3°$ as well as the contact angle value of Ta_2O_5 NTs- Ag_2O NPs sample reached to 38.4°.
3. The results of SBF test showed that Ca/P ratio of TiO_2 NTs-Ag_2O NPs sample is 1.57 as well as Ta_2O_5 NTs-Ag_2O NPs sample is 1.61 which are close to the stoichiometric molar ratio of hydroxyapatite (1.67).
4. The bioactivity test and culture of human osteoblast cells on TiO_2 NTs-Ag_2O NPs and Ta_2O_5 NTs-Ag_2O NPs showed that the coated surfaces could promote matrix mineralization and bone-nodule formation, indicating that a surface chemistry modification superimposed onto nanotopographies could provide an additional benefit to the bone growth behavior.

5.2 Suggestions for Future Work

The aim of the current research was to explore the potential of thin films of TiO_2 and Ta_2O_5 nanotubular arrays with decorated Ag_2O nanoparticles on Ti–6AL–4V alloy for improved mechanical and biological behavior for biomedical implants. The criteria for judgment was the effect of TiO_2 and Ta_2O_5 nanotubular arrays with decorated Ag_2O nanoparticleson mechanical and biological behavior of the Ti–6AL–4V alloy and reducing the delamination and cracking of their ceramics by optimization conditions. The findings of this study establish low cost, long-term, high-quality implants for clinical applications. These novel formulations are expected to enhance the quality of life by improving the failure rates, bone integration, and thus the restoration longevity. Moreover, these materials could reduce the overall treatment cost and thus, increase the accessibility of this treatment among the low-income population. The fabrication cost of these implants is significantly less than those of commercialized products, making a great competitive advantage to enter the related market.

Moreover, another novelty of this work is to increase the antibacterial activity by decoration of Ag_2O nanoparticles in edge of nanotubes. This method causes sufficient antibacterial activities while minimizing the amount of Ag_2O concentration on the coating results in a reduction in ions release in the body. Decoration of Ag_2O nanoparticles on the edges of nanotubes instead of its coating preserves the surface porosity, minimizing its adverse effect on osseointegration and coating density.

However, some of the topic need further investigations for the clinical translation of these products included:

- *In-vivo* bioassay and wet tribological properties of well-adherent Ta/Ta_2O_5 nanotube thin film layer with decorated silver oxide nanoparticles on biomedical-graded Ti-6Al-4V

- *In-vivo* bioassay and wet tribological properties of highly ordered TiO_2 nanotube arrays with decorated silver oxide nanoparticles on biomedical-graded Ti-6Al-4V

and finally commercialize of the implants.

REFERENCES

Al-Mobarak, N., & Al-Swayih, A. (2014). Development of titanium surgery implants for improving osseointegration through formation of a titanium nanotube layer. *Int. J. Electrochem. Sc, 9*, 32-45.

Albu, S. P., Ghicov, A., Aldabergenova, S., Drechsel, P., LeClere, D., Thompson, G. E., Macak, J. M., & Schmuki, P. (2008). Formation of Double-Walled TiO2 Nanotubes and Robust Anatase Membranes. *Advanced Materials, 20*(21), 4135-4139.

Allam, N. K., Feng, X. J., & Grimes, C. A. (2008). Self-assembled fabrication of vertically oriented Ta_2O_5 nanotube arrays, and membranes thereof, by one-step tantalum anodization. *Chemistry of Materials, 20*(20), 6477-6481.

Ambard, A. J., & Mueninghoff, L. (2006). Calcium phosphate cement: review of mechanical and biological properties. *Journal of Prosthodontics, 15*(5), 321-328.

Anselme, K. (2000). Osteoblast adhesion on biomaterials. *Biomaterials, 21*(7), 667-681.

Antony, R. P., Mathews, T., Ramesh, C., Murugesan, N., Dasgupta, A., Dhara, S., Dash, S., & Tyagi, A. (2012). Efficient photocatalytic hydrogen generation by Pt modified TiO 2 nanotubes fabricated by rapid breakdown anodization. *International Journal of Hydrogen Energy, 37*(10), 8268-8276.

Aouadi, & S. M., S., D. M., Rohde, S. L. Wong, K. C. Mitchell, K. A. (2001). Growth and characterization of Cr_2N/CrN multilayer coatings. *Surface and Coatings Technology, 140(3)* 269-277.

Aronov, D., Karlov, A., & Rosenman, G. (2007). Hydroxyapatite nanoceramics: Basic physical properties and biointerface modification. *Journal of the European Ceramic Society, 27*(13), 4181-4186.

ASTM. (2003). ASTM International, West Conshohocken, PA,.

Astrova, E., Borovinskaya, T., Tkachenko, A., Balakrishnan, S., Perova, T., Rafferty, A., & Gun'ko, Y. (2004). Morphology of macro-pores formed by electrochemical etching of p-type Si. *Journal of Micromechanics and Microengineering, 14*(7), 1022.

Balagna, C., Faga, M., & Spriano, S. (2012). Tantalum-based multilayer coating on cobalt alloys in total hip and knee replacement. *Materials Science and Engineering: C, 32*(4), 887-895.

Balakrishnan, M., & Narayanan, R. (2013). Synthesis of anodic titania nanotubes in Na 2 SO_4/NaF electrolyte: a comparison between anodization time and specimens with biomaterial based approaches. *Thin Solid Films, 540*, 23-30.

Balasundaram, T., & Raja, K. (2016). Growth And Characterization Of Titanium Nanotubes Anode For Solar Cell Application By Electrochemical Anodization Method. *Int J Adv Engg Tech/Vol. VII/Issue II/April-June, 359*, 363.

Balaur, E., Macak, J. M., Taveira, L., & Schmuki, P. (2005). Tailoring the wettability of TiO_2 nanotube layers. *Electrochemistry communications, 7*(10), 1066-1070.

Balla, Krishna, V., Banerjee, S., Bose, S., & Bandyopadhyay, A. (2010a). Direct laser processing of a tantalum coating on titanium for bone replacement structures. *Acta Biomaterialia, 6*(6), 2329-2334.

Balla, Krishna, V., Bose, S., Davies, N. M., & Bandyopadhyay, A. (2010b). Tantalum—A bioactive metal for implants. *Jom, 62*(7), 61-64.

Banerjee, S., Mohapatra, S. K., & Misra, M. (2009). Synthesis of TaON nanotube arrays by sonoelectrochemical anodization followed by nitridation: a novel catalyst for photoelectrochemical hydrogen generation from water. *Chemical Communications*(46), 7137-7139.

Baradaran, S, Basirun, W., Zalnezhad, E., Hamdi, M., Sarhan, A. A., & Alias, Y. (2013). Fabrication and deformation behaviour of multilayer Al_2O_3/Ti/TiO_2 nanotube arrays. *Journal of the mechanical behavior of biomedical materials, 20*, 272-282.

Baradaran, S., Zalnezhad, E., Basirun, W., Hamouda, A., Sookhakian, M., Sarhan, A. A., & Alias, Y. (2014). Statistical optimization and fretting fatigue study of Zr/ZrO_2 nanotubular array coating on Ti–6Al–4V. *Surface and Coatings Technology, 258*, 979-990.

Baram, N., & Ein-Eli, Y. (2010). Electrochemical impedance spectroscopy of porous TiO2 for photocatalytic applications. *The Journal of Physical Chemistry C, 114*(21), 9781-9790.

Barton, J. E., Stender, C. L., Li, P., & Odom, T. W. (2009). Structural control of anodized tantalum oxide nanotubes. *Journal of Materials Chemistry, 19*(28), 4896-4898.

Bauer, S., Park, J., von der Mark, K., & Schmuki, P. (2008). Improved attachment of mesenchymal stem cells on super-hydrophobic TiO_2 nanotubes. *Acta Biomaterialia, 4*(5), 1576-1582.

Bayraktar, D., & Tas, A. C. (1999). Chemical preparation of carbonated calcium hydroxyapatite powders at 37 °C in urea-containing synthetic body fluids. *Journal of the European Ceramic Society, 19*(13), 2573-2579.

Bobyn, J., Pilliar, R., Cameron, H., & Weatherly, G. (1980). The optimum pore size for the fixation of porous-surfaced metal implants by the ingrowth of bone. *Clinical orthopaedics and related research, 150*, 263-270.

Boehlert, C., Cowen, C., Quast, J., Akahori, T., & Niinomi, M. (2008). Fatigue and wear evaluation of Ti-Al-Nb alloys for biomedical applications. *Materials Science and Engineering: C, 28*(3), 323-330.

Brammer, K. S., Oh, S., Gallagher, J. O., & Jin, S. (2008). Enhanced cellular mobility guided by TiO_2 nanotube surfaces. *Nano letters, 8*(3), 786-793.

Budinski, K. G. (1991). Tribological properties of titanium alloys. *Wear, 151*(2), 203-217.

Bushroa, A., Masjuki, H., Muhamad, M., & Beake, B. (2011). Optimized scratch adhesion for TiSiN coatings deposited by a combination of DC and RF sputtering. *Surface and Coatings Technology, 206*(7), 1837-1844.

Cai, Q., Paulose, M., Varghese, O. K., & Grimes, C. A. (2005). The effect of electrolyte composition on the fabrication of self-organized titanium oxide nanotube arrays by anodic oxidation. *Journal of Materials Research, 20*(1), 230-236.

Capellato, P., Riedel, N. A., Williams, J. D., Machado, J. P., Popat, K. C., & Claro, A. P. A. (2013). Surface Modification on Ti-30Ta Alloy for Biomedical Application. *Engineering, 5*(09), 707.

Clem, W. C., Chowdhury, S., Catledge, S. A., Weimer, J. J., Shaikh, F. M., Hennessy, K. M., Konovalov, V. V., Hill, M. R., Waterfeld, A., & Bellis, S. L. (2008). Mesenchymal stem cell interaction with ultra-smooth nanostructured diamond for wear-resistant orthopaedic implants. *Biomaterials, 29*(24), 3461-3468.

Crawford, GA, Chawla, N., Das, K., Bose, S., & Bandyopadhyay, A. (2007). Microstructure and deformation behavior of biocompatible TiO_2 nanotubes on titanium substrate. *Acta Biomaterialia, 3*(3), 359-367.

Danese, & N, P. (2002). Antibiofilm approaches: prevention of catheter colonization. *Chemistry & biology, 9*(8), 873-880.

Das, K., Bose, S., & Bandyopadhyay, A. (2009). TiO_2 nanotubes on Ti: influence of nanoscale morphology on bone cell–materials interaction. *Journal of Biomedical Materials Research Part A, 90*(1), 225-237.

De Tacconi, N., Chenthamarakshan, C., Yogeeswaran, G., Watcharenwong, A., De Zoysa, R., Basit, N., & Rajeshwar, K. (2006). Nanoporous TiO_2 and WO_3 films by anodization of titanium and tungsten substrates: influence of process variables on morphology and photoelectrochemical response. *The Journal of Physical Chemistry B, 110*(50), 25347-25355.

Ding, S. J., Ju, C. P., & Lin, J. H. C. (1999). Immersion behavior of RF magnetron-assisted sputtered hydroxyapatite/titanium coatings in simulated body fluid. *Journal of biomedical materials research, 47*(4), 551-563.

Donkov, N., Zykova, A., Safonov, V., & Matveev, E. (2009). Modern Methods of Ta2O5 coatings deposition for biomedical applications. *Plasma Physics, 1*, 153-155.

El-Sayed, A, H., & Birss, V. I. (2010). Controlled growth and monitoring of tantalum oxide nanostructures. *Nanoscale, 2*(5), 793-798.

El-Sayed, & Birss, V. I. (2009). Controlled interconversion of nanoarray of Ta dimples and high aspect ratio Ta oxide nanotubes. *Nano letters, 9*(4), 1350-1355.

El-Sayed, Singh, S., & Kruse, P. (2007). Formation of dimpled tantalum surfaces from electropolishing. *Journal of The Electrochemical Society, 154*(12), C728-C732.

Elias, C. N., Oshida, Y., Lima, J. H. C., & Muller, C. A. (2008). Relationship between surface properties (roughness, wettability and morphology) of titanium and dental

implant removal torque. *Journal of the Mechanical Behavior of Biomedical Materials, 1*(3), 234-242.

Ezazi, M., Quazi, M., Zalnezhad, E., & Sarhan, A. A. (2014). Enhancing the tribo-mechanical properties of aerospace AL7075-T6 by magnetron-sputtered Ti/TiN, Cr/CrN & TiCr/TiCrN thin film ceramic coatings. *Ceramics International, 40*(10), 15603-15615.

Fauchais, P., & Vardelle, A. (2012). Thermal sprayed coatings used against corrosion and corrosive wear: *INTECH Open Access Publishe*r.

Frandsen, C. J., Brammer, K. S., Noh, K., Johnston, G., & Jin, S. (2014). Tantalum coating on TiO_2 nanotubes induces superior rate of matrix mineralization and osteofunctionality in human osteoblasts. *Materials Science and Engineering: C, 37*, 332-341.

Gao, Ang, Hang, R., Huang, X., Zhao, L., Zhang, X., Wang, L., Tang, B., Ma, S., & Chu, P. K. (2014). The effects of titania nanotubes with embedded silver oxide nanoparticles on bacteria and osteoblasts. *Biomaterials, 35*(13), 4223-4235.

Ghani, J., Choudhury, I., & Hassan, H. (2004). Application of Taguchi method in the optimization of end milling parameters. *Journal of Materials Processing Technology, 145*(1), 84-92.

Ghicov, A., Tsuchiya, H., Macak, J. M., & Schmuki, P. (2006). Annealing effects on the photoresponse of TiO_2 nanotubes. *physica status solidi (a), 203*(4), R28-R30.

Gonçalves, R. V., Migowski, P., Wender, H., Eberhardt, D., Weibel, D. E., Sonaglio, F. C., Zapata, M. J., Dupont, J., Feil, A. F., & Teixeira, S. R. (2012). Ta_2O_5 nanotubes obtained by anodization: effect of thermal treatment on the photocatalytic activity for hydrogen production. *The Journal of Physical Chemistry C, 116*(26), 14022-14030.

Gonçalves, R. V., Wojcieszak, R., Uberman, P. M., Teixeira, S. R., & Rossi, L. M. (2014). Insights into the active surface species formed on Ta_2O_5 nanotubes in the catalytic oxidation of CO. *Physical Chemistry Chemical Physics, 16*(12), 5755-5762.

Gong, Dawei, Grimes, C. A., Varghese, O. K., Hu, W., Singh, R., Chen, Z., & Dickey, E. C. (2001). Titanium oxide nanotube arrays prepared by anodic oxidation. *Journal of Materials Research, 16*(12), 3331-3334.

Goudarzi, M., Batmanghelich, F., Afshar, A., Dolati, A., & Mortazavi, G. (2014). Development of electrophoretically deposited hydroxyapatite coatings on anodized nanotubular TiO_2 structures: corrosion and sintering temperature. *Applied Surface Science, 301*, 250-257.

Grimes, A, C., & Mor, G. K. (2009). TiO_2 nanotube arrays: synthesis, properties, and applications: *Springer Science & Business Media*.

Gu, X., Zheng, Y., Cheng, Y., Zhong, S., & Xi, T. (2009). In vitro corrosion and biocompatibility of binary magnesium alloys. *Biomaterials, 30*(4), 484-498.

Guleryuz, H., & Cimenoglu, H. (2005). Surface modification of a Ti–6Al–4V alloy by thermal oxidation. *Surface and Coatings Technology, 192*(2), 164-170.

Guo, P., Xue, Y., Huang, C., Xia, Z., Zhang, G., & Fu, Z. (2009). Optical Properties and Elemental Composition of Ta_2O_5 Thin Films. *Paper presented at the 2009 Symposium on Photonics and Optoelectronics.*

Habibovic, P., Sees, T. M., van den Doel, M. A., van Blitterswijk, C. A., & de Groot, K. (2006). Osteoinduction by biomaterials—physicochemical and structural influences. *Journal of Biomedical Materials Research Part A, 77*(4), 747-762.

Hahn, R., Macak, J., & Schmuki, P. (2007). Rapid anodic growth of TiO_2 and WO_3 nanotubes in fluoride free electrolytes. *Electrochemistry communications, 9*(5), 947-952.

Hayden, S. C., Allam, N. K., & El-Sayed, M. A. (2010). TiO_2 nanotube/CdS hybrid electrodes: extraordinary enhancement in the inactivation of Escherichia coli. *Journal of the American Chemical Society, 132*(41), 14406-14408.

He, Z., Xiao, J., Xia, F., Kajiyoshi, K., Samart, C., & Zhang, H. (2014). Enhanced solar water-splitting performance of TiO_2 nanotube arrays by annealing and quenching. *Applied Surface Science, 313*, 633-639.

Horwood, A, C., El-Sayed, H., & Birss, V. I. (2011). Ta_2O_5 Nanotube Templates for Amperometric Glucose Biosensors. *Paper presented at the Meeting Abstracts*.

Horwood, CA, El-Sayed, H., & Birss, V. (2014). Precise electrochemical prediction of short tantalum oxide nanotube length. *Electrochimica Acta, 132*, 91-97.

Hsieh, M.-F., Perng, L.-H., & Chin, T.-S. (2002). Hydroxyapatite coating on Ti-6Al-4V alloy using a sol–gel derived precursor. *Materials chemistry and physics, 74*(3), 245-250.

Huang, Lin, Ning, C.-Q., Ding, D.-Y., Bai, S., Qin, R., Li, M., & Mao, D.-L. (2010). Wettability and in vitro bioactivity of doped TiO_2 nanotubes. *J. Inorg. Mater, 25*(775–9).

Hulteen, J. C., & Martin, C. R. (1997). A general template-based method for the preparation of nanomaterials. *Journal of Materials Chemistry, 7*(7), 1075-1087.

Huo, K., Zhang, X., Wang, H., Zhao, L., Liu, X., & Chu, P. K. (2013). Osteogenic activity and antibacterial effects on titanium surfaces modified with Zn-incorporated nanotube arrays. *Biomaterials, 34*(13), 3467-3478.

Jafari, S. M., Bender, B., Coyle, C., Parvizi, J., Sharkey, P. F., & Hozack, W. J. (2010). Do tantalum and titanium cups show similar results in revision hip arthroplasty? *Clinical Orthopaedics and Related Research®, 468*(2), 459-465.

Jaworski, R., Pawlowski, L., Roudet, F., Kozerski, S., & Petit, F. (2008). Characterization of mechanical properties of suspension plasma sprayed TiO_2 coatings using scratch test. *Surface and Coatings Technology, 202*(12), 2644-2653.

Jha, H., Roy, P., Hahn, R., Paramasivam, I., & Schmuki, P. (2011). Fast formation of aligned high-aspect ratio TiO_2 nanotube bundles that lead to increased open circuit voltage when used in dye sensitized solar cells. *Electrochemistry communications, 13*(3), 302-305.

Juan, Liao, Zhimin, Z., Anchun, M., Lei, L., & Jingchao, Z. (2010). Deposition of silver nanoparticles on titanium surface for antibacterial effect. *International journal of nanomedicine, 5*, 261.

Karlinsey, R. L. (2005). Preparation of self-organized niobium oxide microstructures via potentiostatic anodization. *Electrochemistry communications, 7*(12), 1190-1194.

Kato, H., Nakamura, T., Nishiguchi, S., Matsusue, Y., Kobayashi, M., Miyazaki, T., Kim, H. M., & Kokubo, T. (2000). Bonding of alkali-and heat-treated tantalum implants to bone. *Journal of biomedical materials research, 53*(1), 28-35.

Kaur, G., Willsmore, T., Gulati, K., Zinonos, I., Wang, Y., Kurian, M., Hay, S., Losic, D., & Evdokiou, A. (2016). Titanium wire implants with nanotube arrays: A study model for localized cancer treatment. *Biomaterials*.

Kawagoe, K., Saito, M., Shibuya, T., Nakashima, T., Hino, K., & Yoshikawa, H. (2000). Augmentation of cancellous screw fixation with hydroxyapatite composite resin (CAP) in vivo. *Journal of biomedical materials research, 53*(6), 678-684.

Kelly, P., & Arnell, R. (2000). Magnetron sputtering: a review of recent developments and applications. *Vacuum, 56*(3), 159-172.

Kerrec, O., Devilliers, D., Groult, H., & Marcus, P. (1998). Study of dry and electrogenerated Ta_2O_5 and Ta/Ta_2O_5/Pt structures by XPS. *Materials Science and Engineering: B, 55*(1), 134-142.

Khalid, A. (2016). *Tribological behavior of micro/nano structured tantalum surfaces by anodization method*.

Kobayashi, K., & Shimizu, K. (1988). Influence of γ-Alumina on the Structure of Barrier Anodic Oxide Films on Aluminum. *Journal of The Electrochemical Society, 135*(4), 908-910.

Kokubo, T., & Takadama, H. (2006). How useful is SBF in predicting in vivo bone bioactivity? *Biomaterials, 27*(15), 2907-2915.

Krishna, D. S. R., & Sun, Y. (2005). Thermally oxidised rutile-TiO_2 coating on stainless steel for tribological properties and corrosion resistance enhancement. *Applied Surface Science, 252*(4), 1107-1116.

Ku, Y., Fan, Z.-R., Chou, Y.-C., & Wang, W.-Y. (2010). Characterization and induced photocurrent of TiO_2 nanotube arrays fabricated by anodization. *Journal of The Electrochemical Society, 157*(6), H671-H675.

Kummer, K. M., Taylor, E. N., Durmas, N. G., Tarquinio, K. M., Ercan, B., & Webster, T. J. (2013). Effects of different sterilization techniques and varying anodized

TiO_2 nanotube dimensions on bacteria growth. *Journal of Biomedical Materials Research Part B: Applied Biomaterials, 101*(5), 677-688.

Kurella, A., & Dahotre, N. B. (2006). Laser induced multi-scale textured zirconia coating on Ti-6Al-4V. *Journal of Materials Science: Materials in Medicine, 17*(6), 565-572.

Lai, Y., Lin, L., Pan, F., Huang, J., Song, R., Huang, Y., Lin, C., Fuchs, H., & Chi, L. (2013). Bioinspired patterning with extreme wettability contrast on TiO_2 nanotube array surface: a versatile platform for biomedical applications. *Small, 9*(17), 2945-2953.

Lamolle, S. F., Monjo, M., Rubert, M., Haugen, H. J., Lyngstadaas, S. P., & Ellingsen, J. E. (2009). The effect of hydrofluoric acid treatment of titanium surface on nanostructural and chemical changes and the growth of MC3T3-E1 cells. *Biomaterials, 30*(5), 736-742.

Lan, M.-Y., Liu, C.-P., Huang, H.-H., Chang, J.-K., & Lee, S.-W. (2013). Diameter-sensitive biocompatibility of anodic TiO_2 nanotubes treated with supercritical CO_2 fluid. *Nanoscale research letters, 8*(1), 1.

Lee, Woo-Jin, & Smyrl, W. H. (2005). Zirconium oxide nanotubes synthesized via direct electrochemical anodization. *Electrochemical and solid-state letters, 8*(3), B7-B9.

Lee, Woo, & Park, S.-J. (2014). Porous anodic aluminum oxide: anodization and templated synthesis of functional nanostructures. *Chemical Reviews, 114*(15), 7487-7556.

Lee, Young-Hee, Bhattarai, G., Park, I.-S., Kim, G.-R., Kim, G.-E., Lee, M.-H., & Yi, H.-K. (2013). Bone regeneration around N-acetyl cysteine-loaded nanotube titanium dental implant in rat mandible. *Biomaterials, 34*(38), 10199-10208.

LeGeros, R. (1988). Calcium phosphate materials in restorative dentistry: a review. *Advances in dental research, 2*(1), 164-180.

Li, Feiyue, Zhang, L., & Metzger, R. M. (1998). On the growth of highly ordered pores in anodized aluminum oxide. *Chemistry of Materials, 10*(9), 2470-2480.

Li, Hongchao, Tang, N., Yang, H., Leng, X., & Zou, J. (2015). Interface feature characterization and Schottky interfacial layer confirmation of TiO_2 nanotube array film. *Applied Surface Science, 355*, 849-860.

Likodimos, V., Stergiopoulos, T., Falaras, P., Kunze, J., & Schmuki, P. (2008). Phase composition, size, orientation, and antenna effects of self-assembled anodized titania nanotube arrays: a polarized micro-Raman investigation. *The Journal of Physical Chemistry C, 112*(33), 12687-12696.

Liu, X., Chu, P. K., & Ding, C. (2004). Surface modification of titanium, titanium alloys, and related materials for biomedical applications. *Materials Science and Engineering: R: Reports, 47*(3), 49-121.

Liu, X., Chu, P. K., & Ding, C. (2010). Surface nano-functionalization of biomaterials. *Materials Science and Engineering: R: Reports, 70*(3), 275-302.

Lockman, Z., Sreekantan, S., Ismail, S., Schmidt-Mende, L., & MacManus-Driscoll, J. L. (2010). Influence of anodisation voltage on the dimension of titania nanotubes. *Journal of Alloys and Compounds, 503*(2), 359-364.

Lv, L., Liu, Y., Zhang, P., Zhang, X., Liu, J., Chen, T., Su, P., Li, H., & Zhou, Y. (2015). The nanoscale geometry of TiO_2 nanotubes influences the osteogenic differentiation of human adipose-derived stem cells by modulating H_3K_4 trimethylation. *Biomaterials, 39*, 193-205.

Macak, JM, Tsuchiya, H., Ghicov, A., Yasuda, K., Hahn, R., Bauer, S., & Schmuki, P. (2007). TiO_2 nanotubes: self-organized electrochemical formation, properties and applications. *Current Opinion in Solid State and Materials Science, 11*(1), 3-18.

Macak, M, J., Tsuchiya, H., & Schmuki, P. (2005). High-Aspect-Ratio TiO_2 Nanotubes by Anodization of Titanium. *Angewandte Chemie International Edition, 44*(14), 2100-2102.

Mattox, & M, D. (2010). *Handbook of physical vapor deposition (PVD) processing*: William Andrew.

Mazare, A., Totea, G., Burnei, C., Schmuki, P., Demetrescu, I., & Ionita, D. (2016). Corrosion, antibacterial activity and haemocompatibility of TiO_2 nanotubes as a function of their annealing temperature. *Corrosion Science, 103*, 215-222.

Mei, S., Wang, H., Wang, W., Tong, L., Pan, H., Ruan, C., Ma, Q., Liu, M., Yang, H., & Zhang, L. (2014). Antibacterial effects and biocompatibility of titanium surfaces with graded silver incorporation in titania nanotubes. *Biomaterials, 35*(14), 4255-4265.

Minagar, S., Berndt, C. C., Wang, J., Ivanova, E., & Wen, C. (2012). A review of the application of anodization for the fabrication of nanotubes on metal implant surfaces. *Acta Biomaterialia, 8*(8), 2875-2888.

Mohamed, A. E. R., & Rohani, S. (2011). Modified TiO_2 nanotube arrays (TNTAs): progressive strategies towards visible light responsive photoanode, a review. *Energy & Environmental Science, 4*(4), 1065-1086.

Mor, GK, Varghese, O. K., Paulose, M., Mukherjee, N., & Grimes, C. A. (2003). Fabrication of tapered, conical-shaped titania nanotubes. *Journal of Materials Research, 18*(11), 2588-2593.

Mor, K, G., Shankar, K., Paulose, M., Varghese, O. K., & Grimes, C. A. (2005). Enhanced photocleavage of water using titania nanotube arrays. *Nano letters, 5*(1), 191-195.

Mor, K, g., Varghese, O. K., Paulose, M., Shankar, K., & Grimes, C. A. (2006). A review on highly ordered, vertically oriented TiO_2 nanotube arrays: fabrication, material properties, and solar energy applications. *Solar energy materials and solar cells, 90*(14), 2011-2075.

Morones, Ruben, J., Elechiguerra, J. L., Camacho, A., Holt, K., Kouri, J. B., Ramírez, J. T., & Yacaman, M. J. (2005). The bactericidal effect of silver nanoparticles. *Nanotechnology, 16*(10), 2346.

Mour, M., Das, D., Winkler, T., Hoenig, E., Mielke, G., Morlock, M. M., & Schilling, A. F. (2010). Advances in porous biomaterials for dental and orthopaedic applications. *Materials, 3*(5), 2947-2974.

Mubarak, A., Hamzah, E., & Toff, M. (2005). Review of physical vapour deposition (PVD) techniques for hard coating. *Jurnal Mekanikal*(20), 42-51.

Narayan, R. J. (2010). The next generation of biomaterial development. *Philosophical Transactions of the Royal Society of London A: Mathematical, Physical and Engineering Sciences, 368*(1917), 1831-1837.

Narayanan, R., & Seshadri, S. (2007). Phosphoric acid anodization of Ti-6Al-4V Structural and corrosion aspects. *Corrosion Science, 49*(2), 542-558.

Nelea, V., Morosanu, C., Iliescu, M., & Mihailescu, I. (2003). Microstructure and mechanical properties of hydroxyapatite thin films grown by RF magnetron sputtering. *Surface and Coatings Technology, 173*(2), 315-322.

Nischk, M., Mazierski, P., Gazda, M., & Zaleska, A. (2014). Ordered TiO_2 nanotubes: the effect of preparation parameters on the photocatalytic activity in air purification process. *Applied Catalysis B: Environmental, 144*, 674-685.

Nunamaker, D. (1985). Total Joint Replacement. *Textbook of Small Animal Orthopaedics. Philadelphia, PA, Lippincott*.

Oh, Seung-Han, Finones, R. R., Daraio, C., Chen, L.-H., & Jin, S. (2005). Growth of nano-scale hydroxyapatite using chemically treated titanium oxide nanotubes. *Biomaterials, 26*(24), 4938-4943.

Oh, Seunghan, Daraio, C., Chen, L. H., Pisanic, T. R., Finones, R. R., & Jin, S. (2006). Significantly accelerated osteoblast cell growth on aligned TiO_2 nanotubes. *Journal of Biomedical Materials Research Part A, 78*(1), 97-103.

Ohtsuki, C., Kokubo, T., & Yamamuro, T. (1992). Mechanism of apatite formation on CaO-SiO_2-P_2O_5 glasses in a simulated body fluid. *Journal of Non-Crystalline Solids, 143*, 84-92.

Park, J., Bauer, S., Schlegel, K. A., Neukam, F. W., von der Mark, K., & Schmuki, P. (2009). TiO_2 nanotube surfaces: 15 nm—an optimal length scale of surface topography for cell adhesion and differentiation. *Small, 5*(6), 666-671.

Paulose, M., Prakasam, H. E., Varghese, O. K., Peng, L., Popat, K. C., Mor, G. K., Desai, T. A., & Grimes, C. A. (2007). TiO_2 nanotube arrays of 1000 μm length by anodization of titanium foil: phenol red diffusion. *The Journal of Physical Chemistry C, 111*(41), 14992-14997.

Paulose, M., Shankar, K., Yoriya, S., Prakasam, H. E., Varghese, O. K., Mor, G. K., Latempa, T. A., Fitzgerald, A., & Grimes, C. A. (2006). Anodic growth of highly

ordered TiO_2 nanotube arrays to 134 μm in length. *The Journal of Physical Chemistry B, 110*(33), 16179-16184.

Peng, L., Eltgroth, M. L., LaTempa, T. J., Grimes, C. A., & Desai, T. A. (2009a). The effect of TiO_2 nanotubes on endothelial function and smooth muscle proliferation. *Biomaterials, 30*(7), 1268-1272.

Peng, L., Mendelsohn, A. D., LaTempa, T. J., Yoriya, S., Grimes, C. A., & Desai, T. A. (2009b). Long-term small molecule and protein elution from TiO_2 nanotubes. *Nano letters, 9*(5), 1932-1936.

Popat, K. C., Eltgroth, M., LaTempa, T. J., Grimes, C. A., & Desai, T. A. (2007). Decreased Staphylococcus epidermis adhesion and increased osteoblast functionality on antibiotic-loaded titania nanotubes. *Biomaterials, 28*(32), 4880-4888.

Prakasam, H. E., Shankar, K., Paulose, M., Varghese, O. K., & Grimes, C. A. (2007). A new benchmark for TiO_2 nanotube array growth by anodization. *The Journal of Physical Chemistry C, 111*(20), 7235-7241.

Prodana, M., Duta, M., Ionita, D., Bojin, D., Stan, M. S., Dinischiotu, A., & Demetrescu, I. (2015). A new complex ceramic coating with carbon nanotubes, hydroxyapatite and TiO_2 nanotubes on Ti surface for biomedical applications. *Ceramics International, 41*(5), 6318-6325.

Rack, H. J., & Qazi, J. (2006). Titanium alloys for biomedical applications. *Materials Science and Engineering: C, 26*(8), 1269-1277.

Rafieerad, AR, Bushroa, A., Zalnezhad, E., Sarraf, M., Basirun, W., Baradaran, S., & Nasiri-Tabrizi, B. (2015). Microstructural development and corrosion behavior of self-organized TiO_2 nanotubes coated on Ti-6Al-7Nb. *Ceramics International*.

Rahmati, B., Sarhan, A. A., Zalnezhad, E., Kamiab, Z., Dabbagh, A., Choudhury, D., & Abas, W. (2016). Development of tantalum oxide (Ta-O) thin film coating on biomedical Ti-6Al-4V alloy to enhance mechanical properties and biocompatibility. *Ceramics International, 42*(1), 466-480.

Raja, KS, Misra, M., & Paramguru, K. (2005). Formation of self-ordered nano-tubular structure of anodic oxide layer on titanium. *Electrochimica Acta, 51*(1), 154-165.

Rampersad, & , S. N. (2012). Multiple applications of Alamar Blue as an indicator of metabolic function and cellular health in cell viability bioassays. *Sensors, 12*(9), 12347-12360.

Raphel, J., Holodniy, M., Goodman, S. B., & Heilshorn, S. C. (2016). Multifunctional coatings to simultaneously promote osseointegration and prevent infection of orthopaedic implants. *Biomaterials, 84*, 301-314.

Ratnawati, G., Jarnuzi. (2015). Synthesis of TiO_2 Nanotube Arrays by Sonication Aided Anodization and Its Application for Hydrogen Generation from Aqueous Glycerol Solution. *Paper presented at the MATEC Web of Conferences*.

Richter, C., Wu, Z., Panaitescu, E., Willey, R. J., & Menon, L. (2007). Ultra-High-Aspect-Ratio Titania Nanotubes. *Advanced Materials, 19*(7), 946-948.

Rico, V., Borrás, A., Yubero, F., Espinós, J. P., Frutos, F., & González-Elipe, A. n. R. (2009). Wetting angles on illuminated Ta_2O_5 thin films with controlled nanostructure. *The Journal of Physical Chemistry C, 113*(9), 3775-3784.

Roman, I., Trusca, R. D., Soare, M.-L., Fratila, C., Krasicka-Cydzik, E., Stan, M.-S., & Dinischiotu, A. (2014). Titanium dioxide nanotube films: Preparation, characterization and electrochemical biosensitivity towards alkaline phosphatase. *Materials Science and Engineering: C, 37*, 374-382.

Roy, C, S., Paulose, M., & Grimes, C. A. (2007). The effect of TiO_2 nanotubes in the enhancement of blood clotting for the control of hemorrhage. *Biomaterials, 28*(31), 4667-4672.

Roy, Mangal, Balla, V. K., Bose, S., & Bandyopadhyay, A. (2010). Comparison of tantalum and hydroxyapatite coatings on titanium for applications in load bearing implants. *Advanced Engineering Materials, 12*(11), B637-B641.

Ruan, C., Paulose, M., Varghese, O. K., & Grimes, C. A. (2006). Enhanced photoelectrochemical-response in highly ordered TiO_2 nanotube-arrays anodized in boric acid containing electrolyte. *Solar energy materials and solar cells, 90*(9), 1283-1295.

Ruan, C., Paulose, M., Varghese, O. K., Mor, G. K., & Grimes, C. A. (2005). Fabrication of highly ordered TiO_2 nanotube arrays using an organic electrolyte. *The Journal of Physical Chemistry B, 109*(33), 15754-15759.

Ruckh, T., Porter, J. R., Allam, N. K., Feng, X., Grimes, C. A., & Popat, K. C. (2008). Nanostructured tantala as a template for enhanced osseointegration. *Nanotechnology, 20*(4), 045102.

Safonov, V., Zykova, A., Smolik, J., Rogowska, R., Lukyanchenko, V., & Kolesnikov, D. (2014). Modification of implant material surface properties by means of oxide nano-structured coatings deposition. *Applied Surface Science, 310*, 174-179.

Sagomonyants, K. B., Hakim-Zargar, M., Jhaveri, A., Aronow, M. S., & Gronowicz, G. (2011). Porous tantalum stimulates the proliferation and osteogenesis of osteoblasts from elderly female patients. *Journal of Orthopaedic Research, 29*(4), 609-616.

Schmuki, P. (2001). Pits and Pores II: Formation, Properties, and Significance for Advanced Materials: *Proceedings of the International Symposium*.

Schwirn, K., Lee, W., Hillebrand, R., Steinhart, M., Nielsch, K., & Gösele, U. (2008). Self-ordered anodic aluminum oxide formed by H_2SO_4 hard anodization. *Acs Nano, 2*(2), 302-310.

Sekino, T. (2010). Synthesis and applications of titanium oxide nanotubes *Inorganic and Metallic Nanotubular Materials* (pp. 17-32): Springer.

Sekler, J., Steinmann, P., & Hintermann, H. (1988). The scratch test: Different critical load determination techniques. *Surface and Coatings Technology, 36*(1-2), 519-529.

Şennik, E., Çolak, Z., Kılınç, N., & Öztürk, Z. Z. (2010). Synthesis of highly-ordered TiO_2 nanotubes for a hydrogen sensor. *International Journal of Hydrogen Energy, 35*(9), 4420-4427.

Shankar, Karthik, Mor, G. K., Fitzgerald, A., & Grimes, C. A. (2007a). Cation effect on the electrochemical formation of very high aspect ratio TiO_2 nanotube arrays in formamide− water mixtures. *The Journal of Physical Chemistry C, 111*(1), 21-26.

Shankar, Karthik, Mor, G. K., Prakasam, H. E., Yoriya, S., Paulose, M., Varghese, O. K., & Grimes, C. A. (2007b). Highly-ordered TiO_2 nanotube arrays up to 220 μm in length: use in water photoelectrolysis and dye-sensitized solar cells. *Nanotechnology, 18*(6), 065707.

Shi, J., Chen, C., Yu, H., & Zhang, S. (2008). Application of magnetron sputtering for producing bioactive ceramic coatings on implant materials. *Bulletin of Materials Science, 31*(6), 877-884.

Shirazi, F., Moghaddam, E., Mehrali, M., Oshkour, A., Metselaar, H., Kadri, N., Zandi, K., & Abu, N. (2014). In vitro characterization and mechanical properties of β-calcium silicate/POC composite as a bone fixation device. *Journal of Biomedical Materials Research Part A, 102*(11), 3973-3985.

Sieber, & Schmuki, P. (2005). Porous tantalum oxide prepared by electrochemical anodic oxidation. *Journal of The Electrochemical Society, 152*(9), C639-C644.

Singh, Kulwant, Krishnamurthy, N., & Suri, A. (2012). Adhesion and wear studies of magnetron sputtered NbN films. *Tribology International, 50*, 16-25.

Singh, Sherdeep, Greiner, M. T., & Kruse, P. (2007). Robust inorganic membranes from detachable ultrathin tantalum oxide films. *Nano letters, 7*(9), 2676-2683.

Siriphannon, Punnama, Kameshima, Y., Yasumori, A., Okada, K., & Hayashi, S. (2002). Formation of hydroxyapatite on $CaSiO_3$ powders in simulated body fluid. *Journal of the European Ceramic Society, 22*(4), 511-520.

Sobieszczyk, S. (2009). Self-organized nanotubular oxide layers on Ti and Ti alloys. *Advances in Materials Sciences, 9*(2), 25-41.

Sondi, I., & Salopek-Sondi, B. (2004). Silver nanoparticles as antimicrobial agent: a case study on E. coli as a model for Gram-negative bacteria. *Journal of Colloid and Interface Science, 275*(1), 177-182.

Sreekantan, S., Lockman, Z., Hazan, R., Tasbihi, M., Tong, L. K., & Mohamed, A. R. (2009). Influence of electrolyte pH on TiO_2 nanotube formation by Ti anodization. *Journal of Alloys and Compounds, 485*(1), 478-483.

Stachowiak, G. W. (2006). Wear: materials, mechanisms and practice: *John Wiley & Sons*.

Su, Z., Grigorescu, S., Wang, L., Lee, K., & Schmuki, P. (2015). Fast fabrication of Ta_2O_5 nanotube arrays and their conversion to Ta_3N_5 for efficient solar driven water splitting. *Electrochemistry communications, 50*, 15-19.

Sun, Y.-S., Chang, J.-H., & Huang, H.-H. (2013). Corrosion resistance and biocompatibility of titanium surface coated with amorphous tantalum pentoxide. *Thin Solid Films, 528*, 130-135.

Swann, S. (1988). Film thickness distribution in magnetron sputtering. *Vacuum, 38*(8), 791-794.

Tan, A., Pingguan-Murphy, B., Ahmad, R., & Akbar, S. (2012). Review of titania nanotubes: fabrication and cellular response. *Ceramics International, 38*(6), 4421-4435.

Tang, Daniel, Tare, R. S., Yang, L.-Y., Williams, D. F., Ou, K.-L., & Oreffo, R. O. (2016). Biofabrication of bone tissue: approaches, challenges and translation for bone regeneration. *Biomaterials, 83*, 363-382.

Tang, Xinhu, & Li, D. (2009). Fabrication, geometry, and mechanical properties of highly ordered TiO_2 nanotubular arrays. *The Journal of Physical Chemistry C, 113*(17), 7107-7113.

Tomsia, A. P., Saiz, E., Song, J., & Bertozzi, C. R. (2005). Biomimetic bonelike composites and novel bioactive glass coatings. *Advanced Engineering Materials, 7*(11), 999-1004.

Toque, Arre, J., Herliansyah, M. K., Hamdi, M., Ide-Ektessabi, A., & Sopyan, I. (2010). Adhesion failure behavior of sputtered calcium phosphate thin film coatings evaluated using microscratch testing. *Journal of the mechanical behavior of biomedical materials, 3*(4), 324-330.

Tsuchiya, Hiroaki, Macak, J. M., Taveira, L., Balaur, E., Ghicov, A., Sirotna, K., & Schmuki, P. (2005a). Self-organized TiO_2 nanotubes prepared in ammonium fluoride containing acetic acid electrolytes. *Electrochemistry communications, 7*(6), 576-580.

Tsuchiya, Hiroaki, & Schmuki, P. (2005b). Self-organized high aspect ratio porous hafnium oxide prepared by electrochemical anodization. *Electrochemistry communications, 7*(1), 49-52.

Vallet-Regí, María, & Arcos, D. (2008). Biomimetic nanoceramics in clinical use: from materials to applications: *Royal Society of Chemistry*.

Varghese, O. K., Paulose, M., Shankar, K., Mor, G. K., & Grimes, C. A. (2005). Water-photolysis properties of micron-length highly-ordered titania nanotube-arrays. *Journal of nanoscience and nanotechnology, 5*(7), 1158-1165.

Vasilev, K., Poh, Z., Kant, K., Chan, J., Michelmore, A., & Losic, D. (2010). Tailoring the surface functionalities of titania nanotube arrays. *Biomaterials, 31*(3), 532-540.

Venkataraman, S. K., Nelson, J. C., Hsieh, A. J., Kohlstedt, D. L., & Gerberich, W. W. (1993). Continuous microscratch measurements of thin film adhesion strengths. *Journal of adhesion science and technology, 7*(12), 1279-1292.

Wang, Daoai, Yu, B., Zhou, F., Wang, C., & Liu, W. (2009). Synthesis and characterization of anatase TiO_2 nanotubes and their use in dye-sensitized solar cells. *Materials Chemistry and Physics, 113*(2), 602-606.

Wang, Hui, Dai, D., & Wu, X. (2008a). Fabrication of superhydrophobic surfaces on aluminum. *Applied Surface Science, 254*(17), 5599-5601.

Wang, Li, H., Wang, J., Chen, S., Ma, Y., & Zhang, Z. (2012a). Study on the anticorrosion, biocompatibility, and osteoinductivity of tantalum decorated with tantalum oxide nanotube array films. *ACS applied materials & interfaces, 4*(9), 4516-4523.

Wang, Lu-Ning, Jin, M., Zheng, Y., Guan, Y., Lu, X., & Luo, J.-L. (2014). Nanotubular surface modification of metallic implants via electrochemical anodization technique. *International journal of nanomedicine, 9*, 4421.

Wang, Na, Li, H., Lü, W., Li, J., Wang, J., Zhang, Z., & Liu, Y. (2011). Effects of TiO_2 nanotubes with different diameters on gene expression and osseointegration of implants in minipigs. *Biomaterials, 32*(29), 6900-6911.

Wang, Na, Li, H., Wang, J., Chen, S., Ma, Y., & Zhang, Z. (2012b). Study on the anticorrosion, biocompatibility, and osteoinductivity of tantalum decorated with tantalum oxide nanotube array films. *ACS applied materials & interfaces, 4*(9), 4516-4523.

Wang, XJ, Li, Y., Lin, J., Yamada, Y., Hodgson, P., & Wen, C. (2008b). In vitro bioactivity evaluation of titanium and niobium metals with different surface morphologies. *Acta Biomaterialia, 4*(5), 1530-1535.

Wataha, J. C. (2000). Biocompatibility of dental casting alloys: a review. *The Journal of prosthetic dentistry, 83*(2), 223-234.

Wei, Jianhua, Igarashi, T., Okumori, N., Igarashi, T., Maetani, T., Liu, B., & Yoshinari, M. (2009). Influence of surface wettability on competitive protein adsorption and initial attachment of osteoblasts. *Biomedical Materials, 4*(4), 045002.

Wu, Guosong, Li, P., Feng, H., Zhang, X., & Chu, P. K. (2015). Engineering and functionalization of biomaterials via surface modification. *Journal of Materials Chemistry B, 3*(10), 2024-2042.

Wu, Xing, Jiang, Q.-Z., Ma, Z.-F., Fu, M., & Shangguan, W.-F. (2005). Synthesis of titania nanotubes by microwave irradiation. *Solid State Communications, 136*(9), 513-517.

Xiao, X., & Liu, R. (2008). Synthesis and bioactivity of highly ordered TiO_2 nanotube arrays. *Applied Surface Science, 255*(2), 365-367.

Xie, K., Li, J., Lai, Y., Lu, W., Zhang, Z. a., Liu, Y., Zhou, L., & Huang, H. (2011). Highly ordered iron oxide nanotube arrays as electrodes for electrochemical energy storage. *Electrochemistry communications, 13*(6), 657-660.

Xu, G., Shen, X., Hu, Y., Ma, P., & Cai, K. (2015). Fabrication of tantalum oxide layers onto titanium substrates for improved corrosion resistance and cytocompatibility. *Surface and Coatings Technology, 272*, 58-65.

Yaghoubi, H., Taghavinia, N., Alamdari, E. K., & Volinsky, A. A. (2010). Nanomechanical properties of TiO_2 granular thin films. *ACS applied materials & interfaces, 2*(9), 2629-2636.

Yang, Lei, Zhang, M., Shi, S., Lv, J., Song, X., He, G., & Sun, Z. (2014). Effect of annealing temperature on wettability of TiO_2 nanotube array films. *Nanoscale research letters, 9*(1), 1-7.

Yang, M., W., Liu, Y. W., Zhang, Q., Leng, Y. X., Zhou, H. F., Yang, P., Chen, J. Y., & Huang, N. (2007). Biomedical response of tantalum oxide films deposited by DC reactive unbalanced magnetron sputtering. *Surface and Coatings Technology, 201*(19–20), 8062-8065.

Yoriya, S., & Grimes, C. A. (2009). Self-assembled TiO2 nanotube arrays by anodization of titanium in diethylene glycol: approach to extended pore widening. *Langmuir, 26*(1), 417-420.

Yoriya, S., Mor, G. K., Sharma, S., & Grimes, C. A. (2008). Synthesis of ordered arrays of discrete, partially crystalline titania nanotubes by Ti anodization using diethylene glycol electrolytes. *Journal of Materials Chemistry, 18*(28), 3332-3336.

Yoriya, S., Paulose, M., Varghese, O. K., Mor, G. K., & Grimes, C. A. (2007). Fabrication of vertically oriented TiO_2 nanotube arrays using dimethyl sulfoxide electrolytes. *The Journal of Physical Chemistry C, 111*(37), 13770-13776.

Young, T. (1805). An essay on the cohesion of fluids. *Philosophical Transactions of the Royal Society of London, 95*, 65-87.

Yu, Wei-qiang, Qiu, J., Xu, L., & Zhang, F.-q. (2009). Corrosion behaviors of TiO_2 nanotube layers on titanium in Hank's solution. *Biomedical Materials, 4*(6), 065012.

Yu, Yuan-Hsiang, Lin, Y.-Y., Lin, C.-H., Chan, C.-C., & Huang, Y.-C. (2014). High-performance polystyrene/graphene-based nanocomposites with excellent anti-corrosion properties. *Polymer Chemistry, 5*(2), 535-550.

Zalnezhad, E, Hamouda, A., Faraji, G., & Shamshirband, S. (2015). TiO_2 nanotube coating on stainless steel 304 for biomedical applications. *Ceramics International, 41*(2), 2785-2793.

Zhang, Chuanyong, Wang, S., Huo, H., Huang, Z., Li, Y., Li, B., & Yang, Y. (2013). Preparation of helical mesoporous tantalum oxide nanotubes through a sol–gel transcription approach. *Chemistry–An Asian Journal, 8*(4), 709-712.

Zhang, Juzheng, Grabstanowicz, L. R., Gao, S., Hosmane, N. S., Huang, B., Dai, Y., Liu, D.-j., & Xu, T. (2012). Visible-light photocatalytic SiO_2/TiO_2−xCx/C nanoporous composites using $TiCl_4$ as the precursor for TiO_2 and polyhydroxyl tannin as the carbon source. *Catalysis Science & Technology*, *2*(2), 390-399.

Zhang, Peng, Wang, T., Zhang, J., Chang, X., & Gong, J. (2015a). Bridging the transport pathway of charge carriers in a Ta_3N_5 nanotube array photoanode for solar water splitting. *Nanoscale, 7*(31), 13153-13158.

Zhao, L., Chu, P. K., Zhang, Y., & Wu, Z. (2009). Antibacterial coatings on titanium implants. *Journal of Biomedical Materials Research Part B: Applied Biomaterials, 91*(1), 470-480.

Zhao, L., Mei, S., Chu, P. K., Zhang, Y., & Wu, Z. (2010). The influence of hierarchical hybrid micro/nano-textured titanium surface with titania nanotubes on osteoblast functions. *Biomaterials, 31*(19), 5072-5082.

Zhao, L., Wang, H., Huo, K., Zhang, X., Wang, W., Zhang, Y., Wu, Z., & Chu, P. K. (2013). The osteogenic activity of strontium loaded titania nanotube arrays on titanium substrates. *Biomaterials, 34*(1), 19-29.

Zwilling, V., Aucouturier, M., & Darque-Ceretti, E. (1999). Anodic oxidation of titanium and Ti-6Al-4V alloy in chromic media. An electrochemical approach. *Electrochimica Acta, 45*(6), 921-929.

LIST OF PUBLICATIONS AND PAPERS PRESENTED

List of Papers (ISI Journals)

Related Publication

1.Sarraf, M., E. Zalnezhad, A. R. Bushroa, A. M. S. Hamouda, S. Baradaran, B. Nasiri-Tabrizi, and A. R. Rafieerad. "Structural and mechanical characterization of Al/Al 2 O 3 nanotube thin film on TiV alloy." Applied Surface Science 321 (2014): 511-519. (**Q1**, ISI-Cited Publication, 5-Year Impact Factor: **2.735**)

2.Sarraf, M., E. Zalnezhad, A. R. Bushroa, A. M. S. Hamouda, A. R. Rafieerad, and B. Nasiri-Tabrizi. "Effect of microstructural evolution on wettability and tribological behavior of TiO 2 nanotubular arrays coated on Ti–6Al– 4V."Ceramics International 41, no. 6 (2015): 7952-7962. (**Q1**, ISI-Cited Publication, 5-Year Impact Factor: **2.540**)

3.Masoud Sarraf, Bushroa Abdul Razak, Ali Dabbagh, Bahman Nasiri-Tabrizi, Noor Hayaty Abu Kasim, Wan Jefrey Basirun"Optimizing PVD conditions for electrochemical anodization growth of well-adherent Ta 2 O 5 nanotubes on Ti–6Al–4V alloy". RSC Advances 6(82), (2016): p. 78999-79015. (**Q1**, ISI-Cited Publication, 5-Year Impact Factor: **3.289**)

4.Masoud Sarraf, Bushroa Abdul Razak , Bahman Nasiri-Tabrizi , Ali Dabbagh ,Noor Hayaty Abu Kasim , Wan Jefrey Basirun, Eshamsul Bin Sulaiman"Nanomechanical properties, wear resistance and in-vitro characterization of Ta2O5 nanotubes coating on biomedical grade Ti-6Al-4V" Journal of the Mechanical Behavior of Biomedical Material (2017):66:p.159-171. (**Q1**, ISI-Cited Publication, 5-Year Impact Factor: **3.152**)

Other Publications

5. Javadi, F. S., Rismanchi, B., **Sarraf, M.,** Afshar, O., Saidur, R., Ping, H. W., & Rahim, N. A. (2013). **"**Global policy of rural electrification**"**. *Renewable and Sustainable Energy Reviews, 19*, 402-416. (**Q1**, *ISI-Cited Publication, 5-Year Impact Factor:* **7.445**)

6. Sarraf, M., Rismanchi, B., Saidur, R., Ping, H. W., & Rahim, N. A. (2013). "Renewable energy policies for sustainable development in Cambodia".*Renewable and Sustainable Energy Reviews, 22*, 223-229. (**Q1**, *ISI-Cited Publication, 5-Year Impact Factor:* **7.445**)

7. M.H. Mahfuz, A. Kamyar, O. Afshar, **M. Sarraf**, M.R. Anisur, M.A. Kibria, R. Saidur, I.H.S.C. Metselaar, **"**Exergetic analysis of a solar thermal power system with PCM storage", Energy Conversion and Management, 78 (2014) 486-492. (**Q1**, *ISI-Cited Publication*, 5-Year Impact Factor: **4.512)**

8. Nasiri-Tabrizi, Bahman, Erfan Zalnezhad, A. M. S. Hamouda, W. J. Basirun, Belinda Pingguan-Murphy, Abbas Fahami, **M. Sarraf**, and A. R. Rafieerad. "Gradual mechanochemical reaction to produce carbonate doped fluorapatite–titania composite nanopowder." *Ceramics International* 40, no. 10 (2014): 15623-15631. (**Q1**, *ISI-Cited Publication*, 5-Year Impact Factor: **2.540**)

9.Rafieerad, A. R., E. Zalnezhad, A. R. Bushroa, A. M. S. Hamouda, **M. Sarraf**, and B. Nasiri-Tabrizi. "**S**elf-organized TiO 2 nanotube layer on Ti–6Al–7Nb for biomedical application." *Surface and Coatings Technology* 265 (2015): 24-31. (**Q1**, *ISI-Cited Publication*, 5-Year Impact Factor: **2.374**)

10. Rafieerad, A. R., A. R. Bushroa, E. Zalnezhad, **M. Sarraf,** W. J. Basirun, S. Baradaran, and B. Nasiri-Tabrizi. "Microstructural development and corrosion behavior of self-organized TiO 2 nanotubes coated on Ti–6Al–7Nb." *Ceramics International* 41 (2015):9: 10844-10855. (**Q1,** *ISI-Cited Publication*, 5-Year Impact Factor: **2.374**)

11.E. Zalnezhad, E. Maleki, S.M. Banihashemian, J.W. Park, Y.B. Kim, **M. Sarraf**, A.A.D.M. Sarhan, S. Ramesh" Wettability, structural and optical properties investigation of TiO2 nanotubular arrays" *Materials Research Bulletin* (2016) 78: p. 179-185. (**Q1**, ISI-Cited Publication, 5-Year Impact Factor: **2.380**)

12. Mohammad Hemmat Esfe, Wei-Mon Yan, Masoud Afrand, **M Sarraf**, Davood Toghraie, Mahidzal Dahari" Estimation of thermal conductivity of Al 2 O 3/water (40%)–ethylene glycol (60%) by artificial neural network and correlation using experimental data" *International Communications in Heat and Mass Transfer* (2016) 74:p. 125-128 (**Q1**, ISI-Cited Publication, 5-Year Impact Factor: **2.893**)

Chapter Book

M. Sarraf, A.R. Bushroa, B. Nasiri-Tabrizi , N.H. Abu Kasim and W.J. Basirun "Anodic nanotubular oxide layers on Ti–6Al–4V alloy for bio-implant applications ", in *Microscopy and imaging science: practical approaches to applied research and education* A. Méndez-Vilas, Editor 2016.

Patent

M. Sarraf, A.R. Bushroa,B. Nasiri-Tabrizi ,E.Zalnezhad, S. Baradaran, N.H.Abu Kasim "A New Approach to Fabricate Al/Al_2O_3 Nanotube Thin Film on Ti-6Al-4V Alloy" UM.TNC2/UMCIC/603/802:PI 2016700835.